Holographic Resolution and Its Application in Memory and Imaging

Thesis by

Wenhai Liu

In Partial Fulfillment of the Requirements

for the Degree of

Doctor of Philosophy

California Institute of Technology

Pasadena, California

2001

(Submitted May 18, 2001)

To my Family

Acknowledgements

It has been such great pleasant five years staying on the beautiful Caltech campus, studying in the friendly Psaltis' kingdom, and sharing the joys, hard works, cookies and coffee during day or late night in the lab. I would like to thank Prof. Demetri Psaltis for his support and guidance during these years, not only as a leader and adviser on my career, but also as a friend and ShiFu in my life.

During all these years, the friendship and kindness of all group members have made it always a joy to me staying in the lab. I would especially thank Ms. Lucinda Acosta and Linda (secretary in EE department), who handled all administrative works patiently and professionally and made my life much easier. Thanks for Ms. Yayun Liu to make the labs such a fun playgound to explore and "steal" all those precious components from each others. Thanks David to install the first computer in my lab which is amazingly still working. Thanks all previous students, Drs. Allen Pu, Mike Levene, JJ Drolet, Ali Adibi, Xu Wang, Xin An in this group for their guiding and helpful discussion, especially thanks to Dr. George Barbastathis for handing over his lab to me, and Dr. Ernest Chuang for working together on the phase conjugate module. Thank Dr. Christophe Moser for sharing the joys on HTMT meetings, Dr. Greg Steckman and Greg Billock on all the discussions on electronic and optical issues. Also unforgettable are all the brain storming with current students, friendly cooperation in the lab, and friendly fighting on optical space and components, especially the kindly help on polymer material from Jose Mumbru, helps on crystal material from Yunping Yang. And I always learn something whenever working and discussing with Zhiwen Liu. Also wish all other guys in the group good luck in the coming years.

During all these years, I would also like to thank my families and all friends, back in china or in the States, for their patience, understand and support on my Ph.D. education and life. Especially thanks to my sister for her role modeling on academic

career since I was a kid. Thanks to Xiaolin, my wife, for all the joys and frustration we went through among those years in school. All the joys and memories have been the major reason to keep me moving on in schools. And finally thanks to Nicky, my buddy and little nephew, who is always patient teaching me his new physics in baby language, showing me the bright prospect in the future, and making me work harder to catch up .

Abstract

Optical information storage and optical information processing are two major applications of holography, with significantly different holographic philosophies. For a holographic memory system, a complex holographic pattern encoded with the storage data is recorded first, and is read out later by a simple pre-designed reference beam. For a holographic information processing system, a pre-designed holographic pattern is stored in the medium first, and is probed by complex incident signal wave fronts. The pre-designed hologram extracts certain components from the complex input and diffract them as specific reference wave fronts. Holographic resolution, or Bragg phase selectivity in spatial and spectral dimensions, plays a key role in both applications. It determines the information capacity to be stored in and reconstructed from the hologram memory, or the information capacity to be extracted and processed by a hologram from the complex signal input. In this thesis, we investigate the holographic resolution in volume holograms and its specific issues in both applications.

In a phase conjugate holographic memory system, we demonstrate the recording and reconstruction of a submicron pixel resolution, leading to the potential of storing 1 Gbit in 1 cm^3 volume holographically. Phase conjugate reconstruction eliminates the optical resolution limit by the imaging optics and reduces the system volume and cost. Phase conjugate reconstruction and its multiplexing in a compact holographic module are investigated.

In general, a volume hologram has two degenerate Bragg phase-matching dimensions besides the spatial and spectral selectivity, in which significant diffraction is present. They provide a potential ability for optically sectioning a two-dimensional slice from the spatial plus spectral hyperspace and for linearly transferring the information onto a two-dimensional sensor array by a single hologram. The resolution of optical sectioning and information transformation is not only determined by the volume hologram diffraction intensity selectivity but also by the holographic architecture

and the transformation aberration.

We study two holographic architectures theoretically and experimentally, on issues of optical sectioning and linear transformation for imaging application. By designing a transmission geometry system, we have achieved a linear 2-D optical sectioning and imaging from a 4-D object hyperspace (3-D spatial plus spectral dimension). By optical sectioning of multiplexed holograms, the ability of imaging 3-D spatial information from an object without a scanning mechanism is demonstrated by a holographic imaging system.

Contents

List of Figures

List of Tables

Chapter 1 Introduction

Holography was invented by Dennis Gabor in 1948 [46], when the new imaging technique using two coherent waves was proposed to enhance the image resolution in microscope application. Since 1960s when the coherent light source — laser was available, holography has been intensively studied on the interests of three dimensional (3-D) object imaging and projection [74], in which the holography can be treated as an analog memory system. The complex signal wave front diffracted from an object is recorded including both amplitude and phase information, inside either a volume photorefractive material, or a thin photosensitive film. It can be reconstructed later, regenerating an image of the object. In the last one or two decades, the majority of research interests on holography application have been concentrated on the new generation digital data storage techniques [104, 108], thanks to the fast development of computer technology and internet that has been driving data memory technology to evolve exponentially on larger capacity and faster access time.

Holographic resolution plays a key role in both holographic imaging and holographic memory applications. It determines the information capacity of hologram storage or information capacity processed by a single hologram.

In a general holographic memory system, the complex signal beam interferes with a coherent reference beam, which is a simple or predesigned wave front and can be easily reproduced. The signal information is recorded as the complex holographic patterns inside the material. The reproduced reference beam is diffracted by the holographic grating inside the storage medium, and recovers the signal wave front. The achievable reconstruction resolution, determined by the holographic recording and reconstruction bandwidth, gives the information capacity each hologram contains. For large capacity data storage, hologram multiplexing technology is normally used. The multiplexing selectivity due to volume Bragg phase-matching determines the reference resolution required for reconstructing a certain page of data.

In a general holographic imaging application, the predesigned holographic gratings are recorded inside the medium, which can work as a signal filter or an optical processor. As a complex probing signal illuminates the hologram, only those wave front components Bragg phase-matching the hologram are diffracted significantly and projected into the reference beams. The projected reference beams can be different from the signal components with a certain information representation, such as in optical correlators and optical interconnects [103, 80]. Or the projected reference beams are a linear transformation of the signal beams, such as in applications of diffractive elements [119], and holographic imaging. The spatial and spectral selectivities of the hologram determine how accurate the signal can be selected and extracted from the complex probing input, and then be projected into a high-resolution information representing reference beam.

In this thesis, we study the holographic resolution in volume holograms experimentally and theoretically in Chapter 2, and address the specific issues in both applications of memory (Chapter 3) and imaging (Chapter 4).

For holographic memory system, submicron resolution pixel patterns are demonstrated. To achieve the holographic resolution in a holographic memory system, phase conjugate reconstruction is used to eliminate the optical resolution limit by imaging system and to reduce the system cost and volume in a compact holographic memory module. The phase conjugate reconstruction and multiplexing are demonstrated and investigated on the issues of efficiency and system performance.

For holographic imaging, the imaging resolution and aberration are investigated theoretically and experimentally for two holographic architectures in Chapter 4. 3-D imaging without a scanning mechanism by a multiple-hologram imaging system is demonstrated.

Both the hologram reconstruction resolution in memory application and the holographic imaging resolution are dominantly determined by the geometric volume Bragg phase-matching effect at one wavelength. On the other hand, there is another interesting resolution issue on the frequency domain or time domain holograms, which depends on the material frequency response properties, the material response time

and relaxation time constant. The frequency or time domain resolution is very interesting to the applications in pulse shaping or fast image recording, where spectral hole burning material is widely used. In Chapter 5, we investigate the dynamic range properties on spectral hole burning material, with the concern for data storage instead of properties in frequency domain.

Chapter 2 Holographic Bandwidth and Resolution

Holographic image resolution and the quality of holograms have been studied since 1960s when the laser and hologram technologies were proposed and demonstrated [83, 24, 25]. The major applications with consideration of holographic image resolution are 3-D image recording and projection such as its application in modern holographic particle velocimetry [12, 13, 58, 133, 116], and 2-D image capture and projection, such as holographic imaging element development [98, 42] and holographic high-resolution lithography [51, 53, 52, 78, 34, 77]. Most of the studies are on thin recording media or thin holographic imaging elements. In this thesis, we will concentrate on the properties of volume holograms, which have the advantages of large dynamic range and fine spatial/wavelength selectivities. The ability of hologram multiplexing in volume holographic media is also crucial for applications in data storage (Chapter 3) and holographic imaging (Chapter 4).

There are two different issues for the holographic image resolution. These two issues coexist in all applications, however with different concerns. One is the resolution of the recovered holograms, which determines the minimum feature size generated by holograms. In other words, it determines how much information can be recovered from the holograms, such as in velocimetry and lithography, where all the optical information is stored in holograms and then regenerated. The resolution of the hologram is determined by the bandwidth of the optical system including the holographic material recording and readout bandwidth, or the effective numerical aperture (NA) of the system [50]. Another resolution is related to the alignment of Bragg phase-matching and the aberration caused by the hologram. This is the major concern in the holographic element development, where information is coming from outside as a complex signal wave front and is processed, filtered, and projected by the holo-

graphic element. It is determined by the holographic diffraction characteristics, such as grating distribution, size and phase-matching of the holographic gratings.

In this chapter, we study the resolution of reconstructed holograms in $LiNbO_3$ 90-degree geometry, with concerns of data storage application in Chapter 3. Later in Chapter 4, we study the resolution and imaging properties of volume holographic elements and their potential application.

2.1 Theoretical simulation

For a normal imaging system, such as a telescope or microscope, the fundamental image resolution is determined by the diffraction limit of the optical system, or the numerical aperture NA [50, 16].

For a holographic system to record an input optical field in a holographic medium, and then to recover the optical field, the final image resolution is limited by both the diffraction limit of optical system in the same way as a normal imaging system, and the effects of the holographic recording and reading out, which we define as holographic recording and readout bandwidth. For a complex input optical field with different spatial frequency components, different grating components are generated and recorded by interference with a reference beam inside the holographic recording medium, such as a photorefractive crystal or photopolymer. However, these different grating components have different recording and readout strength because of the various grating direction, period, and polarization, *i.e.*, angle-dependent grating strength, which depends on the material properties and the grating formation [137].

Here, we study the relative holographic recording and reconstruction strength in $LiNbO_3$ of 90-degree geometry with a complex signal optical field and a simple plane wave reference beam, as shown in Fig. 2.1, which is widely used for holographic correlators and data storage as in Chapter 3. For other geometries, such as transmission [137] and reflection geometry, the difference is only on the angle between the signal beams and reference beam, which induces the different grating period and direction distribution relative the $\boldsymbol{c}$-axis of the crystal. The holographic bandwidth

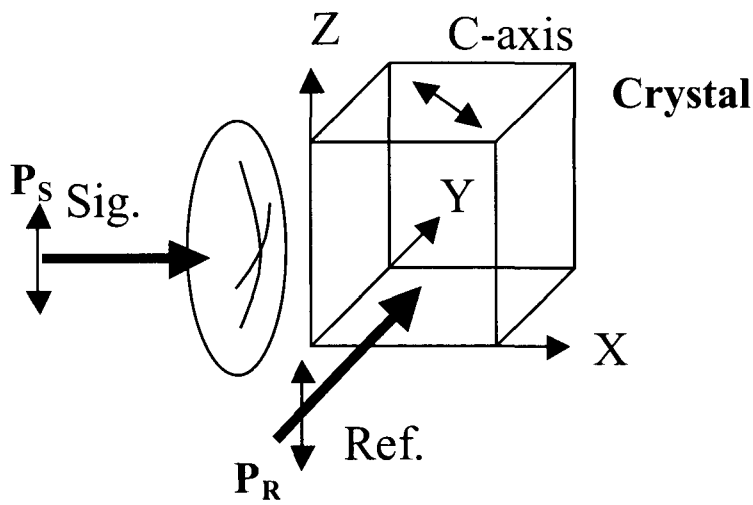

Figure 2.1: The 90-degree geometry for holographic recording in a photorefractive crystal.

for different geometry shows similar behavior from theoretical simulation.

For 90-degree geometry, the crystal is 45-degree cut with $\boldsymbol{c}$-axis along direction $(1, -1, 0)$ in Fig. 2.1. The reference beam is assumed as a plane wave, coming into the crystal at normal direction with wave vector $(0, k_0, 0)$ and an ordinary polarization $\boldsymbol{P_R} = (0, 0, 1)$. The signal beam consists of various spatial frequency components $\boldsymbol{k_y}, \boldsymbol{k_z}$ in or out of the plane of $\boldsymbol{c}$-axis and reference beam.

Considering one spatial frequency component with transverse wave vector $(\boldsymbol{k_y}, \boldsymbol{k_z})$, the signal beam comes into the crystal with wave vector (k_x, k_y, k_z). Here, we consider all optical waves inside the crystal only, and ignore the interface between air and the crystal, which are calculated later for comparison with experiments in section 2.2. Therefore, $k_x^2 + k_y^2 + k_z^2 = k_0^2 = (2\pi n/\lambda)^2$, where n is the refractive index of the material, and the signal beam has an ordinary polarization $\boldsymbol{P_S}$,

$$\boldsymbol{P_S} = \left(-\frac{k_x k_z}{k_0 \sqrt{k_x^2 + k_y^2}}, -\frac{k_y k_z}{k_0 \sqrt{k_x^2 + k_y^2}}, \frac{\sqrt{kx_2 + k_y^2}}{k_0} \right). \tag{2.1}$$

The grating vector is $\boldsymbol{G} = (k_x, k_y - k_0, k_z)$, and both the magnitude G and the

direction $\hat{\boldsymbol{g}}$ are functions of $\boldsymbol{k_y}, \boldsymbol{k_z}$. With the assumption of equal intensity for the reference and signal beams, and using the known parameters of the material, such as the total dopant (Fe) density, initial Fe^{3+} concentration, acceptors density, photovoltaic parameter, photoexcitation cross-section, the carrier combination rate and carrier mobility from previous studies, we can calculate the spatial charge field $\boldsymbol{E_g}$ as a function of $\boldsymbol{k_y}$ and $\boldsymbol{k_z}$ by solving the Kukhtarev equations [68, 69]. The detail derivation is shown in the following section 2.4.

The effective phase grating caused by the space charge field is given by Pockels' effect [118, 129]

$$\Delta\varepsilon \;=\; \boldsymbol{P_S} \cdot (\overline{\overline{\boldsymbol{r}}} \cdot \hat{\boldsymbol{g}}) \cdot \boldsymbol{P_R} E_G, \tag{2.2}$$

where $\overline{\overline{\boldsymbol{r}}}$ is the electro-optic tensor. The effective grating strength as a function of $\boldsymbol{k_y}/k_0, \boldsymbol{k_z}/k_0$ is simulated and shown in Fig. 2.2. Consider two special cases in

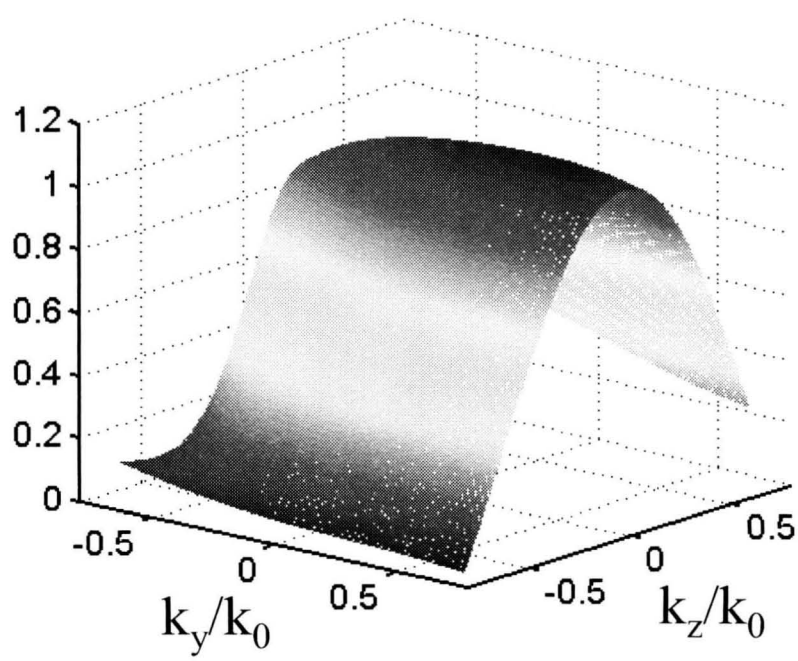

Figure 2.2: Theoretical calculation of the normalized phase grating strength as a function of the signal beam spatial frequencies $\boldsymbol{k_y}, \boldsymbol{k_z}$.

details. First, the signal beams are in the $\boldsymbol{X-Y}$ plane as a function of $\boldsymbol{k_y}$ with

$k_z = 0$. The grating vectors G is also in the plane, and tilted away from the c-axis. And the grating period is a function of k_y. The modulation depth keeps as a constant while signal polarization keeps the same as of the reference along the $(0, 0, 1)$ direction. On the other hand, the signal beam tilts in the $X - Z$ plane with various signal spatial frequency k_z and $k_y = 0$. In addition to the angle-dependent grating direction and period, the polarization of the signal beam is not the same as that of the reference beam, which decreases the modulation depth and the effective photorefractive coefficient. In Fig. 2.3, the theoretical simulation results

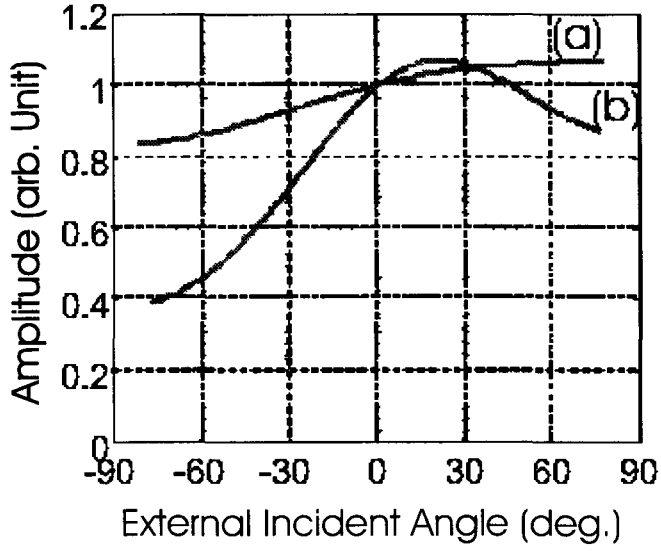

Figure 2.3: The theoretical simulation of the holographic recording and reconstruction amplitudes of $LiNbO_3(Fe)$ in 90-degree geometry as a function of the signal incident angle in the signal-reference plane (a) and out of the signal-reference plane (b).

of the recording and reconstruction efficiencies are shown as functions of the signal external incident angle, which correspond to spatial frequency k_y with $k_z = 0$ in $X - Y$ plane, or spatial frequency k_z with $k_y = 0$ with consideration of the refraction effect at the interface. It indicates that the holographic bandwidth of the $LiNbO_3(Fe)$ is very broad and can record the spatial frequency as broad as pixel size of submicron with wavelength $0.5\,\mu m$.

2.2 Experimental measurement

Theoretical simulation on holographic recording and reconstruction in $LiNbO_3(Fe)$ of 90-degree geometry indicates a broad bandwidth. Here we confirm the theoretical studies by direct measurement of the holographic recording and readout bandwidth, and a holographic reconstruction of a photomask with gradient pixel sizes ranging from $2 \times 2 \quad \mu m^2$ to $0.2 \times 0.2 \quad \mu m^2$.

Measurement of the holographic bandwidth

Fig. 2.4 shows the setup for holographic recording and readout in a $LiNbO_3(Fe)$ 90-degree geometry. The reference beam is a plane wave of ordinary polarization incident at normal direction of the interface. The signal beam is another plane wave coming at different angle in or out of the reference-***c***-axis plane. All the holograms are recorded and read out with normalization to the strength of the normal signal beam incidence.

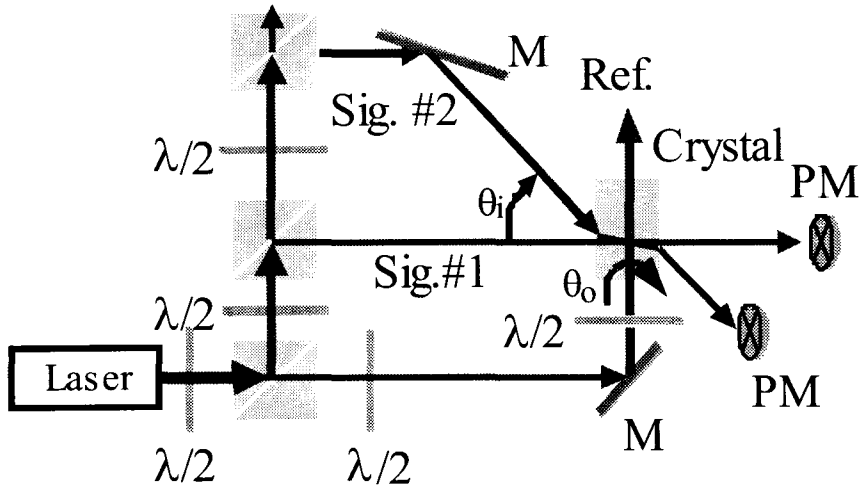

Figure 2.4: Experimental setup for holographic bandwidth measurement. **M**: mirror; **Sig.**: signal beam; **Ref.**: reference beam; **PM**: power meter; $\lambda/2$: half-wavelength plate. For in-plane measurement, **Sig.**#2 rotates by θ_i and is adjusted to have the same intensity as the normal incident **Sig.**#1 inside the crystal by considering the Fresnel reflection loss. The diffraction efficiency for **Sig.**#2 is measured relative to the **Sig.**#1 diffraction efficiency. For out-of-plane measurement, only the **Sig.**#1 is used. The crystal and the reference polarization direction are rotated by θ_o around reference beam direction.

We measure the relative holographic recording and reconstruction intensity for

different signal incident angles in and out of the reference-c-axis plane. The measurement of the hologram intensity is shown in Fig. 2.5 and compared with the theoretical simulation from section 2.1. The Fresnel reflection losses are also taken into consid-

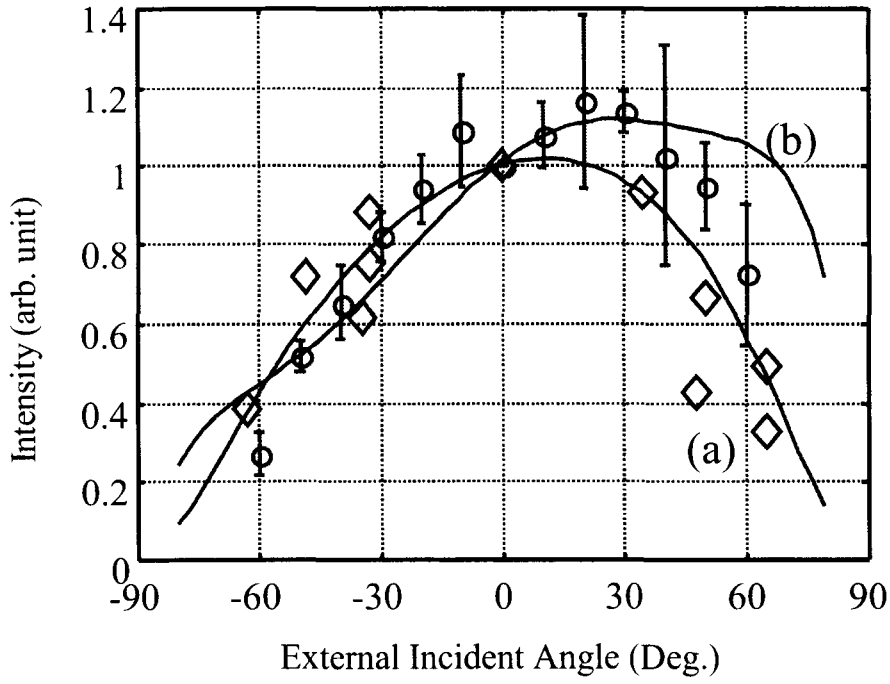

Figure 2.5: (a) The experimental data ($\diamond$) and the theoretical calculation of holographic efficiency in the signal reference plane; (b) The experimental data ($\circ$) and the theoretical calculation of the holographic efficiency out of signal reference plane.

eration in Fig. 2.5 because the crystal used in the experiment is not antireflection coated. The transmission factors at the interface are functions of the signal beam incident angle for in- and out-of-plane components [16]

$$T_{\perp} = \frac{\sin(2\theta_1)\sin(2\theta_2)}{\sin^2(\theta_1+\theta_2)}, \tag{2.3}$$

$$T_{\parallel} = \frac{\sin(2\theta_1)\sin(2\theta_2)}{\sin^2(\theta_1+\theta_2)\cos^2(\theta_1+\theta_2)}, \tag{2.4}$$

where $T_{\perp}, T_{\parallel}$ are the intensity transmission for polarization perpendicular and parallel to the incident plane, and the Snell's law of incident and refraction angles $n_1 \sin\theta_1 = n_2 \sin\theta_2$.

The experimental data are consistent with the theoretical simulation and indicate

broad holographic bandwidth even with consideration of the interface effects.

Experimental demonstration of holographic pixel size

Both the holographic bandwidth calculation and measurement indicate a broad bandwidth for holographic recording and reconstruction of submicron pixels. To demonstrate it experimentally, we design and fabricate a photomask with gradient pixel size ranging from $2 \times 2\ \mu m^2$ to $0.2 \times 0.2\ \mu m^2$. The photomask is used as a spatial light modulator for the signal beam, which is recorded as holograms and reconstructed. Due to the extremely large spatial frequency, high numerical aperture objective lens is required to magnify the image of the mask. Shown in Fig. 2.6, is the direct image of the photomask observed by a Nikon $\times 40$ (NA 0.65) objective lens illuminated by 488 nm Argon laser line. The smallest pixel $0.2 \times 0.2\ \mu m^2$ is already beyond the resolution power of the lens.

To study the quality of the holographic recording and its reconstruction, we use the phase conjugate reconstruction and image it with the same objective lens, as shown in Fig. 2.7.

Comparing the phase conjugate reconstruction of the hologram with the image quality of the photomask by direct imaging, there is no degradation from the direct image, which is limited by the resolving power of the objective lens. To study quantitatively the resolution of the images, the image width of the pixel is plotted as a function of the actually physical width designed and assumed accurately etched on the photomask by electron beam lithography. Fig 2.8 shows the flattening of the image size as the pixel size gets comparable and smaller than the wavelength 488 nm. The solid curve is the theoretical width by convolutions of the pixel physical width and the objective lens resolution $\Delta l \simeq 0.61\lambda/NA$ [50, 16]. The same theoretical curve is shown in Fig. 2.9, and compared with the pixel image width of the phase conjugate construction through the same objective lens. The flattened image size indicates the final resolution of the phase construction image, which depends on the objective lens resolving power and the holographic recording and reconstruction bandwidth. The results in Fig. 2.9 indicate that the final image resolution is predominantly limited by the objective lens NA 0.65 in our experiments. In other words,

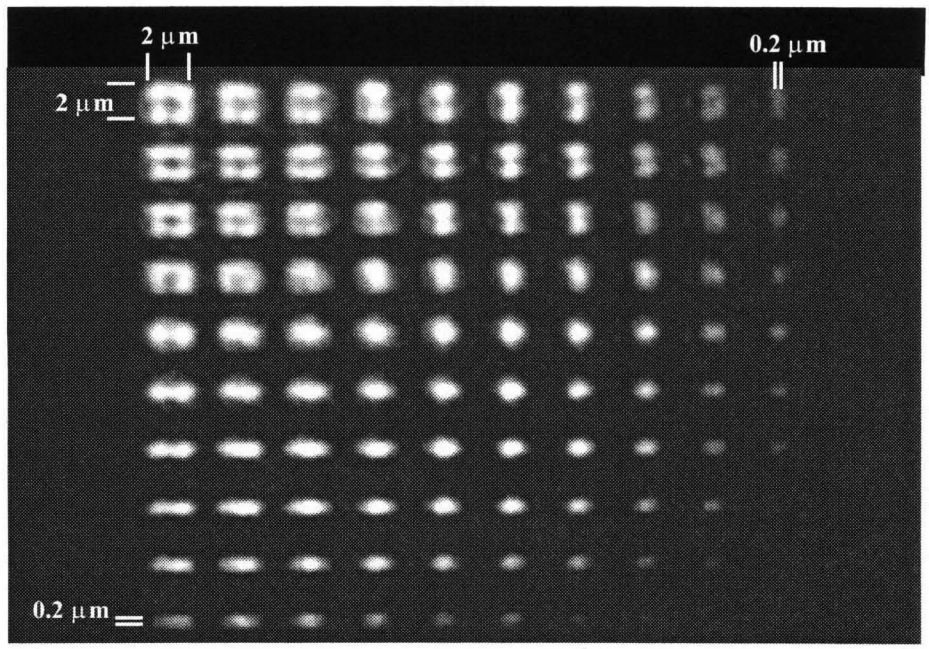

Figure 2.6: The direct image of a resolution photomask with pixels from 2×2 μm^2 to 0.2×0.2 μm^2. (Imaged by a Nikon $\times 40$ NA 0.65 objective lens)

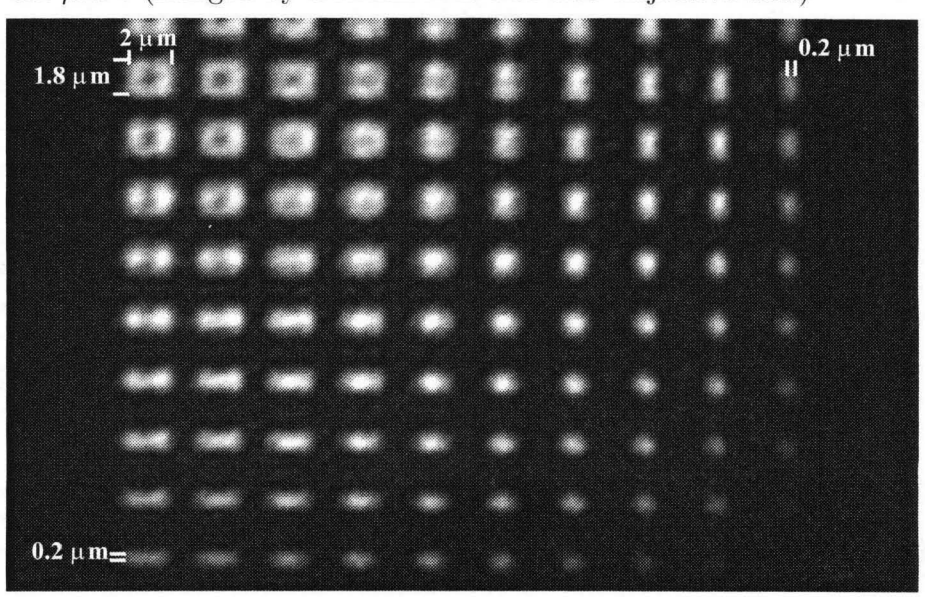

Figure 2.7: The holographic phase conjugate reconstruction of the photomask. (Imaged by a Nikon $\times 40$ NA 0.65 objective lens)

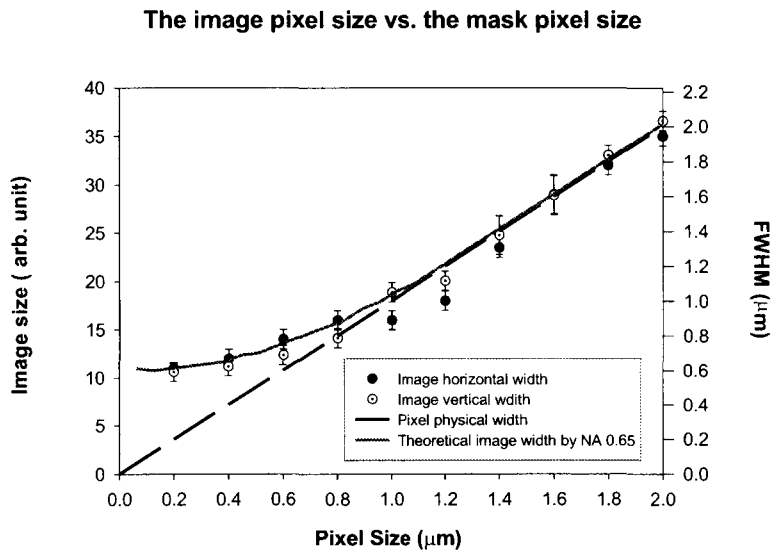

Figure 2.8: The direct image pixel size of a resolution photomask with pixels from 2 $\times$ 2 μm^2 to 0.2 $\times$ 0.2 μm^2. (Imaged by a Nikon $\times$40 NA 0.65 objective lens)

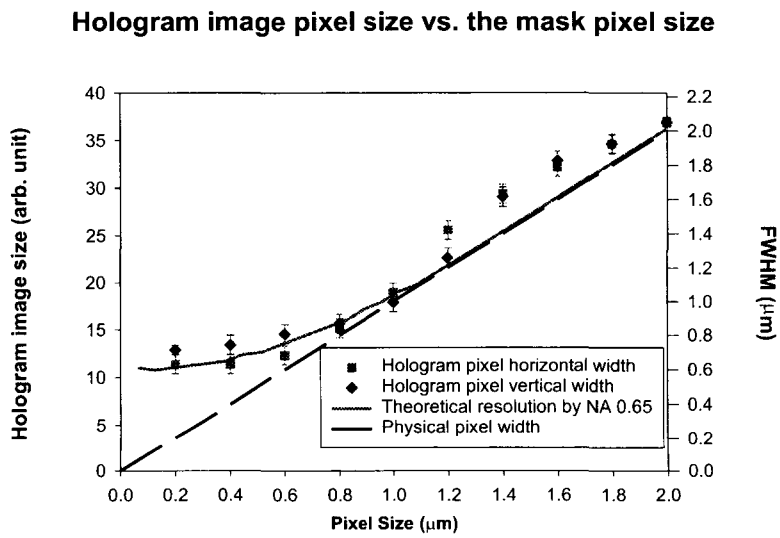

Figure 2.9: The image pixel size of holographic phase conjugate reconstruction of the photomask. (Imaged by a Nikon $\times$40 NA 0.65 objective lens)

the holographic recording and reconstruction bandwidth is comparable with or larger than the objective lens with NA 0.65.

2.3 Discussion

From the theoretical studies and experimental measurement, we show a wide holographic recording and reconstruction bandwidth and demonstrate high resolution of hologram reconstruction in $LiNbO_3(Fe)$ crystals in 90-degree geometry. This high bandwidth leads to a potential superfine pixel recording in data storage application if the spatial light modulator is attached directly to the crystal, or matching liquid is used to overcome the diffraction limit in the air. This is in principle the same mechanism used for oil immersion lenses.

This high holographic bandwidth depends on the property of the photorefractive materials, and is related to the grating orientation and period inside the medium. We study experimentally the same holographic recording and reconstruction of the gradient photomask in Dupont polymer with transmission geometry and fail to reconstruction the $2 \times 2\ \mu m^2$ pixel size with reasonable quality. The possible reason is a much smaller intrinsic holographic bandwidth in Dupont polymer due to the holographic recording dynamics dependence on grating periods and the shrinkage.

Another potential application of the high bandwidth of the holograms is image processing, *i.e.*, extracting the superfine features from outside signal beams and projecting them onto imaging plane. The high bandwidth hologram works more like a fine spatial filter selecting only the features used for recording from the complex signal input and projecting them in the reference direction, such as the usage in a confocal microscope [8]. More detailed studies on imaging with a volume hologram in Chapter 4 show that the resolution is primarily dependent on the alignment and the aberration caused in the degenerate direction, instead of the holographic bandwidth.

2.4 Derivation

In this section, we give the derivation of the angle-dependent phase grating strength in $LiNbO_3(Fe)$ of 90-degree geometry. The derivation follows the solution of Kukhtarev equations, which is widely used as a general model for photorefractive effects [68, 69, 88, 89]. We follow the steps and use the known parameters of the material in previous works [54, 19, 21], while ignoring the thermal generation and non-isotropic of the materials for simplicity.

Formation of Spatial Charge Field

When an intensity pattern is illuminated inside a $LiNbO_3$ crystal,

$$I(\boldsymbol{r}) = I_0 + I_1 e^{j\boldsymbol{G}\cdot\boldsymbol{r}}, \tag{2.5}$$

electrons are excited from the traps by absorbing photon energies and are described by the Kukhtarev equations:

$$\text{Rate equation} \quad \frac{\partial N_D^+}{\partial t} = (sI+\beta)(N_D - N_D^+) - \gamma_R N_D^+ n, \tag{2.6}$$

$$\text{Continuity equation} \quad \frac{\partial n}{\partial t} = \frac{\partial N_D^+}{\partial t} + \frac{1}{q}\nabla\cdot\boldsymbol{J}, \tag{2.7}$$

$$\text{Current density} \quad \boldsymbol{J} = q\mu n\boldsymbol{E} + k_B T\mu\nabla n - p(N_D - N_D^+)I(\boldsymbol{r})\hat{\boldsymbol{c}}, \tag{2.8}$$

$$\text{Poisson's equation} \quad \nabla\cdot\epsilon\boldsymbol{E} = q(N_D^+ - n - N_A), \tag{2.9}$$

where the assorted parameters are listed in Table 2.1.

To linearize the equations, the distributions are assumed to have DC and first-order components:

$$\boldsymbol{E} = \boldsymbol{E_0} + \boldsymbol{E_1} e^{j\mathbf{G}\cdot\mathbf{r}}, \tag{2.10}$$

$$N_D^+ = N_{D0}^+ + N_{D1}^+ e^{j\mathbf{G}\cdot\mathbf{r}}, \tag{2.11}$$

$$n = n_0 + n_1 e^{j\mathbf{G}\cdot\mathbf{r}}, \tag{2.12}$$

$$\boldsymbol{J} = \boldsymbol{J_0} + \boldsymbol{J_1} e^{j\mathbf{G}\cdot\mathbf{r}}, \tag{2.13}$$

N_D	Density of dopants (total Fe concentration)
N_D^+	Density of ionized dopants (Fe^{3+} concentration)
n	Density of electrons in the conduction band
N_A	Compensative acceptors
$I(\boldsymbol{r})$	Optical intensity in the crystal
$\boldsymbol{E}$	Total electric field
$\boldsymbol{J}$	Total current density
β	Thermal generation rate
s	Photoexcitation cross-section
γ_R	Carrier recombination rate
p	Photovoltaic constant
μ	Carrier mobility
ϵ	Dielectric constant of the crystal
q	Charge of the electron
k_B	Boltzmann's constant
T	Temperature
t	Time

Table 2.1: Variables in Kukhtarev equations (2.6)–(2.9).

Substituting them into the Kukhtarev equations and first considering the DC response only, we get the solution as

$$\begin{aligned} n_0 &= \frac{sI_0(N_D - N_{D0}^+)}{\gamma_R N_{D0}^+}(1 - e^{-t\gamma_R N_{D0}^+}) \\ &\approx \frac{sI_0(N_D - N_{D0}^+)}{\gamma_R N_A} \ll N_{D0}^+, \qquad (2.14) \\ N_{D0}^+ &= n_0 + N_A \\ &\approx N_A, \qquad (2.15) \\ \boldsymbol{J_0} &= q\mu n_0 \boldsymbol{E_0} - p(N_D - N_A) I_0 \hat{\boldsymbol{c}}, \qquad (2.16) \end{aligned}$$

where the recombination rate $\gamma_R N_{D0}^+$ is much higher than the excitation rate $sI_0(N_D - N_{D0}^+)$. Therefore, the free electron density n_0 reaches a small equilibrium value rapidly, which we treat as a constant function of light intensity I_0. In equation (2.16), there exists a constant current density $\boldsymbol{J_0}$, which is dominated by the photovoltaic effect. If there is no outside applied voltage, the current density will eventually drop to zero when a constant photovoltaic field $\boldsymbol{E_0} = \boldsymbol{E_{0ph}} = \frac{p(N_D - N_A) I_0 \hat{\boldsymbol{c}}}{q\mu n_0}$ is generated by

accumulated surface charges.

Now for the first-order terms, the Kukhtarev equations give

$$\frac{\partial N_{D1}^{+}}{\partial t} = sI_1(N_D - N_A) - sI_0 N_{D1}^{+} - \gamma_R N_{D1}^{+} n_0 - \gamma_R N_A n_1, \tag{2.17}$$

$$\frac{\partial n_1}{\partial t} = \frac{\partial N_{D1}^{+}}{\partial t} + \frac{j}{q}\boldsymbol{G}\cdot\boldsymbol{J_1}, \tag{2.18}$$

$$\begin{aligned}\boldsymbol{J_1} &= q\mu n_0 \boldsymbol{E_1} + q\mu n_1 \boldsymbol{E_0} + jk_B T\mu n_1 \boldsymbol{G} \\ &\quad -p(N_D - N_A)I_1\hat{\boldsymbol{c}} + pN_{D1}^{+}I_0\hat{\boldsymbol{c}},\end{aligned} \tag{2.19}$$

$$j\boldsymbol{G}\cdot(\epsilon\boldsymbol{E_1}) = q(N_{D1}^{+} - n_1). \tag{2.20}$$

Simplifying the equations for n_1, N_{D1}^{+}, we get two equations

$$\frac{\partial N_{D1}^{+}}{\partial t} = sI_1(N_D - N_A) - (sI_0 + \gamma_R n_0)N_{D1}^{+} - \gamma_R N_A n_1, \tag{2.21}$$

$$\begin{aligned}\frac{\partial n_1}{\partial t} - \frac{\partial N_{D1}^{+}}{\partial t} &= n_1\left[j\mu\boldsymbol{G}\cdot\boldsymbol{E_0} - \frac{\mu k_B T G^2}{q} - \frac{q\mu n_0}{\epsilon}\right] + N_{D1}^{+}\left[\frac{q\mu n_0}{\epsilon} + j\frac{pI_0\boldsymbol{G}\cdot\hat{\boldsymbol{c}}}{q}\right] \\ &\quad -j\frac{p\boldsymbol{G}\cdot\hat{\boldsymbol{c}}}{q}(N_D - N_A)I_1.\end{aligned} \tag{2.22}$$

By substituting equation (2.21) into equation (2.22) to get a second-order differential equation, and ignoring the second-order derivative $\frac{\partial^2}{\partial t^2}(n_1 - N_{D1}^{+})$ [19], we can finally find the solution for the space charge field $\boldsymbol{E_1}$ along the direction of the grating $\boldsymbol{G}$ with the approximations $\gamma_R N_A \gg sI_0$ and $N_A \gg n_0$:

$$E_1(t) = E_{1\infty}\left(1 - e^{-t/\tau}\right), \tag{2.23}$$

$$E_{1\infty} = \frac{j}{G}\frac{I_1}{I_0}\frac{k_B T G^2 + jqG_{\hat{\boldsymbol{c}}}E_0 + \frac{jp\gamma_R}{\mu s}N_A G_{\hat{\boldsymbol{c}}}}{q + \frac{\epsilon}{N_D - N_A}\left[\frac{N_D}{N_A}\left(\frac{k_B T G^2}{q} + jG_{\hat{\boldsymbol{c}}}E_0\right) + \frac{j}{q\mu s}\gamma_R N_A G_{\hat{\boldsymbol{c}}}\right]}, \tag{2.24}$$

$$G_{\hat{\boldsymbol{c}}} = \boldsymbol{G}\cdot\hat{\boldsymbol{c}}. \tag{2.25}$$

By using the traditional photorefractive notations:

$$\text{modulation depth} \quad m = \frac{I_1}{I_0}, \tag{2.26}$$

$$\text{diffusion field} \quad E_D = \frac{k_B T G^2}{q G_{\hat{\mathbf{c}}}}, \tag{2.27}$$

$$\text{saturation space charge field} \quad E_q = \frac{q N_A (N_D - N_A)}{\epsilon G_{\hat{\mathbf{c}}} N_D}, \tag{2.28}$$

$$\text{photovoltaic field} \quad E_{0ph} = \frac{p \gamma_R N_A}{q \mu s}, \tag{2.29}$$

$$\text{drift field} \quad E_\mu = \frac{\gamma_R N_A}{\mu G}, \tag{2.30}$$

$$\text{drift field} \quad E_{\mu\hat{\mathbf{c}}} = \frac{\gamma_R N_A}{\mu G_{\hat{\mathbf{c}}}}, \tag{2.31}$$

$$\text{dielectric relaxation time} \quad \frac{1}{\tau_d} = \frac{\epsilon}{q\mu} \frac{\gamma_R N_A}{s I_0 (N_D - N_A)}, \tag{2.32}$$

we can simplify equation (2.24) as

$$E_{1\infty} = m \frac{G_{\hat{\mathbf{c}}}}{G} E_q \frac{j E_D - (E_0 + E_{0ph})}{(E_q + E_D) + j \left(E_0 + \frac{N_A}{N_D} E_{0ph} \right)}. \tag{2.33}$$

Also, the complex time constant τ in equation (2.23) is given by

$$\frac{1}{\tau} = \frac{1}{\tau_d} \frac{1 + \frac{E_D}{E_q} + j \left(E_0 + \frac{N_A}{N_D} E_{0ph} \right) / E_q}{1 + \frac{E_D}{E_\mu} + j E_0 E_{\mu\hat{\mathbf{c}}}}. \tag{2.34}$$

When a large number of holograms are multiplexed in the same location, the recording time t for each hologram is much smaller than the time constant $|\tau|$, therefore the space charge field grating has the amplitude

$$\begin{aligned} |E_1| &\approx |E_{1\infty} \frac{t}{\tau}| \\ &\approx m \sqrt{\frac{E_D^2 + (E_0 + E_{0ph})^2}{(E_{\mu\hat{\mathbf{c}}} + E_D)^2 + E_0^2}} E_\mu \frac{t}{\tau_d}. \end{aligned} \tag{2.35}$$

Phase grating by electro-optic effects

The dielectric constant of the material changes under the applied electric field due

to the Pockel's and Kerr's effects [129]:

$$\Delta\bar{\bar{\epsilon}} = -\frac{1}{\epsilon_0}\bar{\bar{\epsilon}} \cdot \Delta\bar{\bar{\eta}} \cdot \bar{\bar{\epsilon}}, \tag{2.36}$$

$$\Delta\bar{\bar{\eta}} = \Delta\overline{\overline{(\frac{1}{n^2})}} = \bar{\bar{\bar{r}}} \cdot \boldsymbol{E} + \bar{\bar{\bar{S}}}\boldsymbol{E}\boldsymbol{E}. \tag{2.37}$$

In photorefractive $LiNbO_3$ crystal, the linear Pockel's effect in equation (2.37) is dominant.

Due to the $3m$ symmetry of the $LiNbO_3$ crystal, the electro-optic tensor $\bar{\bar{\bar{r}}}$ is given as

$$\bar{\bar{\bar{r}}} = \begin{bmatrix} r_{xxx} & r_{xxy} & r_{xxz} \\ r_{yyx} & r_{yyy} & r_{yyz} \\ r_{zzx} & r_{zzy} & r_{zzz} \\ r_{23x} & r_{23y} & r_{23z} \\ r_{13x} & r_{13y} & r_{13z} \\ r_{12x} & r_{12y} & r_{12z} \end{bmatrix} = \begin{bmatrix} 0 & -r_{22} & r_{13} \\ 0 & r_{22} & r_{13} \\ 0 & 0 & r_{33} \\ 0 & r_{51} & 0 \\ r_{51} & 0 & 0 \\ -r_{22} & 0 & 0 \end{bmatrix}, \tag{2.38}$$

and the dielectric tensor

$$\bar{\bar{\epsilon}} = \begin{bmatrix} \epsilon_1 & 0 & 0 \\ 0 & \epsilon_1 & 0 \\ 0 & 0 & \epsilon_3 \end{bmatrix}.$$

Using the conventional orthogonal coordinates along the crystal axes to represent the electric field grating in equation (2.35), $\boldsymbol{E_1} = (E_{1\hat{\boldsymbol{a}}}, E_{1\hat{\boldsymbol{b}}}, E_{1\hat{\boldsymbol{c}}})$, the dielectric tensor

grating from equation (2.36) is

$$\Delta\bar{\bar{\epsilon}} = -\frac{\epsilon_1^2}{\epsilon_0}\Bigg(\begin{bmatrix} 0 & -r_{22} & r_{51}\frac{\epsilon_3}{\epsilon_1} \\ -r_{22} & 0 & 0 \\ r_{51}\frac{\epsilon_3}{\epsilon_1} & 0 & 0 \end{bmatrix} E_1\hat{\boldsymbol{a}} + \begin{bmatrix} -r_{22} & 0 & 0 \\ 0 & r_{22} & r_{51}\frac{\epsilon_3}{\epsilon_1} \\ 0 & r_{51}\frac{\epsilon_3}{\epsilon_1} & 0 \end{bmatrix} E_1\hat{\boldsymbol{b}} + \begin{bmatrix} r_{13} & 0 & 0 \\ 0 & r_{13} & 0 \\ 0 & 0 & r_{33}\frac{\epsilon_3^2}{\epsilon_1^2} \end{bmatrix} E_1\hat{\boldsymbol{c}}\Bigg). \tag{2.39}$$

Angle-dependent diffraction efficiency

The diffraction efficiency of the phase grating in equation (2.39) can be calculated with Born approximation, due to the weak gratings usually recorded in data storage applications [19, 137]. We have the diffraction field amplitude $E_d \propto |\Delta\epsilon|$ under the Bragg phase-matching condition, where we ignore the geometric volume integral effects for different signal beam angles, and only consider the effective grating strength $|\Delta\epsilon|$, which is strongly dependent on the beam angles and polarization $\boldsymbol{P_R}, \boldsymbol{P_S}$:

$$|\Delta\epsilon| = \boldsymbol{P_R} \cdot \Delta\bar{\bar{\epsilon}} \cdot \boldsymbol{P_S}. \tag{2.40}$$

Considering the normal 90-degree recording geometry as shown in Fig. 2.1 and transforming the coordinates along the crystal axes $(\hat{\boldsymbol{a}}, \hat{\boldsymbol{b}}, \hat{\boldsymbol{c}})$ in Fig. 2.10, we have the normal reference plane wave vector $\boldsymbol{K_R} = k_0(-\frac{\sqrt{2}}{2}\hat{\boldsymbol{a}}, 0, \frac{\sqrt{2}}{2}\hat{\boldsymbol{c}})$, where $k_0 = \frac{2\pi n}{\lambda}$, and ordinary polarization $\boldsymbol{P_R} = \hat{\boldsymbol{b}}$. For the signal beam with transverse spatial frequency $\boldsymbol{K_S} = k_x\hat{\boldsymbol{x}} + k_y\hat{\boldsymbol{y}} + k_z\hat{\boldsymbol{z}}$, we have

$$\boldsymbol{K_S} = k_0(-\cos\alpha\cos\beta\hat{\boldsymbol{a}}, -\sin\alpha\hat{\boldsymbol{b}}, -\cos\alpha\sin\beta\hat{\boldsymbol{c}}), \tag{2.41}$$

$$\boldsymbol{P_S} = (-\sin\alpha\cos\beta\hat{\boldsymbol{a}}, \cos\alpha\hat{\boldsymbol{b}}, -\sin\alpha\sin\beta\hat{\boldsymbol{c}}), \tag{2.42}$$

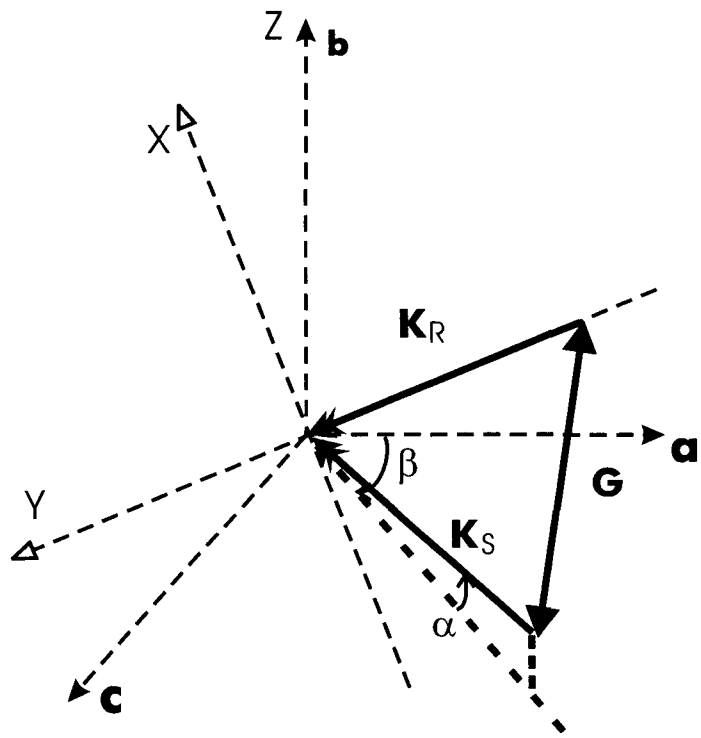

Figure 2.10: The coordinates of the normal 90-degree recording geometry along the crystal axes.

where

$$k_y = k_0 \cos\alpha \sin(\frac{\pi}{4} - \beta), \tag{2.43}$$

$$k_z = -k_0 \sin\alpha. \tag{2.44}$$

The grating vector is

$$\boldsymbol{G} = \boldsymbol{K_R} - \boldsymbol{K_S} \tag{2.45}$$

$$= k_0 \left(-\frac{\sqrt{2}}{2} + \cos\alpha\cos\beta\,\hat{\boldsymbol{a}}, \sin\alpha\,\hat{\boldsymbol{b}}, \frac{\sqrt{2}}{2} + \cos\alpha\sin\beta\,\hat{\boldsymbol{c}} \right). \tag{2.46}$$

Plugging equations (2.35, 2.39, 2.42, 2.46) into the effective grating strength equa-

Room temperature	$k_BT/q = 0.0259V$
Dielectric constant	$\epsilon_1 = 78$
	$\epsilon_3 = 32$
Electro-optical coefficients	$r_{13} = 9.6 \times 10^{-10} cm/V$
	$r_{22} = 6.8 \times 10^{-10} cm/V$
	$r_{33} = 30.9 \times 10^{-10} cm/V$
	$r_{51} = 32.6 \times 10^{-10} cm/V$
Electron mobility	$\mu = 16 cm^2/V sec$
Ordinary refractive index	$n_0 = 2.3489$
Dopant density	$N_D = 1.89 \times 10^{18} cm^{-3}$
Acceptor density	$N_A = 1 \times 10^{18} cm^{-3}$
Photoexcitation cross-section	$s = 0.97 cm^2/J$
Recombinaton rate	$s/\gamma_R = 5.45 \times 10^5 sec/J \cdot cm$
Photovoltaic field	$E_{0ph} = 1.1 \times 10^4 V/cm$
Drift field	$E_\mu = 2.6 \times 10^5 \frac{\sqrt{2}k_0}{G} V/cm$
Diffusion field	$E_D = 1.11 \times 10^4 \frac{G^2}{\sqrt{2}k_0 G_{\hat{\boldsymbol{c}}}} V/cm$

Table 2.2: Numerical values of the variables in Kukhtarev equations for $LiNbO_3(Fe)$ crystal in our experiment.

tion (2.40), we have the effective angle-dependent grating strength

$$\begin{aligned} |\Delta\epsilon| &= \frac{\epsilon_1^2}{\epsilon_0}\frac{k_0}{G}E_1\left[-\frac{\sqrt{2}}{2}r_{22}\sin\alpha\cos\beta + r_{22}\sin\alpha\cos\alpha(1+\cos^2\beta) + \frac{\sqrt{2}}{2}r_{13}\cos\alpha\right. \\ &\quad \left. + r_{13}\cos^2\alpha\sin\beta - r_{51}\frac{\epsilon_3}{\epsilon_1}\sin^2\alpha\sin\beta\right], \end{aligned} \tag{2.47}$$

where the space charge field E_1 is given by equation (2.35) and

$$G = k_0\sqrt{2+\sqrt{2}\cos\alpha(\sin\beta-\cos\beta)}, \tag{2.48}$$

$$\begin{aligned} G_{\hat{\boldsymbol{c}}} &= \boldsymbol{G}\cdot\hat{\boldsymbol{c}} \\ &= k_0\left(\frac{\sqrt{2}}{2}+\cos\alpha\sin\beta\right). \end{aligned} \tag{2.49}$$

By numerical calculation with the known parameters of the $LiNbO_3$ in previous studies [129, 54, 19, 21, 99, 86, 127], we get all the parameters and the field in equations for $\lambda = 488\ nm$ in Table 2.2.

Calculating the relative grating strength in equation (2.47) as a function of signal beam angle α, β, and expressing it relative to the spatial frequencies in equations (2.43), (2.44), we get a 2-dimensional distribution function as shown in Fig. 2.2.

We notice that in equation (2.16), when there is no applied voltage $E_0 = 0$, there is a constant current density inside the crystal due to the photovoltaic effect. This current finally diminishes due to the surface charge buildup, which generates a constant field $\boldsymbol{E_0} = \frac{p(N_D - N_A)I_0\hat{\boldsymbol{c}}}{q\mu n_0}$. For a large number of holograms multiplexing in data storage application, the surface charge is saturated most of the time, *i.e.*, $\boldsymbol{E_0} = \frac{p(N_D - N_A)I_0\hat{\boldsymbol{c}}}{q\mu n_0}$. Under this condition, the angle-dependent grating strength is calculated as shown in Fig. 2.2. In the case of an oven-fresh crystal, $E_0 = 0$, the angle-dependent grating strength from equation (2.47) is shown in Fig. 2.11, which is similar to the saturation result. The comparison of the results on the cross-section between in and out of reference-$\boldsymbol{c}$-axis plane is shown in Fig. 2.12. Both cases show a broad holographic recording and reconstruction bandwidth, without considering the interface Fresnel losses.

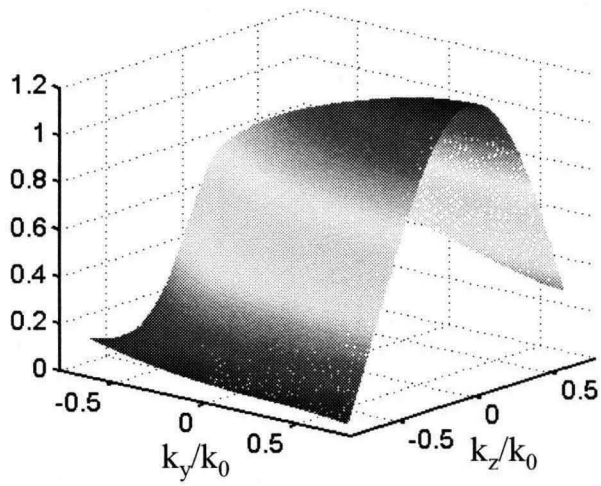

Figure 2.11: Theoretical calculation of the normalized phase grating strength as a function of the signal beam spatial frequencies $\boldsymbol{k_y}, \boldsymbol{k_z}$, for an oven-fresh crystal without external applying electric field.

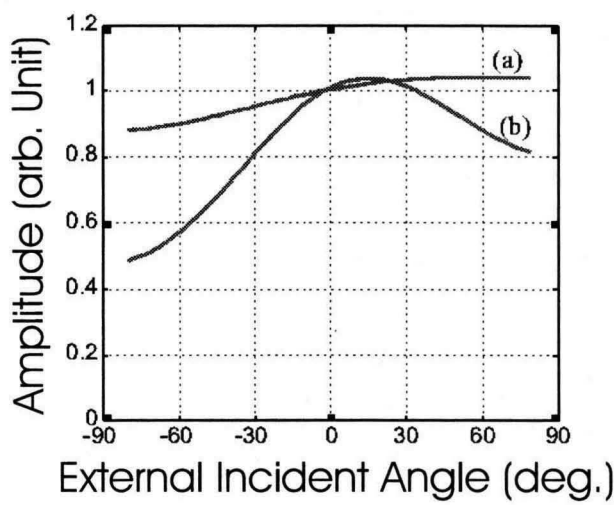

Figure 2.12: The theoretical simulation of the holographic recording and reconstruction amplitudes of $LiNbO_3(Fe)$ in 90-degree geometry as a function of the signal incident angle: (a) in the signal-reference plane and (b) out of the signal-reference plane, for an oven-fresh crystal without applying electric field.

Chapter 3 Holographic Phase Conjugate Memory

Holographic memory is a potential data storage technology that can provide very large storage density and high recording and accessing speed [108, 59, 55, 111, 105]. The theoretical storage capacity of this technology is on the order of V/λ^3 [126] (where V is the volume of the holographic medium and λ is the wavelength of light), *i.e.*, a storage density limit of about one bit per cubic wavelength. Furthermore, holography has the inherent advantage of massive parallelism. Unlike conventional storage media, such as magnetic hard disks and CD-ROMs, which access only one bit at a time, each access of a holographic memory yields an entire data page — potentially megabits at a time.

Due to Bragg phase-matching effects, thousands of holograms can be multiplexed within the same volume of recording material by angular multiplexing [125, 90, 92, 5, 6], shift multiplexing [107], fractal multiplexing [106, 103], peristrophic multiplexing [31], wavelength multiplexing [131, 112, 114, 130, 136], offering the potential of very high storage densities.

Figure 3.1 shows a typical angle-multiplexed holographic memory in 90-degree geometry. Information is recorded in the holographic medium through the interference of two coherent beams of light. We refer to the information carrying beam as the signal beam, and the interfering beam as the reference beam. The resulting interference pattern causes an index grating (the hologram) to be written in the material. When the hologram is subsequently illuminated with one of the original writing reference beams, light is diffracted from the grating in such a way that the signal beam is reproduced.

Much of the progress that has been made can be attributed to better understanding on how to take advantage of the Bragg selectivity of 3-D to multiplex holograms,

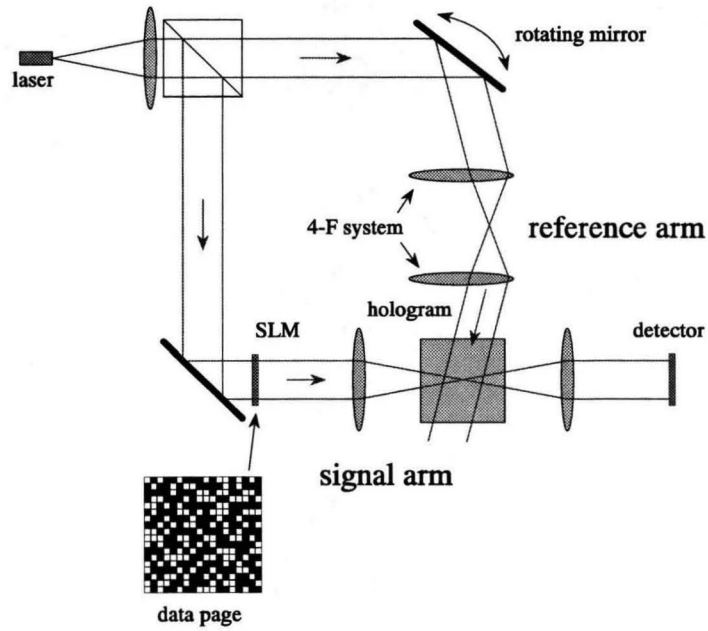

Figure 3.1: Experimental setup for a holographic random access data storage system with angle multiplexing in a photorefractive crystal of 90-degree geometry.

as well as continuous research on holographic material properties and dynamics. The major barriers to develop a commercial holographic memory system are the materials (dynamic range, stability), the optical-electronic components (such as spatial light modulator (SLM), detector array, multiplexing mechanism and devices), and the large system volume and high cost.

In this chapter, we investigate a holographic random access memory (HRAM) module with phase conjugate reconstruction and present experimental results from this architecture. It has faster random access time than hard disk (100 μsec or less) and similar bandwidth as silicon storage with a lower cost. The phase conjugation leads to high-resolution signal image recovery with a compact and inexpensive optical system. And we believe that HRAM can be a competitive memory technology if optoelectronic technology can achieve the following three milestones:

1) small SLM and detector pixel sizes on the order of 1 μm;

2) high recording sensitivity of the holographic material with no more than 1 J/cm^2 to reach saturation;

3) inexpensive high spatial density laser diodes with at least 500 mW of output power

in the near-infrared or visible wavelength.

3.1 Phase conjugate reconstruction

Despite the high theoretical limit on the storage density of volume holographic storage (one bit per cubic wavelength of material) [126], the practical implementation of holographic systems is often bulky due to the large space occupied by the various components that are necessary to provide the recording and readout mechanisms for the crystal. The system of Figure 3.1 is fairly simple with a relatively small number of components; however, the spacing requirements of the imaging lenses impose constrains on how closely these components can be placed. For example, assuming SLM and detector array dimensions of 1 cm and high quality lenses with $F/\# = 1$, the focal distance between the arrays, lenses, and crystal must also be at least 1 cm. The system of Figure 3.1 would then occupy a volume of approximately 6 cm$\times$5 cm$\times$1 cm which is 30 times larger than the volume of the recording material [27].

The reason we normally need to place lenses within the signal path is to undo the effects of diffraction. When we record a hologram of the signal beam diverging from the input SLM and reconstruct it with the original reference beam, we produce a virtual image of the input data page at the position of SLM, and thus require a lens to refocus it onto the detector array. We can eliminate the lens system between the SLM and detector array if we reconstruct a real image instead of a virtual one. One way to do this is to use phase conjugate readout [37, 38, 45].

Phase conjugation

Phase conjugate definition comes from the complex analytic description of optical field in electromagnetic waves [128, 51]. Considering an electromagnetic wave propagating along the forward z-direction, its electric field can be written as

$$\boldsymbol{E} = \boldsymbol{A}(\boldsymbol{r})e^{j(\omega t - kz - \phi(\boldsymbol{r}))}, \tag{3.1}$$

where ω is the frequency and k is the wave number. The amplitude $\boldsymbol{A}$ and the phase

$\phi(\boldsymbol{r})$ are real functions of position (x, y, z). Defining a complex amplitude

$$\boldsymbol{A_c}(\boldsymbol{r}) = \boldsymbol{A}(\boldsymbol{r})e^{-j\phi(\boldsymbol{r})}, \tag{3.2}$$

the electric field written in analytic representation would be

$$\boldsymbol{E} = \boldsymbol{A_c}(\boldsymbol{r})e^{j(\omega t - kz)}. \tag{3.3}$$

The phase conjugate wave of an electric field in equation (3.3) is given as

$$\boldsymbol{E}^* = \boldsymbol{A_c}(\boldsymbol{r})^* e^{j(\omega t + kz)}, \tag{3.4}$$

which is the complex conjugate of the spatial dependence in equation (3.3). It represents an electromagnetic wave propagating along the backward z-direction with a complex amplitude $\boldsymbol{A_c}(\boldsymbol{r})^*$, and it has exactly the same wave fronts at any point in space as the wave in equation (3.3).

To consider the electromagnetic wave in equation (3.3) propagating along z-direction in a diffracting medium, such as a holographic material with a nonuniform refractive index $n(x, y, z)$, the wave equation by Maxwell's equations is

$$\nabla^2 \boldsymbol{E} - \mu_0 \varepsilon \frac{\partial^2 \boldsymbol{E}}{\partial t^2} = 0. \tag{3.5}$$

The complex amplitude $\boldsymbol{A_c}(\boldsymbol{r})$ must satisfy

$$\nabla_\perp^2 \boldsymbol{A_c} + \left[\frac{\omega^2}{c^2} n^2(x, y, z) - k^2\right] \boldsymbol{A_c} - 2jk \frac{\partial}{\partial z} \boldsymbol{A_c} = 0, \tag{3.6}$$

where the subscript $\perp$ represents spatial derivatives transverse to the z-axis, and the complex amplitude is assumed varying slowly so that we ignore the second derivative $|\partial^2 \boldsymbol{A_c}/\partial z^2| \ll |k \partial \boldsymbol{A_c}/\partial z|$. At the same time, considering the complex conjugate of

(3.6), and assume that the refractive index $\varepsilon = \varepsilon_0 n^2$ is real

$$\nabla_\perp^2 \boldsymbol{A}_c^* + \left[\frac{\omega^2}{c^2} n^2(x,y,z) - k^2\right] \boldsymbol{A}_c^* + 2jk\frac{\partial}{\partial z}\boldsymbol{A}_c^* = 0, \tag{3.7}$$

this is exactly the same wave equation for the phase conjugate wave in equation (3.4) propagating the backward z-direction. Physically this means that if there is a phase conjugate wave $\boldsymbol{E}^*$ generated for $\boldsymbol{E}$ in equation (3.3), the phase conjugate wave have exactly the same wave front as $\boldsymbol{E}$ while propagating along the backward direction inside the medium, as shown in Fig. 3.2.

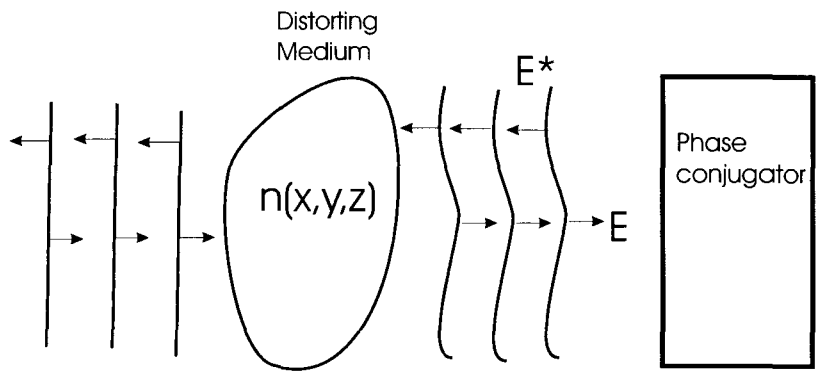

Figure 3.2: Propagation of phase conjugate waves.

Phase conjugation in an absorption medium

For all the phase conjugate discussion, the phase conjugate wave equation (3.7) is true only if the medium is assumed as lossless. However, for all practical materials and photorefractive recording crystals, there is absorption inside.

To consider the effect of the absorption on the phase conjugation, we assume $\varepsilon = \varepsilon_0 n^2 - j\beta$, where the refractive index $n(\boldsymbol{r})$ and absorption coefficient $\beta(\boldsymbol{r})$ are real. The electromagnetic wave propagating along z-direction in the absorption medium and its phase conjugate wave are assumed as

$$\boldsymbol{E} = \boldsymbol{A_c}(\boldsymbol{r}) e^{-\alpha z} e^{j(\omega t - kz - \phi(\boldsymbol{r}))}, \tag{3.8}$$

$$\boldsymbol{E}^* = \boldsymbol{A_c}(\boldsymbol{r})^* e^{-\alpha z} e^{j(\omega t + kz)}, \tag{3.9}$$

where α is a real constant. Substituting the wave (3.8) into the Maxwell's equation

(3.5), the complex amplitude $\boldsymbol{A_c(r)}$ satisfies

$$\begin{aligned} \nabla_\perp^2 \boldsymbol{A_c} + \left[\frac{\omega^2}{c^2} n^2(x,y,z) - k^2 + \alpha^2\right] \boldsymbol{A_c} &- 2(\alpha + jk)\frac{\partial}{\partial z}\boldsymbol{A_c} \\ &= j(\mu_0\omega^2\beta - 2k\alpha)\boldsymbol{A_c}. \end{aligned} \tag{3.10}$$

Under condition that $\mu_0\omega^2\beta(\boldsymbol{r}) = 2k\alpha$, *i.e.*, the absorption is uniform inside the medium, the equation (3.10) is

$$\nabla_\perp^2 \boldsymbol{A_c} + \left[\frac{\omega^2}{c^2} n^2(x,y,z) - k^2 + \alpha^2\right] \boldsymbol{A_c} - 2(\alpha + jk)\frac{\partial}{\partial z}\boldsymbol{A_c} = 0. \tag{3.11}$$

And its mathematical complex conjugate gives

$$\nabla_\perp^2 \boldsymbol{A_c^*} + \left[\frac{\omega^2}{c^2} n^2(x,y,z) - k^2 + \alpha^2\right] \boldsymbol{A_c^*} - 2(\alpha - jk)\frac{\partial}{\partial z}\boldsymbol{A_c^*} = 0, \tag{3.12}$$

which is exactly the wave equation of the phase conjugation in (3.9). Therefore, in a uniform absorption medium, when an identical wave front is generated with opposite propagation direction, the phase conjugate wave front will be exactly the same as the original one inside the medium, except the amplitude exponential decaying dependence along the propagation direction.

When the absorption is not uniform, and we assume that: $\mu_0\omega^2\beta(\boldsymbol{r}) = 2k\alpha + \mu_0\omega^2\alpha_1(\boldsymbol{r})$, the equation (3.10) is

$$\begin{aligned} \nabla_\perp^2 \boldsymbol{A_c} + \left[\frac{\omega^2}{c^2} n^2(x,y,z) - k^2 + \alpha^2\right] \boldsymbol{A_c} &- 2(\alpha + jk)\frac{\partial}{\partial z}\boldsymbol{A_c} \\ &= j\mu_0\omega^2\alpha_1\boldsymbol{A_c}, \end{aligned} \tag{3.13}$$

and its mathematical complex conjugate

$$\begin{aligned} \nabla_\perp^2 \boldsymbol{A_c^*} + \left[\frac{\omega^2}{c^2} n^2(x,y,z) - k^2 + \alpha^2\right] \boldsymbol{A_c^*} &- 2(\alpha - jk)\frac{\partial}{\partial z}\boldsymbol{A_c^*} \\ &= -j\mu_0\omega^2\alpha_1\boldsymbol{A_c^*}. \end{aligned} \tag{3.14}$$

However, for an electromagnetic wave propagating along the (-z)-direction as

$$\boldsymbol{E}_2 = \boldsymbol{A_c}(\boldsymbol{r})_2 e^{-\alpha z} e^{j(\omega t + kz)}, \tag{3.15}$$

Maxwell's equation leads to

$$\begin{aligned} \nabla_\perp^2 \boldsymbol{A}_{c2} + \left[\frac{\omega^2}{c^2} n^2(x,y,z) - k^2 + \alpha^2\right] \boldsymbol{A}_{c2} &- 2(\alpha - jk)\frac{\partial}{\partial z}\boldsymbol{A}_{c2} \\ &= j\mu_0\omega^2\alpha_1 \boldsymbol{A}_{c2}, \end{aligned} \tag{3.16}$$

which is different from the complex conjugate in (3.14).

Therefore, for a medium with nonuniform absorption distribution, which usually happens in the real world, there is no phase conjugate wave front which has the identical wave front inside the medium as the forward propagating wave.

However, by Born approximation, we can write the counter-propagating wave as $\boldsymbol{A}_{c2} = \boldsymbol{A}_c^* + \boldsymbol{A}_c^\dagger$, where $\boldsymbol{A}_c^*$ satisfying equation (3.14). Then from equation (3.16), we have

$$\begin{aligned} \nabla_\perp^2 \boldsymbol{A}_{c2}^\dagger + \left[\frac{\omega^2}{c^2} n^2(x,y,z) - k^2 + \alpha^2\right] \boldsymbol{A}_{c2}^\dagger &- 2(\alpha - jk)\frac{\partial}{\partial z}\boldsymbol{A}_{c2} \\ &= j\mu_0\omega^2\alpha_1 (\boldsymbol{A}_c^\dagger + 2\boldsymbol{A}_c^*), \end{aligned} \tag{3.17}$$

which leads to $|\boldsymbol{A}_c^*| \gg |\boldsymbol{A}_c^\dagger|$ under approximation $2k\alpha \gg \mu_0\omega^2|\alpha_1(\boldsymbol{r})|$. Therefore, for an absorption medium with a relative small nonuniform absorption grating inside, the counter-propagating beam is consisted of the phase conjugate beam plus a small scattered wave front from the absorption grating. In practical materials with more or less nonuniform absorption distribution, this means that the phase conjugation does exist with a background from the scattering noise.

Phase conjugation in holography

Phase conjugation is normally achieved and correctly explained by four-wave mixing in nonlinear media [51] either through stimulated Brillouin scattering, nonlinear Kerr effect in real time, or through the photorefractive effect in holography, where

recording and readout are separated. From either process, three electromagnetic waves are mixed and generate the fourth wave as $E_4 \propto E_1 E_2^* E_3^*$. When E_1, E_2* are a phase conjugate pair such that $E_1 E_2* \sim const.$, the fourth wave will be the phase conjugation as $E_4 \sim E_3^*$.

The dilemma of requiring one pair of phase conjugate beams to generate another pair of phase conjugate beams is solved by using two counter propagating plane waves for E_1 and E_2, which can be achieved by two beams from outside or by internal reflection in a self-pumped phase conjugate mirror architecture [51]. By this simple arrangement, the phase conjugation of a complex wave front E_3 can be achieved.

Based on this principle, a lensless phase conjugate holographic memory system can be achieved as shown in Fig. 3.3, in which a hologram is recorded in the normal

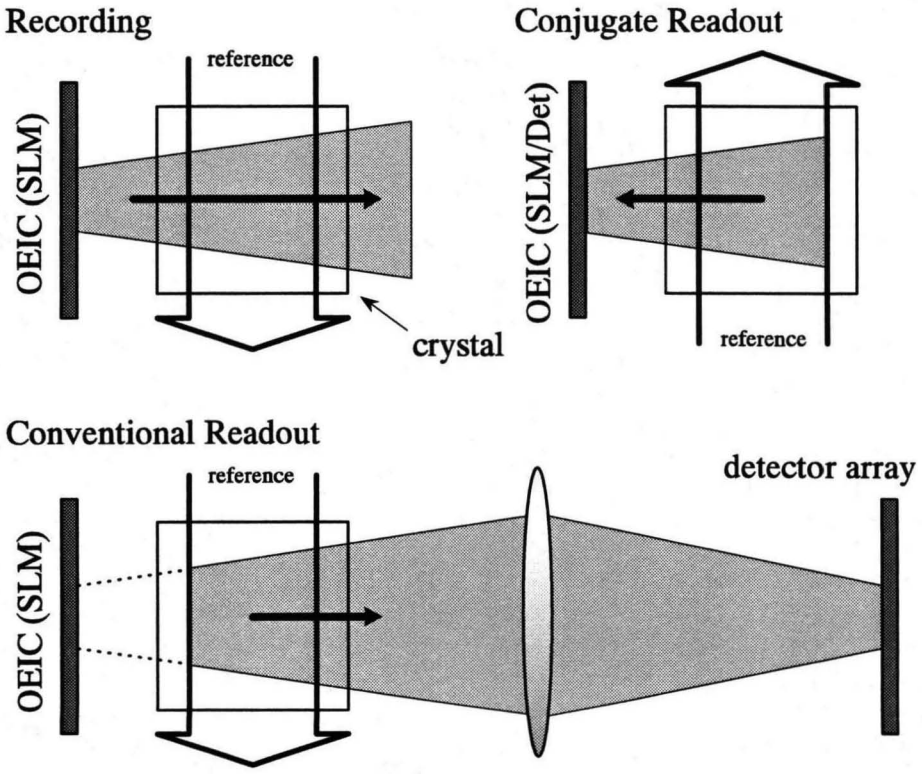

Figure 3.3: Compared to a normal forward reconstruction of a hologram, a phase conjugate reconstruction can regenerate a real image of the signal at the original location without a lens.

90-degree geometry between the signal beam encoded by a spatial light modulator and a reference beam. The hologram is read out with the phase conjugate of the

reference beam, propagating in the opposite direction as the one used for recording. This causes the signal reconstruction from the hologram to propagate back along the direction from which it originally comes, reversing the original signal diffraction, and refocusing exactly at the plane of the SLM array. To generate the conjugate reference we may use a phase conjugate mirror [38], or in the case of a plane wave reference beam, we may simply use a counter-propagating plane wave at each angle. The experimental demonstration of the phase conjugation by plane wave reference beams and its quality are also shown in Fig. 2.7. A more realistic compact demonstration module on optical bench is shown in Fig. 3.4 with a phase conjugate reconstruction of one data page.

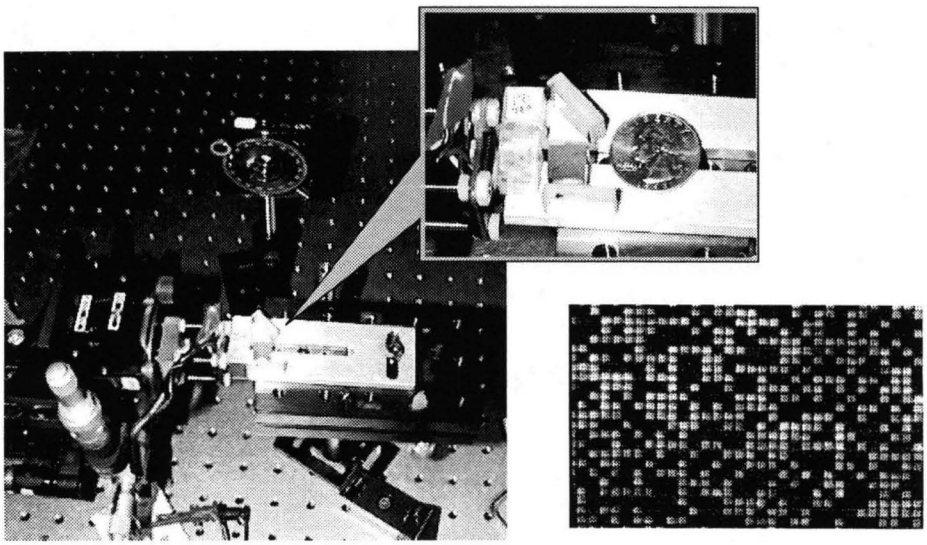

Figure 3.4: An experimental demonstration setup of the compact phase conjugate holographic memory system, and a phase conjugate reconstruction of one data page (pixel size $12 \times 12\ \mu m^2$).

The quality of the counter-propagating reference beam

From the discussion above, the counter-propagating reference beam is required to have the same wave front along the path as the reference beam used for recording. For plane wave reference beams, this means that the reference beam should be well collimated and have no deformation when going through the recording medium and being reflected by the plane mirror.

However, this is very difficult in the real world. As shown in Fig. 3.5, the reference

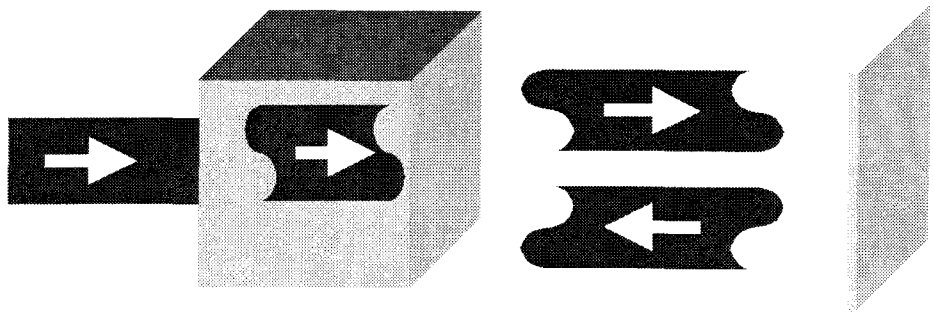

Figure 3.5: The wave fronts of the recording reference beams and their counter-propagating beam for phase conjugate reconstruction.

beam and its counter-propagating beam can deviate from a perfect plane wave due to collimating quality, the quality of all optical interface and the mirror surface, plus the deformation due to the refractive index nonuniformity inside the crystal. To study the sensitivity of the phase conjugate reconstruction on the wave front changes of the reference beam and its reflection, we simulate it numerically by a simple assumption of a spherical reference beam instead of a plane wave, as shown in Fig. 3.6. Due to the opposite propagation direction, the readout reference beam has a different wave front from the recording beam inside the crystal, which causes the phase mismatching along the signal diffraction direction. By Born approximation and considering to the first order of the diffracted signal along the ray direction only [75], the diffracted field is given by

$$\begin{aligned} E_d(\boldsymbol{r'}) &\approx \int dk_{dy}dk_{dz}e^{j\boldsymbol{k_d}\cdot\boldsymbol{r'}}\int_V d^3\boldsymbol{r}\, E_i E_{R0} E_{S0} e^{-j\frac{2\pi(x^2+z^2)}{R\lambda}} \\ &\quad \times e^{j(\boldsymbol{K}_g+\boldsymbol{k}_i-\boldsymbol{k}_d)\cdot\boldsymbol{r}}, \qquad (3.18) \\ &\sim Ce^{j\boldsymbol{k}_d\cdot\boldsymbol{r'}}e^{-j\frac{2\pi z^2}{R\lambda}}\int_D dx\, e^{-j\frac{2\pi x^2}{R\lambda}}, \qquad (3.19) \end{aligned}$$

where the radius R is the spherical wave curvature, and D is the thickness of the crystal along the signal path. Due to the curvature of the spherical wave front, there is a phase delay $\delta\theta = \pi(x^2+z^2)/(R\lambda)$ from a perfect plane wave. Using the counter-propagating reference beam to read out, the wave front phase difference between the recording and readout is $2\delta\theta$, which leads to a phase mismatch along the signal

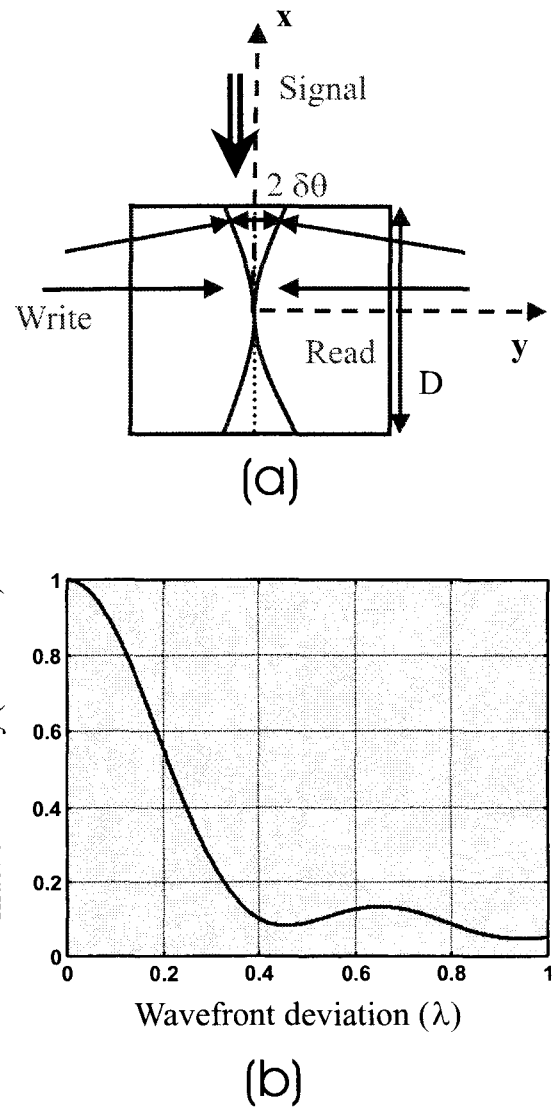

Figure 3.6: (a) A simple model of spherical reference beam and its reflection for holographic readout. (b) The numerical simulation of the diffraction intensity as a function of the wave front deviation of the reference beam from a plane wave.

construction path. The numerical simulation shows the signal diffraction intensity as a function of the deviation of the reference from a plane wave measured by the maximal phase delay at the crystal aperture in Fig. 3.6 (b).

It indicates that the phase conjugate signal reconstruction is very sensitive to the reference beam deviation from a perfect plane wave. When the wave front has a variation of one-fifth of the wavelength, the signal intensity drops to half. This explains the experimental phenomena that the phase conjugate reconstruction diffraction efficiency is always much lower than the normal forward construction in the lab. The simple model used here assumes the reference beams as spherical waves, however similar results apply for the cases when the reference beam is deviated from plane wave with a random phase deformation, either due to the interface non-smoothness or the phase modulation going through the crystal. Also, the wave front deformation sensitivity is consistent with the angle selectivity of a plane wave readout. The first null of the angle selectivity $\Delta\theta = \lambda/D$, corresponds to a phase changes up to $\pm\lambda/2$ across the wave front comparing with the one used for recording. This consistency comes from the Bragg phase-matching. When the reading beam has a wave front phase changes up to λ, the diffracted signals start to cancel each other and average out the amplitude instead of adding together constructively.

Experimental studies of the reference quality for phase conjugation

Due to the interface quality, the phase deformation through the crystal in the lab, and the experimental collimating quality which is at the order of one-wavelength across the beam aperture in the lab, we observe a large uncertainty of the phase conjugate reconstruction efficiency. To determine the significance of various effects, we use the angle selectivity measurement to evaluate the beam deformation from the collimated beam in the lab.

The experimental setup is shown in Fig. 3.7, where a simple 90-degree $LiNbO_3$ crystal is used for recording between two well-collimated plane waves in the lab. And the angle selectivity by the same reference beam is measured, which gives the intrinsic angle resolution or Bragg phase-matching selectivity of the volume hologram at $\Delta\theta = \lambda/D$. Then, different beams either by forward direction $R1$ or counter-

propagation $R2$ are used to readout and their angle selectivities are compared with the selectivity curve by the original reference beam.

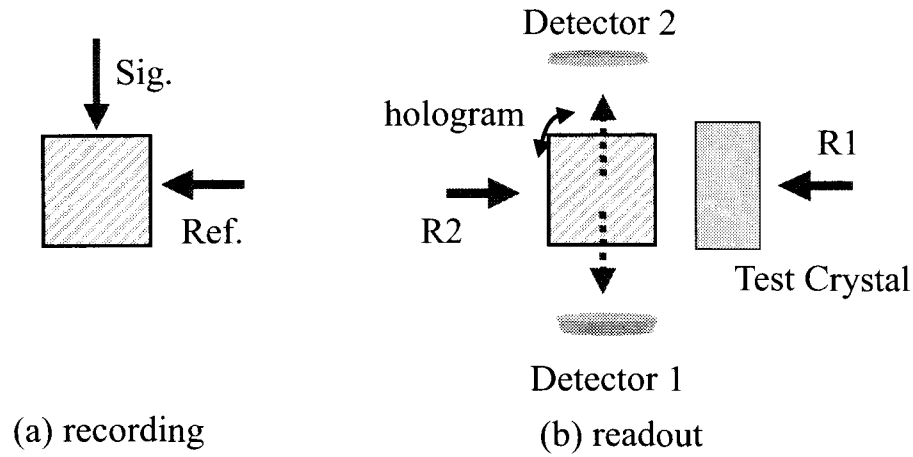

Figure 3.7: (a) A simple 90-degree geometry recording with two well-collimated plane waves. (b) The holographic angular selectivity measurement with different reference beams.

Fig. 3.8 shows various results by forward reference beam $R1$ going through different testing objects. Curve (a) shows the angle selectivity of the volume hologram measured with the original plane wave reference, which gives the angle resolution of the hologram. For a reference beam $R1$, which has a different angle spectrum from the original plane wave, its angle selectivity on this volume hologram gives its angular spectrum with a resolution limited by curve (a). As shown in Fig. 3.8, the plane wave passes through a commercial beamsplitter or an oven-freshed photorefractive crystal. Assuming the beamsplitter or crystals are optically uniform inside, the plane wave is deformed only by the interface surface quality. The commercial beamsplitter and crystal #1 – #3 give angle selectivity curves comparable to (a) with slightly broadening effects. Curves (d) and (g) give large broaden effects, which indicate a severe deformation to the wave front. We test all the crystal used in the lab, the surface quality of some of them are definitely not good. Even though they cause no trouble for normal holographic recording and reconstruction, they can not be phase conjugate reconstructed by assuming the reference beams as plane waves after going through the crystal.

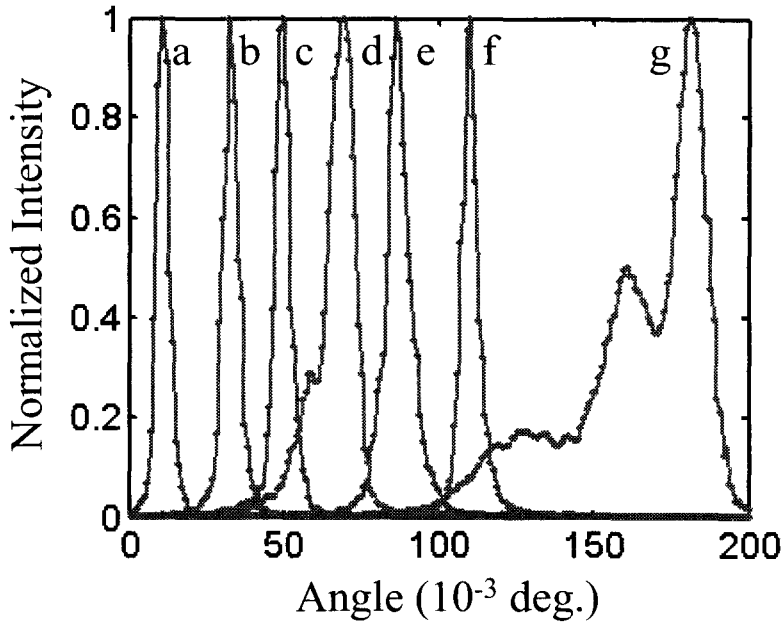

Figure 3.8: The angular selectivity of the hologram by a forward reference beam, which is (a) the original recording plane wave reference beam; (b) a plane wave reference beam going through crystal #1; (c) a plane wave going through a commercial beamsplitter; (d) a plane wave going through crystal #1 difference area; (e),(f),(g) a plane wave going through crystal #2, #3, #4 respectively.

Similar wave front deformation effects also happen inside the crystal when it is used for the holographic recording. This is caused not only by the surface polishing quality, but also by the nonuniform refractive index due to the photorefractive effects during hologram recording. Fig. 3.9 and 3.10 show the angle selectivity curves by counter-propagating reference beam $R2$ in Fig. 3.7.

Fig. 3.9 demonstrates the effect of the wave front deformation on the pseudo phase conjugate by reflection from a plane mirror when the reference beam passed through the photorefractive crystal. On the other hand, for a real phase conjugate reconstruction of the reference beam, the angle selectivity matched the original forward beam even though the wave front is deformed by the same phase modulation through the crystal.

Fig. 3.10 has a large reference beam aperture D, which leads to a stronger dependence on the wave front deformation as shown in Fig. 3.6. Therefore, for the normal

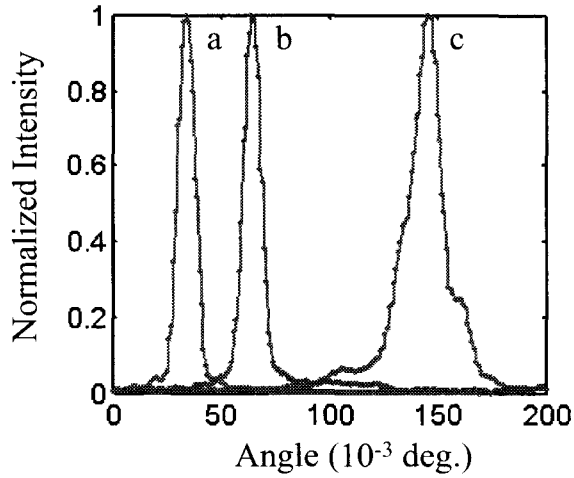

Figure 3.9: The angle selectivity of the hologram by (a) the original recording plane wave reference beam; (b) a phase conjugate beam of the forward reference beam through the crystal; (c) the reflection of the forward reference beam through the crystal by a plane mirror.

forward readout in (a-b), the angle selectivity is narrower than Fig. 3.9(a-b). On the other hand, the pseudo phase conjugate readouts (c-d) have much wider selectivity than Fig. 3.9 (c). Also demonstrated in Fig. 3.10 is that during the recording process, the phase deformation effect inside the crystal gets worse due to the photovoltaic effect. As shown, when the hologram is recorded longer, the angular selectivities in (b) or (d) are both wider than (a) or (c) from a weak hologram. Experimental studies indicate an inconsistent behavior of the phase modulation effect inside the crystal, which depends on the crystal processing procedure, such as oven refreshing, cooling condition, recording intensity, et al.

Hologram multiplexing and pseudo phase conjugate reconstruction

To demonstrate the multiple hologram recording and phase conjugate reconstruction in a compact architecture as shown in Fig. 3.4, we study the angular multiplexing with plane wave reference beams and a fixed random binary data mask as the signal beam.

Fig. 3.11 shows the comb function of multiplexing 40 holograms with plane waves as signal beams, with $M\# = 1$. Fig. 3.12 shows the comb function for phase conjugate reconstruction for the same 40 holograms by reflection of the plane reference beam

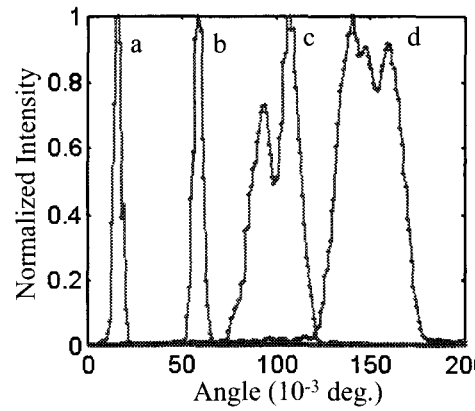

Figure 3.10: The angle selectivity of the hologram by a forward reference beam (a) (c), or its reflection by a plane mirror for the forward reference beam through the crystal (b) (d). (a), (c) are the same weak hologram, and (b), (d) from a same strong hologram, which leads to a broadened selectivity due to the photorefractive effect.

passing through the crystal, with $M\# = 0.5$. Due to the wave front deformation of the pseudo phase conjugate reference beams, the phase conjugate has wider angle deviation and lower diffraction efficiency than the forward reconstruction, as shown in Fig. 3.13. Also shown is the angle broadening effect due to the phase modulation inside the crystal during hologram recording, which leads to a broadened angular selectivity for the first recorded holograms than the last recorded ones. This effect impacts more to phase conjugate readout than forward ones, and has the same impact on all phase conjugate holograms. Similar comb functions for 100 angle multiplexed holograms are shown in Fig. 3.14 and 3.15, with $M\# \approx 0.2$. $M\#$ for forward reconstruction is relatively lower due to the erasure of the holograms during the first scanning of the phase conjugate comb function.

Encoding the signal beam by a fixed random binary data mask with pixel size $12 \times 12\ \mu m^2$, the signal beams scatter around the compact setup, which not only increases the scattering background due to the limited space for spatial filtering, but also makes phase conjugate reconstruction more sensitive to the reference wave front deformation. Fig. 3.16 shows the phase conjugate reconstruction comb function of 50 angle multiplexed pages and its scattering background measurement. As it shows, the

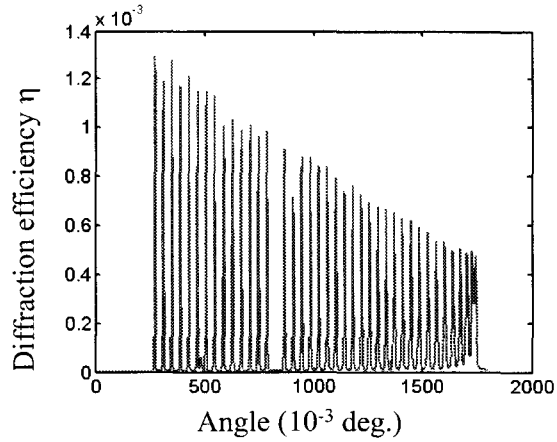

Figure 3.11: The forward reconstruction comb function of 40 angle multiplexed holograms with plane waves as signal beams.

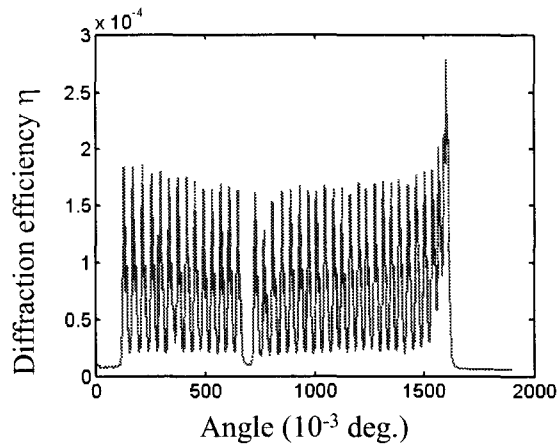

Figure 3.12: The phase conjugate reconstruction comb function of 40 angle multiplexed holograms with plane waves as signal beams.

signal intensity is at the level of the background. By correcting the background profile, we can have the diffraction efficiency of 50 phase conjugate readout in Fig. 3.17, where $M\# \approx 0.1$. To multiplex more holograms into the crystal, the phase conjugate signal level gets so small due to the limited $M\#$ and the wave front deformation to the pseudo phase conjugation as shown in Fig. 3.18 - 3.19, that the detector array we used in the lab can not extract the data image with reasonable signal to noise ratio (SNR). Fig. 3.20 shows the SNR measurement for phase conjugate reconstruction of multiplexed data pages up to $M = 50$, where the reconstructed image samples are shown in Fig. 3.21.

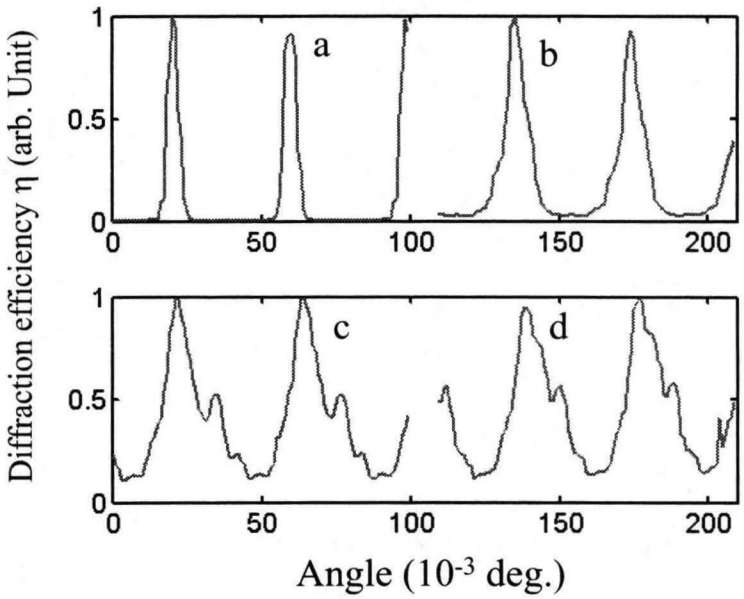

Figure 3.13: The angle selectivities of the 40 angle multiplexed holograms, (a) forward reconstruction of the last recorded holograms; (b) forward reconstruction of the first recorded holograms; (c) phase conjugate reconstruction of the last recorded holograms; (d) phase conjugate reconstruction of the first recorded holograms.

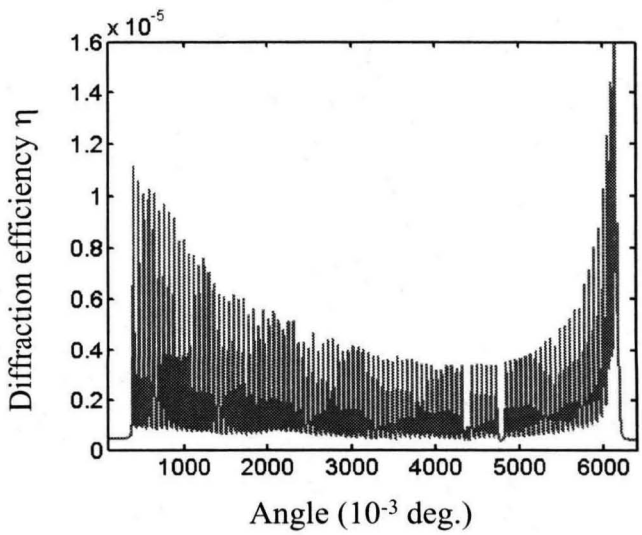

Figure 3.14: The forward reconstruction comb function of 100 angle multiplexed holograms with plane waves as signal beams.

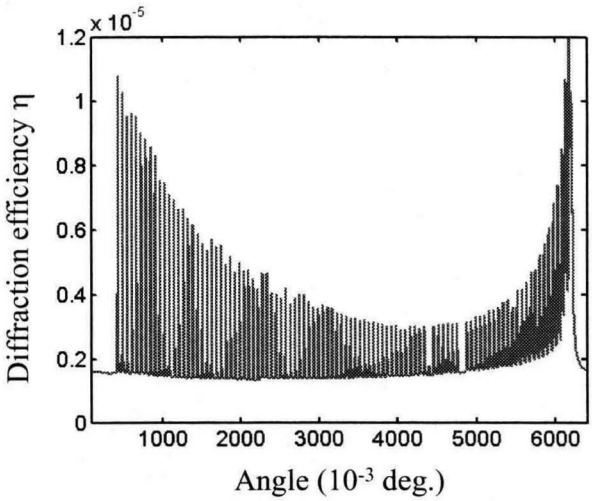

Figure 3.15: The phase conjugate reconstruction comb function of 100 angle multiplexed holograms with plane waves as signal beams.

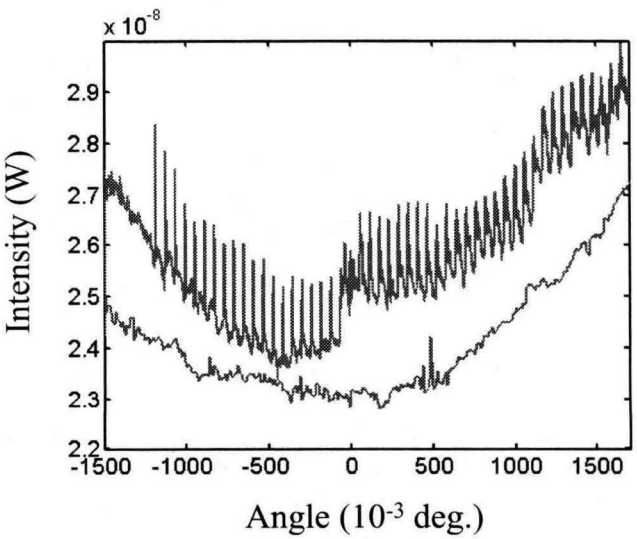

Figure 3.16: The phase conjugate reconstruction intensity comb function of 50 angle multiplexed data pages and the background measurement.

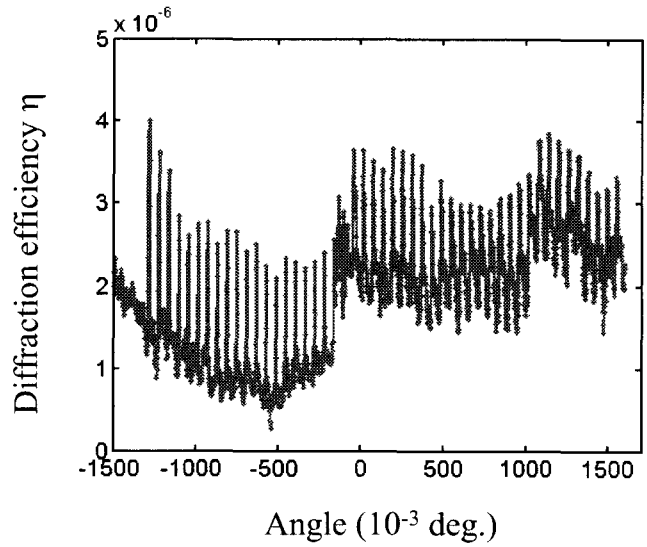

Figure 3.17: The phase conjugate diffraction efficiency comb function of 50 angle multiplexed data pages.

3.2 Pixel matching and SLM

To read out the holographic images, normally a 2-D sensor, such as CCD or CMOS detector, is used, where the pixel size in the 2-D sensor determines the spatial resolution of the image. To retrieve all the information from the holograms, we always oversample the image by amplifying the holographic image so that the image spatial resolution is larger than the image sensor pixel size.

For the binary data storage application, holographic image or binary black/white is used, which requires only one corresponding detector pixel for reconstruction. Oversampling not only wastes the hardware resource, but also makes the 0/1 discrimination algorithm sophisticated. Therefore, a pixel-to-pixel matching is expected for the hologram and the image sensor. Due to the intrinsic back-tracking property of the phase conjugate reconstruction, a real image of the same size and location as the SLM is reconstructed, which makes phase conjugation a natural method for pixel-to-pixel matched readout.

One ideal solution is to implement a smart pixel with both functions of SLM and photo sensor by merging liquid crystal and silicon technologies [30, 64]. During recording, the signal beam is encoded by the liquid crystal modulator before entering

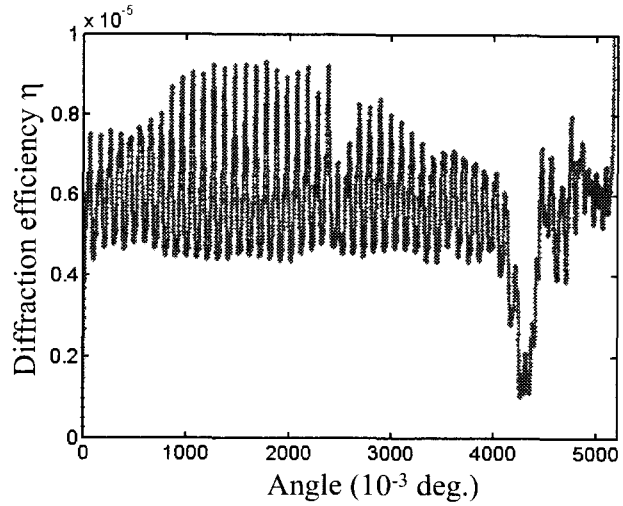

Figure 3.18: The phase conjugate reconstruction intensity comb function of 50 angle multiplexed data pages and the background measurement.

the storage medium. During readout, the same pixel pattern is reconstructed onto the pixel and is detected by the sensor. A prototype of the smart pixel chip is demonstrated in the system [41, 39, 27], but combining liquid crystal and silicon technologies makes the chip design and fabrication complicated, also increases the pixel size, which leads to a decreased data page size and smaller storage capacity.

Another method is to use a beamsplitter to direct the signal reconstruction to a detector array with the same pixel size as the SLM. This architecture is simple, opt to commercial SLM and detector array, with the drawback of lower photon efficiency and required pixel-match alignment.

Experimentally we demonstrate the pixel-matching reconstruction of holograms and compared the image quality between the phase conjugate reconstruction and the normal forward reconstruction, as shown in Fig. 3.22. Fig. 3.22 (a) shows the normal forward reconstruction of 90-degree geometry with angle multiplexing. A pair of custom-designed lenses form a 4-F system to deliver $1:1$ image of the SLM onto a CMOS detector. Fig. 3.22 (b) shows a compact phase conjugate readout with plane wave reference for recording and its reflection for readout. In both setups, we use a Kopin liquid crystal SLM with pixel size $24 \times 24\ \mu m^2$ and effective area of each pixel around $12 \times 15\ \mu m^2$. A CMOS detector with pixel size of $12 \times 12\ \mu m^2$ is

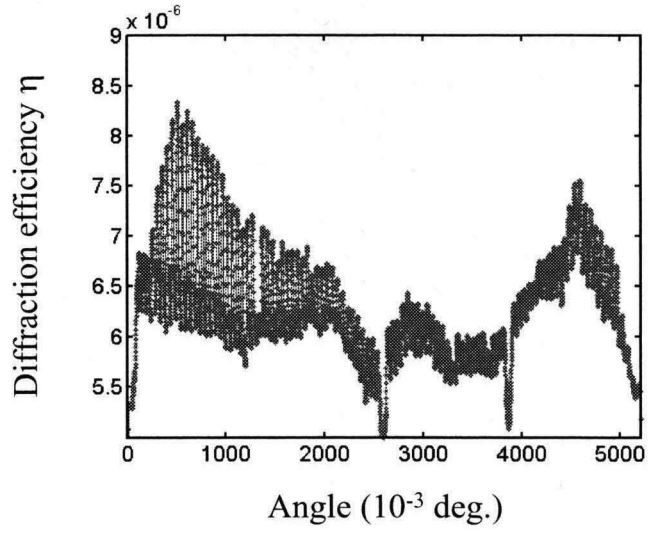

Figure 3.19: The phase conjugate diffraction efficiency comb function of 50 angle multiplexed data pages.

carefully aligned to corresponding pixels on the SLM image. For the phase conjugate reconstruction, the physical size of the image and the SLM are identical through the SLM area, while for the 1 : 1 imaging system for the forward reconstruction, delicate alignment for the correct image size and pixel matching alignment across the whole image area are required. Fig. 3.23 shows these instruments in the setup for the compact phase conjugate system in our lab.

Fig. 3.24 shows the experimental demonstration of the forward pixel matching by the 4-F imaging system. Single pixel horizontal and vertical lines can be seen on the images. Also, an image of an 8 $\times$ 8 superpixel check board on SLM is shown. Due to the fill-in factor of the SLM pixel effective area and the oversampling of each SLM pixel by 2 $\times$ 2 detector pixel, we align the detector pixels so that one in every 2 $\times$ 2 pixels gives the strongest signal for each ON pixel on SLM. Therefore, in every two vertical pixels, there is a dark one next to it due to the 50% fill-in factor in this direction. By picking up only the signal from the central detector pixel, sharp single pixel check board can be extracted and demonstrated the pixel-matching, as shown in Fig. 3.25.

To study the quality of the image quantitatively, we use a simple signal to noise

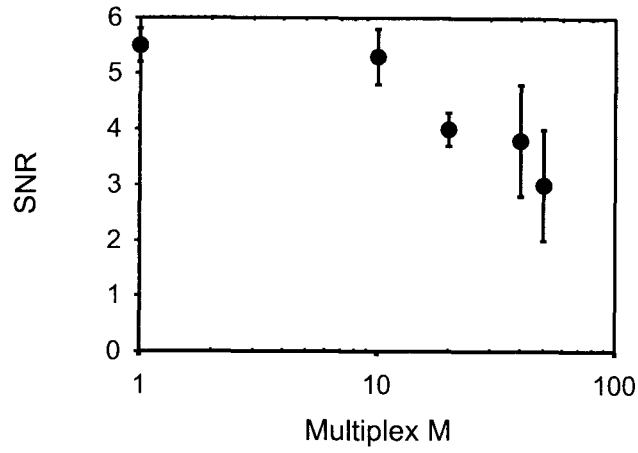

Figure 3.20: The phase conjugate reconstruction SNR measurement for M multiplexed data pages.

ratio (SNR) definition for the binary images. SNR is defined as

$$SNR = \frac{M_{ON} - M_{OFF}}{\sqrt{D_{ON}^2 + D_{OFF}^2}}, \tag{3.20}$$

where M_{ON}, M_{OFF} are the mean intensity values of ON/OFF pixels, and D_{ON}, D_{OFF} are the deviation of ON/OFF pixel intensity distribution. Fig. 3.26 shows the histogram of the intensities of a pixel-matched image, which leads to a $SNR = 7.25$.

Attached figures 3.27, 3.28, and 3.29 are some image samples of the direct pixel match by the 4-F imaging system, holographic reconstruction in the forward architecture and the phase conjugate reconstruction. All of them demonstrate the pixel level matching resolution, with Fig. 3.30 showing a pixel intensity histogram from a phase conjugate reconstruction. To compare the image reconstruction qualities between the normal forward reconstruction and the phase conjugate reconstruction, the SNR results are compared in Fig. 3.31. They have comparable SNR results, while phase conjugate reconstruction gives more reliable performance due to the easier alignment than the 4-F imaging system.

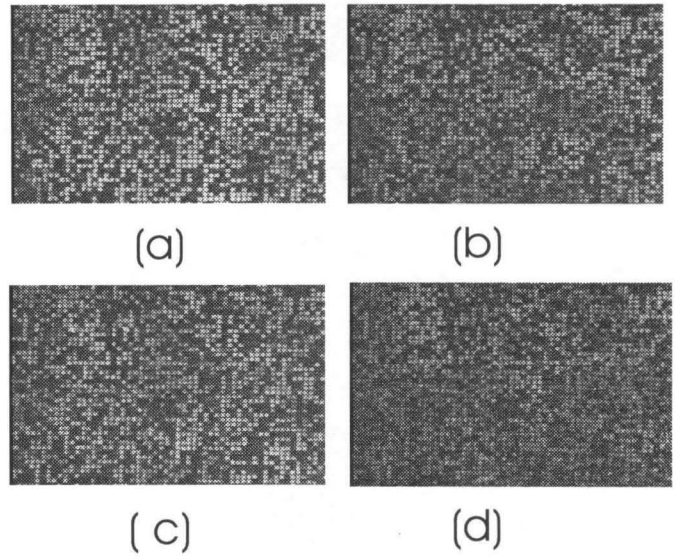

Figure 3.21: The phase conjugate reconstruction of data pages from multiplexed holograms: (a) SNR=5.4 for $M = 10$; (b) SNR=4.4 for $M = 20$; (c) SNR=4.0 for $M = 40$; (d) SNR=3.5 for $M = 50$.

3.3 Capacity and pixel size

With a photorefractive crystal sitting on top of silicon, as shown in Fig. 3.32 [38, 39], a read/write holographic random access memory (HRAM) is a potential competitive technique to store more data with faster data accessing rate, smaller silicon area, lower cost and smaller volume, compared with the traditional silicon Dynamic Random Access Memory (DRAM). Instead of storing data on the silicon area, pages of data are stored as holograms inside the same crystal volume. The silicon devices are only interfaces to read/write holograms to the memory.

Semiconductor electronics have been and will continue to be the driving force on developing faster, smaller, cheaper and more powerful computer and memory system. According to the National Technology Roadmap For Semiconductors [1], the semiconductor industry has maintained a 25-30% peryear cost reduction per function and the average 10.5% per year reduction rate in feature size throughout its history. It is projected to keep this historic trend for another decade until it reaches physical limits as feature sizes approach 100 nm.

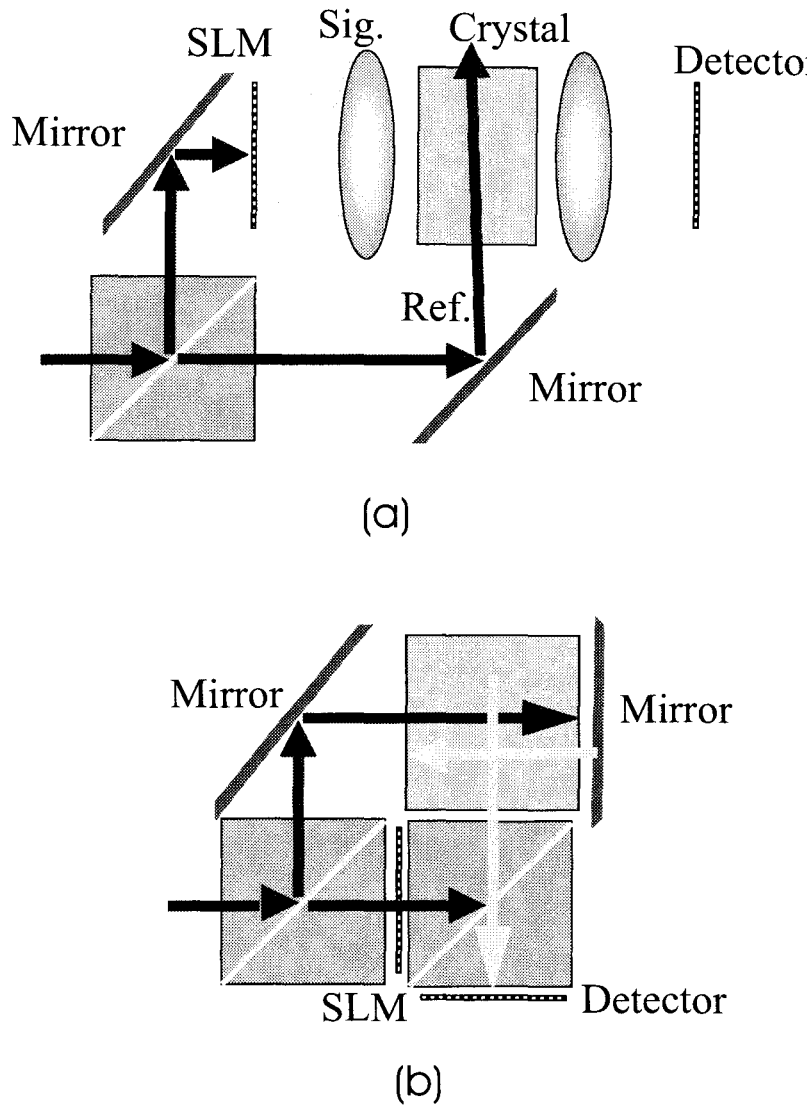

Figure 3.22: (a) A 90-degree angle-multiplexing holographic memory system, with an imaging system to pixel-match the SLM to the detector array. (b) A compact phase conjugate holographic memory system, with a pair of SLM and detector array of the same pixel size and aligned with pixel-to-pixel matching.

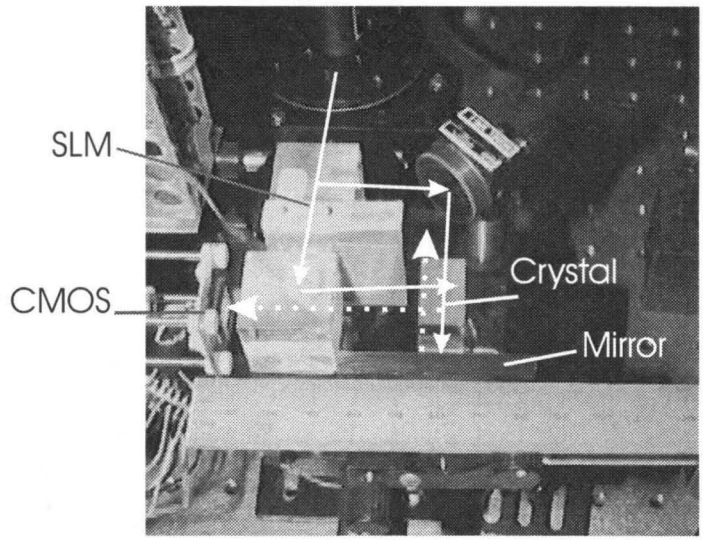

Figure 3.23: A compact phase conjugate holographic setup on optical bench, with a pair of SLM (pixel $24 \times 24\ \mu m^2$) and detector array (pixel $12 \times 12\ \mu m^2$) aligned with pixel-to-pixel matching.

To build a holographic memory competitive with silicon storage, it is essential to be more cost-efficient, faster data accessing and smaller in volume.

Cost per megabyte and pixel size

For the holographic module, the cost includes mainly three parts: silicon interface C_{Si}, optical elements C_{Opt}, including crystals and liquid crystal array, and the multiplexing optical source C_{Laser}, such as VCSEL array. Table 3.1 gives a rough estimation of the cost for large number of production. To compare with the cost of silicon storage DRAM, which is proportional to the silicon area, we assume the same cost for the same silicon area in both holographic memory and DRAM. The cost ratio per megabyte R_c of holographic memory to the silicon storage will be

$$R_c = \frac{C_{Si} + C_{Opt} + C_{Laser}}{C_{si}} \cdot \frac{R_p}{M}, \tag{3.21}$$

where the R_p is the ratio of each pixel area for the SLM and detector in HRAM to each pixel area on DRAM silicon chip, M is the number of holograms multiplexed

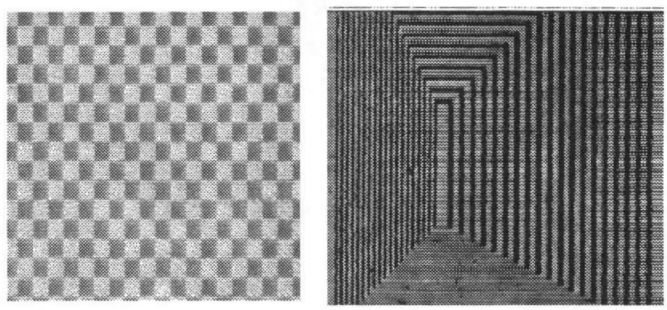

Figure 3.24: Pixel-matched images by the forward 4-F imaging system: (a) an 8×8 superpixel check board; (b) patterns with single pixel horizontal and vertical lines.

Component	**Estimated cost**
$LiNbO_3$ ($1cm^3$)	\$10
Liquid crystal	\$5
Beamsplitters and lens	\$6
Silicon ($1cm^2$)	\$115
Laser diode array (500)	\$25-100
Total:	\$161-236

Table 3.1: Estimated cost of components in the holographic memory module, assuming production in large quantities.

in the crystal on top of the silicon. With the fixed cost of silicon area C_{Si}, optical elements C_{Opt}, and laser source C_{Laser}, the key to have a small cost ratio R_c is to have small R_p and large M, which means a high storage density in holographic memory comparing with the DRAM.

The number of holograms to be recorded and readout with reasonable bit error rate, is limited by the dynamic range and sensitivity, or $M\#$ of the material [91]. Even though recording and reading 10,000 holograms at one location of a LiNbO3 crystal was demonstrated with a similar system [5, 6], it requires tremendous technical efforts.

For current state-of-the-art commercial SLM and detector array, the pixel area is typically 5×5 μm^2 or larger. The current commercial DRAM is 1 μm^2 per

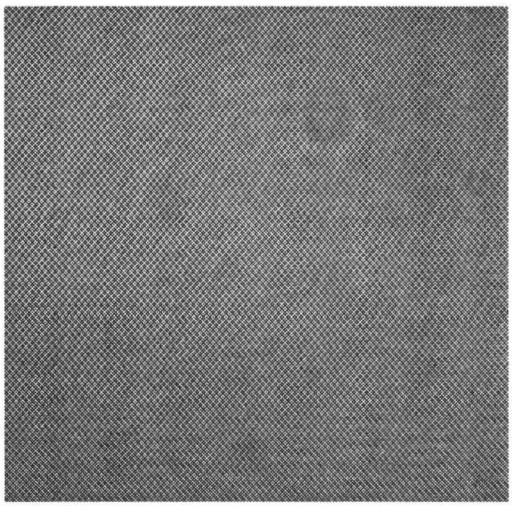

Figure 3.25: Pixel-matched image of a single pixel check board by the forward 4-F imaging system, where only the central detector pixel out of every 2×2 detector pixels is sampled.

bit [1], which leads to a pixel area ratio $R_p = 16$. With typical $M = 1000$, we have $R_p/M = 1.6\%$, which leads to a small and promising R_c. However, if the DRAM keeps the historical shrinking trend as projected, the DRAM cell will be 0.04 $\mu m^2/bit$ in 2006. To keep the R_p around 25, the pixel size of the holographic data pages has to be 1×1 μm^2 or even smaller, which is achievable for the holographic memory system, as shown in Chapter 2.

Experimental demonstration of different pixel sizes

Fig. 3.33 shows the experimental setup for the holographic recording and phase conjugate reconstruction with different pixel size. Binary random data mask is used for signal encoding, and a telescope system is used to image the data page or its hologram reconstruction, since there is no detector with such small pixel size for pixel matching experiments.

Pixel size ranges from 8×8 μm^2 to 1×1 μm^2 for binary data. The direct images by the imaging system and their SNR measurements are shown in Fig. 3.34. The similar results of the phase conjugate reconstruction are shown in Fig. 3.35.

Fig. 3.36 shows the SNR measurements of the direct images and the phase con-

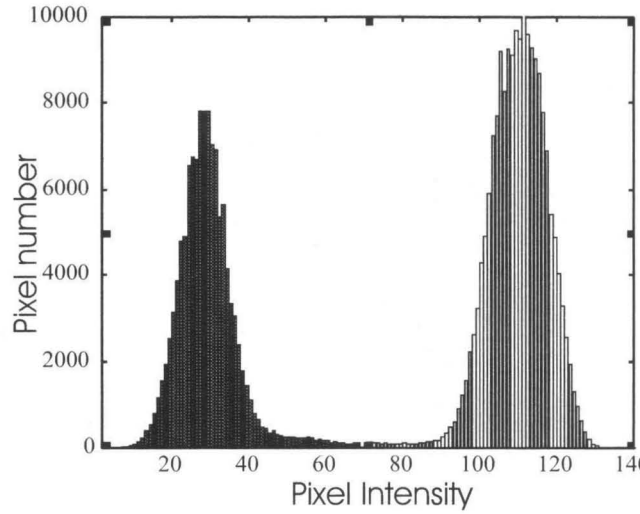

Figure 3.26: The intensity distribution of a pixel-matched image of a single pixel check board by the forward 4-F imaging system, where $M_{ON} = 110.4$, $M_{OFF} = 29.9$, $D_{ON} = 7.67$, $D_{OFF} = 8.01$.

jugate reconstruction as a function of the pixel size. The SNR decreases as the pixel size gets smaller due to the imaging quality of the telescope system and the electronic noise of the detector. For the data recovery, it is more important to know the bit error rate (BER), which defines the possibility of readout 0/1, when a real bit of data 1/0 is recorded, as shown in Fig. 3.37. By assuming a Gaussian distribution of the ON/OFF pixel intensity on the images, the BER can be calculated as shown in Fig. 3.34 – 3.35. If we assume that the BER p is caused by random noise, the real capacity of the recording channel can be calculated by Shannon's theory as [23]

$$I = 1 + p \log_2 p + (1-p) \log_2 (1-p). \tag{3.22}$$

When there is no BER $p = 0$, $I = 1$ bit for each binary pixel. When BER $p > 0$, I represents the information capacity for each binary pixel in out storage system. For the BER we got in our phase conjugate reconstruction in Fig. 3.35, $p < 1 \times 10^{-}4$, which gives $I > 0.99$ bit per pixel. Therefore, the capacity is approximately inversely proportional to the pixel area down to 1×1 μm^2.

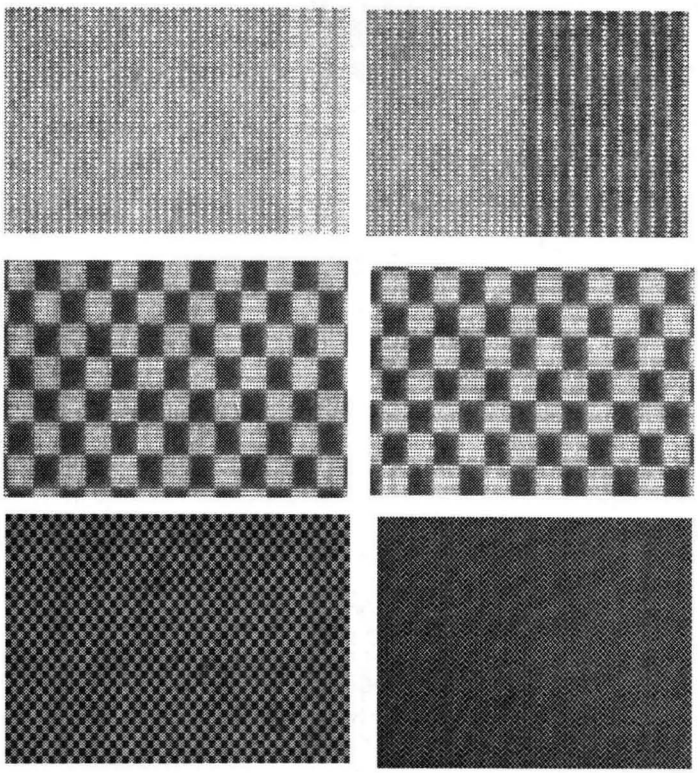

Figure 3.27: The pixel-matched images from the 4-F direct image system. The last row are images of 2 × 2 pixel check board and single pixel check board patterns with only center pixels from every 2 × 2 detector superpixel being shown.

3.4 Discussion

To achieve a practical working compact memory module, there are a few more technically challenging issues on the components.

Multiplexing laser source and data rate

With the recent development of compact laser emitters, such as laser diodes and Vertical-Cavity Surface-Emitting Laser (VCSEL) devices [63, 26, 115], it has become feasible to consider the possibility of incorporating arrays of hundreds of microscopic laser sources in a holographic memory. We can implement a VCSEL array into a compact phase conjugate memory module, in which each angle multiplexed hologram is addressed by a dedicated laser source, as shown in Fig. 3.38. The properly aligned laser array elements have the wavelength deviation much smaller than the hologram wavelength selectivity ($10^{-5}\lambda$ for 1 cm-thick crystal). With a mirror placed on the

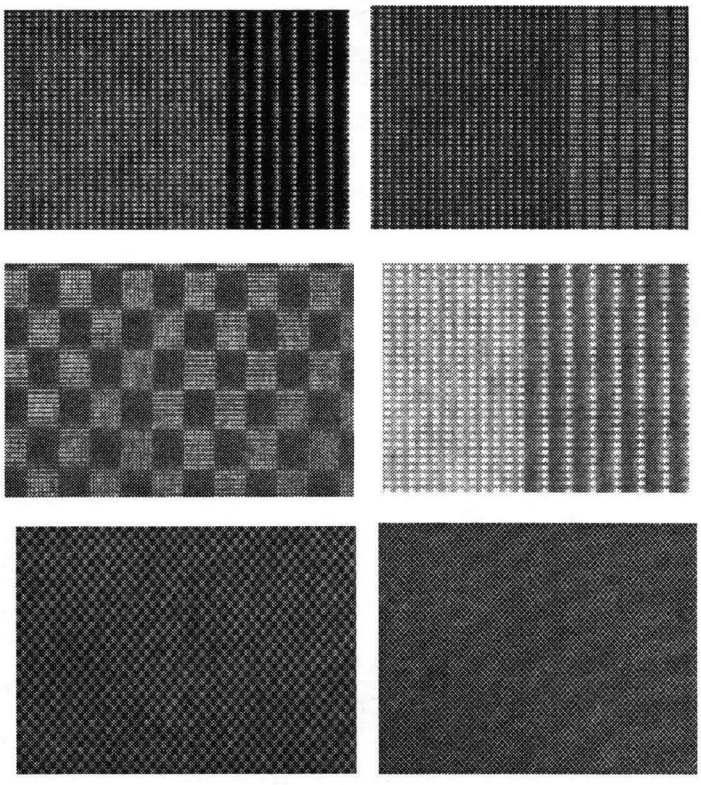

Figure 3.28: The pixel-matched holographic reconstruction images from the 4-F direct image system. The last row are images of 2 $\times$ 2 pixel check board and single pixel check board patterns with only center pixels from every 2 $\times$ 2 detector superpixel being shown.

opposite face of the crystal, such that it lies at the focus of the Fourier transforming lens, the proper conjugate beam can be generated with the symmetrically opposite laser source and overlap the original writing beam path inside the crystal.

Another potential multiplexing method is to use a wavelength tunable source. Tunable laser is intensively studied in terms of tuning range, stability, power, and working wavelength in the areas of DWDM (Dense Wavelength Division Multiplexing) and data storage [57, 33, 66, 87]. With only one emitting source, there is no beam shifting inside the crystal as the angle multiplexing, as shown in Fig. 3.39.

Since the time it takes to produce the proper readout reference beam is determined by the switching time of the laser sources, which is in the nanosecond regime for VCSEL array or microsecond regime for distributed Bragg reflector (DBR) tunable laser, the random access time and the readout rate become limited by the required

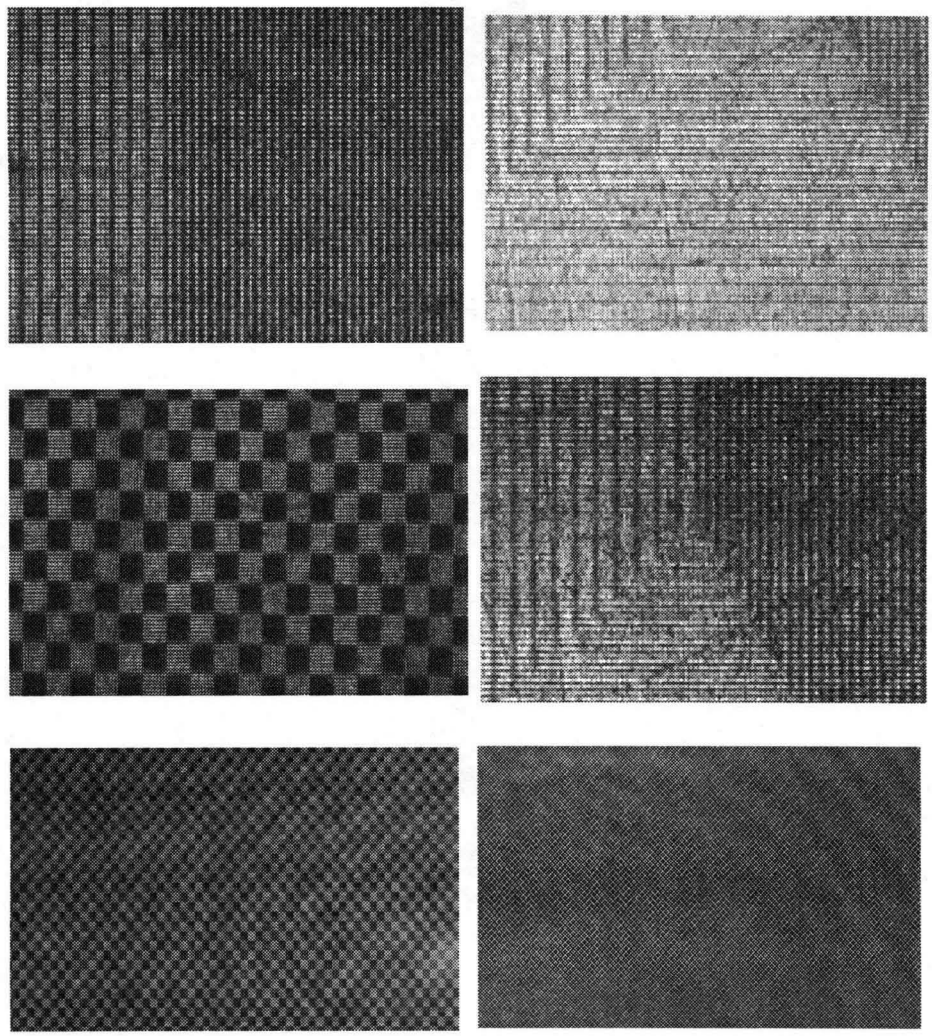

Figure 3.29: The pixel-matched images from phase conjugate reconstruction. The last row are images of 2 × 2 pixel check board and single pixel check board patterns with only center pixels from every 2 × 2 detector superpixel being shown.

integration time of the detector, which is

$$\text{Detector integration time} = \frac{N_e h\nu N^2}{\left(\frac{M\#}{M}\right)^2 P_i}, \tag{3.23}$$

where N_e is the number of electrons per pixel that we need to integrate for the given detector sensitivity and level of background noise, h is Planck's constant (6.63×10^{-34} J·s), ν is the light frequency, N^2 is the total number of pixels in the detector array, $M\#$ is the system metric [102] of the holographic medium, M is the number of multiplexed

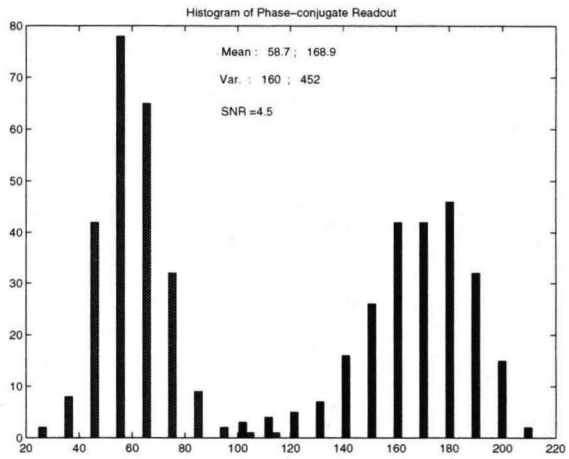

Figure 3.30: The intensity distribution of a pixel-matched image of a single pixel check board by the phase conjugate reconstruction.

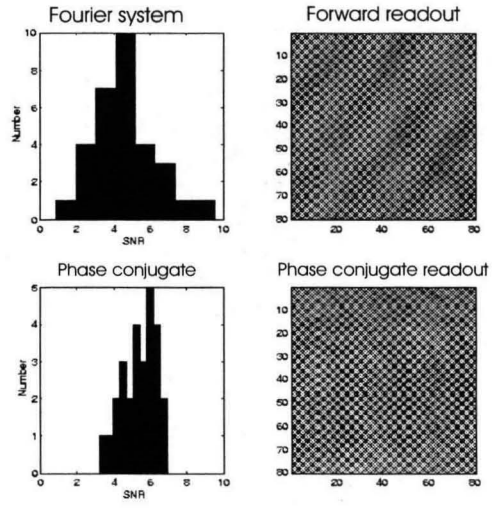

Figure 3.31: The quantitative comparison of pixel-matched image SNR between normal forward holographic reconstruction and phase conjugate reconstruction.

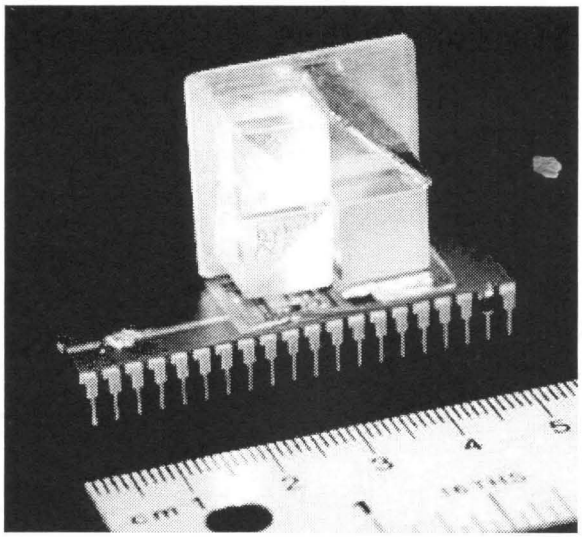

Figure 3.32: A compact phase conjugate holographic memory module with a photorefractive crystal and optical elements seating on top of an optoelectronic integrated circuit interface. The SLM and the necessary multiplexing laser source are not shown.

holograms, and P_i is the incident readout power. For example, if we use a crystal of $M\# = 10$ to record 500 holograms of a 1000×1000 pixel array, and we read out with 100 mW of laser power, requiring 300 electrons per pixel, the integration time, and hence the random access time, would be 2.4 μs. This corresponds to a sustained readout transfer rate, from the hologram to the silicon detectors, of 53 GB/s.

System volume density, recording rate and pixel size

An analysis of the system storage density (including the recording medium and all the optical components) of the holographic memory module of Figure 3.38 shows that the module storage density peaks at about 40 Mb/cm^3 for an optimum pixel size of 5 μm [27]. There is an optimum pixel size because as the pixel size decreases, the light in the signal path spreads more due to diffraction, causing us to use larger apertures for the crystal and beamsplitters.

A more aggressive design is to rely on total internal reflection to contain the beam diffraction within the boundaries of the module, so that the optical elements can be made close to the size of the SLM array, as far as the size of the laser array is relatively much smaller than the SLM. Experiments demonstrated that accurate recordings and phase conjugate reconstruction are obtained for the internally reflected

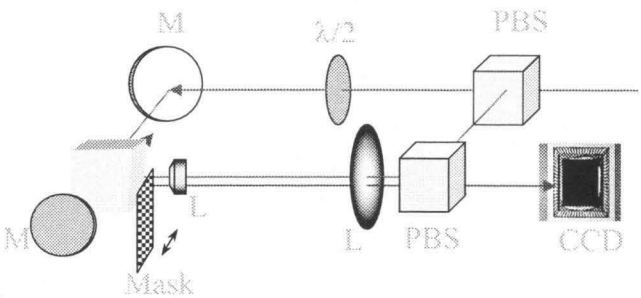

(a)

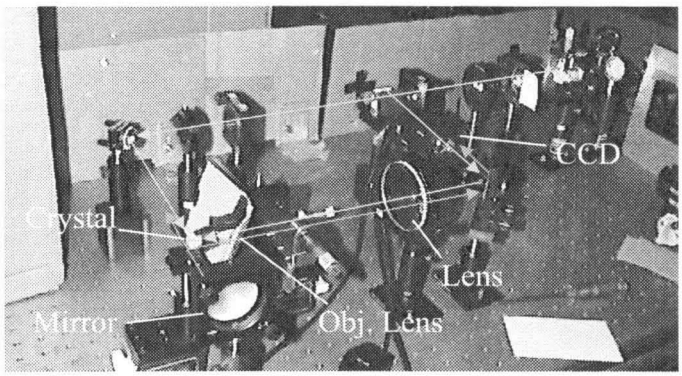

(b)

Figure 3.33: The experimental setup for holographic recording and phase conjugate reconstruction of a binary data mask with various pixel sizes.

signal beams [95]. In this case, the system density can be raised to the order of 2 Gb/cm^3, if SLM pixel sizes fall to 1 μm.

In addition, a larger page capacity increases the recording rate of the memory module, which is

$$\text{Recording rate} = \frac{N^2 ISLp}{(M\#)/M} \tag{3.24}$$

where N^2 is the total number of pixels per data page, I is the incident recording intensity, S is the sensitivity per unit length of the recording medium, L is the crystal thickness, and p is the light efficiency of the SLM. Assuming a crystal of $M\# = 10$ to record 500 holograms of a 1000 $\times$ 1000 pixel array, with I=100 mW/cm^2, S=0.1 cm/J, L=1 cm, and p=50%, we obtain a recording rate of 31 kB/s. This is typical for experiments currently performed.

Increasing the recording rate to make it comparable to the readout rate is highly

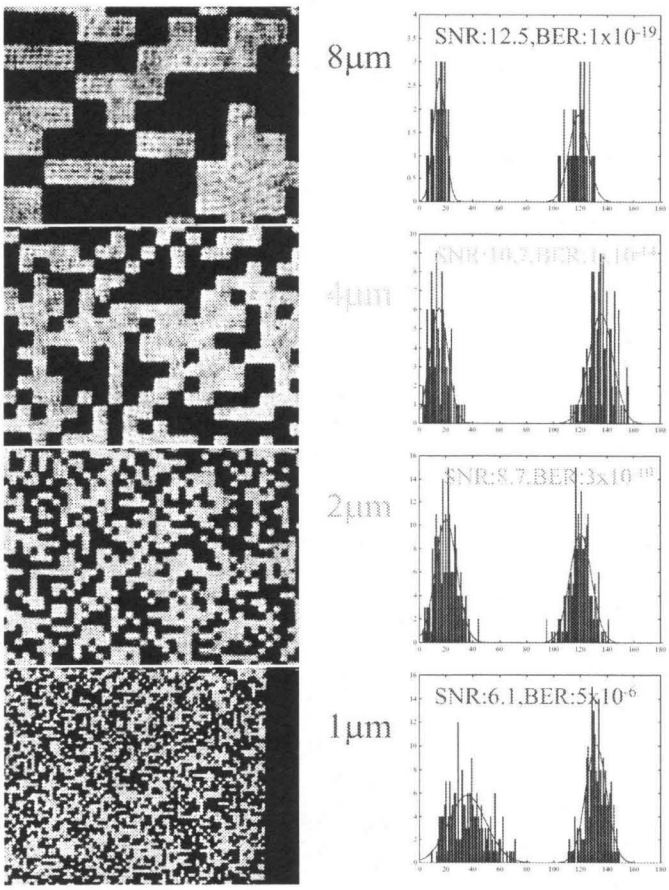

Figure 3.34: The direct images of random binary data masks with pixels ranging from $8 \times 8\ \mu m^2$ to $1 \times 1\ \mu m^2$, and their SNR measurements.

desirable for a practical system. By bringing the pixel sizes down to 1 μm and increasing the size of each data page to $10,000 \times 10,000$ pixels while still holding the array size to about 1 cm^2, we immediately gain two orders of magnitude in the sustained recording rate due to the increased parallelism. The trade-off is to give up some readout speed due to increasing the detector integration time for each pixel in equations (3.23).

Liquid crystal SLM and digital mirror array device(DMD)

For a spatial light modulator (SLM), the most important characterization is the energy efficiency, contrast ratio, and uniformity. A new micro-electro-mechanical system (MEMS) device is developed at Texas Instrument, Inc. (TI), digital mirror array (DMD), which tilts an array of tiny mirrors fabricated on a silicon wafer to

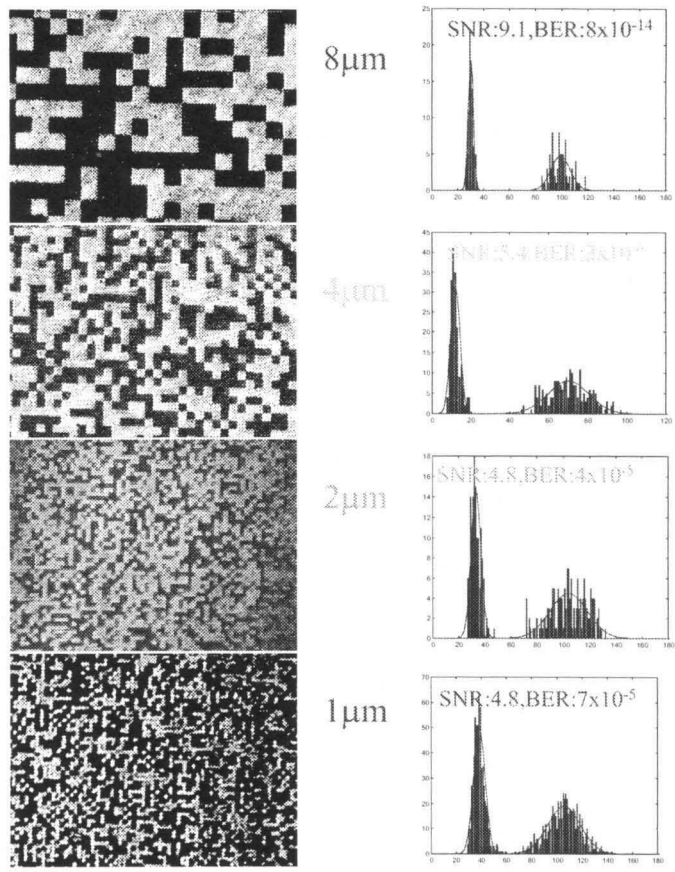

Figure 3.35: The phase conjugate reconstruction of random binary data masks with pixels ranging from 8×8 μm^2 to 1×1 μm^2, and their SNR measurements.

generate On/OFF pixels by individual mirror element. Due to the high fill-in factor, high reflection efficiency and fast responding time, it leads much better image quality as a spatial light modulator comparing with traditional transparent liquid crystal SLM on issues of uniformity, refreshing rate contrast, and efficiency. Also, it is easier to be scaled down to micrometer pixel size, comparing to the liquid crystal cell limited a certain thickness requirement.

In this study, we compare the performance between a liquid crystal SLM (Kopin model LVGA AMLCD evaluation kit) and the TI DMD SVGA device. The Kopin liquid crystal SLM has 640×480 pixels, with pixel pitch 24 μm, and contrast specification at 100. The TI DMD device has 800×600 pixels, with pixel pitch 17 μm.

The liquid crystal SLM modulates the light intensity going through the liquid

crystal by changing the polarization direction of the lights inside the liquid crystal. Because of the necessary wiring for each pixel control and the edge effects at each pixel, the effective area of each pixel is only 33%. The light throughout efficiency for all pixel ON is measured as only 27% in the lab. The contrast ratio is measured as 107 between all ON and all OFF pixels. On the other hand, the TI DMD device consists of MEMS mirror array on silicon bases with all control circuit behind the mirror, which leads to high reflection efficiency and large effective area at 16×16 μm^2 out of 17×17 μm^2 for each pixel. The experimental measurement gives 76% of energy efficiency for all ON pixels, and contrast ratio of 736 between all ON and OFF pixels.

The other concern for SLM is uniformity. The liquid crystal normally has a poor uniformity, because it is sensitive to the thickness variation through the whole screen. A nonuniform image causes poor signal-noise ratio, or requires special algorithm to distinguish the local ON/OF pixel during hologram readout, because of the tight photon budget of hologram readout. Fig. 3.40 shows the comparison between the TI DMD device and the Kopin SLM. The pixel intensity deviation of the DMD device is only half of that from liquid crystal SLM.

Due to the higher energy efficiency, higher contrast, and more uniform images, the TI DMD device is a better choice as SLM for holographic recording and reconstruction.

In Fig. 3.41, holograms with different spatial frequency on the DMD device and liquid crystal SLM are recorded and read out. The image contrast from the LC SLM is getting worse when the spatial frequency gets higher. On the other hand, the image on DMD is uniform and sharp. The quantitative measurements of the SNR clearly show a better result for DMD device in Fig. 3.42. Also shown is the SNR measurement of the random binary data pages. On average, the SNR from the DMD hologram recording is much better than the results from LC SLM.

For liquid crystal SLM, the refreshing rate is normally less than 100 frames per second due to the slow response time of liquid crystal. On the other hand, the TI DMD device has a responding time < 20 μs for each pixel, which makes it possible

for fast hologram recording. To demonstrate the application of the fast hologram recording, Dupont polymer is used for the hologram recording. Fig. 3.43 shows the holograms recorded in polymer with a refreshing rate of 10 μs. No holograms can be achieved by LC SLM with this refreshing rate.

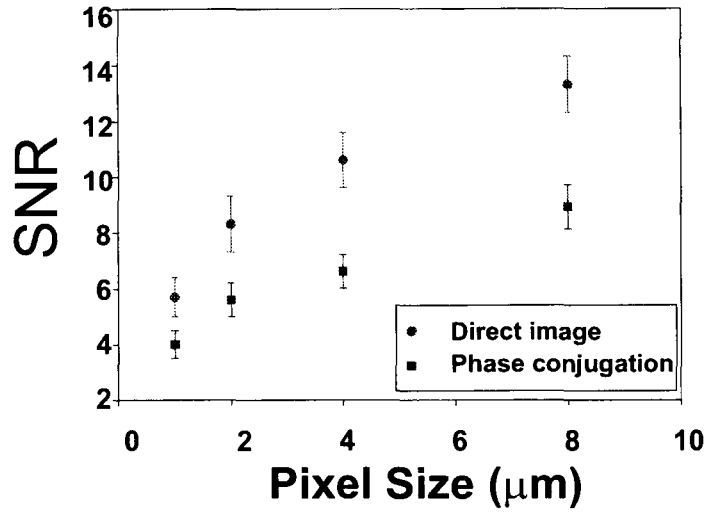

Figure 3.36: The SNR measurements for direct image and phase conjugate reconstruction of binary data masks as a function of the pixel size.

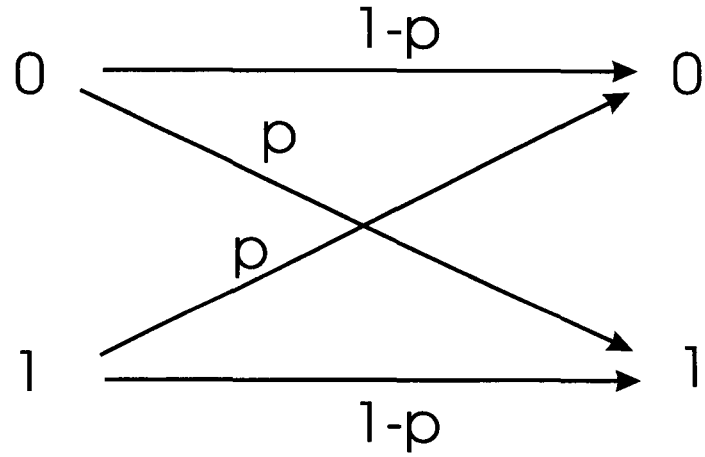

Figure 3.37: The information channel capacity with an error rate p.

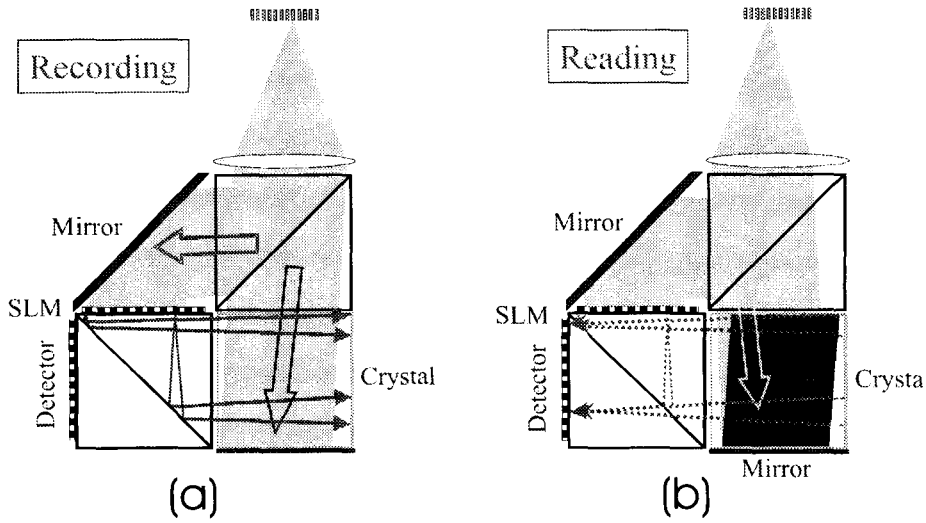

Figure 3.38: The compact phase conjugate module with a VCSEL array for angular multiplexing. (a) one VCSEL source is selected for recording a certain page; (b) the symmetric VCSEL source is selected to generate the pseudo phase conjugate readout beam in the medium.

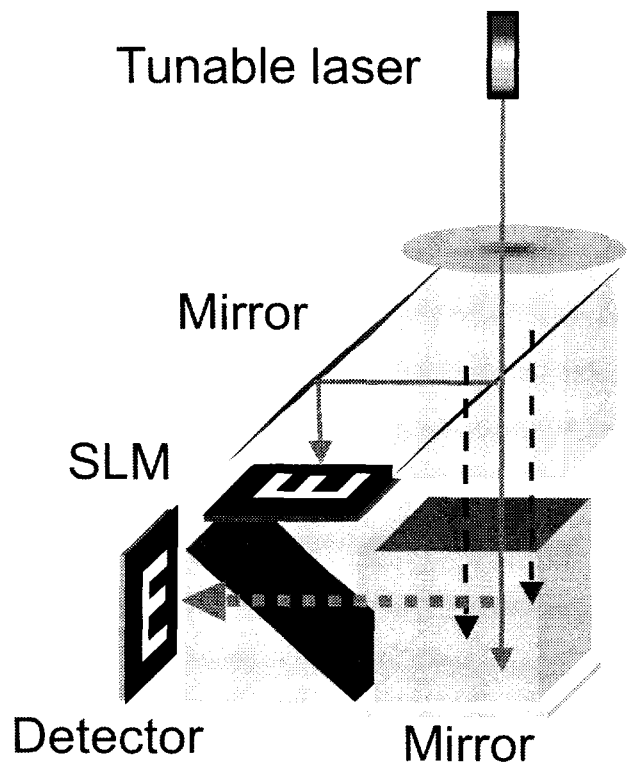

Figure 3.39: The compact phase conjugate module with a tunable laser diode for wavelength multiplexing.

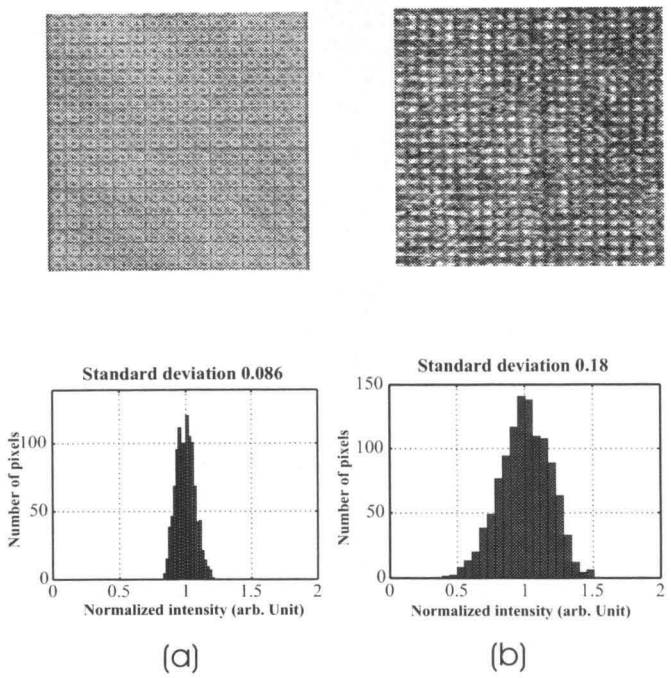

Figure 3.40: The uniformity comparison between (a) a TI DMD device and (b) a Kopin liquid crystal SLM.

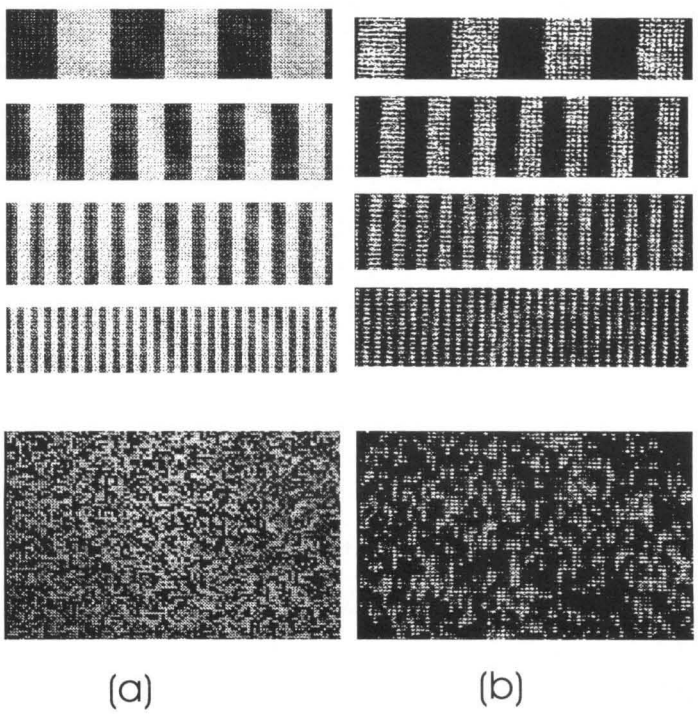

Figure 3.41: The holographic reconstruction of images recorded with (a) a TI DMD device and (b) a Kopin liquid crystal SLM.

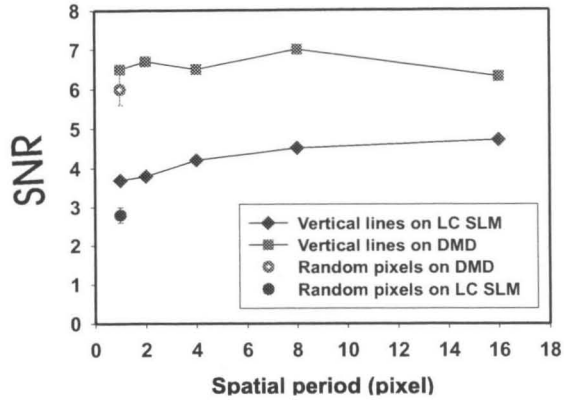

Figure 3.42: The SNR measurement from the holographic reconstruction of images recorded with (a) a TI DMD device and (b) a Kopin liquid crystal SLM. The SNR is measured as a function of the spatial frequency, where the LC-SLM image SNR decreases as the spatial frequency increases, while TI DMD images are almost independent of the spatial modulation frequency.

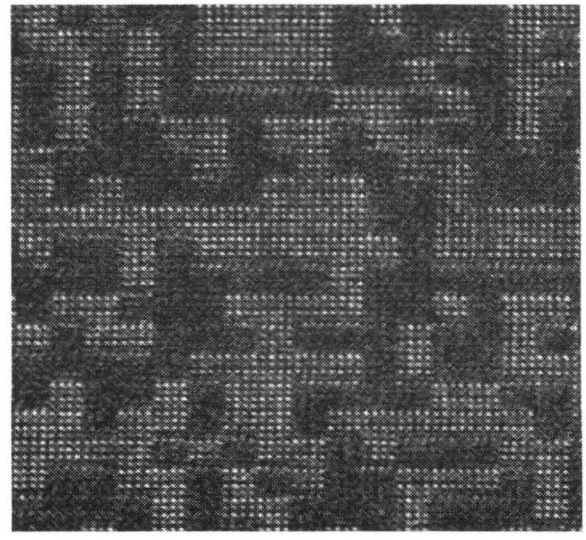

Figure 3.43: The holographic reconstruction of a hologram recorded with a TI DMD device in a frame rate of 10 μs in Dupont polymer.

Chapter 4 Four-Dimensional Holographic Imaging

Imaging recording and projection in three-dimensional (3-D) spaces used to be a driving factor for holography research and application development. In 1948, Dennis Gabor proposed a new imaging technology [46] as *holography*, in which coherent waves were used in a two-step, lensless imaging process. Later, he demonstrated its application in microscope imaging [47, 48]. Holography did not attract public attention until the 1960s, when E. N. Leith demonstrated the imaging and reconstruction of three-dimensional objects [74]. In all these imaging applications, a coherent reference wave is used to generate an interference pattern with the scattered coherent waves from the objects. This interference pattern is recorded on a photosensitive material as a hologram, which reconstructs the signal wave front when the same reference wave is illuminated on the material. All the information from the signal wave front, including amplitude and phase, is stored inside the material and can be reconstructed as original wave fronts. In 1971, Gabor was awarded the Nobel prize in physics for his invention.

However, due to the limits of the material performance, the quality and feasibility, the 3-D imaging and projection has not been the major application for holography. Instead, holography has been intensively investigated as a potential information storage technology [49, 72, 101, 108, 40, 40, 20, 104], as discussed in Chapter 3, or information processing elements, such as in neural networks [103, 80, 109], optical correlators [76, 110, 62], optical interconnections [71, 18, 122, 123], and diffracting elements [124, 73, 120, 119]. In these applications, known information or diffraction patterns are designed and recorded as holograms inside the holographic material. Signals with unknown wave front or information illuminate the hologram and are diffracted, filtered, and optically processed by the holographic pattern due to the se-

lective Bragg phase-matching ability of holograms. By properly designing holograms and architecture, it is possible to use a hologram as an imaging element to extract and form an image onto an image sensor.

Modern imaging technology is widely used in all areas of daily life and scientific practices, where image information is expected to be projected by an optical system onto a two-dimensional (2-D) image sensor, such as films, or more widely used nowadays, charge-coupled devices (CCD) and complementary metal oxide semiconductor (CMOS) devices, which can digitize the intensity information and store, process and reconstruct them in computers. To extract the 3-D spatial information from an object with the 2-D sensors, an instrument with the ability to selectively extract information from the 3-D information and to project it correspondingly onto 2-D is required, which is called optical sectioning. Current imaging optics can only extract information of a single 2-D section from 3-D spaces, such as a normal microscope with an imaging lens of small focal depth, or as a single point, such as a confocal microscope with a pinhole spatial filter and a near-field microscope with a point light source. To extract 3-D information, there must be some scanning mechanism, either mechanical scanning, such as the focus depth of objective lens scanning, the illumination point source scanning [85, 15], laser scanning confocal microscope [56, 36], or optical scanning, such as coherent phase interference scanning [134, 65].

By combining the abilities of selective wave front processing and multiplexing, volume holograms can achieve multi-dimensional tomographic imaging [9]. The key advantages are:

1. Volume holograms are selective diffraction elements due to the sensitive Bragg phase-matching. For a certain hologram, only the Bragg matching wave front is diffracted strongly and extracted with none other signal component affected.
2. Multiplexing ability makes it possible to process different wave front components at the same time without affecting each other.

In this chapter, we study two holographic architectures used for 3-D imaging theoretically and experimentally. Real-time 3-D imaging of fluorescent microspheres is demonstrated. To our knowledge, this technique is currently the only method that

allows simultaneous 3-D spatial imaging and spectroscopic imaging without use of a scanning mechanism.

4.1 Theoretical principles

Three-dimensional imaging and the confocal microscope

All optical imaging systems transfer the information about an object to the receiver, where the information carrying light is delivered and diffraction-corrected by the optical elements to the proper photosensor. Most of the imaging elements work on planar objects and deliver the image by applying an analog linear transformation on the transverse field intensity distribution, as shown in Fig. 4.1. To get the images

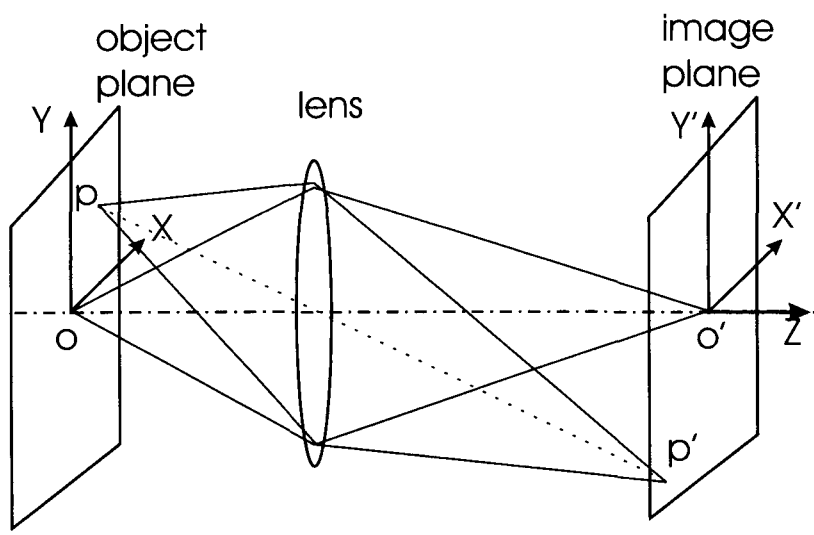

Figure 4.1: Planar imaging by an optical lens.

of different planes along different depths, we can change the focal length or scan the image plane.

One practical example is the human eyes, which just work as lens, collecting the light from the outside world and forming a real image onto the retina. We look at objects at different distances by adjusting the focal length of our eyes. However, the depth sensitivity is not very high for human eyes, which gives us a comfortable view of the world with all distances even when the eyes are focused only on a single plane at one time.

The light distribution around the geometrical focal plane is well-known and was first calculated by Zernike and Nijboer in 1949 [132, 16]. Considering the light distribution near a focal point O of an aberration free lens with circular aperture, the light intensity at point P relative to focus point O with a depth transition z and transverse distance r is given as [16]

$$
\begin{aligned}
I(u,v) &= (\frac{2}{u})^2[U_1^2(u,v)+U_2^2(u,v)]I_0, && (4.1)\\
u &= \frac{2\pi}{\lambda}(\frac{a}{f})^2 z, && (4.2)\\
v &= \frac{2\pi}{\lambda}(\frac{a}{f})r, && (4.3)\\
I_0 &= (\frac{\pi a^2|A|^2}{\lambda f^2})^2, && (4.4)\\
U_n(u,v) &= \sum_{s=0}^{\infty}(-1)^s(\frac{u}{v})^{n+2s}J_{n+2s}(v), && (4.5)
\end{aligned}
$$

where a is the radius of the circular aperture, A is the light amplitude at the aperture, f is lens focal length, U_n represents Lommel functions and J_n is Bessel functions.

For the light intensity distribution in the geometrical focal plane, $z = 0$,

$$
I(0,v) = \left[\frac{2J_1(v)}{v}\right]^2 I_0, \qquad (4.6)
$$

which is the familiar Airy formula [3] determining the image resolution

$$
\begin{aligned}
\delta r &= 0.610\frac{\lambda}{NA}, && (4.7)\\
NA &= \frac{a}{f}. && (4.8)
\end{aligned}
$$

For the light intensity along the axis, $v = 0$,

$$
I(u,0) = \left(\frac{\sin u/4}{u/4}\right)^2 I_0, \qquad (4.9)
$$

where the first null is

$$\delta z = \frac{2\lambda}{(NA)^2}, \tag{4.10}$$

with numerical aperture NA in equation (4.8).

For the traditional concept, where a loss of 20% in intensity from the center of the image is regarded as permissible [16], the focal tolerance δz for $I(u,0) \simeq 0.8I_0$ is given as

$$\delta z' \simeq \frac{0.5\lambda}{(NA)^2}. \tag{4.11}$$

Fig. 4.2 shows the intensity distribution function in the geometrical focal plane and along the axis in equations (4.6–4.9).

The transverse resolution and the focal depth tolerance determine the spatial resolution of the object in 3-D space, which is called voxel, when the object is illuminated uniformly. Due to the shift invariance in the transverse dimension, a transverse optical section across the focal point is projected onto the image plane as pixels with resolution determined by δr in equation (4.7). All the light from other locations in the 3-D object is out of focus and generates a relatively uniform background on the image plane, which determines the image contrast and signal to noise ratio. To get the full 3-D spatial information, scanning along the axis direction is required.

In the confocal microscope in Fig. 4.3, the object is illuminated by a focused beam, which gives the same spatial intensity illumination profile as determined by equation (4.1). Collecting the scattered signal, the intensity distribution function at the image plane will be $I(u,v)^2$, which leads to a higher transverse and depth resolution for each voxel, at the expense of detecting a single voxel at a time. Using a pinhole of the same size as the transverse resolution to filter the image point in front of the detector, the stray lights from the different locations except the illuminated focused point are blocked, which achieves a high signal to noise ratio for the intensity from the focused object point. A 3-D scanning is required to get the full spatial

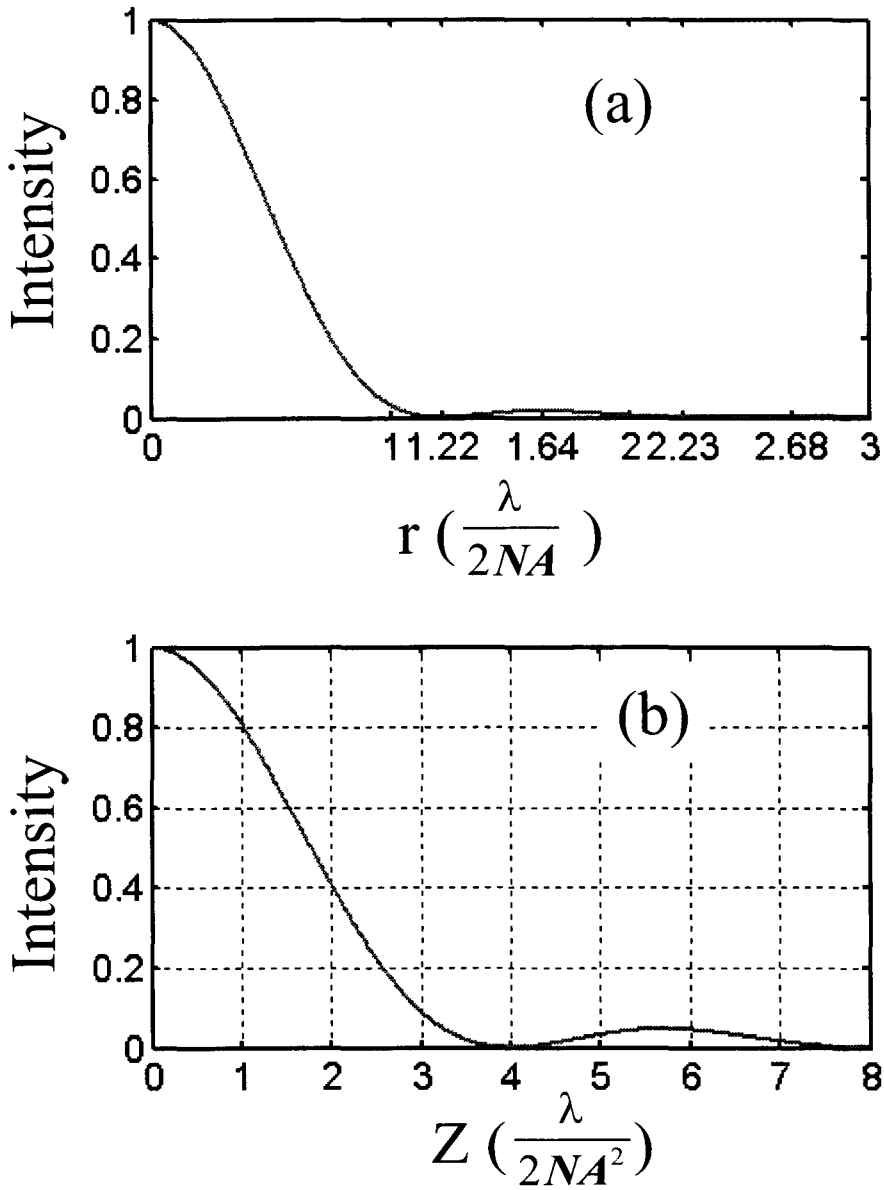

Figure 4.2: The intensity distribution around a focus point of an ideal aberration-free lens, (a) in the geometric focal plane, or (b) along the axis.

information.

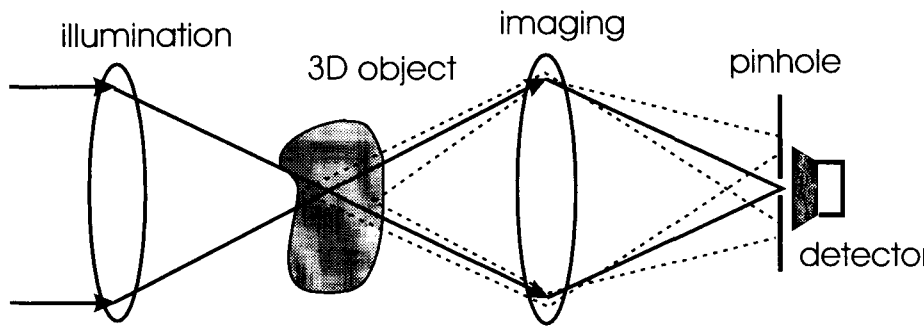

Figure 4.3: The confocal microscope architecture.

Due to the Bragg phase-matching, a volume hologram can selectively diffract a certain wave pattern while leaving other components in the signal beam untouched. This can serve as a good spatial or spectral filter, and is very important for 3-D information extraction, as shown in Fig. 4.4. A confocal microscope with volume holograms as the filter instead of a pinhole has been demonstrated [8].

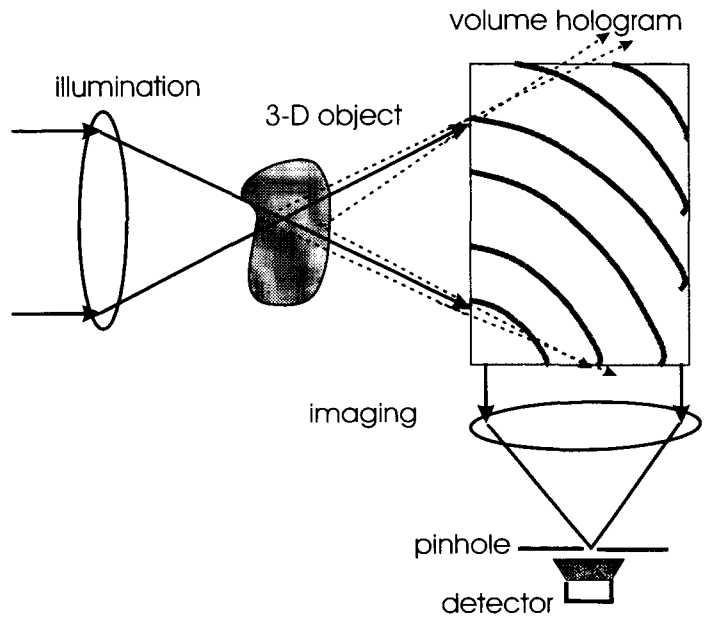

Figure 4.4: The confocal microscope architecture with a volume hologram filter.

Imaging using volume holograms

The previous holographic spatial filter can be recorded with a point source and its corresponding coherent reference beam, as shown in Fig. 4.5. The recording signal

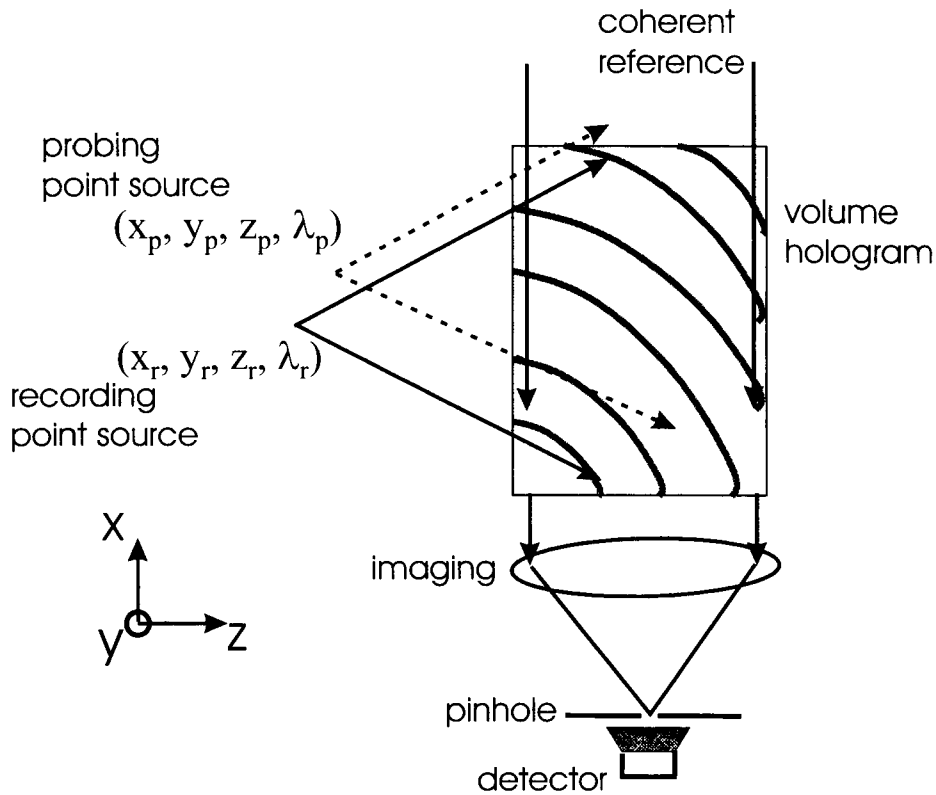

Figure 4.5: The recording of a volume holographic spatial filter with a point source and its corresponding coherent plane wave reference beam in 90-degree geometry. Another point source at different wavelength is used as a probe.

beam from a point source $(x_r, y_r, z_r, \lambda_r)$ and its coherent reference plane wave beam along $\hat{\boldsymbol{x}}$ axis with a small angle $u \ll 1$ are

$$E_s(\boldsymbol{r}) = \exp\left[i2\pi\frac{z-z_r}{\lambda_r} + i\pi\frac{(x-x_r)^2+(y-y_r)^2}{\lambda_r(z-z_r)}\right], \tag{4.12}$$

$$E_{ref}(\boldsymbol{r}) = \exp\left[-i2\pi\left(1-\frac{u^2}{2}\right)\frac{x}{\lambda_r} + i2\pi u\frac{z}{\lambda_r}\right]. \tag{4.13}$$

The recorded modulation of the material refractive index inside the material is given

to the first order as

$$\Delta\varepsilon(\boldsymbol{r}) = |E_{ref}(\boldsymbol{r}) + E_s(\boldsymbol{r})|^2 \tag{4.14}$$

$$\sim E_s^*(\boldsymbol{r})E_{ref}(\boldsymbol{r}), \tag{4.15}$$

where the other three terms in the interference pattern are mismatched in our reconstruction. Here, we do not consider the holographic recording and readout bandwidth as we discussed in Chapter 2. The holographic recording and reconstruction determine the fundamental spatial resolution that the volume hologram can reconstruct or spatially distinguish in the imaging application. However, comparing the spatial resolution discussed in this chapter and the results obtained in Chapter 2, we see that the spatial resolution by shift selectivity in imaging applications is much larger than the fundamental holographic resolution, which is limited by the holographic bandwidth. Therefore, we ignore the holographic bandwidth effect and treat the hologram pattern here as one achieved by a perfect point source.

When a probing point source $(x_p, y_p, z_p, \lambda_p)$ illuminates the volume hologram,

$$E_p(\boldsymbol{r}) = \exp\left[i2\pi\frac{z-z_p}{\lambda_p} + i\pi\frac{(x-x_p)^2+(y-y_p)^2}{\lambda_p(z-z_p)}\right], \tag{4.16}$$

the diffracted field integrated over the holographic grating by Born approximation is given as

$$E_d(\boldsymbol{r'}) = \iiint_V E_p(\boldsymbol{r})\Delta\varepsilon(\boldsymbol{r})\exp\left(i2\pi\frac{|\boldsymbol{r}-\boldsymbol{r'}|}{\lambda_p}\right)d^3\boldsymbol{r}. \tag{4.17}$$

The diffraction is phase-matched and significant, when the probing point source is identical to the recording source $(x_r, y_r, z_r, \lambda_r) = (x_p, y_p, z_p, \lambda_p)$. Otherwise, the diffraction is Bragg-mismatched and can be ignored. The phenomenon is called angle, shift or wavelength selectivity depending on the changes between the recording and probing sources. This sensitive spatial and spectral selectivity is the main motivation for using a volume hologram as spatial filter in confocal microscope. In addition to the spatial filtering, the hologram diffraction also depends on the wavelength of

the recording and probing beams. Therefore, the confocal microscope with a volume hologram actually detects the light intensity from a voxel in 3-D object space within a certain wavelength range $\Delta\lambda$ determined by the volume hologram wavelength selectivity. This 3-D spatial voxel plus spectral resolution is defined as a *texel* in 4-D hyperspace.

There are normally two degenerate directions existing in a single hologram. One is the direction out of signal-reference plane, along which the wave vector changes are minimized in K-sphere. Another is a combination with wavelength and spatial shifting, which forms a new wave vector matching condition for the same holographic gratings in a different K-sphere. The signals from these degeneracies are also Bragg matched and diffracted significantly. These degeneracies are normally avoided in holographic storage applications, because the diffraction intensity invariance along these directions causes cross-talks between difference data pages during reconstruction.

In confocal microscope applications, these degenerate directions are perpendicular to the axis of illumination, therefore their effect is limited by the confocal illumination.

On the other hand, these invariances can be used for a single hologram to optically section a 2-D slice from an illuminated 3-D spatial plus spectrum — 4-D hyperspace of an object, and to diffract them in the reference direction.

With a geometry in Fig. 4.5, numerical studies [9] have shown that an optically sectioning curved surface in the 3-D object spatial and spectral space can be achieved by the single hologram recorded with a point source at certain wavelength in Fig. 4.6.

By multiplexing different holograms recorded with point sources at different spatial locations and wavelengths, multiple sections from the object lying in 4-D hyperspace can be obtained and projected onto different portion of a 2-D sensor, leading to an imaging system with the ability to extract information from 4-D space without need of scanning mechanism, as shown in Fig. 4.7.

In the following sections, we investigate the imaging ability of a single hologram under different geometries theoretically and experimentally.

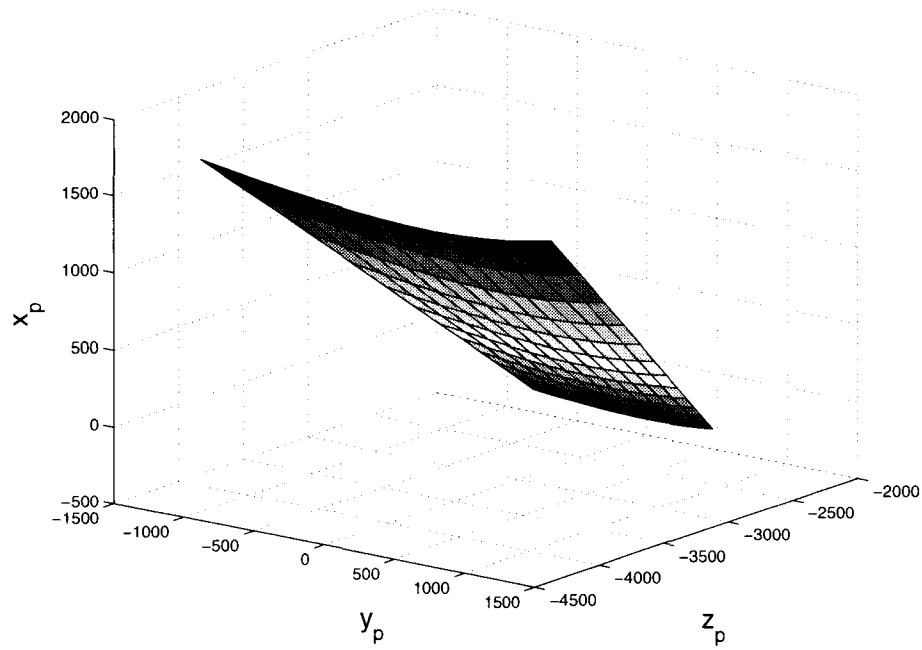

Figure 4.6: A numerically calculated degenerate surface (space and color) of the architecture in Fig. 4.5. The shape drawn in the figure represents the shape of the 2-D slice that the sensor extracts from the 4-D object and projects onto a contiguous area of the detector. (Each point on the grid represents one object texel and its corresponding pixel on the detector [9].)

4.2 Imaging properties of a 90-degree geometry volume hologram

Numerical studies on the spatial and wavelength selectivity of a single volume hologram recorded using a spherical wave and a plane reference wave in 90-degree geometry show significant diffraction from an optical cross-section in the 3-D spatial plus spectral object hyperspace [9], as shown in Fig. 4.5 and 4.6. The optical sectioning resolution, or the minimum distinguishable texel dimension by a volume hologram is determined by the spatial angle, shift, and wavelength selectivity. They are well understood through all the studies of holographic storage applications with various multiplexing mechanisms [125, 131, 112, 114, 130, 31, 10, 71, 17, 107, 79]. In all these studies on storage, only the intensity diffraction efficiency is considered, without considering the details of diffracted patterns around the Bragg-mismatching area. They are not important to the storage data, which are only intended to be read out at the

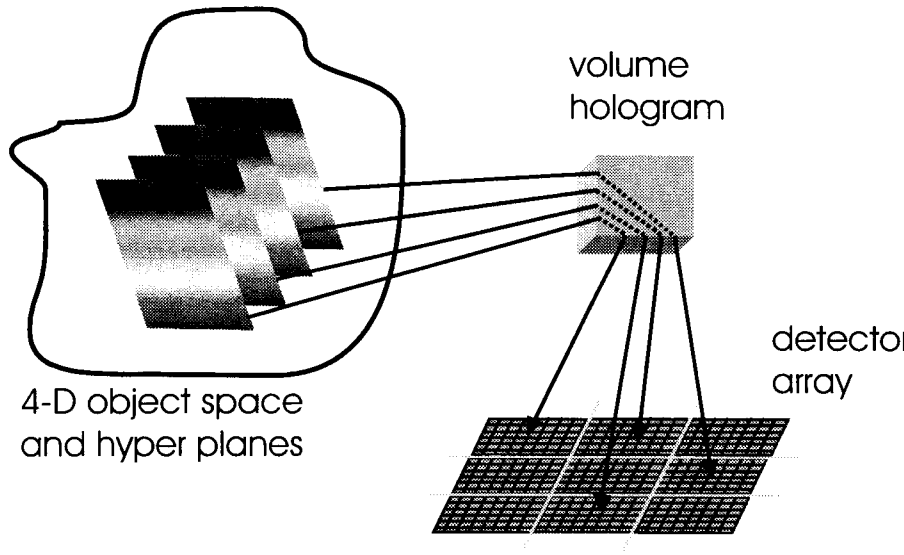

Figure 4.7: Multiple volume holograms optically section different hyperplanes from an object 4-D hyperspace and project them onto different 2-D image sensors.

Bragg phase-matching condition. However, for the imaging application with a complex signal incident, the diffraction pattern around the Bragg-mismatching condition leads to the background noise from the mismatching light source next to the Bragg phase-matching light source, which determines the imaging contrast and signal noise ratio.

Also, in data storage applications, the diffraction invariance along the degenerate directions in the optical sectioning hyperplane are generally not used, due to the nonperfect phase-matching condition in degenerate directions. The nonperfect phase-matching causes the signal bearing information to be distorted. For some special applications, these phenomena are investigated and demonstrated, such as the spatial degeneracy in hologram control and optical correlators [76, 71], or the wavelength degeneracy in two-wavelength nondestructive hologram reconstruction [11, 70, 135, 28, 35], where special care and design are required to correct and control the quality of the reconstructed signal beams.

By making use of the degenerate directions for imaging applications, we expect the hologram diffraction to generate an analog linear transformation from the optical section to the 2-D image sensor. The imaging transformation and aberration along

the degenerate direction are more critical than having a strong diffraction efficiency in the optical section plane. Here, we study and demonstrate the imaging performance in 90-degree geometry with a spherical wave used as a signal by experiments and numerical simulation.

4.2.1 Experimental studies on the imaging quality

To verify and investigate the imaging performance by a single volume hologram in 90-degree geometry, we experimentally record a volume hologram using a point source, and test its diffraction intensity and image performance using a probing point source, as shown in Fig. 4.8. Due to lack of a tunable laser source, we study only the 3-D spatial imaging effect in experiments, and investigate the behavior in the wavelength dimension by theoretical simulation.

Spatial selectivity of holographic intensity diffraction

A 45-degree cut $LiNbO_3(Fe)$ cubic crystal is used as the holographic recording medium. A plane wave reference beam comes into the crystal at $-\hat{\boldsymbol{x}}$ direction. An objective lens $\times 40$, $NA = 0.65$ focuses a collimated plane wave as a point source for signal beam at $\sim 2\ mm$ from the crystal surface. Reading out the hologram at the same location with the same wavelength, a plane wave is diffracted in the reference direction, as shown in Fig. 4.9, where (a) shows the signal beam profile recorded by the holograms with the beam angle deviation corresponding to numerical aperture $NA = 0.65$ inside the crystal of $n = 2.21$, and (b) is the Fourier plane image by a lens of 15 cm focus length, located at the same location as the reference beam's focal point on the detector during hologram recording.

In the ideal case, when the probing point source is shifted in either the $\hat{\boldsymbol{x}}$ or $\hat{\boldsymbol{z}}$ direction at the same wavelength, there is no diffraction due to Bragg mismatching. While shifting in the $\hat{\boldsymbol{y}}$ direction at the same wavelength, the diffraction intensity is as strong as the Bragg phase-matching condition due to the degeneracies. Fig. 4.10 shows the experimental spatial selectivity curves.

The $\hat{\boldsymbol{x}}$ direction is the typical shift multiplexing direction [107, 10, 107, 76, 7, 75],

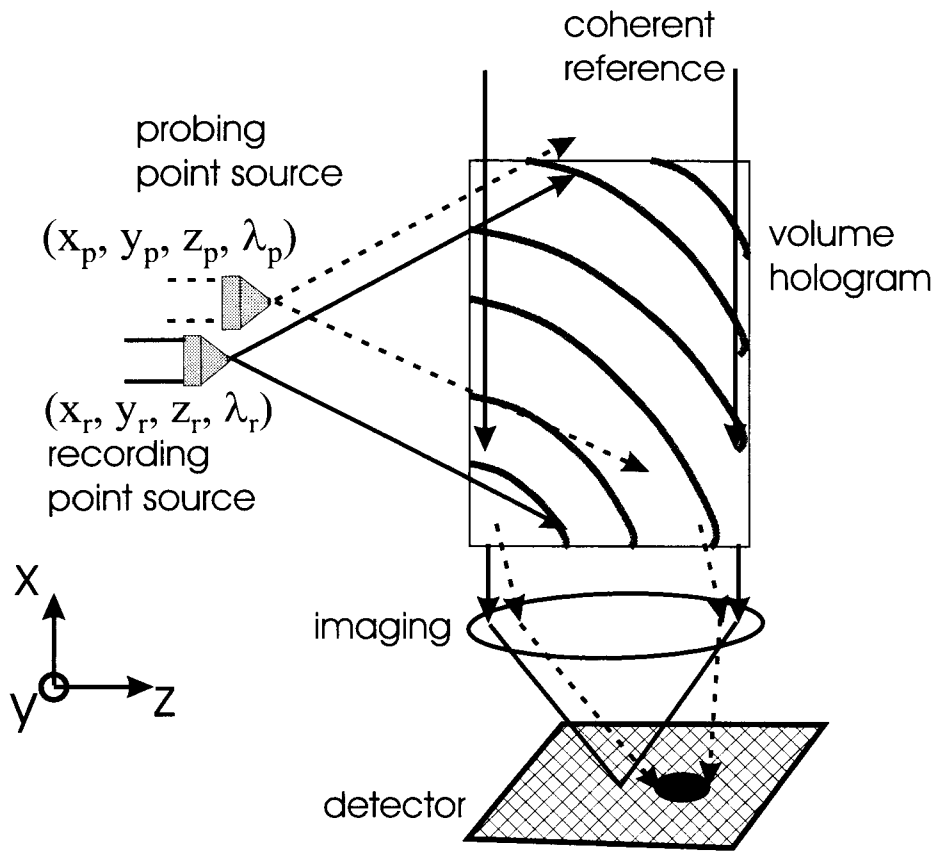

Figure 4.8: Experimental scheme for testing holographic imaging performance by a 90-degree volume hologram between a spherical wave and a plane reference wave. The spherical wave is generated by a focused beam with an objective lens. The diffracted reference beam is measured by an intensity detector or a Fourier plane image sensor.

where the first null is

$$\Delta x = \frac{\lambda}{2NA}. \tag{4.18}$$

Considering the transverse size of the focused spot during recording, the practical selectivity is given as

$$\Delta x = \frac{\lambda}{2NA} + \frac{\lambda}{2NA}. \tag{4.19}$$

For the numerical aperture $NA = 0.65$ at wavelength 480 nm, the shift selectivity is 0.74 μm, smaller than the experimental translation resolution, and consistent with

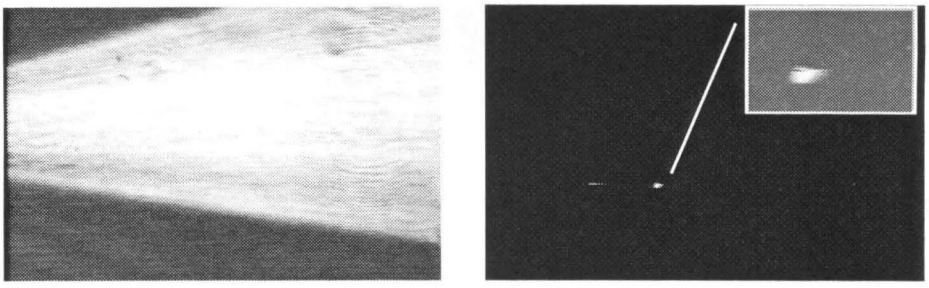

Figure 4.9: The holographic Bragg phase-matching reconstruction in Fig. 4.8: (a) the diffracted reference beam profile inside the crystal due to the numerical aperture of the signal beam by an objective lens $NA = 0.65$; (b) the Fourier plane image of the diffracted reference beam by a lens with focal length 15 cm.

the measurements in Fig. 4.10 (a).

The $\hat{\boldsymbol{y}}$ direction in Fig. 4.8 is Bragg degenerate, and the diffraction efficiency is uniform in a large range, as shown in the measurements in Fig. 4.10. Due to the limited experimental alignment accuracy and the small shift selectivity tolerance in the $\hat{\boldsymbol{x}}$ direction, a small coupling between the $\hat{\boldsymbol{x}}$ and $\hat{\boldsymbol{y}}$ translation stages in the lab leads to the changes of the diffraction efficiency measurements along the $\hat{\boldsymbol{y}}$ direction. Similar coupling effects can also be observed in the measurements in the $\hat{\boldsymbol{z}}$ direction depth selectivity, which leads to twin peaks due to the nonstability of the translation stage in the $\hat{\boldsymbol{x}}$ direction while moving along the $\hat{\boldsymbol{z}}$ direction. The intensity distribution of shifting in the transverse $\boldsymbol{x} - \boldsymbol{y}$ plane is also shown in Fig. 4.11 (a), where only a thin line along the $\hat{\boldsymbol{y}}$ direction is Bragg-matched.

The depth selectivity along the $\hat{\boldsymbol{z}}$ direction is shown in Fig. 4.10 (c) with a larger shift peak than the $\hat{\boldsymbol{x}}$ direction. The selectivity is due to the change of the signal beam angle inside the crystal while the point source is shifted along the depth. However, due to the spherical wave nature, the central paraxial part is always Bragg-matched. This is also obvious in the 2-D intensity distribution when shifting in the horizontal $\boldsymbol{x} - \boldsymbol{z}$ plane as shown in Fig. 4.11 (b), where the holographic diffraction is always partially Bragg matched when the point source is shifting within the range of the numerical aperture. The experimental bias in intensity to one tilting direction is due

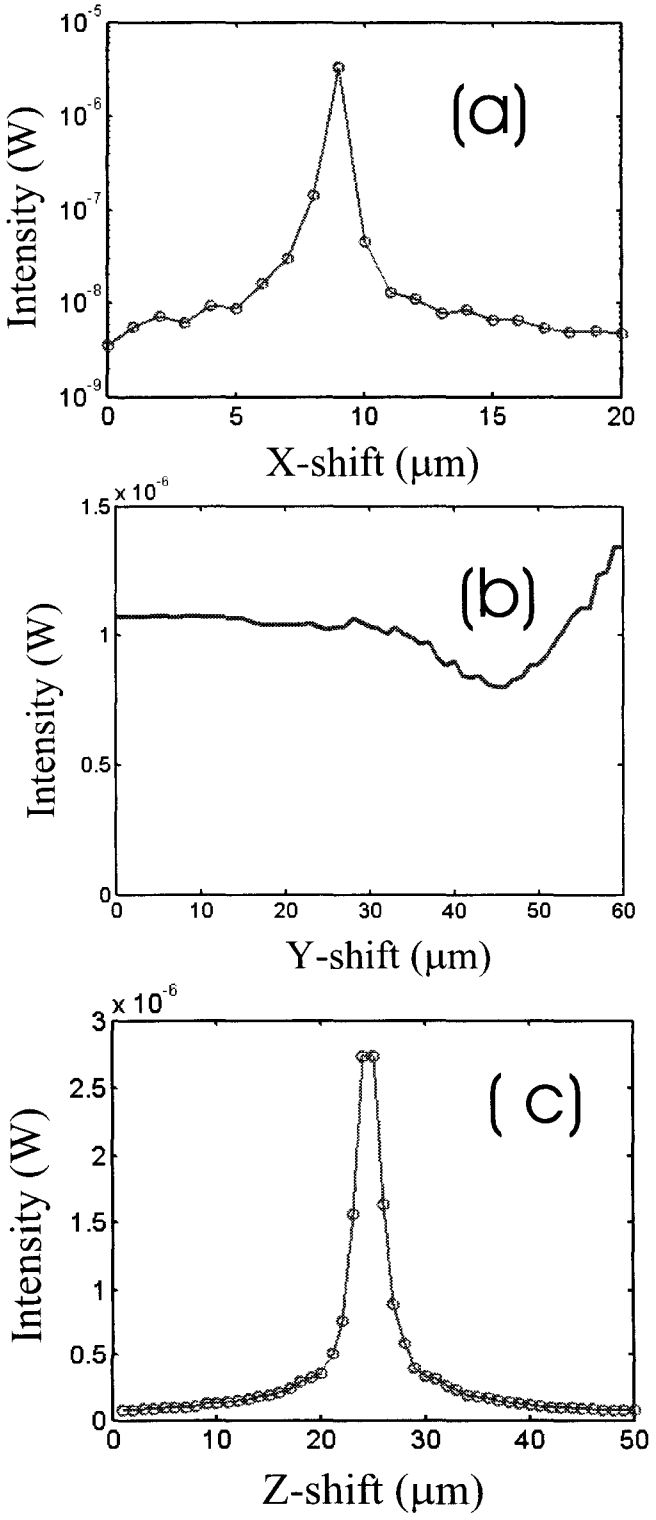

Figure 4.10: The holographic spatial selectivity measurement of 90-degree geometry with a spherical wave as the signal beam in Fig. 4.8. (a) the shift selectivity along the $\hat{\boldsymbol{x}}$ direction in logarithm scale; (b) the shift selectivity along the degenerate $\hat{\boldsymbol{y}}$ direction; (c) the shift selectivity along the depth $\hat{\boldsymbol{z}}$ direction.

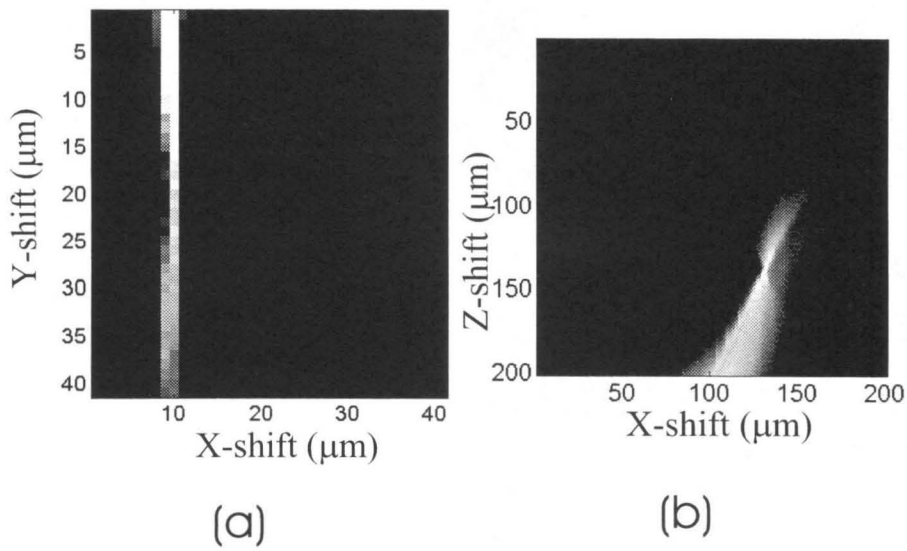

Figure 4.11: The holographic spatial shifting measurement of 90-degree geometry with a spherical wave as the signal beam in Fig. 4.8. (a) the holographic diffraction intensity distribution for spatial shifting in the transverse $\hat{\boldsymbol{x}} - \hat{\boldsymbol{y}}$ plane; (b) the holographic diffraction intensity distribution for spatial shifting in the longitudinal $\hat{\boldsymbol{x}} - \hat{\boldsymbol{z}}$ plane.

to the absorption effects in the crystal and the nonuniformity of the signal intensity along the $\hat{\boldsymbol{z}}$ direction. When the point source is shifting along the $(\hat{\boldsymbol{x}}, 0, -\hat{\boldsymbol{z}})$ direction, the Bragg phase-matching part of the angle range is along this direction also in the crystal, and is closer to the reference diffraction output surface along the $\hat{\boldsymbol{z}}$ direction, and has less absorption. On the other hand, when the point source is shifted along the $+\hat{\boldsymbol{z}}$ direction, the light intensity inside the crystal is higher due to the energy dissipation along the angle spreading, which leads to higher diffraction intensity in the lower side of Fig. 4.11 (b).

The depth selectivity along the $\hat{\boldsymbol{z}}$ direction is studied and analyzed theoretically in more details in section 4.2.2.

The image pattern of spatial shifting

As predicted in theoretical calculations in reference [9] and confirmed in experiments as shown in Fig. 4.10–4.11, one line along the $\hat{\boldsymbol{y}}$ direction through the recording point source in the object 3-D space is Bragg-matched with the same wavelength as

the recording beams. This vertical line is expected to be linearly transformed into the image plane, as shown in Fig. 4.11 (a). All the other locations shifted from the recording point along the $\hat{x}, \hat{z}$ direction are Bragg mismatched and generate only a weak scattering background to the image plane. With another degeneracy in wavelength dimension, different y-degenerate lines at different wavelengths are linearly transformed into the image space, which forms a curved 2-D image plane in the 4-D image hyperspace as predicted by theory [9].

Here, we measure the detailed image patterns for the spatial shifting effects at the recording wavelength. The wavelength dimension is studied theoretically due to the lack of a proper tunable laser source.

Fig. 4.12 shows the measured Fourier plane image patterns when the point source is shifted in either $\hat{x}, \hat{y}$ or $\hat{z}$ direction.

As shown in (a) and (c) shifting in $\hat{x}$, $\hat{z}$ directions, the intensity of the image decreases significantly and the patterns spread out along the vertical direction in the image plane. The interesting patterns are those in (b), when the signal is shifted along the degenerate $\hat{y}$ direction, where we expect to have a linear transformation without decaying intensity. All images in (b) show strong diffraction patterns and shift along the vertical direction accordingly to the signal point source translation. However, the image pattern is not kept as a point image, instead having strong aberration effects. This will cause large distortion of the image along the $\hat{y}$ direction, which is not acceptable in an imaging application.

The holographic imaging aberration in this 90-degree geometry can be corrected digitally after the image is captured by the detector, or maybe corrected optically by specially designing the hologram recorded inside the crystal. To fully understand the aberration pattern, we need to have a better theoretical understanding and a numerical model for holographic design.

4.2.2 Theoretical simulation on the imaging quality

Numerical model

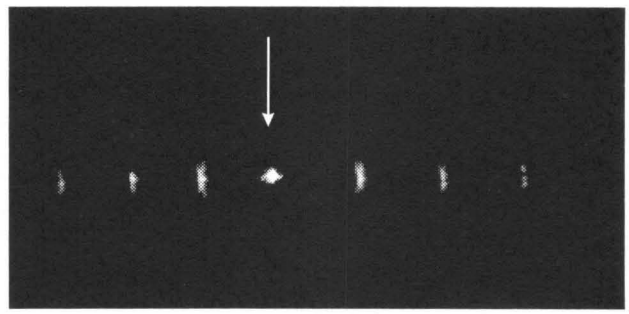

(a)

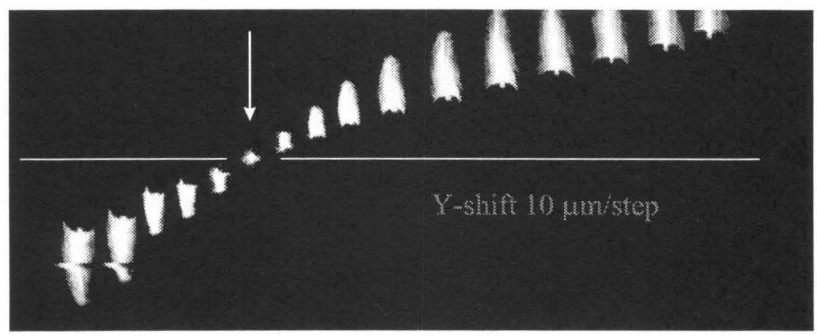

(b)

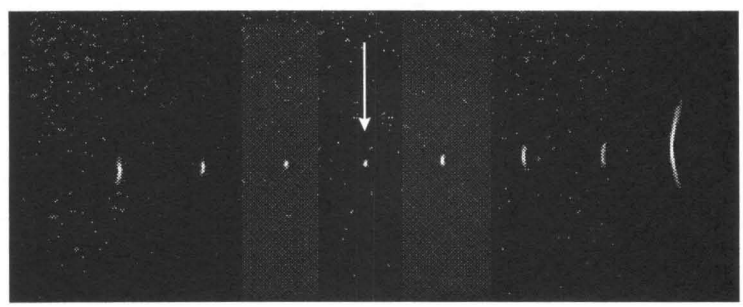

(c)

Figure 4.12: The holographic diffraction image patterns in 90-degree geometry with a spherical wave as the signal. (a) the image patterns as the signal point source shifts along the $\hat{\boldsymbol{x}}$ direction, 2 μm for each step; (b) the image patterns as the signal point source shifts along the degenerate $\hat{\boldsymbol{y}}$ direction, 10 μm for each step; (c) the image patterns as the signal point source shifts along the depth $\hat{\boldsymbol{z}}$ direction, 6 μm for each step. Due to the selectivity in the $\hat{\boldsymbol{x}}, \hat{\boldsymbol{z}}$ directions, images in (a) and (c) are enhanced for visibility. The arrows point to the Bragg phase-matching position with the signal at the recording position.

The 3-D spatial diffraction by a holographic pattern with a finite volume is a difficult mathematical problem due to the three-dimensional dependence. For 90-degree geometry shown in Fig. 4.8, the diffraction field by a probing beam $(x_p, y_p, z_p, \lambda_p)$ is determined by equation (4.17) using the Born approximation. There is no simple analytic solution to the 3-D spatial integral for a complex holographic grating inside the material. Numerical solution also requires tremendous computing time and memory, because the spatial resolution of the numerical integral has to be much smaller than the wavelength due to the phase sensitivity of the integral.

In reference [9], Dr. Barbastathis, et al. simplify the 3-D spatial integral down to a 1-D integral using paraxial and geometrical approximations. However, the formulas are still mathematically sophisticated, not physically intuitive, and hard to apply to different holographic geometries due to the specific geometry dependency in the formulas. Here, we develop a simple numerical model just for the 3-D spatial numerical integral with much fewer requirements on computing time and memory, which can also be applied to any geometric structure for holographic recording and reconstruction close to Bragg phase-matching condition.

As shown in equation (4.17), the diffracted field from the holographic pattern is given by

$$E_d(\boldsymbol{r'}) = \iiint_V E_p(\boldsymbol{r})\Delta\varepsilon(\boldsymbol{r}) \exp\left(i2\pi\frac{|\boldsymbol{r}-\boldsymbol{r'}|}{\lambda_p}\right) d^3\boldsymbol{r}, \tag{4.20}$$

where we ignore a normalization constant factor. Also, the interface effects are not considered in this model, which is taken into account easily by calculating the refraction angle numerically during the computation.

As shown in Fig. 4.8, we are interested in calculating the intensity pattern for the $\boldsymbol{y''} - \boldsymbol{z''}$ Fourier plane image by a lens of focal length f, which is determined by the Fourier transformation of equation (4.20):

$$E_F(x'-f, y'', z'') = \iint_{-\infty}^{\infty} E_d(x'; y', z') \exp\left(-i2\pi\frac{y'y''+z'z''}{\lambda_p f}\right) dy'dz'. \tag{4.21}$$

By equations (4.15),(4.20) and using the paraxial approximation, we get

$$
\begin{aligned}
E_F(x'-f,y'',z'') &= \iiint_V d^3\boldsymbol{r} E_p(\boldsymbol{r})\Delta\varepsilon(\boldsymbol{r}) \iint_{-\infty}^{\infty} dy'dz' \\
&\quad \exp\left[i2\pi\frac{-(x'-x)}{\lambda_p} + i\pi\frac{(y-y')^2+(z-z')^2}{\lambda_p(x-x')}\right] \\
&\quad \times \exp\left(-i2\pi\frac{y'y''+z'z''}{\lambda_p f}\right), \qquad (4.22) \\
&= \iiint_V d^3\boldsymbol{r} E_p(\boldsymbol{r})\Delta\varepsilon(\boldsymbol{r}) \exp\left[i2\pi(1-\frac{y''^2}{2f^2}-\frac{z''^2}{2f^2})\frac{x-x'}{\lambda_p}\right] \\
&\quad \times \exp\left[-i2\pi\frac{y''y}{\lambda_p f} - i2\pi\frac{z''z}{\lambda_p f}\right], \qquad (4.23) \\
&= \iiint_V d^3\boldsymbol{r} E_p(\boldsymbol{r},\lambda_p) E_s^*(\boldsymbol{r};\boldsymbol{r}_{\boldsymbol{r}},\lambda_r) E_{ref}(\boldsymbol{r},\lambda_r) \\
&\quad E_d^*(\boldsymbol{r};\boldsymbol{r}'',\lambda_p), \qquad (4.24)
\end{aligned}
$$

where the diffracted wave front $E_d(\boldsymbol{r};\boldsymbol{r}'',\lambda_p)$ is defined by

$$
\begin{aligned}
E_d(\boldsymbol{r};\boldsymbol{r}'',\lambda_p) &= \exp\left[-i2\pi(1-\frac{y''^2}{2f^2}-\frac{z''^2}{2f^2})\frac{x-x'}{\lambda_p}\right] \\
&\quad \times \exp\left[i2\pi\frac{y''y}{\lambda_p f} + i2\pi\frac{z''z}{\lambda_p f}\right], \qquad (4.25) \\
&= \exp\left[i\boldsymbol{k}_d(\boldsymbol{r}'',\lambda_p)\cdot\boldsymbol{r}\right], \qquad (4.26)
\end{aligned}
$$

i.e., a plane wave propagating along the $-\hat{\boldsymbol{x}}$ direction with transverse spatial frequency $\frac{y''}{f}k\hat{\boldsymbol{y}} + \frac{z''}{f}k\hat{\boldsymbol{z}}$ at wavelength λ_p,

$$
\boldsymbol{k}_d(\boldsymbol{r}'',\lambda_p) = \frac{2\pi}{\lambda_p}\left[-(1-\frac{y''^2}{2f^2}-\frac{z''^2}{2f^2})\hat{\boldsymbol{x}} + \frac{y''}{f}\hat{\boldsymbol{y}} + \frac{z''}{f}\hat{\boldsymbol{z}}\right]. \qquad (4.27)
$$

Substituting the recording and probing beams in equations (4.12)–(4.16), and

representing them in terms of wavevector k-space,

$$
\begin{aligned}
E_s(\boldsymbol{r};\boldsymbol{r}_r,\lambda_r) &= \exp\left(i\boldsymbol{k}_s\cdot(\boldsymbol{r}-\boldsymbol{r}_r)\right), && (4.28)\\
\boldsymbol{k}_s(\boldsymbol{r};\boldsymbol{r}_r,\lambda_r) &= \frac{2\pi}{\lambda_r}\frac{\boldsymbol{r}-\boldsymbol{r}_r}{|\boldsymbol{r}-\boldsymbol{r}_r|}, && (4.29)\\
E_p(\boldsymbol{r};\boldsymbol{r}_p,\lambda_p) &= \exp(i\boldsymbol{k}_p\cdot(\boldsymbol{r}-\boldsymbol{r}_p)), && (4.30)\\
\boldsymbol{k}_p(\boldsymbol{r};\boldsymbol{r}_p,\lambda_p) &= \frac{2\pi}{\lambda_p}\frac{\boldsymbol{r}-\boldsymbol{r}_p}{|\boldsymbol{r}-\boldsymbol{r}_p|}, && (4.31)\\
E_{ref}(\boldsymbol{r},\lambda_r) &= \exp(i\boldsymbol{k}_{ref}\cdot\boldsymbol{r}), && (4.32)\\
\boldsymbol{k}_{ref}(\lambda_r) &= \frac{2\pi}{\lambda_r}\left[-\left(1-\frac{u^2}{2}\right)^2\hat{\boldsymbol{x}}+u\hat{\boldsymbol{z}}\right], && (4.33)
\end{aligned}
$$

the diffracted image pattern in equation (4.24) is

$$
\begin{aligned}
E_F(x'-f,y'',z'') &= \iiint_V d^3\boldsymbol{r}\exp\left[i\boldsymbol{k}_p\cdot(\boldsymbol{r}-\boldsymbol{r}_p)-i\boldsymbol{k}_s\cdot(\boldsymbol{r}-\boldsymbol{r}_r)\right]\\
&\qquad\times\exp\left[i(\boldsymbol{k}_{ref}-\boldsymbol{k}_d)\cdot\boldsymbol{r}\right]. \qquad (4.34)
\end{aligned}
$$

Equation (4.34) is the typical form of four wave mixing, or holographic Bragg phase-matching integral. The integral is maximized under Bragg phase-matching condition, when the phase factor:

$$
\begin{aligned}
\phi &= \boldsymbol{k}_p(\boldsymbol{r};\boldsymbol{r}_p,\lambda_p)\cdot(\boldsymbol{r}-\boldsymbol{r}_p)-\boldsymbol{k}_s(\boldsymbol{r};\boldsymbol{r}_r,\lambda_r)\cdot(\boldsymbol{r}-\boldsymbol{r}_r)+(\boldsymbol{k}_{ref}-\boldsymbol{k}_d)\cdot\boldsymbol{r} \qquad (4.35)\\
&= 0. \qquad (4.36)
\end{aligned}
$$

For simple geometries, where the four wave vectors $\boldsymbol{k}_p, \boldsymbol{k}_s, \boldsymbol{k}_{ref}$ and $\boldsymbol{k}_d$ are simple functions of $\boldsymbol{r}$, the diffracted field can be integrated analytically from equation (4.34). For more general conditions, such as the spherical waves in Fig. 4.8, no simple analytic form can be achieved due to the complex functions for $\boldsymbol{k}_p, \boldsymbol{k}_s$ in equations (4.29),(4.31). Only a numerical solution is possible.

To simplify the numerical integral, we consider the integral in equation(4.34) over a small cubic volume ΔV_i centered around $\boldsymbol{r}_i$ only, as shown in Fig. 4.13. For point sources at $\boldsymbol{r}_r, \boldsymbol{r}_p$, the integral area ΔV_i is within the far field and the wave front is

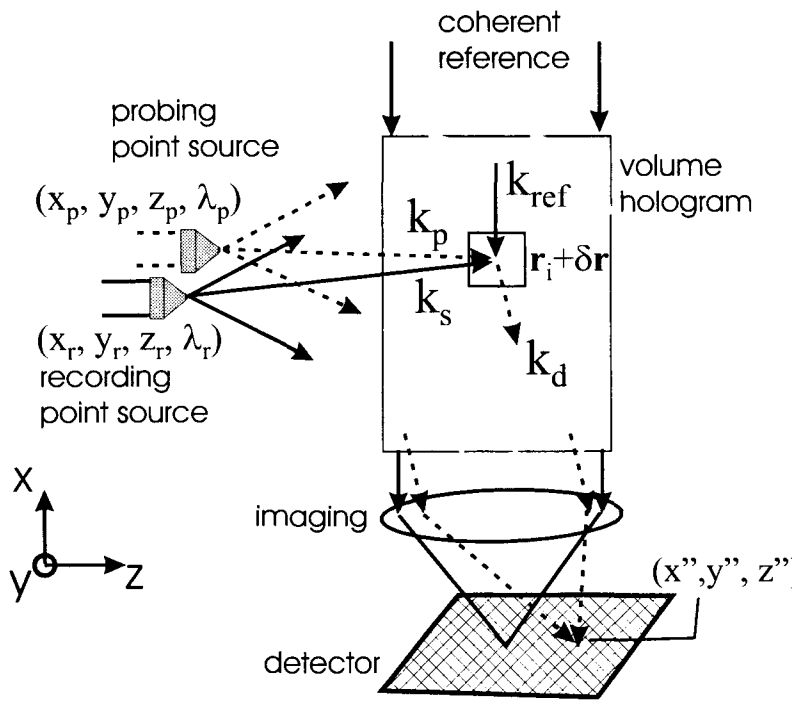

Figure 4.13: The 3-D integral of a small cubic volume of the holographic grating. The small cubic volume $\Delta V = \Delta x \times \Delta y \times \Delta z$ is centered at $\boldsymbol{r}_i$. The full integral over the volume V is $\iiint_V d^3\boldsymbol{r} = \sum_i \iiint_{\Delta V_i} d^3\boldsymbol{\delta r}$.

approximately a plane wave [75, 50], its wavevectors in equations (4.29),(4.31) can be simplified as

$$\boldsymbol{k}_s(\boldsymbol{r} = \boldsymbol{r}_i + \boldsymbol{\delta r}; \boldsymbol{r}_r, \lambda_r) = \frac{2\pi}{\lambda_r}\left(\frac{\boldsymbol{r}_i - \boldsymbol{r}_r}{|\boldsymbol{r}_i - \boldsymbol{r}_r|} + \frac{\boldsymbol{\delta r}_{\perp 1}}{|\boldsymbol{r}_i - \boldsymbol{r}_r|}\right) + \bigcirc\left((\frac{|\boldsymbol{\delta r}|}{|\boldsymbol{r}_i - \boldsymbol{r}_r|})^2\right) \quad (4.37)$$

$$\boldsymbol{k}_p(\boldsymbol{r} = \boldsymbol{r}_i + \boldsymbol{\delta r}; \boldsymbol{r}_p, \lambda_p) = \frac{2\pi}{\lambda_p}\left(\frac{\boldsymbol{r}_i - \boldsymbol{r}_p}{|\boldsymbol{r}_i - \boldsymbol{r}_p|} + \frac{\boldsymbol{\delta r}_{\perp 2}}{|\boldsymbol{r}_i - \boldsymbol{r}_p|}\right) + \bigcirc\left((\frac{|\boldsymbol{\delta r}|}{|\boldsymbol{r}_i - \boldsymbol{r}_p|})^2\right) \quad (4.38)$$

where $\boldsymbol{\delta r}_{\perp 1}, \boldsymbol{\delta r}_{\perp 2}$ are the components of $\boldsymbol{\delta r}$ perpendicular to $\boldsymbol{r}_i - \boldsymbol{r}_r, \boldsymbol{r}_i - \boldsymbol{r}_p$ respectively

$$\boldsymbol{\delta r}_{\perp 1} = \boldsymbol{\delta r} - \boldsymbol{\delta r}\cdot(\boldsymbol{r}_i - \boldsymbol{r}_r)\frac{\boldsymbol{r}_i - \boldsymbol{r}_r}{|\boldsymbol{r}_i - \boldsymbol{r}_r|^2}, \quad (4.39)$$

$$\boldsymbol{\delta r}_{\perp 2} = \boldsymbol{\delta r} - \boldsymbol{\delta r}\cdot(\boldsymbol{r}_i - \boldsymbol{r}_p)\frac{\boldsymbol{r}_i - \boldsymbol{r}_p}{|\boldsymbol{r}_i - \boldsymbol{r}_p|^2}. \quad (4.40)$$

By using the far-field approximation $|\boldsymbol{\delta r}| \ll |\boldsymbol{r}_i - \boldsymbol{r}_r|, |\boldsymbol{r}_i - \boldsymbol{r}_r|$, we have the phase

factor in equation (4.35) in volume ΔV_i as

$$\phi(\boldsymbol{\delta r};\boldsymbol{r}_i) = \phi_i(\boldsymbol{r}_i) + \boldsymbol{\Delta K}_i\cdot\boldsymbol{\delta r}, \tag{4.41}$$

$$\phi_i(\boldsymbol{r}_i) = \frac{2\pi|\boldsymbol{r}_i-\boldsymbol{r}_p|}{\lambda_p} - \frac{2\pi|\boldsymbol{r}_i-\boldsymbol{r}_r|}{\lambda_r} + (\boldsymbol{k}_{ref}(\lambda_r) - \boldsymbol{k}_d(\lambda_p))\cdot\boldsymbol{r}_i, \tag{4.42}$$

$$\boldsymbol{\Delta K}_i(\boldsymbol{r}_i) = \frac{2\pi}{\lambda_p}\frac{\boldsymbol{r}_i-\boldsymbol{r}_p}{|\boldsymbol{r}_i-\boldsymbol{r}_p|} - \frac{2\pi}{\lambda_r}\frac{\boldsymbol{r}_i-\boldsymbol{r}_r}{|\boldsymbol{r}_i-\boldsymbol{r}_r|} + \boldsymbol{k}_{ref}(\lambda_r) - \boldsymbol{k}_d(\lambda_p). \tag{4.43}$$

The 3-D integral of the diffracted field in equation (4.34) is reduced to a finite summation over a finite volume

$$E_F(x'-f,y'',z'') = \sum_i \exp(i\phi_i(\boldsymbol{r}_i)) \iiint_{\Delta V_i} d^3\boldsymbol{\delta r}\exp\left(i\boldsymbol{\Delta K}_i\cdot\boldsymbol{\delta r}\right), \tag{4.44}$$

$$= \sum_i \exp(i\phi_i(\boldsymbol{r}_i))\Delta V \mathrm{sinc}\left(\frac{\Delta K_{ix}\Delta X}{2\pi}\right)\mathrm{sinc}\left(\frac{\Delta K_{iy}\Delta Y}{2\pi}\right) \times\mathrm{sinc}\left(\frac{\Delta K_{iz}\Delta Z}{2\pi}\right), \tag{4.45}$$

where the small cubic volume $\Delta V = \Delta X \times \Delta Y \times \Delta Z$.

Equation (4.45) gives the basics for our numerical model, which can be used to all different simple geometries we consider for holographic imaging applications, as far as the far field and Born approximations are valid. The validity of the model is checked numerically by verifying well-known simple holographic geometries, such as angle and wavelength selectivity of plane waves in transmission, reflection and 90-degree geometry. Also, the simulation on holographic imaging is compared and proven to be consistent with experimental measurements, as shown in following sections.

Selectivity by simulation and comparison with experiments

The selectivities of the $\hat{\boldsymbol{x}}, \hat{\boldsymbol{z}}$ directions and wavelength determine the final resolution of the holographic imaging. To better understand the resolution, we need to be able to calculate the selectivity theoretically. From the numerical model, we can simulate the diffraction efficiencies as the probing condition changes, and from the simulation results, we expect to derive a simple approximation formula to calibrate the selectivities analytically.

1. Shift selectivity:

In Fig. 4.14, the numerical simulation of the diffraction efficiency across the detector is calculated as a function of the horizontal translation δx. A sharp selectivity curve is achieved, as we expected from experiments in Fig. 4.10.

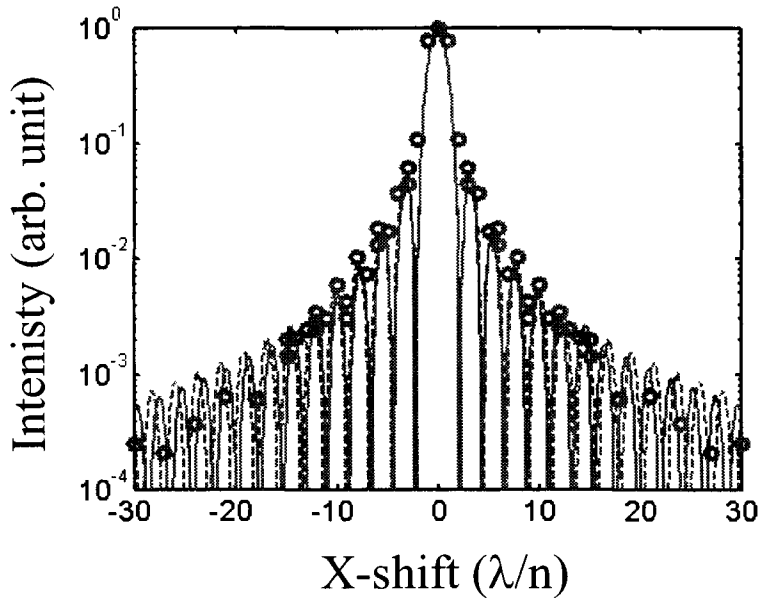

Figure 4.14: The numerical simulation and theoretical calculation of shift selectivity of 90-degree geometry. The simulation parameter is assumed $NA = 0.5$, $n = 2.2$. (o): the numerical simulation; (solid line): theoretical integral of selectivity curve in equation (4.49); (dot line): the approximation as a *sinc* function in equation (4.50).

The shift selectivity is well studied in [107, 10, 76, 7, 75], where paraxial approximation, or the phase integral along the path are used to get approximate analytic expressions. However, the accuracy of these results for a large numerical aperture we expect to use in holographic imaging system need to be justified.

For the path integral approximation [75], the ray optics approximation is assumed and the integral of the phase along the ray path is calculated to give the diffraction efficiency. This approximation can be justified by equation (4.45) in the numerical simulation model. Even though the Bragg mismatched diffracted pattern is not concentrated on the center of Bragg phase-matching condition, the diffracted intensity is still dominated at the Bragg phase-matching direction, therefore only the single diffraction component along this direction need to be calculated. The diffracted

amplitude along this direction is determined by the phase factor $\phi_i(\boldsymbol{r}_i)$ in equation (4.45).

For shift selectivity along the $\hat{\boldsymbol{x}}$ direction $\Delta x \ll z_0$, the phase changes along the Bragg phase-matching or the recording/diffracting direction is, as shown in Fig. 4.15 :

$$\begin{aligned}
\phi(\boldsymbol{r}_i, \Delta x) &= \frac{2\pi}{\lambda_n}(\sqrt{(x+\Delta x)^2 + z_0^2} - \sqrt{x^2 + z_0^2}, && (4.46)\\
&= \frac{2\pi}{\lambda_n}\frac{\Delta x x}{\sqrt{x^2 + z_0^2}}, && (4.47)\\
E_d &\simeq \int_{-D/2}^{D/2} dx \exp(i\frac{2\pi}{\lambda_n}\frac{\Delta x x}{\sqrt{x^2 + z_0^2}}), && (4.48)\\
&\simeq \int_{-NA/n}^{NA/n} d\alpha \exp(i\frac{2\pi\Delta x}{\lambda_n}\frac{\alpha}{\sqrt{1+\alpha^2}}), && (4.49)
\end{aligned}$$

where $\lambda_n = \lambda_0/n$, numerical aperture $NA = \frac{nD}{2z_0}$, and the final integral is independent to the depth z_0. When the numerical aperture NA/n is small, using the first order approximation $\frac{\alpha}{\sqrt{1+\alpha^2}} \approx \alpha$, equation (4.49) is simplified to

$$|E_d| \simeq \text{sinc}\left(\frac{2NA\Delta x}{\lambda_0}\right), \qquad (4.50)$$

which gives a *sinc* function with the first null at $\frac{\lambda_0}{2NA}$, as shown in equation (4.18).

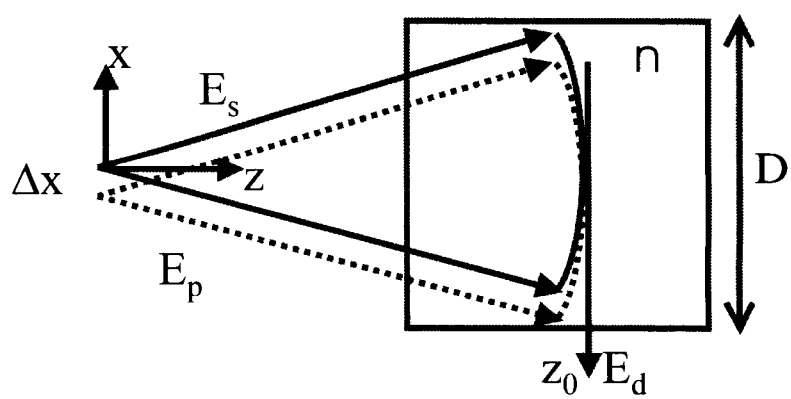

Figure 4.15: The phase integral approximation along the Bragg diffraction path for selectivity calculation.

For $NA = 0.5, n = 2.2$ in our numerical simulation, the phase integral and the first order *sinc* approximation have little difference, and both give a nice representation of the shift selectivity profile, as shown in Fig. 4.14. Also, compared with the experimental results as shown in Fig. 4.16 (a), the *sinc* approximation is consistent.

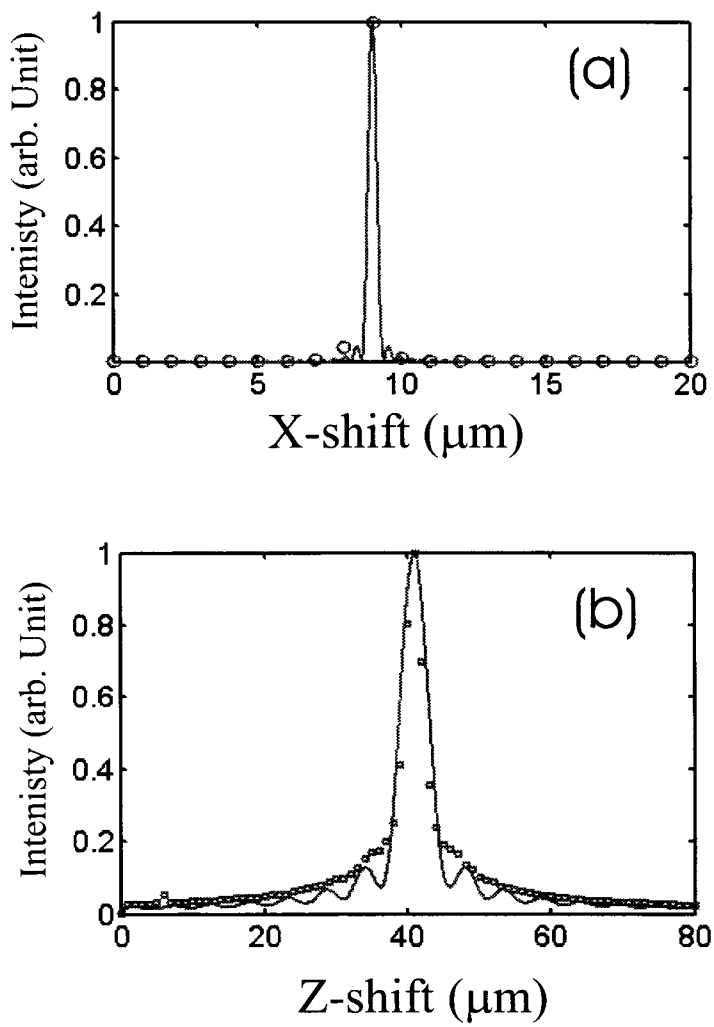

Figure 4.16: The experimental measurement of (a) shift selectivity, (b) depth selectivity, and their theoretical phase integral approximation.

2. Depth selectivity along the $\hat{z}$ direction

Using the same procedure as for the shift selectivity in the $\hat{x}$ direction, a phase integral model is constructed for an analytic expression of the depth selectivity. The phase changes along the Bragg phase-matching direction for depth shifting $\Delta z \ll z_0$

are

$$\phi(\boldsymbol{r}_i, \Delta z) = \frac{2\pi}{\lambda_n} \frac{\Delta z z_0}{\sqrt{x^2 + z_0^2}}, \tag{4.51}$$

$$E_d \simeq \int_{-NA/n}^{NA/n} d\alpha \, \exp(i \frac{2\pi \Delta z}{\lambda_n} \frac{1}{\sqrt{1+\alpha^2}}). \tag{4.52}$$

To the first order approximation, $\frac{1}{\sqrt{1+\alpha^2}} \simeq 1 - \alpha^2/2$, we have the depth selectivity as Fresnel integrals $C(s), S(s)$

$$|E_d| \simeq \frac{\sqrt{C^2(s) + S^2(s)}}{s}, \tag{4.53}$$

$$s = NA\sqrt{\frac{2\Delta z}{n\lambda_0}}, \tag{4.54}$$

$$C(s) = \int_0^s \cos(\frac{\pi t^2}{2}) \, dt, \tag{4.55}$$

$$S(s) = \int_0^s \sin(\frac{\pi t^2}{2}) \, dt. \tag{4.56}$$

The first minimum of function $\frac{\sqrt{C^2(s)+S^2(s)}}{s}$ occurs at $s = 1.91$, as shown in Fig. 4.17. This gives for the depth selectivity Δz

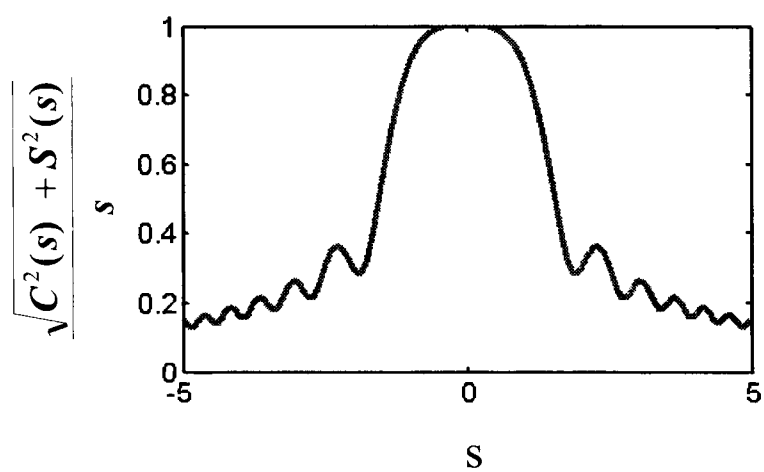

Figure 4.17: A function of Fresnel integrals, where the first minimum at $s = 1.91$.

$$\Delta z = 1.82 \frac{n\lambda_0}{NA^2}. \tag{4.57}$$

Fig. 4.18 shows both integrals of depth selectivity in equation (4.52) and the Fresnel integral in equation (4.53). For numerical aperture $NA = 0.5, n = 2.2$ in the simulation, the Fresnel integral is a good approximation. Both integrals fit well with the numerical simulation results, even though the integral on the phase path considers the Bragg matching direction only while the numerical simulation includes all different diffracted components. Fig. 4.16 also shows that the phase integral is consistent with the experimental results.

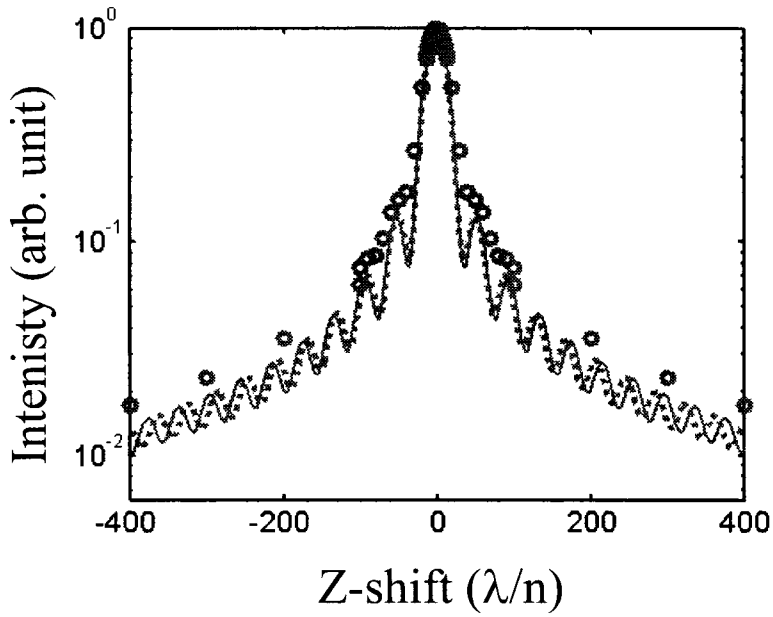

Figure 4.18: Numerical simulation and theoretical calculation of depth selectivity of 90-degree geometry. The simulation parameters are $NA = 0.5, n = 2.2$. (○): the numerical simulation; (solid line): theoretical phase integral of selectivity curve in equation (4.52); (dot line): the approximation as a Fresnel function in equation (4.53).

3. Wavelength selectivity

One advantage of the numerical simulation is that we can address all the performance issues without the experimental limitations. Here, we study the wavelength selectivity without a suitable tunable laser for experiments.

Fig. 4.19 shows the selectivity function as the wavelength of the probing beam is made to be different from the original recording beam. Also, to get an approximated

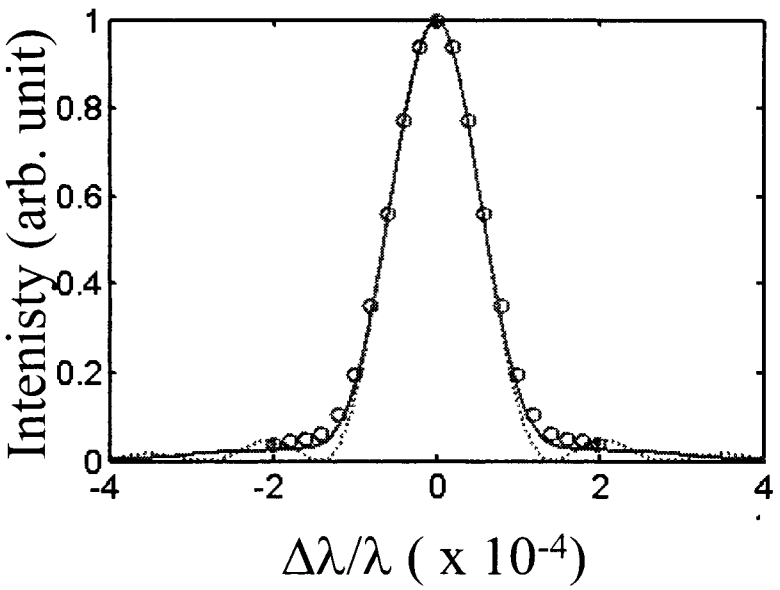

Figure 4.19: The numerical simulation and theoretical calculation of wavelength selectivity of 90-degree geometry. The simulation parameters are: $NA = 0.5$, $n = 2.2$. (o): the numerical simulation; (solid line): theoretical phase integral of selectivity curve in equation (4.62); (dot line): the approximation as a *sinc* function in equation (4.60).

analytic formula for the selectivity, we calculate the wavelength by phase integral as

$$\phi(\boldsymbol{r}_i, \frac{\Delta\lambda}{\lambda}) = \frac{2\pi n\Delta\lambda}{\lambda_0^2}(x + \sqrt{x^2 + z_0^2}), \tag{4.58}$$

$$E_d \simeq \int_{-\frac{z_0 NA}{n}}^{\frac{z_0 NA}{n}} dx \, \exp(i\frac{2\pi n\Delta\lambda}{\lambda_0^2}x), \tag{4.59}$$

$$|E_d| \simeq \text{sinc}\left(\frac{2NA\, z_0\Delta\lambda}{\lambda_0^2}\right), \tag{4.60}$$

where the first null for wavelength selectivity is

$$\frac{\Delta\lambda}{\lambda_0} = \frac{\lambda_0}{2NAz_0}, \tag{4.61}$$

which also depends on the depth z_0.

Considering the thickness of the crystal along the depth of the signal beam, a more accurate wavelength selectivity is obtained as the average of the *sinc* function

for various depths,

$$|E_d|^2 \simeq \frac{1}{z_2 - z_1} \int_{z_1}^{z_2} dz \left| \mathrm{sinc}\left(\frac{2NAz\Delta\lambda}{\lambda_0^2} \right) \right|^2 . \tag{4.62}$$

Fig. 4.19 shows both the single *sinc* function with the depth at the middle of the crystal and the averaged *sinc* functions. The latter fits better with the numerical simulation results, while the wavelength selectivity in equation (4.61) still gives a reasonable estimation of the wavelength selectivity.

The diffracted image pattern, imaging quality and background noise

As the simulation and experiments shown in Fig. 4.12, the diffracted pattern is not just along the Bragg phase-matching direction as the phase integral approximation. Instead, the diffraction generates a 2-D intensity distribution pattern on the Fourier image plane. The patterns along the degenerate direction determine the imaging quality, while the patterns along the selectivity direction lead to the scattering background of the image. Numerical simulation on the image patterns helps us understand and design a system for better imaging quality and less background noise.

Fig. 4.20 shows the Fourier plane image pattern as the probing beam is moving in the selectivity directions $\hat{\boldsymbol{x}}, \hat{\boldsymbol{z}}$ or wavelength tuning. The image patterns are visually enhanced while their intensity satisfies the selectivity curves in Fig. 4.14, 4.18, 4.19. The diffraction intensity decreases dramatically when the probe beam is away from the Bragg phase-matching condition. Being consistent with the experimental observation in Fig. 4.12, as the intensity of the Bragg mismatched image pattern decreases, the pattern intensity distribution changes and spreads out of the original reference focal point, which contributes to the background.

Consider the selectivity along the $\hat{\boldsymbol{x}}$ shifting direction, and assume there is a series of object point sources aligned along the $\hat{\boldsymbol{x}}$ direction with a distance $\frac{3\lambda}{n}$, $n = 2.2$ between each other. This distance is slightly larger than the shift selectivity $\Delta x = \frac{\lambda}{2NA}$, $NA = 0.5$, as shown in Fig. 4.21 (a). The central point source is Bragg-matched and projects a sharp image onto the $\boldsymbol{y'}$-$\boldsymbol{z'}$ image plane in Fig. 4.21 (b), while all other point sources generate a small background around the central pixel in Fig. 4.21 (c).

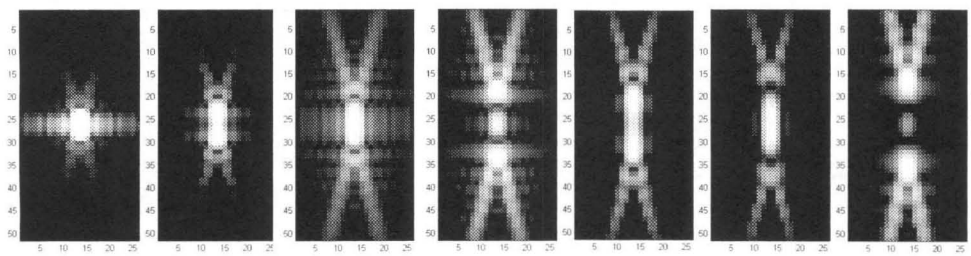

(a)

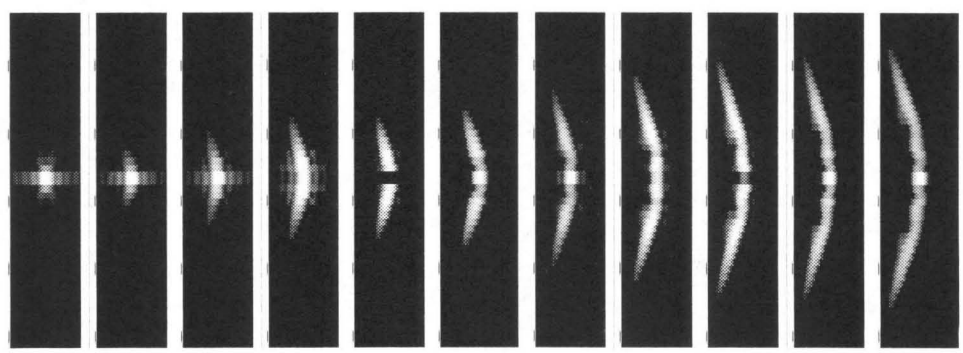

(b)

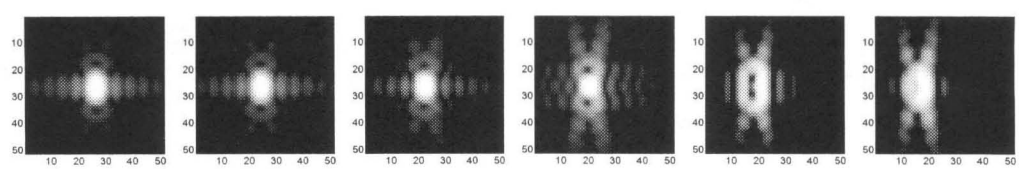

(c)

Figure 4.20: Numerical simulation of the image pattern as the probe beam is shifted along the selective directions. The simulation parameters are: $NA = 0.5$, $n = 22$. (a) The probe beam is shifted along the $\hat{\boldsymbol{x}}$ direction by $\frac{3\lambda}{n}$ for each step, causing weaker and distorted image patterns. (b) The probe beam is shifted along the depth $\hat{\boldsymbol{z}}$ direction by $\frac{10\lambda}{n}$ for each step. The intensity of the image decay is slower than $\hat{\boldsymbol{x}}$ shifting, and the intensity deviates dramatically along the $\hat{\boldsymbol{y}}$ direction. (c) The simulated image pattern as the wavelength of the probing beam is shifting from the original recording wavelength by $\frac{\Delta\lambda}{\lambda} = 4 \times 10^{-5}$ for each pattern.

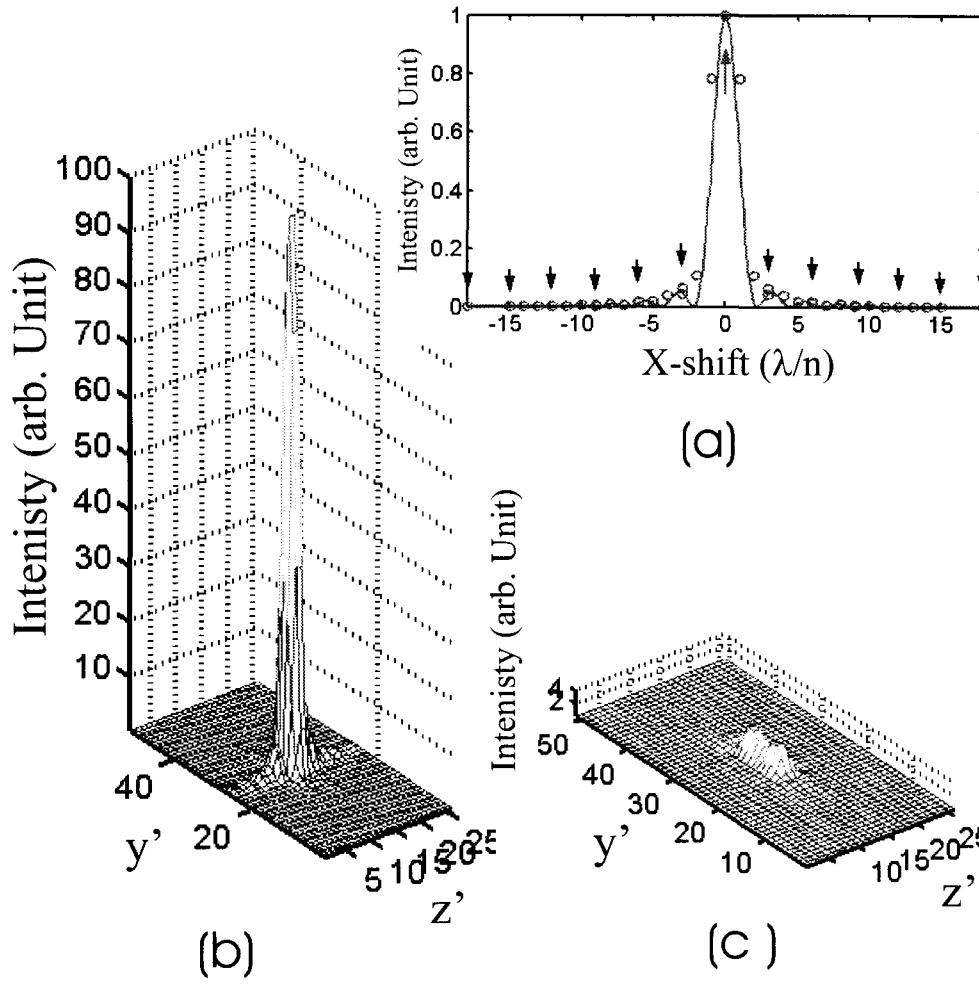

Figure 4.21: The numerical simulation of a series of point sources aligned on the $\hat{\boldsymbol{x}}$ direction. Simulation parameters are: $NA = 0.5$, $n = 2.2$. (a) shift selectivity curves and the location of objective point sources; (b) image intensity pattern for the central Bragg-matched object point source; (c) background pattern from the mismatched object points along $\hat{\boldsymbol{x}}$ direction.

Similarly, a series of object point sources sitting along the $\hat{z}$ direction generate a much higher background due to the wide depth selectivity curve, as shown in Fig. 4.22.

Fig. 4.23 shows the image pattern from the wavelength selectivity when a chromatic objective source is located at the Bragg phase-matching position. The component with the recording wavelength generates a central image on the image plane, while the other wavelength components generate a very weak distorted background.

All previous imaging patterns demonstrate the optical sectioning ability along the spatial $\hat{x}$, $\hat{z}$ direction and wavelength dimension with reasonable signal to noise ratio. Now we study the degenerate direction, which is expected to be a linear transformation from object space to image space. Fig. 4.24 shows the image pattern, as a probing point source is shifted along the degenerate $\hat{y}$ direction. Being consistent with the experimental measurement in Fig. 4.12 (b), the image pattern moves linearly as the objective point shifts linearly along the $\hat{y}$. However, the intensity distribution pattern is severely distorted. Even though the experimental measurement and simulation indicate a constant intensity diffraction efficiency along the degenerate direction, the actual image pattern gets weaker due to the large aberration of the image, as shown in Fig. 4.24 (b), where a linearly aligned point source in object space along the $\hat{y}$ direction only generates a decaying "butterfly" pattern on the image plane. This aberration indicates that a degenerate diffraction efficiency is not necessarily degenerate on the pattern distribution. For a successful imaging system, either a special holographic grating or geometry is required to limit the aberration, or a possible digital recovery algorithm to rebuild the information from the aberration is needed.

4.3 Imaging properties of a transmission geometry volume hologram

As discussed in section 4.2, to obtain a 2-D optical section using a single hologram, the linear transformation of diffracted image pattern from the object space along the degenerate directions is crucial. The spherical waves in 90-degree geometry contain

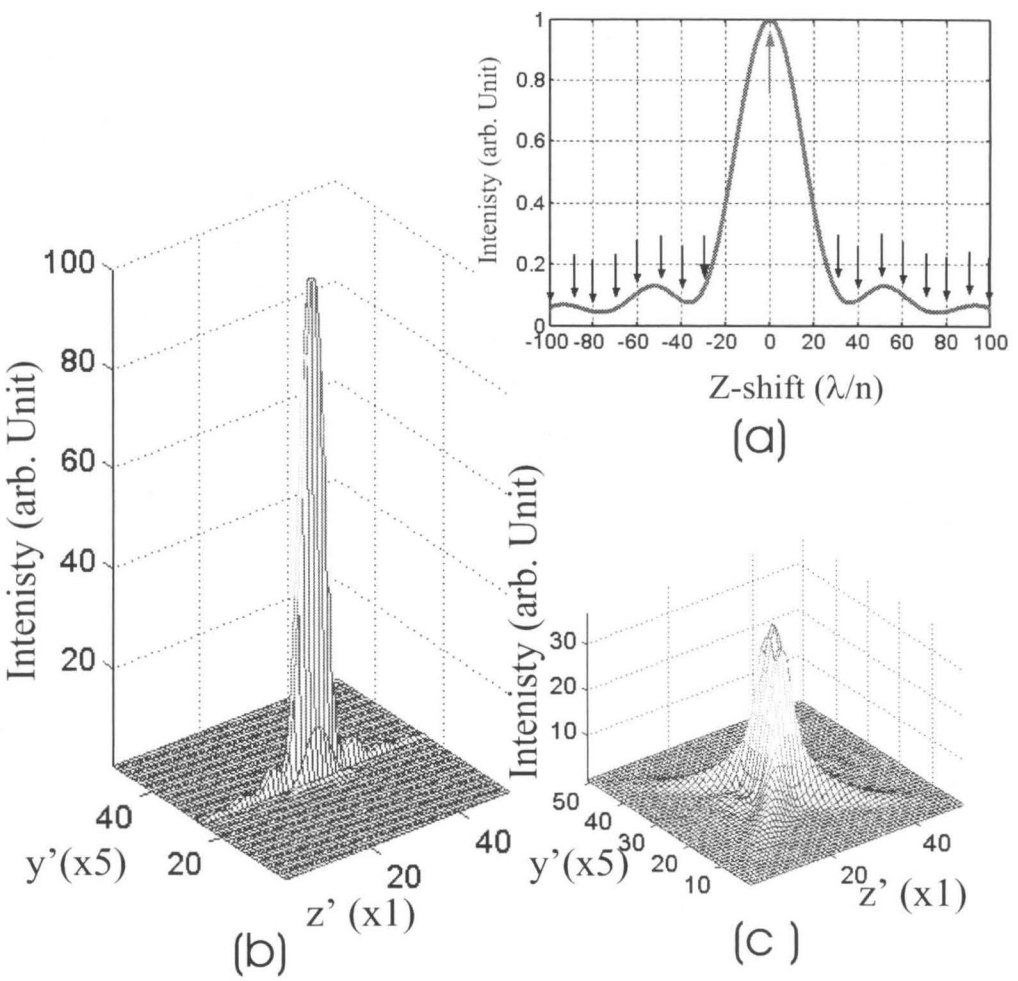

Figure 4.22: Numerical simulation of a series of point sources aligned on the $\hat{z}$ direction and the image pattern and background. Simulation parameters are: $NA = 0.5, n = 2.2$. (a) depth selectivity curves and the location of objective point sources; (b) image intensity pattern for the central Bragg-matched object point source; (c) background pattern from the mismatched object points along the $\hat{z}$ direction.

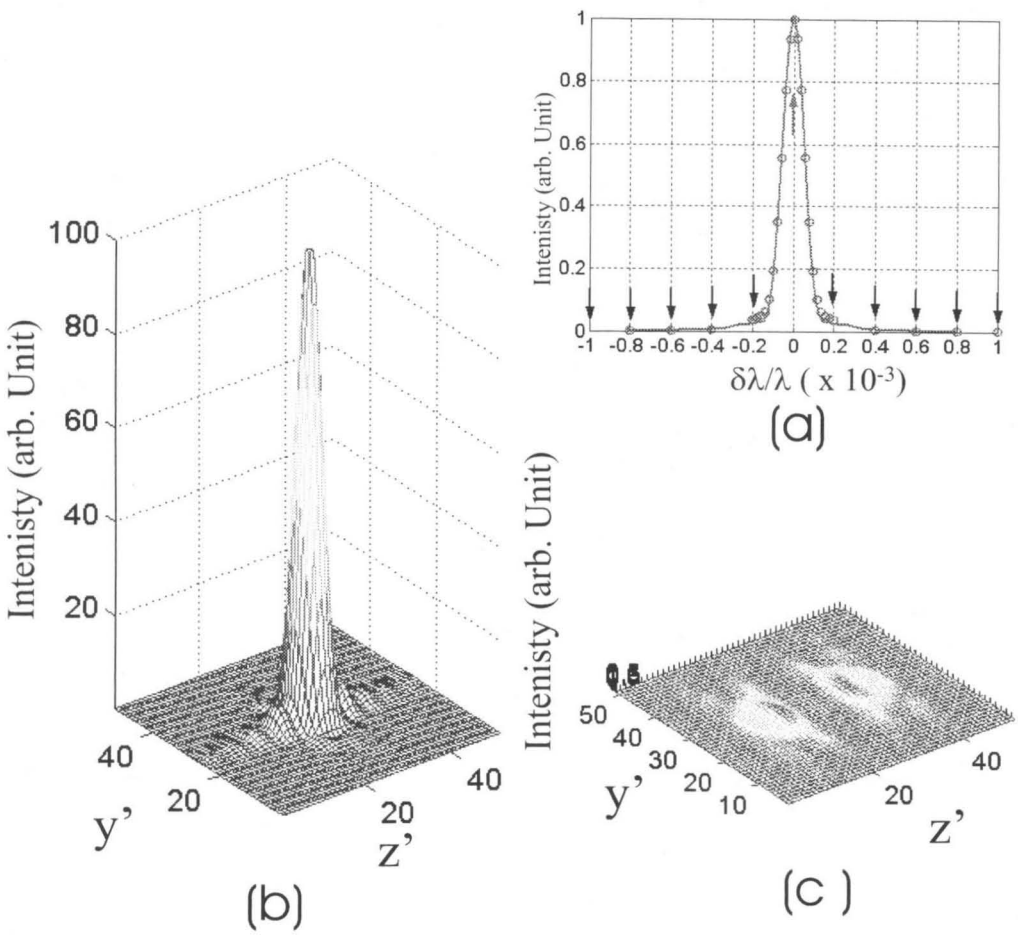

Figure 4.23: Numerical simulation of a chromatic point source located at the original Bragg phase-matching position. Simulation parameters are: $NA = 0.5$, $n = 2.2$. (a) wavelength selectivity curves and the intensity spectrum of a chromatic objective point source; (b) image intensity pattern for the central Bragg-matched wavelength from the object point source; (c) background pattern from the mismatched wavelength components from the same object point.

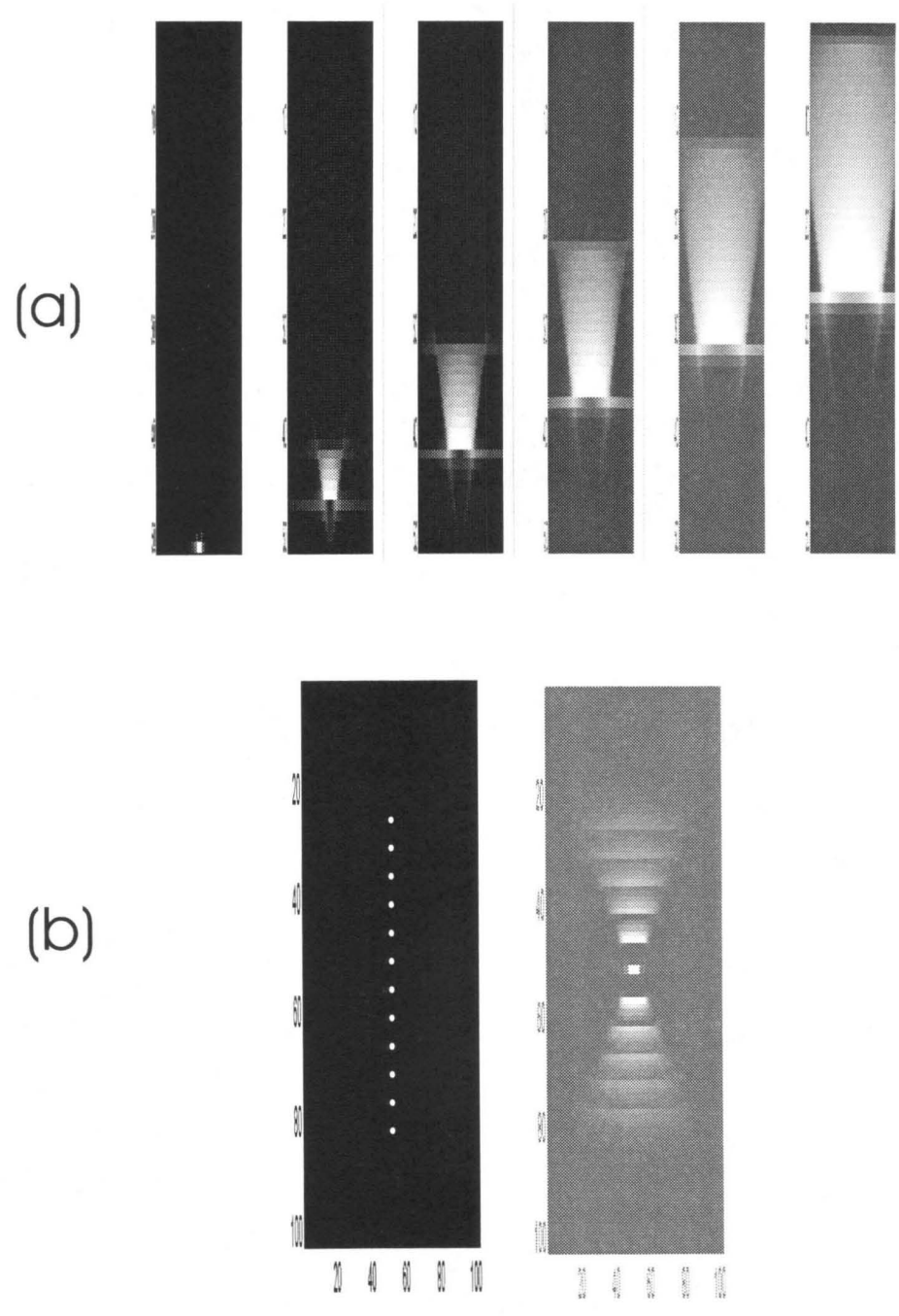

Figure 4.24: Numerical simulation of a point source shifting along the degenerate $\hat{\boldsymbol{y}}$ direction. Simulation parameters are: $NA = 0.5$, $n = 2.2$. (a) image patterns as a point source is shifted along the $\hat{\boldsymbol{y}}$ direction by $\frac{20\lambda}{n}$ between each step. (b) image plane responses for a set of point source linearly aligned on the $\hat{\boldsymbol{y}}$ direction. The large aberration leads to decaying "butterfly" intensity distributed patterns.

2-D spatial components, which lead to a sophisticated degenerate diffraction pattern due to the different selectivity effects of various spatial components. This geometry acts better as a spatial filter for single spatial point diffraction in confocal microscope application [8]. On the other hand, plane waves in a holographic transmission geometry have simple characteristics for degenerate diffraction out of the signal-reference plane. In this section, we study the imaging characteristics of a transmission geometry shown in Fig. 4.25 by the numerical simulation model, and demonstrate the 3-D imaging in experiments.

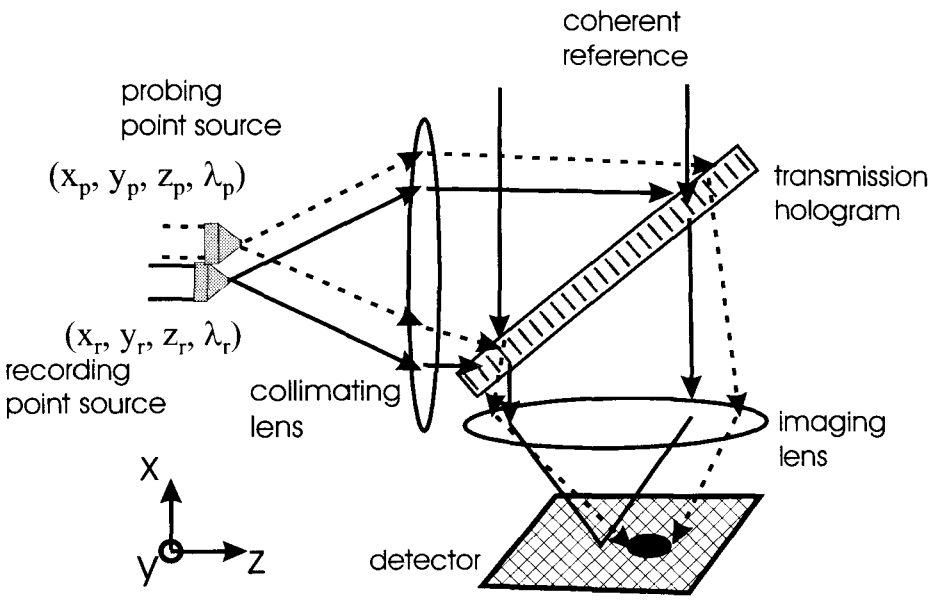

Figure 4.25: The transmission geometry hologram recording with point source (x_r, y_r, z_r, λ_r) and probing with another point source (x_p, y_p, z_p, λ_p).

A collimated signal beam from the point source (x_r, y_r, z_r, λ) and its coherent reference beam generate a simple holographic pattern in the transmission geometry in the photorefractive material with thickness D. When the probing beam collimated from a point source (x_p, y_p, z_p, λ_p) illuminates the hologram, the diffracted reference is detected at the Fourier plane sensor as a 2-D pattern. Considering the imaging properties of the collimating lens, which transforms a 3-D object space to an image space, the holographic imaging structure with a collimating lens is the same in principles as the one using spherical waves discussed in section 4.2. However, the collimating lens decreases the spherical curvature of the signals from the object space near the

focus dramatically, which generates a uniform single spatial grating inside the hologram. This simple holographic grating leads to a linear diffraction transformation along the degenerate directions, at the cost of using an additional collimating lens, which also determines the imaging resolution and aberration. We assume that both the collimating and imaging lenses have ideal aberration-free imaging properties in our studies.

4.3.1 Selectivities and imaging transformation

Selectivity in the $\hat{x}_p$ direction

Assume the recording point source is located on the focal point of the collimating lens with focal length f_c, the recording signal beam coming into the crystal is a plane wave along $\hat{z}$, where the collimating lens axis is at $x = y = 0$. When the probing point shifts by x_p in the $\hat{x}$ direction, the collimated signal beam is tilted in the $-\frac{x_p}{f_c}$ direction, where $x_p \ll f_c$. This leads to the angle selective properties in transmission geometry, which are well known, as shown in the wavevector k-space Fig. 4.26. Generally, in a transmission geometry with the assumption of infinite

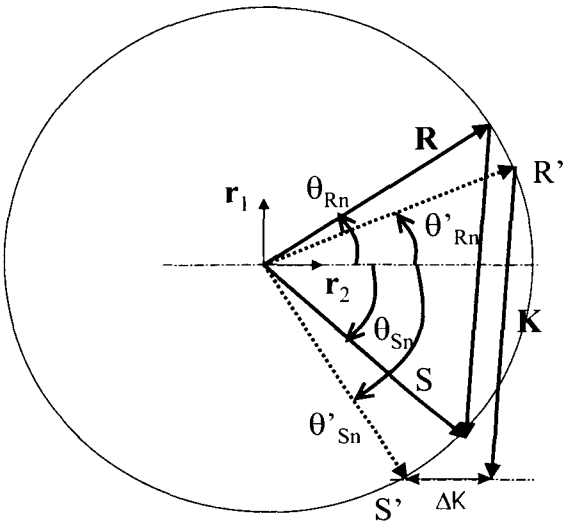

Figure 4.26: The angle selectivity of a general transmission geometry hologram by two plane waves $\boldsymbol{R}, \boldsymbol{S}$, and readout with a tilted reference $\boldsymbol{R'}$. The hologram is assumed with infinite transverse dimension along $\boldsymbol{r}_1$ and a thickness D along $\boldsymbol{r}_2$.

dimensions in the crystal plane $\boldsymbol{r}_{\|}$ and thickness D along $\boldsymbol{r}_{\perp}$, the incident angles for

the reference and signal inside the material are assumed θ_{Rn}, θ_{Sn}, and the grating $\boldsymbol{K}$

$$\boldsymbol{K} = k_n \left[(\sin\theta_{Rn} + \sin\theta_{Sn})\boldsymbol{r}_{\parallel} + (\cos\theta_{Rn} - \cos\theta_{Sn})\boldsymbol{r}_{\perp} \right]. \tag{4.63}$$

Reading out with a reference beam at angle θ'_{Rn}, the diffracted beam is determined at θ'_{Sn} with Bragg mismatching vector $\Delta K \boldsymbol{r}_{\perp}$,

$$\Delta\theta_{Rn} = \theta'_{Rn} - \theta_{Rn} \ll 1, \tag{4.64}$$

$$\Delta\theta_{Sn} = \theta'_{Sn} - \theta_{Sn}, \tag{4.65}$$

$$= -\frac{\cos\theta_{Rn}}{\cos\theta_{Sn}}\Delta\theta_{Rn}, \tag{4.66}$$

$$\Delta K = k_n(\tan\theta_{Sn} + \tan\theta_{Rn})\cos\theta_{Rn}\Delta\theta_{Rn}. \tag{4.67}$$

This leads to a linear transformation form the object plane point source $\delta(\boldsymbol{r_p} - \boldsymbol{r_r} - \Delta x_p \hat{\boldsymbol{x}}, \lambda_p = \lambda_r)$ to a corresponding point image on the image plane $\eta\delta(\boldsymbol{r'_d} - \boldsymbol{r'_r} - \Delta z'_d \hat{\boldsymbol{z}'})$, by the geometry relations in Fig. 4.25:

$$\Delta\theta_S = -\frac{\Delta x_p}{f_c} = \frac{n\cos\theta_{Sn}}{\cos\theta_S}\Delta\theta_{Sn}, \tag{4.68}$$

$$\Delta\theta_R = -\frac{\Delta z'_d}{f_i} = \frac{n\cos\theta_{Rn}}{\cos\theta_R}\Delta\theta_{Rn}, \tag{4.69}$$

$$\frac{\Delta x_p}{f_c}\cos\theta_S = -\frac{\Delta z'_d}{f_i}\cos\theta_R, \tag{4.70}$$

$$\eta = \mathrm{sinc}^2\left(\frac{\Delta K\, D}{2\pi}\right), \tag{4.71}$$

$$= \mathrm{sinc}^2\left(\frac{\Delta x_p}{f_c \Delta\alpha}\right), \tag{4.72}$$

$$\Delta\alpha = \frac{\lambda}{D}\frac{1}{\cos\theta_S(\tan\theta_{Sn} + \tan\theta_{Rn})}, \tag{4.73}$$

where the collimating and imaging lens focal length is f_c, f_i respectively, and the incident angles of the signal, reference beams θ_S, θ_R are determined by the holographic imaging system, and $\Delta x_p, \Delta z'_d \ll f_c, f_i$.

Fig. 4.27 shows the theoretical angle selectivity of the diffraction intensity curve in equation (4.72), which is consistent to the numerical simulation intensity.

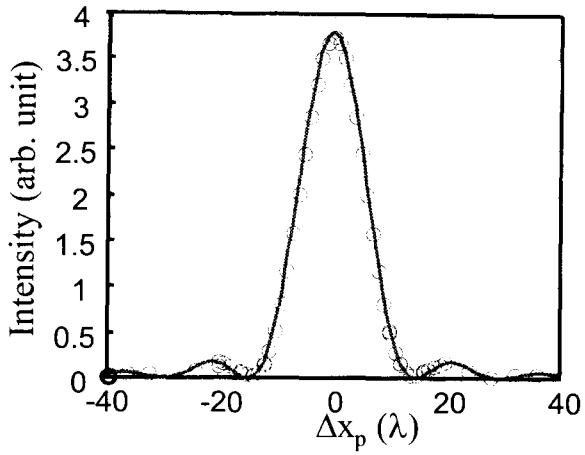

Figure 4.27: The angular selectivity of a general transmission geometry hologram in Fig. 4.25. The simulation condition is: $f_c = f_i = 10^4\lambda$, $D = 1400\lambda$, $NA = 0.5$, $n = 2.2$, $\theta_R = \theta_S = \pi/4$. (○) the simulation results of the intensity integral over the 2-D image pattern on image plane. (solid line): the theoretical $sinc^2$ function in equation (4.72).

The numerical simulation can also give the 2-D intensity distribution as the probing beam shifts along the $\hat{\boldsymbol{x}}$ direction, as shown in Fig. 4.28. The image patterns show a linear spatial transformation of the probing point source, and the intensity is modulated due to the angle selectivity. If a 1-D object with the same recording wavelength is located along the $\hat{\boldsymbol{x}}$ direction across the recording point source, only a small portion of it is diffracted by the hologram and projected on the image plane, as shown in Fig. 4.29, where the object is assumed to be a series of point sources with 2λ spacing along the $\hat{\boldsymbol{x}}_{\boldsymbol{p}}$ direction, and the image is a line of points along $\hat{\boldsymbol{z}}'_{\boldsymbol{p}}$ with an intensity profile. This profile determines the $\hat{\boldsymbol{x}}_{\boldsymbol{p}}$ spatial resolution in the object space with the same recording wavelength at 12λ under the simulation conditions. And the corresponding image resolution in $\hat{\boldsymbol{z}}'_{\boldsymbol{p}}$ is given by equation (4.70).

Selectivity in wavelength

With a similar process as previous angular selectivity in a transmission hologram as shown in Fig. 4.26, we get the response to a probing point source $\delta(\boldsymbol{r}_p = \boldsymbol{r}_r, \lambda_p =$

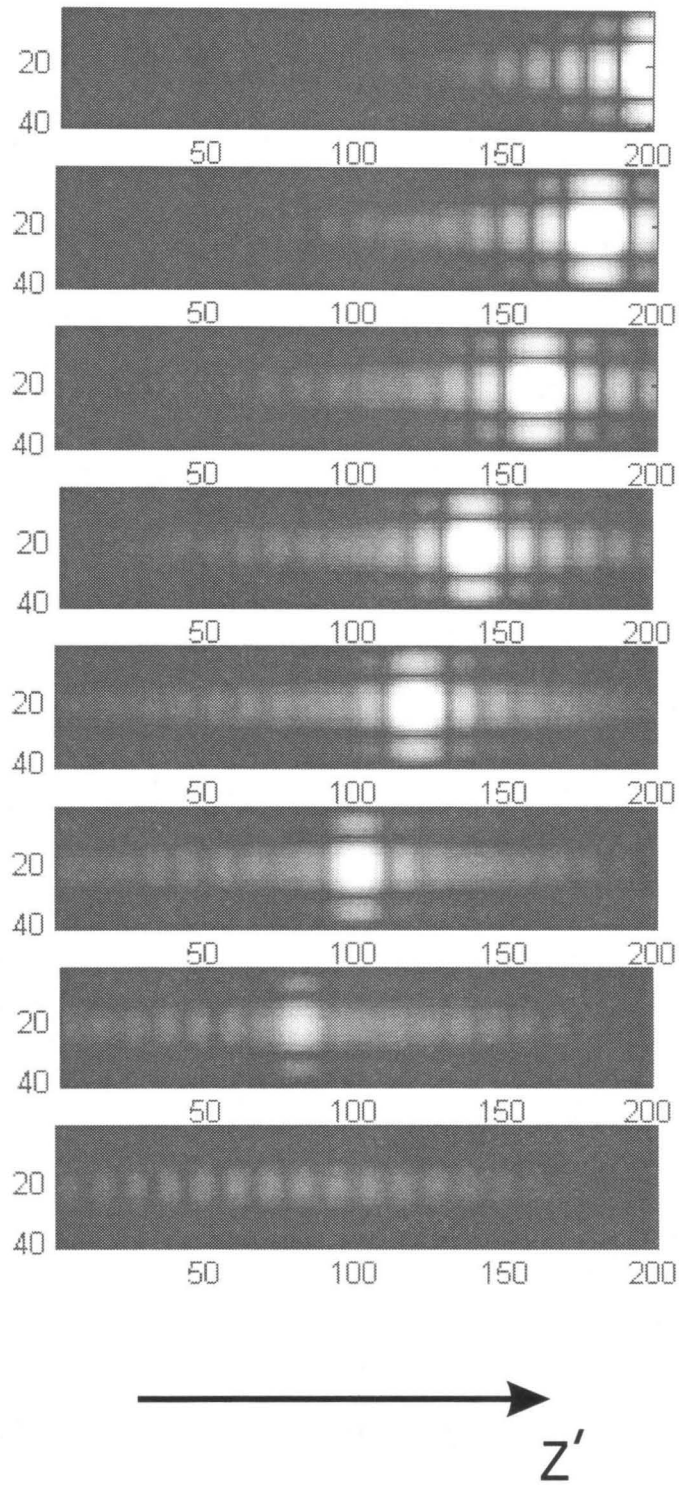

Figure 4.28: The intensity distribution pattern on the image plane of a general transmission geometry hologram in Fig. 4.25. The simulation conditions are the same as in Fig. 4.27. From top to bottom, the probing point source at the recording wavelength is moving from the recording position to the $\hat{\boldsymbol{x}}_{\boldsymbol{p}}$ direction by 2λ per step. The image pattern intensity and location change are as in equations (4.72), (4.70).

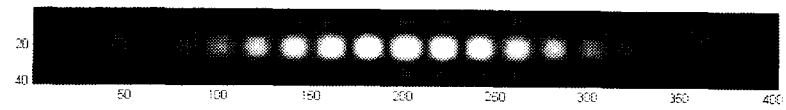

(a)

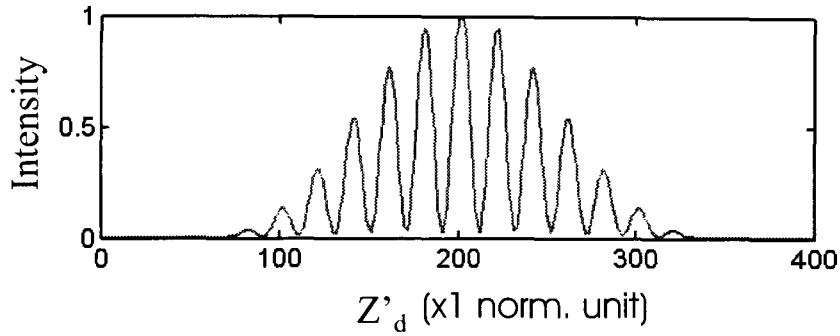

(b)

Figure 4.29: The intensity distribution pattern on the image plane of a general transmission geometry hologram in Fig. 4.25 for linear distributed point sources with spacing 2λ along the $\hat{\boldsymbol{x}}_{\boldsymbol{p}}$ direction in objective space. The simulation conditions are the same as in Fig. 4.27. The fullwidth of half magnitude of the intensity profile gives the spatial resolution along $\hat{\boldsymbol{x}}_{\boldsymbol{p}}$ at 12λ in objective space.

$\lambda_r + \Delta\lambda)$ on the image plane as a point image $\eta\,\delta(\boldsymbol{r'_d} - \boldsymbol{r'_r} - \Delta z'_d\hat{\boldsymbol{z}}', \lambda_p)$:

$$\frac{\Delta z'_d}{f_i} = -n\frac{\Delta\lambda}{\lambda}\frac{\sin\theta_{Rn} + \sin\theta_{Sn}}{\cos\theta_R}, \tag{4.74}$$

$$\eta(\frac{\Delta\lambda}{\lambda}) = \mathrm{sinc}^2\left(\frac{\Delta\lambda}{\lambda\Delta\beta}\right), \tag{4.75}$$

$$\Delta\beta = \frac{\lambda}{nD}\frac{\cos\theta_{Rn}}{1-\cos\left(\theta_{Sn}+\theta_{Rn}\right)}, \tag{4.76}$$

where equation (4.76) gives the well-known wavelength selectivity.

Fig. 4.30 shows the intensity selectivity curve from equation 4.75 and is consistent with the simulation intensity integral over the 2-D distribution on the image plane. Fig. 4.31 shows the 2-D image pattern as the probing wavelength is changed. The image pattern keeps being a point image while shifting along the $\hat{\boldsymbol{z}}'_{\boldsymbol{d}}$ direction and decreases in intensity according to equations (4.74 – 4.75). If a chromatic point source

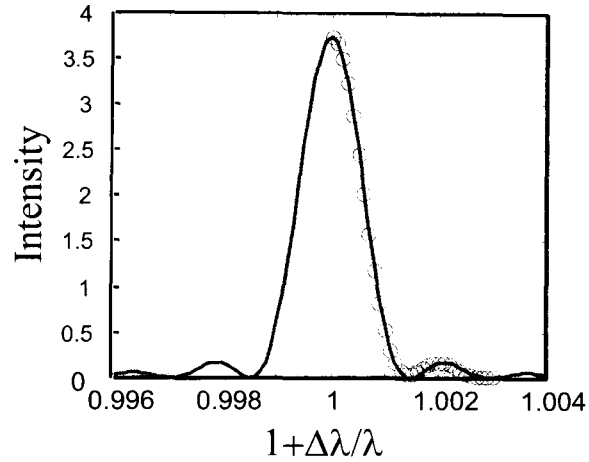

Figure 4.30: The diffraction intensity on the image plane of a general transmission geometry hologram in Fig. 4.25 as the wavelength of the probing point source changes at the original recording location. The simulation conditions are the same as in Fig. 4.27.

with wavelength sampling at $\Delta\lambda/\lambda = 4 \times 10^{-}4$ is used to probe the hologram, the image pattern generated on the image plane is shown in Fig. 4.32. The intensity profile along the image plane $\hat{\boldsymbol{z}'_d}$ direction determines the image resolution of a chromatic point source in the objective space. Comparing with the image resolution due to the object spatial selectivity along the $\hat{\boldsymbol{x}}_{\boldsymbol{p}}$ direction as shown in Fig. 4.29, the image resolution of chromatic effect is $\times 2$ of the image resolution due to angle selectivity along $\hat{\boldsymbol{x}}_{\boldsymbol{p}}$, which can be given from equations (4.70 – 4.76):

$$\frac{\Delta z'_d(\frac{\Delta\lambda}{\lambda} = \Delta\beta)}{\Delta z'_d(\frac{\Delta x_p}{f_c} = \Delta\alpha)} = \frac{(\sin\theta_{Rn} + \sin\theta_{Sn})(\tan\theta_{Rn} + \tan\theta_{Sn})\cos\theta_{Rn}}{1 - \cos(\theta_{Sn} + \theta_{Rn})}, \quad (4.77)$$

which gives 2 under the simulation conditions in Fig. 4.32.

Selectivity in the depth $\hat{\boldsymbol{z}}_{\boldsymbol{p}}$ direction

As the probing point source shifts along the axis of the collimating lens in Fig. 4.25, the probing wave front for the hologram is not a plane wave anymore, instead it becomes a spherical wave with curvature determined by the collimating lens f_c and the shifting Δz_p. The diffraction characteristics are determined by different spatial components of the probing beam, which has no analytic solution as the cases in

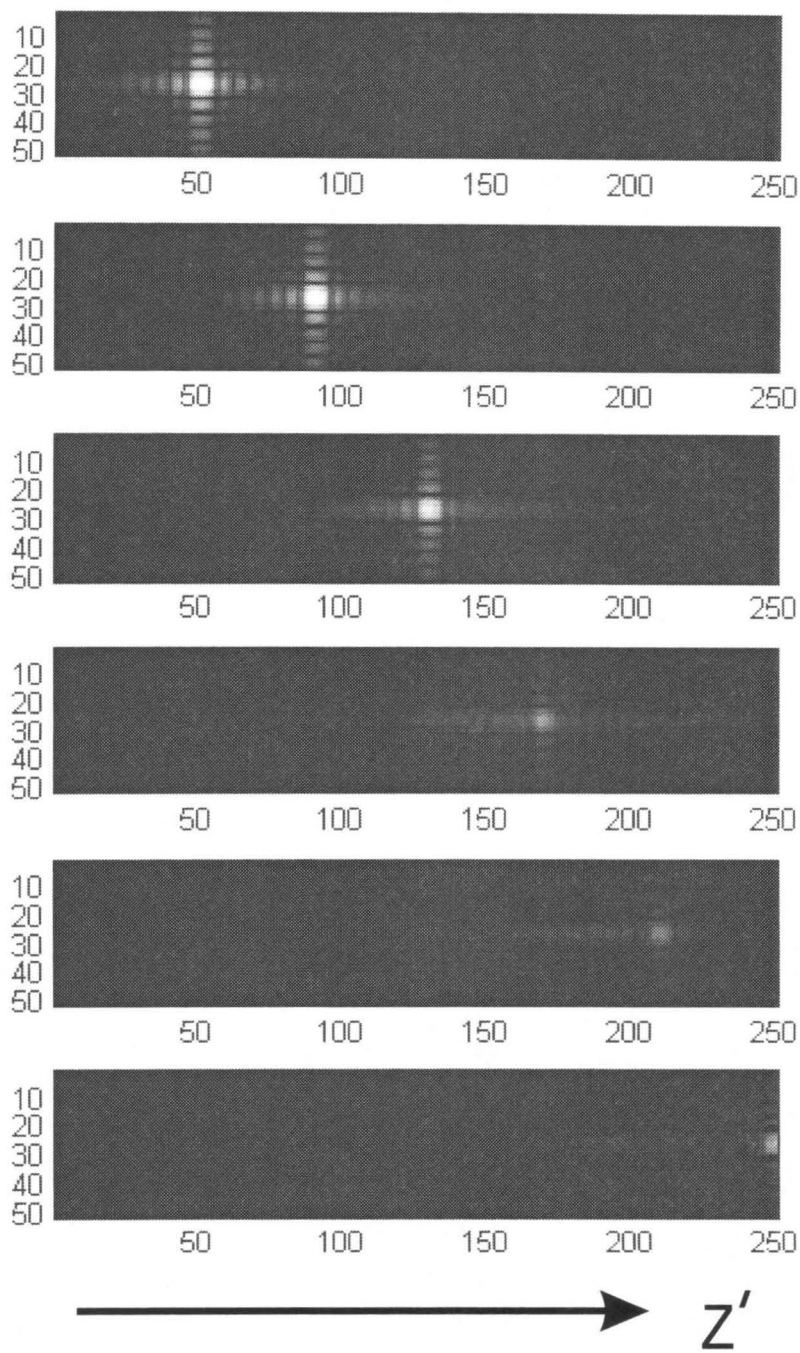

Figure 4.31: The intensity distribution pattern on the image plane of a general transmission geometry hologram in Fig. 4.25 as the probing point source changes wavelength from the recording wavelength by $\Delta\lambda/\lambda = -4 \times 10^{-4}$ for each step. The simulation conditions are the same as in Fig. 4.27.

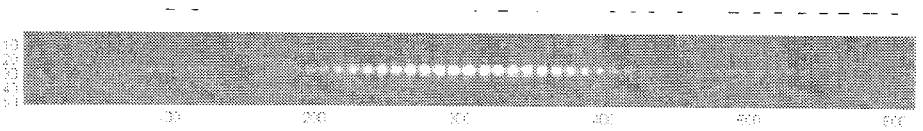

(a)

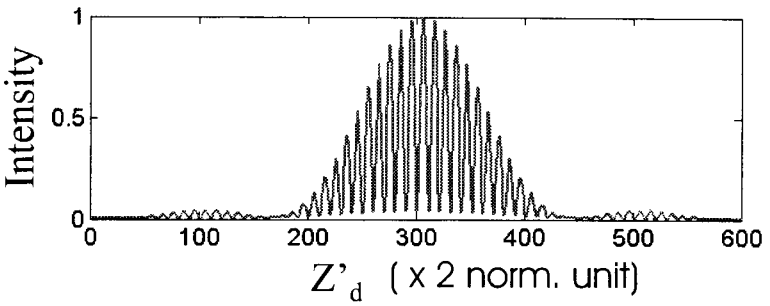

(b)

Figure 4.32: The intensity distribution pattern on the image plane of a general transmission geometry hologram in Fig. 4.25 for a chromatic point source located at the original recording position with wavelength sampling rate $\frac{\Delta\lambda}{\lambda} = 4 \times 10^{-4}$. The simulation conditions are the same as in Fig. 4.27. The fullwidth of half magnitude of the intensity profile gives the spatial image resolution along $\hat{\boldsymbol{z}}'_{\boldsymbol{d}}$ at 120 normalized units ($= 10^{-5} f_i$ in our simulation) on the image plane.

section 4.2.

To get a simple analytic approximate formula for the intensity depth selectivity, we consider the diffracted intensity to be composed of the diffracted intensity from various spatial frequency components in the incident probing beam. Ignoring the diffracted intensity changes along the degenerate $\hat{\boldsymbol{y}}_{\boldsymbol{p}}$ direction, and only considering the intensity diffraction efficiency for spatial frequency component δk_x governed by the equation (4.72), we have the approximation

$$\eta(\Delta z_p) \approx \frac{1}{2u} \int_{-u}^{u} \mathrm{sinc}^2 \left(\frac{k_x}{k\Delta\alpha} \right) dk_x, \tag{4.78}$$

where the range of the transverse spatial component u is determined by the defocusing effect, when the probing point source shifts in $\hat{\boldsymbol{z}}_{\boldsymbol{p}}$ and the numerical aperture of the

collimating lens is $NA = \frac{L}{2f_c}$,

$$u \approx k\frac{L\Delta z_p}{2f_c^2}, \tag{4.79}$$

$$|\Delta z_p| \ll f_c. \tag{4.80}$$

Simplifying the integral in equation (4.78) by the *sinc* integral function $Si(z)$,

$$\eta = \frac{1}{\alpha}\int_0^{\alpha} \mathrm{sinc}^2\left(\frac{t}{\Delta\alpha}\right) dt \tag{4.81}$$

$$= -\frac{\Delta\alpha^2}{\pi^2}\mathrm{sinc}^2\left(\frac{\alpha}{\Delta\alpha}\right) + \frac{\Delta\alpha}{\pi\,\alpha} Si(\frac{2\pi\alpha}{\Delta\alpha}), \tag{4.82}$$

$$Si(s) = \int_0^{s} \frac{\sin t}{t} dt, \tag{4.83}$$

$$\alpha = \frac{L\Delta z_p}{2f_c^2}. \tag{4.84}$$

The integral in equation (4.81) has a universal line shape as shown in Fig. 4.33, in which the function drops to half value at $\alpha = 0.90\Delta\alpha$. If the half intensity shift is defined as the depth selectivity $\Delta z_{p\frac{1}{2}}$, then

$$\Delta z_{p\frac{1}{2}} = 1.80\frac{f_c^2}{L}\Delta\alpha, \tag{4.85}$$

which gives $\Delta z_{p\frac{1}{2}} = 26\lambda$ under the simulation conditions. Fig. 4.33 shows the approximate intensity selectivity and the numerical simulation on the intensity integral over the image patterns, which are consistent to each other.

The 2-D intensity distribution pattern on the image plane is shown in Fig. 4.34, where the point source at the original recording wavelength is shifted along the depth $\hat{\boldsymbol{z}}_{\boldsymbol{p}}$ direction. The image pattern diffuses very fast in the $\hat{\boldsymbol{z}}'$, $\hat{\boldsymbol{y}}'$ directions while the intensity drops. Due to the area diffusion, the real image point is expected to achieve higher signal to noise ratio than the intensity selectivity, as shown in Fig. 4.35.

Selectivity in the depth $\hat{\boldsymbol{z}}_{\boldsymbol{p}}$ direction from a chromatic source

For observations using a chromatic source, the image resolution along $\hat{\boldsymbol{z}}'$ is dominated by the wavelength selectivity as mentioned in previous discussions. Similarly

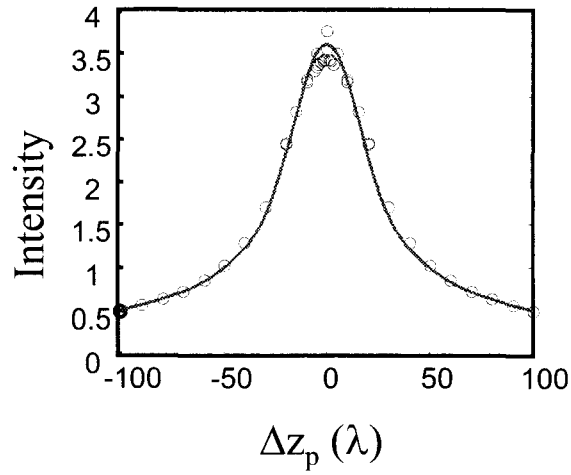

Figure 4.33: The diffraction intensity on the image plane of a general transmission geometry hologram in Fig. 4.25 as the probing point source shifts along the depth $\hat{\boldsymbol{z}}_{\boldsymbol{p}}$ direction. The simulation conditions are the same as in Fig. 4.27. (circle) the numerical simulation; (solid line) the approximate integral as in equation (4.82).

for the depth selectivity which determines the depth resolution of optical sectioning, the coupling between the depth selectivity at different wavelengths from the recording wavelength need to be addressed. When the probing point source shifts along the $\hat{\boldsymbol{z}}_{\boldsymbol{p}}$ direction at different wavelengths from the recording one, the intensity selectivity is simulated and compared with the depth selectivity at the recording wavelength in Fig. 4.36.

The intensity shift functions in the $\hat{\boldsymbol{z}}_{\boldsymbol{p}}$ direction at different wavelengths are all within the side lobe of the selectivity of the original recording wavelength. The depth resolution is dominated by the spatial selectivity given in equation (4.85).

4.3.2 Degenerate directions and imaging quality

Selectivity along the $\hat{\boldsymbol{y}}_{\boldsymbol{p}}$ direction

When the probing point source is shifted along $\hat{\boldsymbol{y}}_{\boldsymbol{p}}$ as $\delta(\boldsymbol{r}_p = \boldsymbol{r}_r + \Delta\boldsymbol{y}_{\boldsymbol{p}}, \lambda_p = \lambda_r)$,

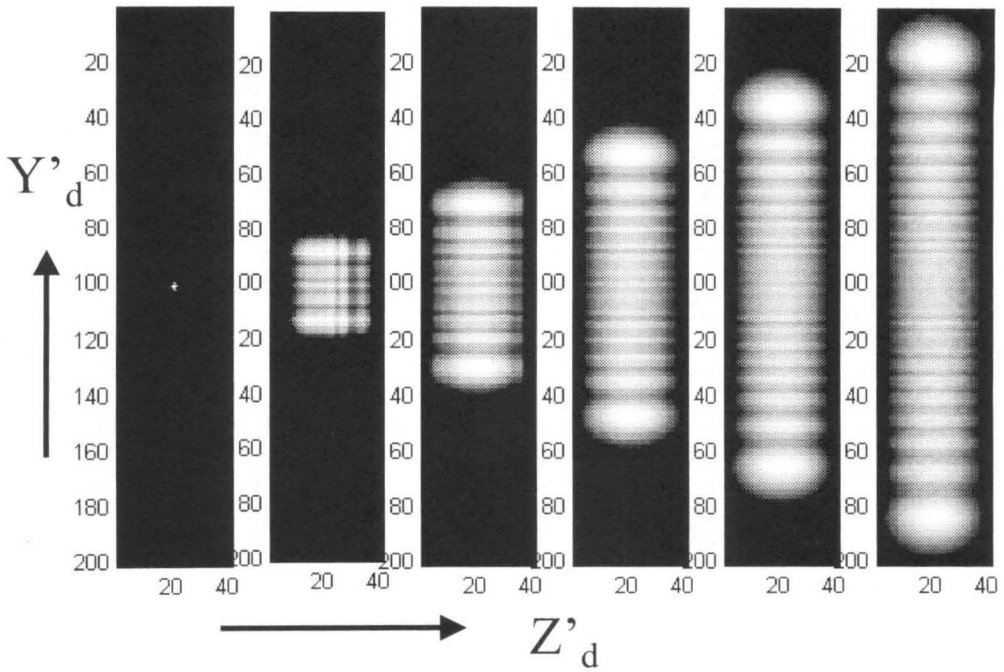

Figure 4.34: The diffraction intensity on the image plane of a general transmission geometry hologram in Fig. 4.25 as the probing point source shifts along the depth $\hat{\boldsymbol{z}}_{\boldsymbol{p}}$ direction by 20λ for each step, at the recording wavelength. The simulation conditions are the same as in Fig. 4.27.

the response on the image plane is a point image $\eta\,\delta(\boldsymbol{r'_d} - \boldsymbol{r'_r} - \Delta\boldsymbol{r'_d}, \lambda_p)$ as

$$\eta = \mathrm{sinc}^2\left(\frac{y_p^2}{f_c^2}\frac{1}{\Delta\alpha_y}\right), \tag{4.86}$$

$$\Delta\boldsymbol{r'_d} = -\frac{f_i}{f_c}\Delta y_p\hat{\boldsymbol{y}}' - \frac{\Delta y_p^2}{2f_c^2}f_i\hat{\boldsymbol{z}}'_{\boldsymbol{d}}, \tag{4.87}$$

$$\Delta\alpha_y = 2\sqrt{n^2 - \frac{1}{4}}\frac{\lambda}{D}, \tag{4.88}$$

under the simulation geometry. Fig. 4.37 shows the intensity selectivity curve, which is consistent with the numerical simulation results. And Fig. 4.38 shows the 2-D image pattern for the point source shifting along the $\hat{\boldsymbol{y}}_{\boldsymbol{p}}$ direction. The image pattern not only linearly shifts along the $\hat{\boldsymbol{y}}'_{\boldsymbol{d}}$ direction, but also drifts in the $-\hat{\boldsymbol{z}}'_{\boldsymbol{d}}$ direction as determined by equation (4.87).

Degenerate diffraction in shifting and wavelength

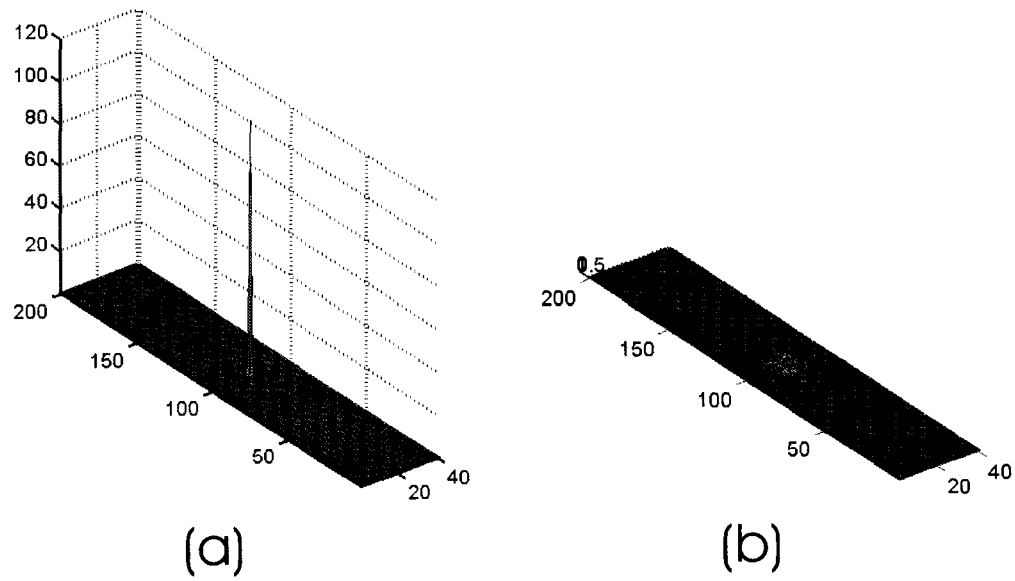

Figure 4.35: The diffraction intensity distribution on the image plane of a general transmission geometry hologram in Fig. 4.25 (a) by the probing point source located at the original recording location; (b) a series of point sources located on the $\hat{\boldsymbol{z}}_{\boldsymbol{p}}$ axis with a distance of 20λ, except the Bragg phase-matching position in (a).

In the simple transmission geometry with plane waves as signal and reference, there are two dimensions where exact Bragg phase-matching can be achieved. As the wave vector k-space shown in Fig. 4.39, for a single grating K recorded by beams $\boldsymbol{R_1}, \boldsymbol{S_1}$, pairs of $\boldsymbol{R_2}, \boldsymbol{S_2}$ can also be Bragg phase-matched with uniform diffraction efficiency with the same wavelength k_0 as in recording. In addition, on a different k-sphere with a different wavelength k_1 in Fig. 4.39, there is a similar pair of $\boldsymbol{R_3}, \boldsymbol{S_3}$ with different angles, which can be Bragg phase-matched by the same holographic grating.

These two degeneracies lead to the linear response of the probing point source in

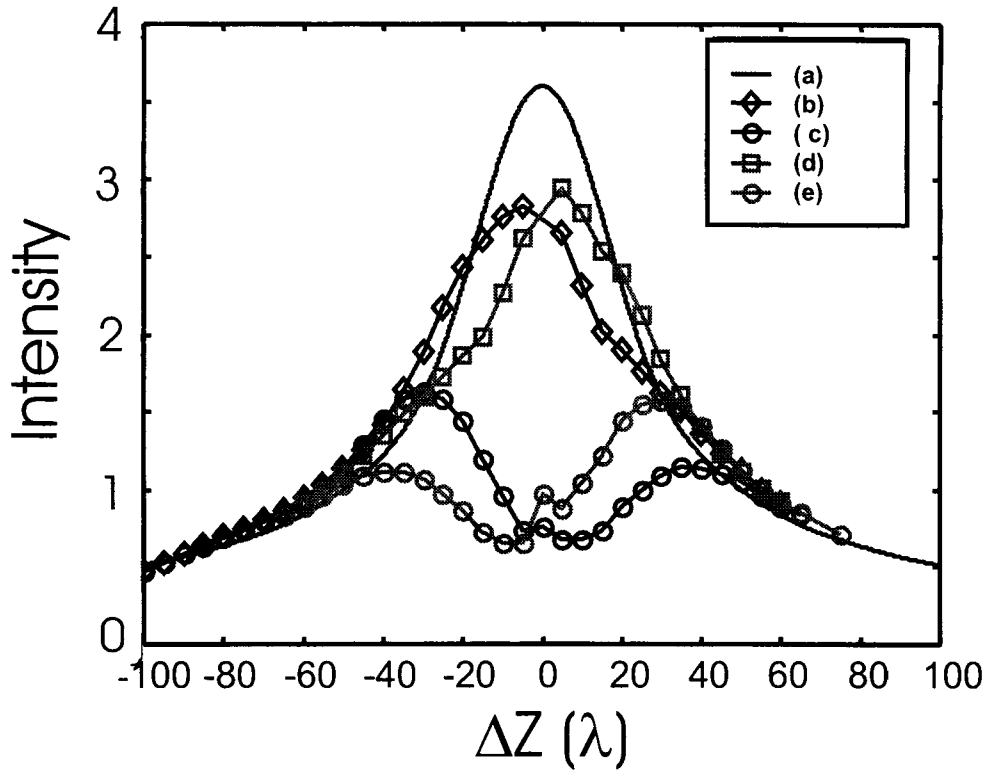

Figure 4.36: The diffraction intensity on the image plane of a general transmission geometry hologram in Fig. 4.25 as the probing point source shifts along the depth $\hat{\boldsymbol{z}}_{\boldsymbol{p}}$ at different wavelengths (a) the original wavelength $\frac{\Delta\lambda}{\lambda} = 0$; (b) $\frac{\Delta\lambda}{\lambda} = -5 \times 10^{-4}$; (c) $\frac{\Delta\lambda}{\lambda} = -10^{-3}$; (d) $\frac{\Delta\lambda}{\lambda} = 5 \times 10^{-4}$; (e) $\frac{\Delta\lambda}{\lambda} = 10^{-3}$. The simulation conditions are the same as in Fig. 4.27.

Fig. 4.25 $\delta(\Delta \boldsymbol{r}_p, \Delta\lambda_p)$ onto the image plane $\delta(\Delta \boldsymbol{r'}_d, \Delta\lambda)$, when

$$\Delta\lambda_p = 0, \tag{4.89}$$

$$\Delta \boldsymbol{r}_p = \Delta \boldsymbol{x_p} + \Delta \boldsymbol{y_p}, \tag{4.90}$$

$$\Delta \boldsymbol{r'}_d = \Delta \boldsymbol{z'_d} + \Delta \boldsymbol{y'_d}, \tag{4.91}$$

$$\frac{\Delta x_p}{f_c} = -\frac{\Delta z'_d}{f_i} \ll 1, \tag{4.92}$$

$$= \frac{-\sin\theta + \sqrt{\cos\theta^2 - (n^2 - \sin\theta^2)t^2}}{\sin\theta + \sqrt{\cos\theta^2 - (n^2 - \sin\theta^2)t^2}}, \tag{4.93}$$

$$\frac{\Delta y_p}{f_c} = -\frac{\Delta y'_d}{f_i}, \tag{4.94}$$

$$= \frac{-\sqrt{2}\sqrt{n^2 - \sin\theta^2}\, t}{\sin\theta + \sqrt{\cos\theta^2 - (n^2 - \sin\theta^2)t^2}}, \tag{4.95}$$

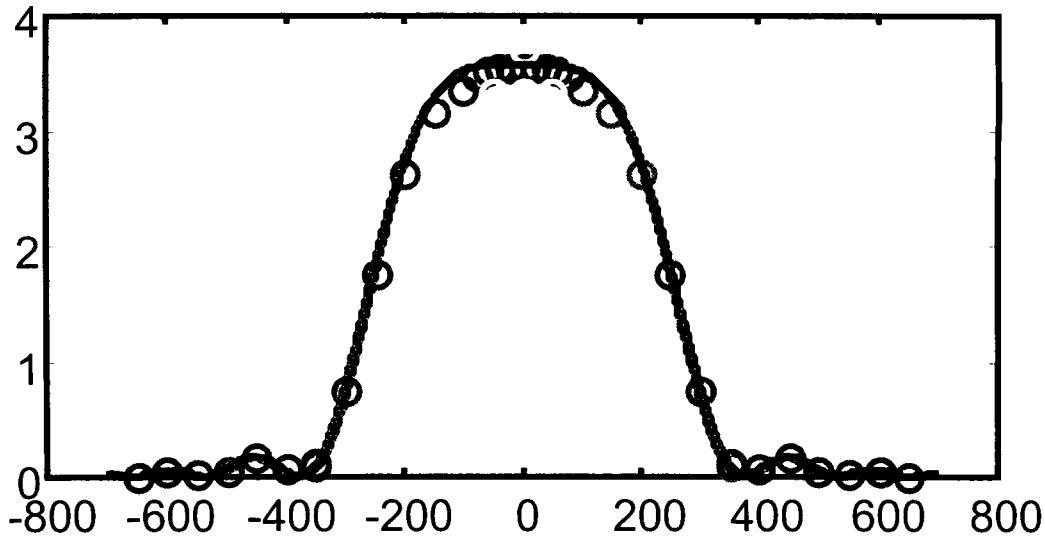

Figure 4.37: The diffraction intensity on the image plane of a general transmission geometry hologram in Fig. 4.25 as the probing point source shifts along the $\boldsymbol{y_p}$ direction at the original wavelength. The simulation conditions are the same as in Fig. 4.27.

or

$$\frac{\Delta x_p}{f_c} = -\frac{\Delta \lambda_p}{\lambda}, \tag{4.96}$$

$$= \frac{\Delta z'_d}{f_i}, \tag{4.97}$$

where the incident angle $\theta_R = \theta_S = \theta$, and the parameter $|t| < 1$. The linear transformation relation is shown in Fig. 4.40,

Assuming a 2-D object on the objective plane with a single wavelength component, the optical sectioning by a single transmission hologram is a vertical curve given by equations (4.93 – 4.95) on the objective plane, which is linearly transformed onto the image plane. For the same object with chromatic lights, an 2-D hyper slice is optically sectioned from the 3-D information hyperspace (2-D spatial on the $\boldsymbol{x_p} - \boldsymbol{y_p}$ plane plus spectrum dimension) with the wavelength and $\boldsymbol{x_p}$ coupling relation in equation (4.96). This optical section is projected onto the image plane, and gives us a 2-D image of the $\boldsymbol{x_p} - \boldsymbol{y_p}$ plane with a $\boldsymbol{z'_d}$ related color filtering effect. The image spatial resolution is determined by equations (4.70, 4.74, 4.77) along the $\hat{\boldsymbol{x}}_{\boldsymbol{p}}$ or $\hat{\boldsymbol{z}}'_{\boldsymbol{d}}$ direction on the

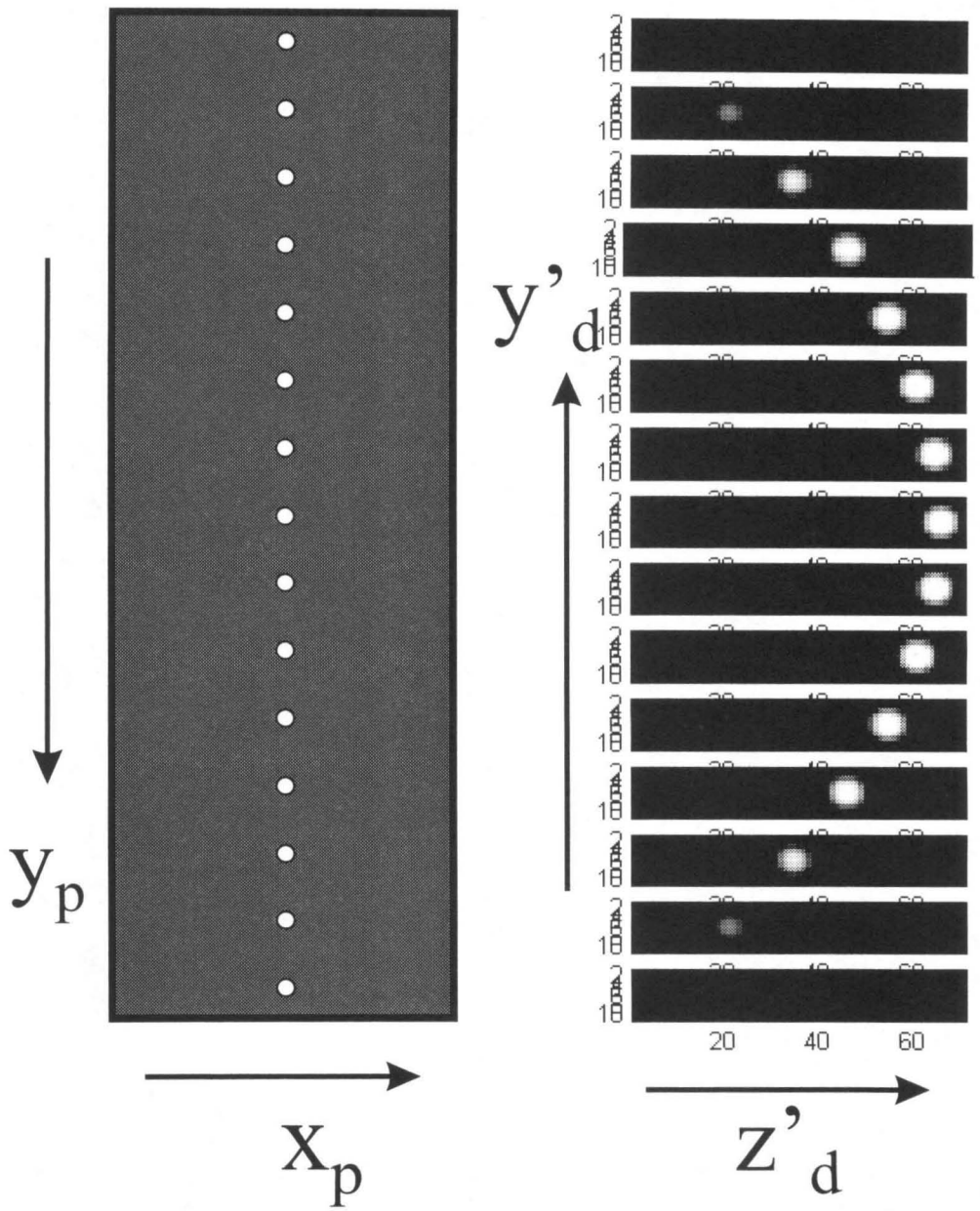

Figure 4.38: The diffraction image pattern on the Fourier plane of a general transmission geometry hologram in Fig. 4.25 as the probing point source shifts along the $\hat{\boldsymbol{y}}_{\boldsymbol{p}}$ direction by 50λ for each step at the original wavelength. The simulation conditions are the same as in Fig. 4.27.

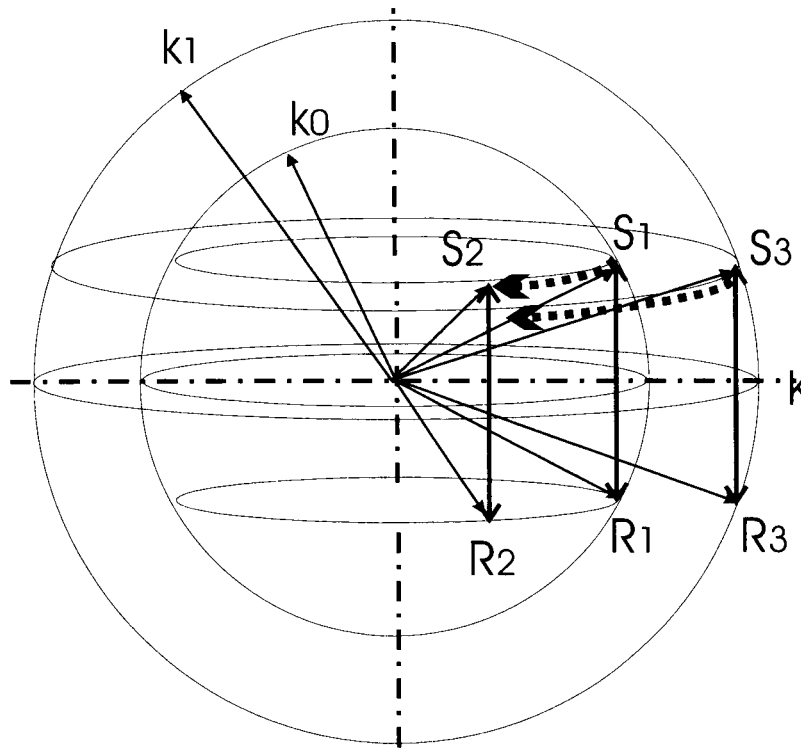

Figure 4.39: The wave vector k-sphere for a holographic grating $\boldsymbol{K}$ recorded by $\boldsymbol{R_1}, \boldsymbol{S_1}$ at wavelength k_0. The hologram can be Bragg phase-matched by a pair of beams $\boldsymbol{R_2}, \boldsymbol{S_2}$ rotated around $\boldsymbol{K}$ direction at the same wavelength. At a different wavelength k_1, there is another pair of beams $\boldsymbol{R_3}, \boldsymbol{S_3}$ with corresponding tilting angle, that can be Bragg phase-matched while rotated around the $\boldsymbol{K}$ direction.

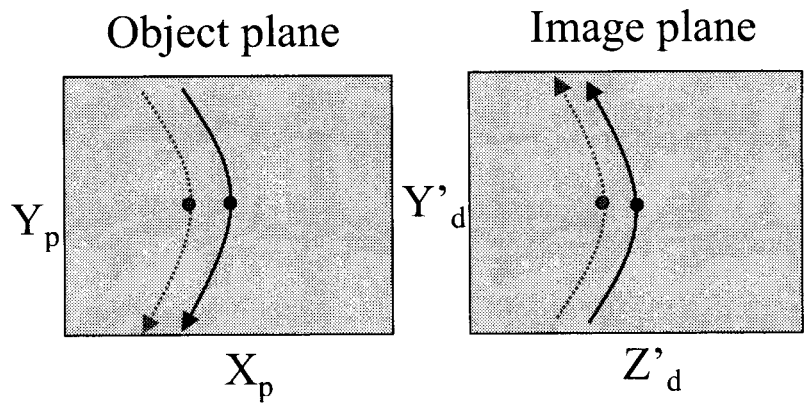

Figure 4.40: The Bragg phase-matching transformation from the objective plane to the image plane in the transmission geometry imaging system in Fig. 4.25. For the same wavelength, the spatial degenerate shifting is determined by equations (4.91 – 4.95). For a different wavelength, the Bragg phase-matching position shifts horizontally by equation (4.96).

image plane. The optical sectioning resolution is given by equation (4.85) for depth selectivity and equation (4.76) for wavelength selectivity.

4.3.3 Experimental measurements

From the theoretical analysis and numerical simulation, the transmission geometry is expected to give a linear transformation from the objective space to the 2-D imaging plane along both $\hat{\boldsymbol{y}}_{\boldsymbol{p}}$ direction and the $\hat{\boldsymbol{x}}_{\boldsymbol{p}} - \lambda$ degenerate coupling direction, which makes it possible to form a 2-D image in the optical sectioning plane. The experiments are done to measure the optical section resolution along the depth and wavelength dimensions, and to demonstrate the 2-D imaging ability of a single hologram.

The experimental setup is shown in Fig.4.41, where two collimated plane waves are used to record a transmission hologram in either x-cut $LiNbO_3$ crystal or photopolymer material in (a). During the probing process (b), the probing signal can be either the focused point source of the laser line, or a pinhole illuminated by a white light source, or a 2-D object (photomask) illuminated by laser or a white light source, or a 3-D object with spatial light distribution (fluorescent microspheres in liquid or gel samples). The probing source can be scanning in 3-D spatial direction

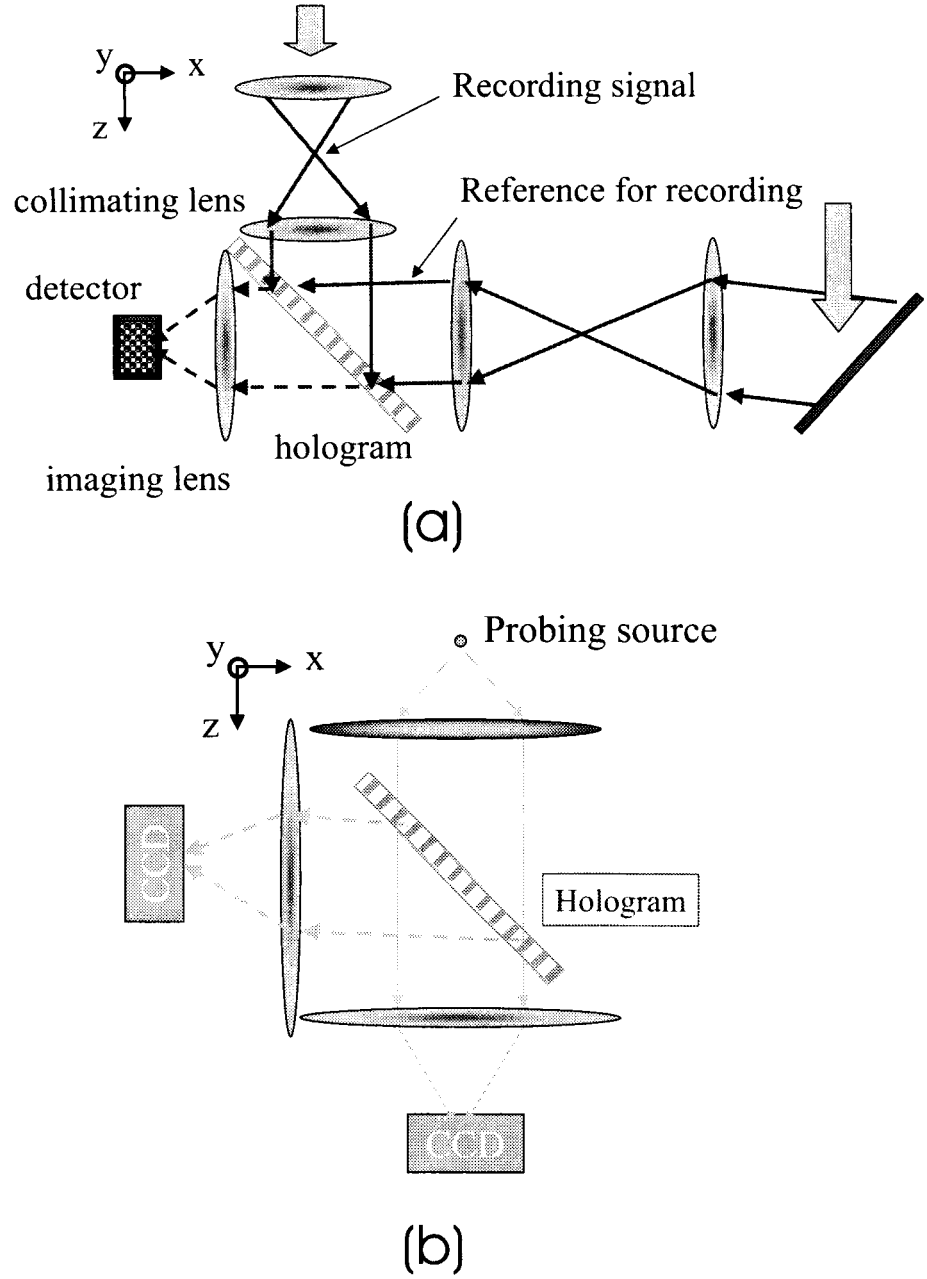

Figure 4.41: The experimental setup for holographic imaging with a transmission geometry. (a) A transmission geometry hologram is recorded using two collimated plane waves. (b) The probing light source is collimated and illuminates the hologram, which can be directly imaged by a microscope system composed of a collimating lens and a forward imaging lens. The diffracted beam from the hologram is collected by another imaging lens and detected by either a power meter or 2-D image sensor.

by translation stage. The diffracted signal can be measure by a power meter or a 2-D image sensor.

The measurements of spatial selectivity

Fig. 4.42 shows one experimental measurement of the transverse $\hat{\boldsymbol{x}}_{\boldsymbol{p}}$ and depth $\hat{\boldsymbol{z}}_{\boldsymbol{p}}$ intensity selectivity curves with a DuPont photopolymer 100 μm thickness. The theoretical calculation of the corresponding selectivity in equations (4.70, 4.85), with the experimental parameters and refractive index $n = 1.6$ for polymer, matches the measurement very well. The higher side lobe of experimental data in the $\hat{\boldsymbol{x}}$ selectivity is due to the saturation of the hologram (with $\eta > 20\%$). The depth sectioning resolution ($2\Delta z_{p\frac{1}{2}}$) is over 800 μm for the thin DuPont polymer. Smaller optical section depth can be achieved by using thicker material and larger numerical aperture objective lens.

Degenerate Bragg phase-matching diffraction by wavelength-shift coupling

In Fig. 4.43, the image pattern of a probing point source shifting along $\hat{\boldsymbol{x}}_{\boldsymbol{p}}$ direction is recorded. The probing point source is a 5 μm pinhole illuminated with the same wavelength as recording wavelength. The image pattern is a point pixel at the original reference focal point only when the pinhole is located at the recording location, as shown in Fig. 4.43 (a). However, when the pinhole is illuminated by a white light source, the image pattern is a pixel point shifting along $\hat{\boldsymbol{z}}'_{\boldsymbol{d}}$ direction while the pinhole is shifting, as shown in Fig. 4.43 (b). This is caused by the wavelength-shift coupling Bragg phase-matching in equations (4.96 – 4.97), which determines the corresponding wavelength response on the image location.

2-D imaging by a single hologram

Fig. 4.44 demonstrates the ability of forming a 2-D image by a single transmission hologram with degeneracies in spatial and wavelength dimensions. A 2-D object mask is used as the probing source, and is illuminated by the recording wavelength. Due to the degenerate direction along $\boldsymbol{y}_{\boldsymbol{p}}$, a vertical line image across the recording point is projected onto the image plane in Fig. 4.44 (a), as discussed in equations (4.91 – 4.95). However, for a chromatic object (the mask illuminated by white light source),

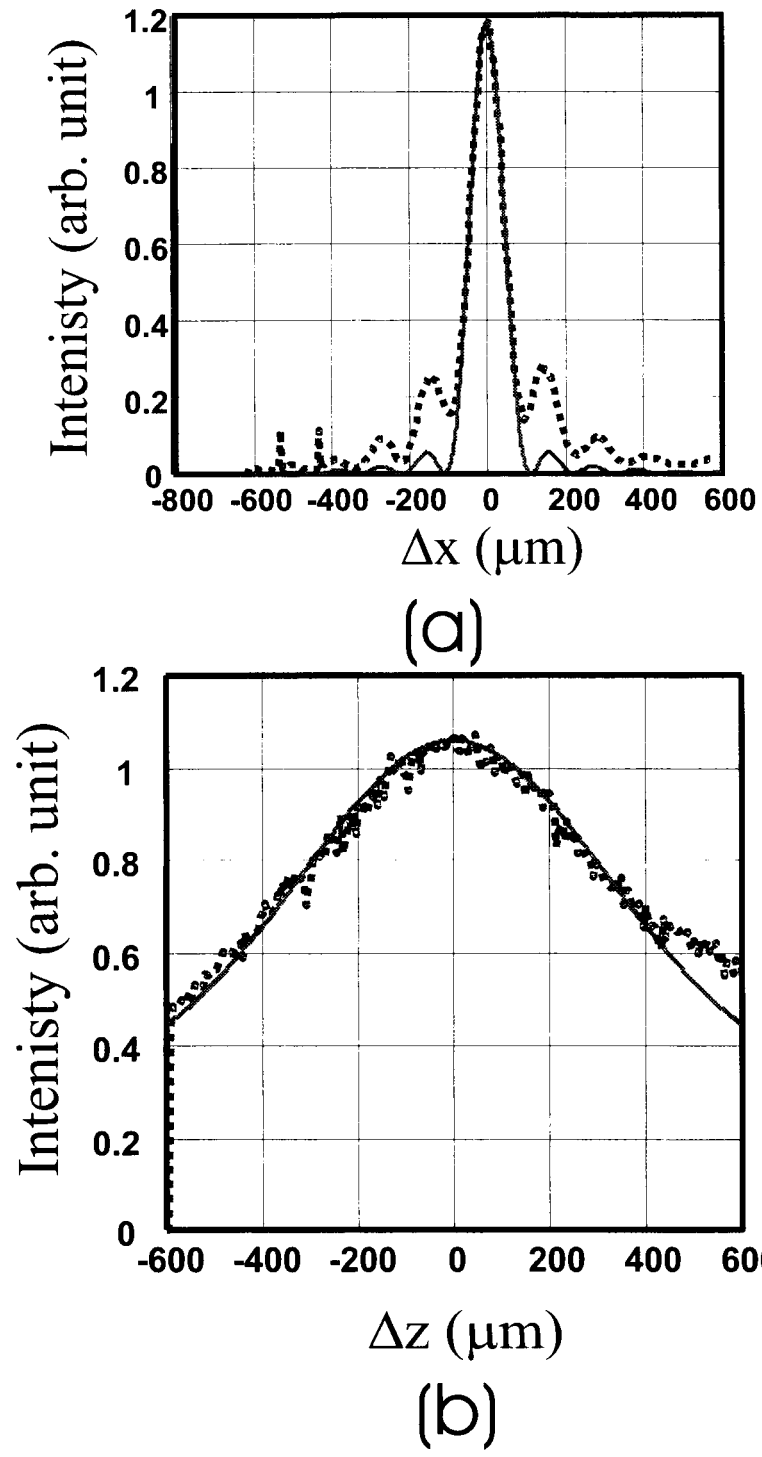

Figure 4.42: Experimental measurements and theoretical intensity selective calculation of shift selectivity of DuPont polymer 100 μm thick in a transmission geometry in Fig. 4.41. The collimating objective lens is $\times 10$, NA= 0.25, the DuPont polymer is assumed $n = 1.5$, and the wavelength 488 nm. (a) Shift selectivity in $\hat{\boldsymbol{x}}_{\boldsymbol{p}}$ direction, where equation (4.70) gives $\Delta x_p = 104$ μm at the first null. (b) Depth selectivity in $\hat{\boldsymbol{z}}_{\boldsymbol{p}}$ direction, equation (4.85) gives $\Delta z_{p\frac{1}{2}} = 400$ μm at the half magnitude.

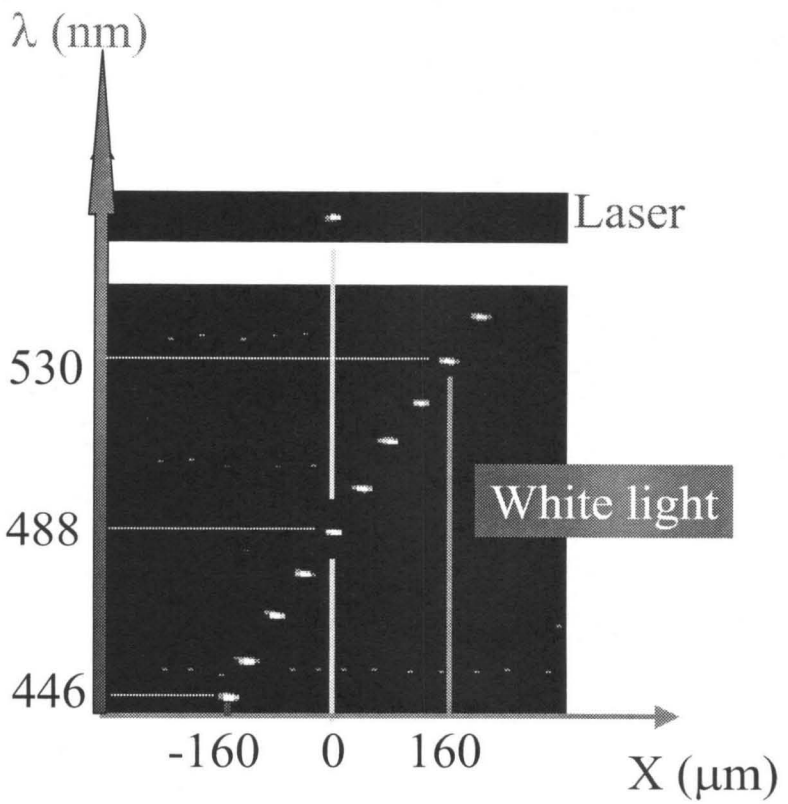

Figure 4.43: The experimental demonstration of Bragg phase-matching by wavelength shift coupling in a transmission geometry in Fig. 4.41. The experimental parameters are: $LiNbO_3$ crystal thickness 5 mm, collimating objective lens $\times 10$, $NA = 0.25$, and the recording wavelength 488 nm. (a) The image pattern while the probing pinhole is illuminated by 488 nm. (b) The image pattern as the white light illuminated pinhole is shifting in $\hat{\boldsymbol{x}}_{\boldsymbol{p}}$ direction. The image point is shifted correspondingly in $\hat{\boldsymbol{z}}'_{\boldsymbol{d}}$ direction with different wavelength component determined by equations (4.96 – 4.97).

the additional degeneracy by different wavelength components forms the 2-D color-coded image in Fig. 4.44 (b), where the wavelength-$\boldsymbol{z}'_{\boldsymbol{d}}$ relation is shown in Fig. 4.43 (b).

4.4 Experimental 3-D imaging

Holographic imaging makes use of the spatial and wavelength degenerate Bragg phase-matching effects in a single hologram for optical sectioning a 2-D slice from a 4-D objective hyperspace (3-D spatial plus spectral dimensions), and projecting it linearly

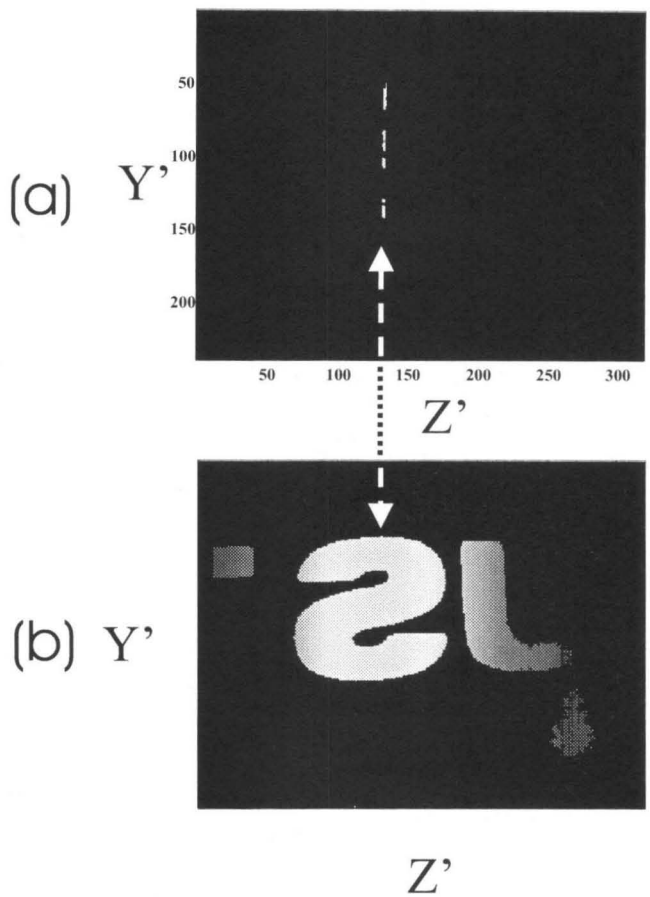

Figure 4.44: The experimental demonstration of 2-D imaging by the Bragg phase-matching in spatial and wavelength-shift coupling dimension of a single transmission geometry hologram in Fig. 4.41. The experimental parameters are the same as in Fig. 4.43. (a) The image pattern of a 2-D mask across the original recording point source location and illuminated by 488 nm. A vertical line image is formed due to the spatial degeneracy along $\hat{\boldsymbol{y}}_{\boldsymbol{p}}$ direction. (b) The image pattern as the white light illuminating the 2-D mask. At different $\hat{\boldsymbol{z}'}_{\boldsymbol{d}}$ position, different wavelength component Bragg phase matches and forms the 2-D color-coded image, determined by equations (4.96 – 4.97).

onto a 2-D detector, where each pixel corresponds to a texel volume in the object 4-D hyperspace. Comparing to normal imaging system that sections a 2-D slice from 3-D and projects a single voxel volume onto an individual pixel onto the detector, the holographic imaging extracts additional information on the spectra, with the expense of lower photon flow for each pixel corresponding to texel volume.

The other major advantage of holographic imaging is that the volume hologram only selectively diffracts the Bragg phase-matching signal components and has little effect on other components. With holographic multiplexing techniques, multiple holograms can be built into the system simultaneously and process different signal components at the same time. By sectioning different slices from the 4-D hyperspace, the number of texels detected at one time would be much larger than the number of voxels a normal 2-D imaging system can achieved. This increases the information collection rate, however with the requirement of larger photon flux for holographic imaging system to have the same signal noise ratio of each pixel on the 2-D image sensor.

Here we demonstrate multiple-slice sectioning at once by multiplexing holograms, which achieves the ability to extract 3-D spatial information at a single shot.

4.4.1 Experimental demonstration with multiplexed holograms

To achieve the highest diffraction efficiency and reasonable spatial resolution, we used PQ polymer with thickness 2 mm for our holographic recording in Fig. 4.41, which expects to give a depth selectivity $\Delta z_{p\frac{1}{2}} = 2\ \mu m$ according to equation (4.85) for wavelength 488 nm and objective lens $\times 40$, $NA = 0.65$.

Fig. 4.45 shows the depth selectivity measurement. A single strong hologram in the transmission geometry with diffraction efficiency $> 15\%$ without baking the material after recording in Fig. 4.45 (a). The depth selectivity is consistent with the theoretical calculation in equation (4.82) under the experimental condition. However, the measured FWHM is 13 μm, much larger than the prediction of $2\Delta z_p = 4\ \mu m$

in equation (4.85). This is cause by the focal depth of the collimating lens, which has a focal depth 4 μm from equation (4.10), which is comparable to the depth selectivity of the hologram. A pair of objective lens is used for scanning the focal point along the depth for depth-selectivity measurement, which broadens the FWHM of the experiment measurement. However, due to the slow decreasing side lobes of the hologram depth selectivity, the theoretical calculation in equation (4.82) gives the correct selectivity curve in Fig. 4.45.

Fig. 4.45 (b) shows the depth selectivity of three-multiplexed hologram in the same PQ polymer, with an average diffraction efficiency 7%. The three holograms are recorded with different recording depth z_r at 50 μm distance. Also, the reference beams have different angle for three holograms, which optically section three slices at different depth from the 3-D objective spatial dimension and project them onto different area of the image sensor.

Even though the three peaks in Fig. 4.45 (b) are well separated, the broad and slow-decreasing side lobe of the depth selectivity causes cross talks before them, which leads to background noise on the images, which is also demonstrated in Fig. 4.46. In Fig. 4.45, a focused point source is used to scan the depth for the three holograms. As the $z_p = z_{r1}$, the recording position for the first hologram in Fig. 4.45 (a), a bright image point is generated on the detector corresponding to the recording position of the reference, while there are cross talks (or side lobe images) on the other two locations corresponding to the other two holograms, with the pattern predicted in Fig. 4.34. Fig. 4.46 (b) shows a similar case when the probing source Bragg phase-matches the second hologram.

4.4.2 3-D imaging of fluorescent microspheres

To demonstrate the ability of 3-D imaging of real 3-D objects, we use fluorescent micropsheres as our observation targets. Fluorescent microspheres are poly spheres doped with certain dyes, which can be excited by some wavelength and emit fluorescent lights. They are widely used in biomedical research in confocal microscopes and

fluorescent microscopes [82, 60, 56].

We use 15 μm diameter microspheres, excited by 488 nm and emitting fluorescent light at central peak wavelength 515 nm [94] in our experiments. Fig. 4.47 shows the comparison of the imaging quality between holographic imaging and a normal microscope imaging in Fig. 4.41. Two layers of microspheres are sealed in solid polymer with a distance 100 μm between. The visual image quality of single hologram imaging and a normal microscope system with the same collimating and imaging lenses is comparable, due to the high spatial selectivity achieved by the holographic imaging elements. However, due to the intrinsic color filtering effect in holographic imaging, the signal level for the detector pixels in holographic imaging is much lower than the normal microscope.

To demonstrate the multiple optical sectioning and real-time imaging of 3-D space, a liquid sample of fluorescent microspheres is used. Fig. 4.48 (a) shows the optical sectioning and imaging by a single hologram in PQ polymer in Fig. 4.45 (a). With three holograms multiplexed in the PQ polymer as in Fig. 4.48 (b), three optical sectionings from different depths are projected onto the detector at the same time in Fig. 4.48 (b) in real time.

4.4.3 Discussion

Fig. 4.49 shows the experimental setup on an optical table in the lab and the potential system integration for a practical holographic imaging system.

To design a practical holographic imaging module, several important issues are to be addressed.

1. The resolution: Due to the existence of collimating and imaging lenses, the resolution of a holographic 3-D imaging system cannot achieve higher resolution than the normal microscope. Also, the aberrations and the finite space-bandwidth product of these lenses limit the objective space volume from where the signals can be collected and projected onto the holograms.

New architectures and more sophisticated computer designed holographic patterns

could directly image the object without collimating lenses. Further investigation and theoretical, and experimental verification are required to explore the potentials of such approaches.

2. Photon efficiency: As we mentioned earlier, the 4-D hyperspace sectioning makes the photon counts on each detector to decrease, which leads to a lower signal to noise ratio, or a higher photon flux requirement. This might be a problem for fluorescent samples due to the photobleaching effects on the fluorophores. This is especially a problem for the wavelength sectioning, where the volume holograms have typically a high wavelength selectivity and decrease the photo efficiency for spatial signal detection. For most of the applications in microscopes, the spectral information resolution required is far less than the holographic imaging achieved.

3. Strong hologram multiplexing: To keep the photo efficiency as high as possible, we require the imaging holograms to have large diffraction efficiency, which is not an easy task for most of the volume holographic materials. Photopolymers are a good choice only if strong holograms in them can achieve high wave front reconstruction quality, or high spatial selectivity for spatial optical sectioning resolution. Localized recording in doubly-doped photorefractive crystals [95, 2, 22, 96, 97] is another potential method to overcome this problem.

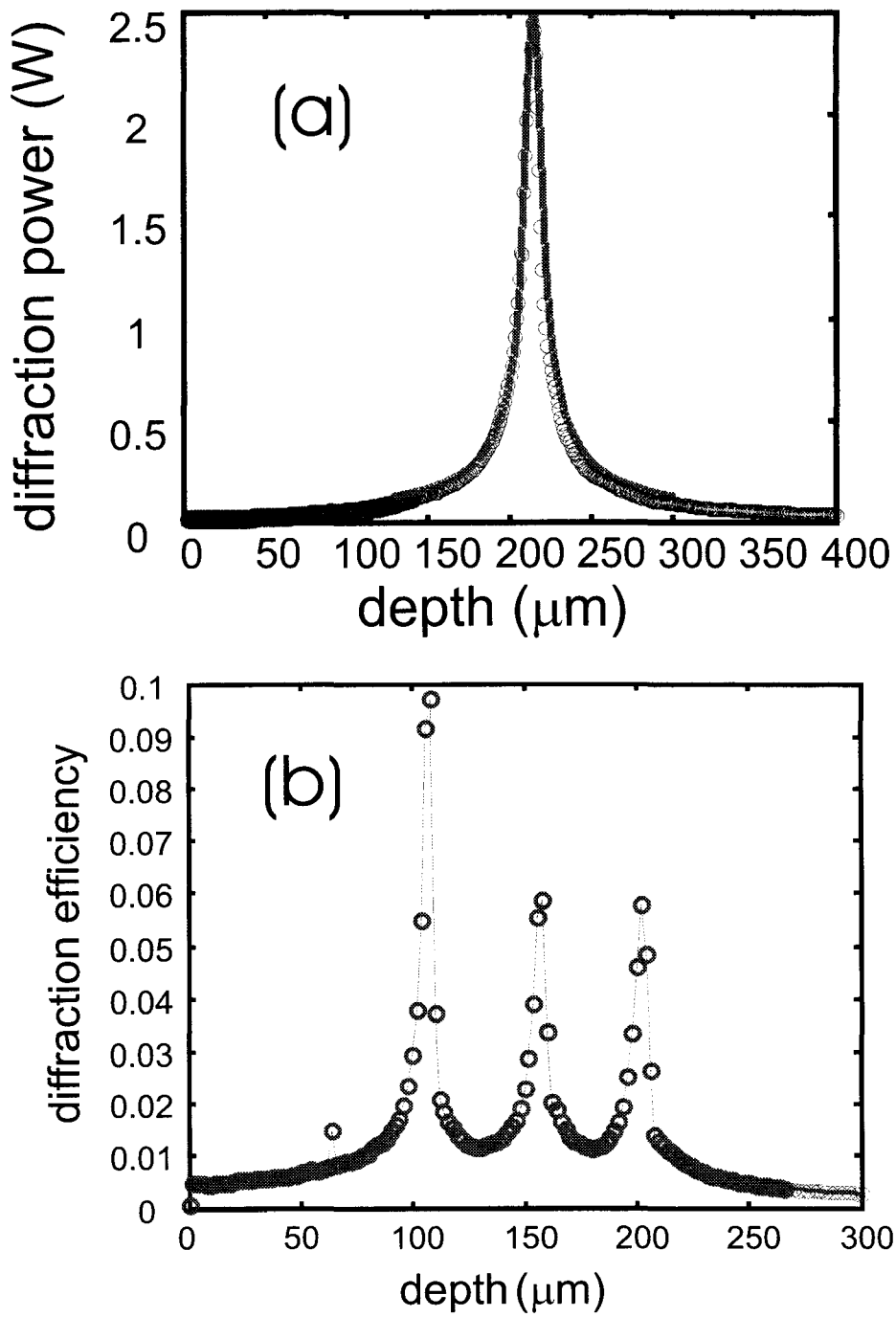

Figure 4.45: The depth selectivity measurement and comparison to the theoretical prediction in a PQ polymer of 2 mm thick. Experimental setup is as in Fig. 4.41 with: collimating objective lens $\times 40$ NA=0.65, wavelength 488 nm. (a) A single strong hologram with diffraction efficiency $> 15\%$. The depth selectivity is consistent with the theoretical calculation by equation (4.82). (b) Three holograms multiplexed with different recording depth z_r at 50 μm apart.

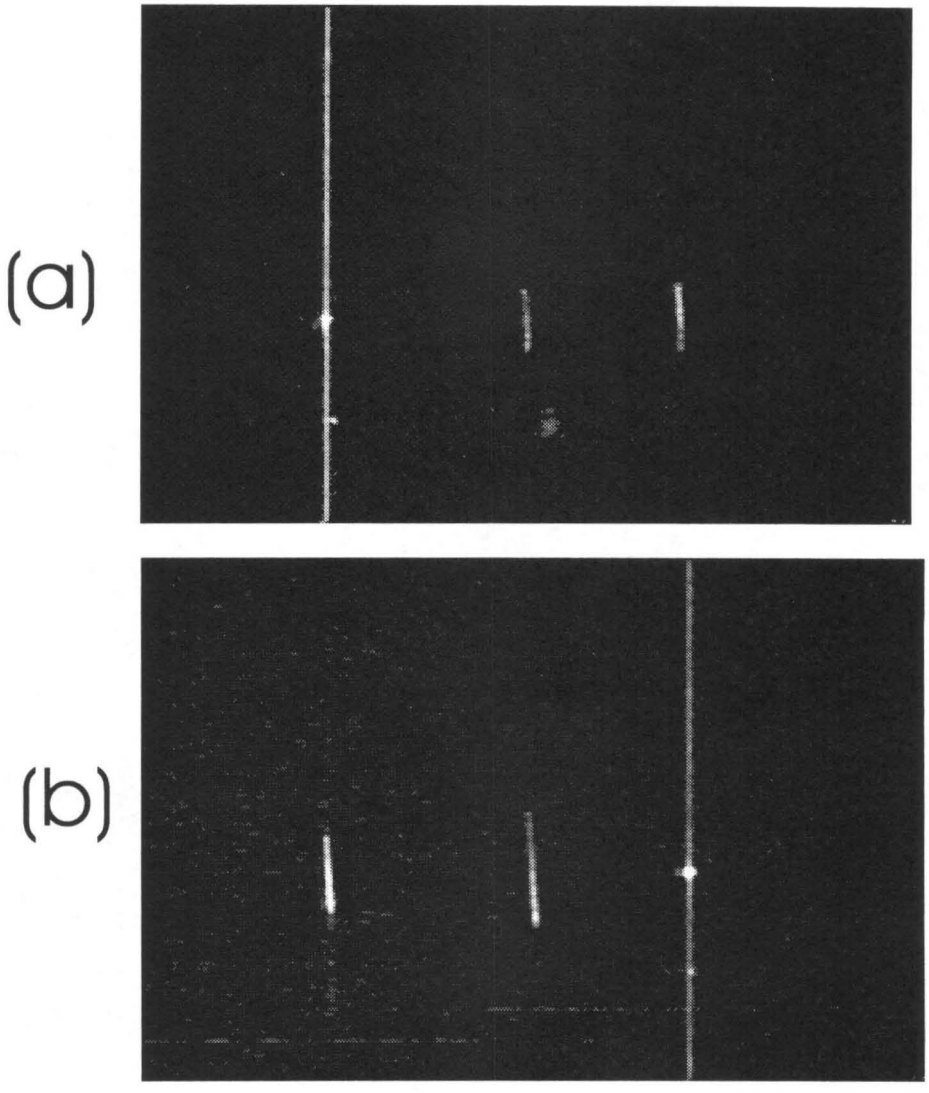

Figure 4.46: The image pattern as a single-point source is scanned along the depth of the three multiplexed holograms. (a) The probing source is Bragg-matched to the first hologram, generates a bright point image for it, with two weak depth mismatched patterns for the other two depths. (b) The probe point source is Bragg-matched to the second hologram.

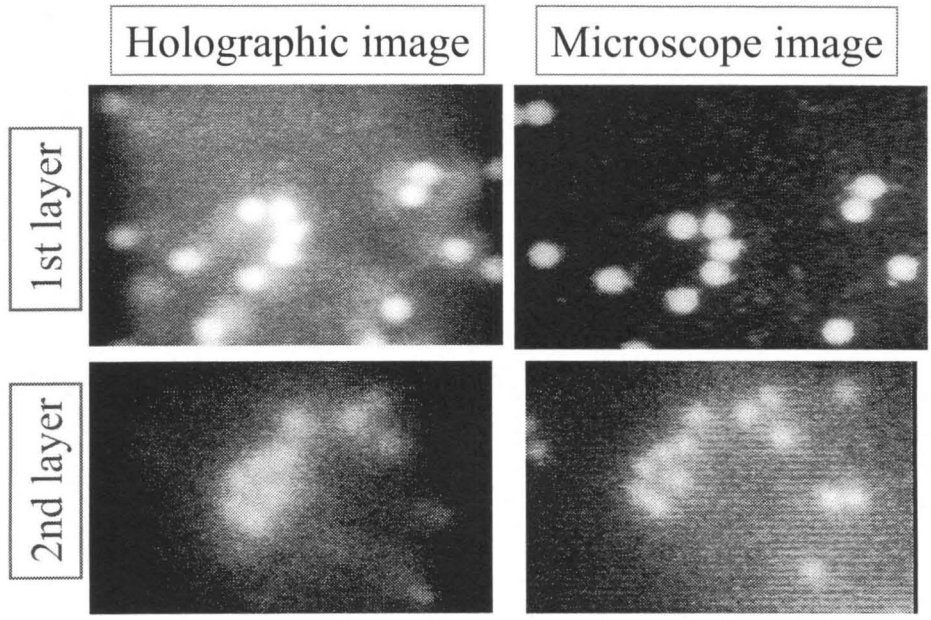

Figure 4.47: The images of fluorescent microspheres (15 μm diameter) excited by 488 nm and emitting at peak fluorescent wavelength 515 nm, by holographic and normal microscope imaging systems with the same collimating and imaging lenses in Fig. 4.41.

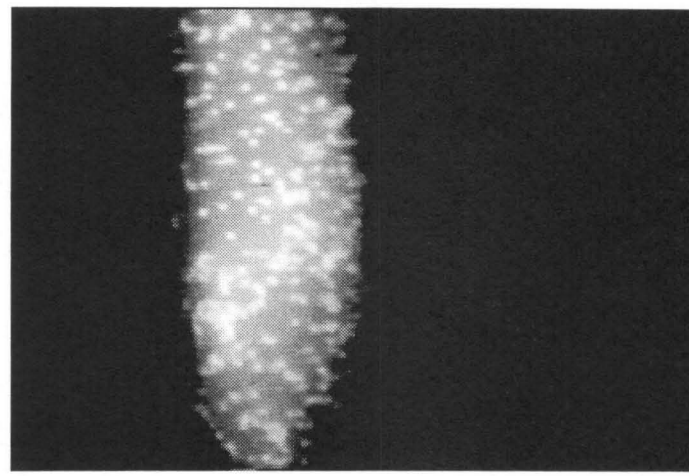

(a)

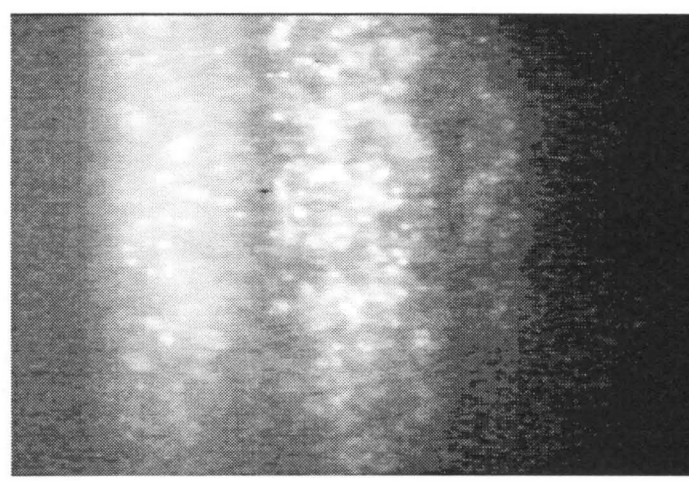

(b)

Figure 4.48: The images of fluorescent microspheres (15 μm diameter) in a liquid sample, excited by 488 nm and emitting at peak fluorescent wavelength 515 nm. (a) Using a single hologram with the depth sectioning ability as in Fig. 4.45 (a). (b) Using three multiplexed holograms to image three different-depth optical sections.

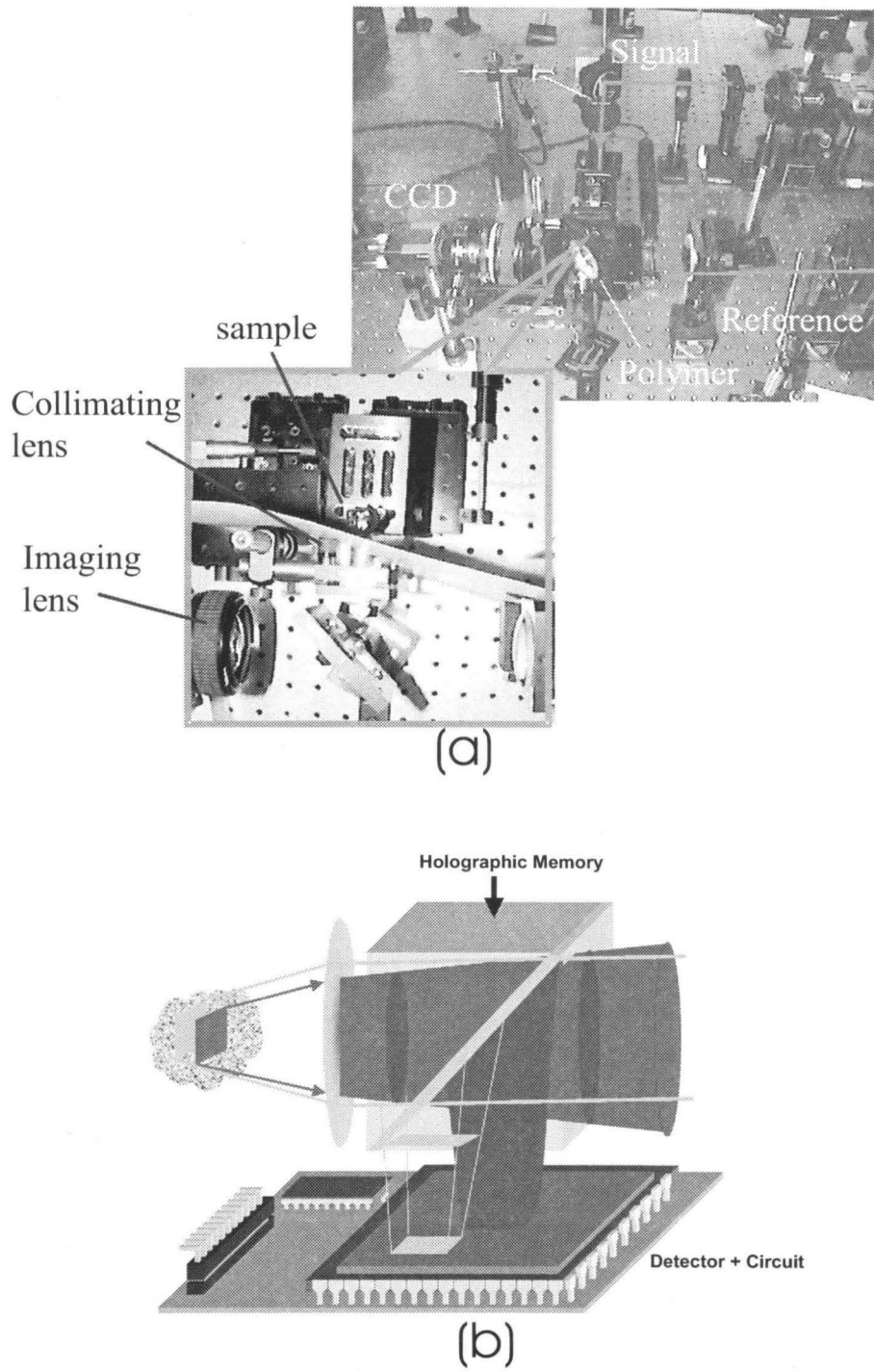

Figure 4.49: (a) The experimental setup on the optical table in the lab. (b) A potential holographic imaging module system design.

Chapter 5 M-number for Spectral Hole Burning Material

For data storage application, the dynamic range of the storage medium is a major factor determining the storage density and capacity, besides the resolution and geometry limits. $M\#$ [93] is widely used as a system measure of the holographic diffraction efficiency of superimposing M holograms at a single location in photorefractive crystals or photopolymers. Another interesting material widely explored for holographic recording is the spectral hole burning material. In this chapter, we study the system dynamic measure of the spectral hole burning medium of hologram multiplexing at a single location and a single wavelength.

Theoretical studies show that there is a $M\#$ as a system measure for pure absorption gratings and pure index gratings induced by multiple absorption gratings through the Kramers-Kronig relations. $M\#$ is calculated as the product of the number of superimposed holograms M and the square root of their equalized diffraction efficiency. It is proven to be a function of the absorption bleaching range of the media only, and independent of the number of holograms superimposed M. Pure index gratings give similar $M\#$ as pure absorption gratings with consideration of the residual absorption existed in practical spectral hole burning media. Experiments on multiple absorption holograms angle-multiplexed at one location with one wavelength give $M\#$ results consistent with the theoretical calculation.

5.1 Spectral hole burning material

Holography in spectral hole burning materials has been receiving attention in the last decade as a potential technology for optical data storage due to their extremely fine wavelength selectivity [113]. In contrast to the conventional holograms multiplexing

in a single sample by the use of Bragg selectivity, spectral hole burning uses extreme frequency selectivity of molecule absorption under low temperature to multiplex holograms at different frequencies.

The fine frequency selectivity of the material comes from the zero-phonon lines (ZPL) investigation, which started in the first half of the 1950s with the theoretical studies of the optical spectra of impurity crystals [117]. ZPL is related to the electron transition between electronic energy levels of a guest atom or molecule. The ZPL of an absorption center is normally extremely narrow and has a typical Lorenzian lineshape [43, 29]. For an absorption center in amorphous materials, the absorption lines consist of the ZPL and a phonon wing, which depends on the temperature. The homogeneous linewidth, Γ_h, is given by

$$\Gamma_h = \frac{1}{2\pi T_1} + \frac{1}{\pi T_2}, \tag{5.1}$$

where T_1 is the lifetime of the excited state and T_2 is the dephasing time caused by phonon scattering [32, 4]. At normal room temperature, the dephasing time T_2 is much smaller than the lifetime T_1, leading to a broad homogeneous absorption transition. However, when the material is cooled down to low temperature, the dephasing process becomes sufficiently long that the homogeneous linewidth is dominated by the ZPL. The relative integrated intensity of ZPL among the absorption lines (including the phonon wing) is proportional the the Debye-Waller factor, and gets larger when the temperature is lower.

Even though the ZPL lines are only depending on the electron energy level transition in the absorption center, they are never the same in a real material, because the optical ZPL is sensitive to the different local environmental conditions for different absorption centers. These differences cause a frequency shift of different absorption centers and lead to the inhomogeneous broadening in the material, which is much broader than the ZPL. Therefore, when a single wavelength laser illuminates the material, only a subset of the molecules from the inhomogeneous distribution are excited and leave a population hole in the absorption line centered at the incident

wavelength. Due to the large ratio of the inhomogeneous broadening and the homogeneous linewidth, a large number (up to 10^4) of wavelength channels are available in the spectral hole burning materials [113, 81].

The research in spectral hole burning until now is concentrated on exploring the frequency domain to increase the number of holograms. No studies on the conventional hologram multiplexing at a single location with a single wavelength have been done, limited by the intrinsic small diffraction efficiency of a single pure absorption grating inside the medium [67]. On the other hand, a new Frequency Phase Swept holographic recording technique (FPS) [14] can produce large diffraction efficiency by recording multiple exposures of the same hologram at different optical frequencies in frequency selective materials. 12,000 persistent holograms by FPS were demonstrated in frequency domain by B. Plagemann and his colleagues [100] and a hologram diffraction efficiency of 5% was achieved. This effect can be understood by considering the superposition of multiple absorption and index gratings (the latter generated by the Kramers-Kronig relation). Many homogeneous absorption lines of the spectrally selective material are used to build up a single hologram with a large diffraction efficiency. This opens the possibility of multiplexing at the same location and at the same frequency and implies its potential application in data storage and complex multiple-pulse shaping.

In this study, we investigate the conventional hologram multiplexing in spectral hole burning materials and study the dynamic range with combination of the conventional Bragg selectivity and the FPS technology. A system measure of the diffraction efficiencies of multiple holograms superimposed in the same volume is called $M\#$, which is used extensively with photorefractive crystals and photopolymers [93]. It is defined by $M\# = \sqrt{\eta}M$, where M is the number of superimposed holograms and η is the equalized diffraction efficiency of each individual hologram. We apply the same idea onto the spectral hole burning material, and study $M\#$ on both pure absorption grating recording and the pure index grating recording by FPS. The calculated $M\#$ is independent of the number of holograms superimposed, which gives a good system measure of spectrally selective material dynamic range for hologram multiplexing.

5.2 Absorption bleaching model

To study the absorption hologram recording and its diffraction efficiency inside a spectral hole burning material, we construct a simple theoretical model based on the bleaching process and analytically calculate $M\#$ for multiple holograms superimposed at the same location.

During the spectral hole burning process, the material is frozen at a temperature of liquid helium 1.7 K. Under this condition, the inhomogeneous broadening of the material absorption line is only caused by the different environmental conditions for the absorption centers. Illuminated by light of a single wavelength, only a subset of the molecules being sensitive to that frequency are excited and undergo a photochemical reaction. The absorption constant of the material at that frequency decreases due to the depletion of the molecules absorbing at that frequency[84]. Therefore, an absorption hole in the broad inhomogeneous absorption line will be generated with a linewidth determined by its homogeneous Lorentzian line shape. The bleaching kinetics of the amplitude absorption constant $\alpha(\omega, \mathbf{r}, t)$ of the spectral selective material upon exposure can be modeled by assuming a first order photoprocess as

$$\alpha(\omega, \mathbf{r}, t) = B + A\frac{\gamma^2}{(\omega_b - \omega)^2 + \gamma^2} \exp\left(-KI(\omega_b, \mathbf{r}, t)t\right) \tag{5.2}$$

$$\alpha_o = A + B, \tag{5.3}$$

where $I(\omega_b, \mathbf{r}, t)$ is the intensity pattern of exposure with hole burning frequency ω_b, K is a kinetic parameter that depends on the material sensitivity. B is the nonburnable absorption constant caused by the broad phonon wing in the absorption spectrum, and represents an absorption background that persists after prolonged bleaching. A represents the bleachable absorption — the dynamic range of the absorption hole burning in the material, which is caused by the zero phonon absorption line of those absorption centers and has a narrow Lorentzian lineshape centered at the hole burning frequency ω_b. α_o is the overall absorption constant at time $t = 0$. This model is a simplification of a more rigorous model [61, 44, 121], that takes into account quantum

efficiency distribution, polarization dependence, and random orientation of absorbing centers. However, this simple model fits quantitatively well to the first order with the experimental absorption bleaching kinetics .

For non-slant holographic recording in transmission geometry, the sample is illuminated by two coherent light beams I_1, I_2, which generate an interference intensity pattern as

$$I(\mathbf{r}) = I_o\left[1 + V\cos\left(\mathbf{kr}\right)\right], \tag{5.4}$$

with the modulation depth $V = 2\sqrt{I_1 I_2}/I_0$, and the overall intensity $I_0 = I_1 + I_2$. The modulated intensity pattern creates an excited state grating by either photorefractive effects or photoreaction within the material, and leads to frequency and time dependent spatial modulation of the absorption coefficient α and refractive index n:

$$\alpha(\mathbf{r}, \omega, \mathbf{t}) = \alpha_0(\omega, t) + \alpha_1(\omega, t)\cos(\mathbf{kr}) \tag{5.5}$$

$$n(\mathbf{r}, \omega, \mathbf{t}) = n_0(\omega, t) + n_1(\omega, t)\cos(\mathbf{kr}). \tag{5.6}$$

For uniform grating in transmission geometry, the diffraction efficiency, $\eta = I_d/I_r$, defined as the intensity ratio of the diffraction and reference beams, can be calculated by Kogelnik's couple wave theory [67] as

$$\eta(\omega, t) = \exp\left(\frac{-2\alpha_0(\omega, t)d}{\cos\theta}\right)\left[\sinh^2\left(\frac{\alpha_1(\omega, t)d}{2\cos\theta}\right) + \sin^2\left(\frac{\beta_1(\omega, t)d}{2\cos\theta}\right)\right], \tag{5.7}$$

where the propagation constant $\beta_1 = 2\pi n_1/\lambda$, d is the thickness of the recording medium and θ is the incident angle of recording beams inside the material.

Multiple holographic gratings can be recorded at the same volume by exposure of different intensity patterns $I_i(\mathbf{r}, t)$ on it

$$I_i(\mathbf{r}, t) = I_o\left[1 + V_i\cos\left(\mathbf{k_i r}\right)\right], \tag{5.8}$$

where we assume that the intensity grating is uniform throughout the medium. In

materials with small optical density, this approximation is valid because the light intensity is approximately uniform inside to the first order. For materials with large optical density, one has to consider the depletion of the beam intensity along the depth inside the medium. The latter case is treated numerically in 5.3.

With the assumption of uniform intensity patterns through the material of small optical density during recording, the absorption constant after M holograms recorded at the single burning frequency ω_b is equal to

$$\alpha_M = B + A\exp\left(-KI_o\sum_{i=1}^{M}\left(1+V_i\cos\left(\mathbf{k_i r}\right)\right)t_i\right) \tag{5.9}$$

$$= B + A\exp\left(-KI_o\sum_{i=1}^{M}t_i\right)\exp\left(-KI_o\sum_{i=1}^{M}V_i\,t_i\cos\left(\mathbf{k_i r}\right)\right), \tag{5.10}$$

where V_i is the modulation depth of the i^{th} hologram.

All hologram grating strengths are equalized when all modulation depths are equal to V (where we assume $V = 1$ for our calculation) and the exposure energy for each hologram is set equal as $KI_o\tau$. When recording a large number of holograms, each hologram strength only consumes a small portion of the whole dynamic range, $KI_o\tau \ll 1$. Eq. (5.10) can be expanded in a cosine series by using modified Bessel functions, $\mathbf{I_n}\left(KI_0\tau\right)$. Considering only the first order grating terms which generate the correct signal reconstruction, Eq. (5.10) is simplified as

$$\alpha_M = B + A\exp\left(-MKI_o\tau\right)\left[\mathbf{I_0}(KI_o\tau) - 2\mathbf{I_1}(KI_o\tau)\sum_{i=1}^{M}\cos\left(\mathbf{k_i r}\right)\right] \tag{5.11}$$

$$= B + \overline{\alpha_o} - \alpha_1\sum_{i=1}^{M}\cos((\mathbf{k_i r})\,. \tag{5.12}$$

The remained average absorption $\overline{\alpha_o}$ of the bleachable dynamic range after the recording of M holograms, is equal to

$$\overline{\alpha_o} = A\exp\left(-MKI_o\tau\right)\mathbf{I_0}(KI_o\tau), \tag{5.13}$$

and the equalized grating strength α_1 of each hologram is equal to

$$\alpha_1 = 2A \exp(-MKI_o\tau)\, \mathbf{I_1}(KI_o\tau). \tag{5.14}$$

Absorption holograms: transmission geometry

For the pure absorption gratings, the recording and read-out are using the same single optical frequency. We have studied different recording geometries, such as transmission, reflection, and 90-degree. Similar results are obtained for each case, with the transmission geometry being the easiest to explain. Also, the transmission geometry is the most practical architecture with consideration of the energy bleaching, as discussed in section 5.3 on numerical modeling. Experimental results in transmission geometry are obtained and compared with the theoretical studies in section 5.5.

The diffraction efficiency of a pure absorption grating in the non-slant transmission geometry, is obtained by Eq. (5.7)

$$\eta = \exp\left(-\frac{2Bd}{\cos\theta}\right) \exp\left(-\frac{2\overline{\alpha_o}d}{\cos\theta}\right) \left(\frac{\alpha_1 d}{2\cos\theta}\right)^2, \tag{5.15}$$

where we assumed weak gratings $\frac{\alpha_1 d}{\cos\theta} \ll 1$. This is satisfied in cases when many holograms are multiplexed in a material with small optical density.

For multiple absorption gratings given in Eq. (5.13 – 5.14), the equalized diffraction efficiency for each hologram is

$$\begin{aligned} \eta &= \exp\left(-\frac{2Bd}{\cos\theta}\right) \exp\left[-\frac{2Ad}{\cos\theta}\mathbf{I_0}(KI_o\tau)\exp(-MKI_o\tau)\right] \left(\frac{Ad}{\cos\theta}\right)^2 \\ &\quad \times \exp(-2MKI_o\tau)\mathbf{I_1}^2(KI_o\tau) \qquad (5.16) \\ &= \exp\left(-\frac{2Bd}{\cos\theta}\right) \exp\left[-\frac{2Ad}{\cos\theta}\mathbf{I_0}(\frac{E}{M})e^{-E}\right] \left(\frac{Ad}{\cos\theta}\right)^2 \\ &\quad \times e^{-2E}\mathbf{I_1}^2(\frac{E}{M}), \qquad (5.17) \end{aligned}$$

where $E = MKI_o\tau$ represents the total energy exposure for absorption bleaching. The diffraction efficiency η is a sophisticated function of M, the number of holograms multiplexed inside the material. However, for the maximum diffraction efficiency

η over E with a given large number of multiplexed holograms M, it satisfies the approximation $E/M \ll 1$, which leads to the approximation for modified Bessel functions: $\mathbf{I_0}(E/M) \approx 1$ and $\mathbf{I_1}(E/M) \approx E/(2M)$. This simplifies the diffraction efficiency η in Eq. (5.17) as

$$\eta = \exp\left(-\frac{2Bd}{\cos\theta}\right) \exp\left[-\frac{2Ad}{\cos\theta}e^{-E}\right] \left(\frac{Ad}{2\cos\theta}\right)^2 e^{-2E} \left(\frac{E}{M}\right)^2 \tag{5.18}$$

$$= \left(\frac{M\#}{M}\right)^2 \tag{5.19}$$

$$M\# = \exp\left(-\frac{Bd}{\cos\theta}\right) \left(\frac{Ad}{2\cos\theta}\right) \max_{overE}\left[Ee^{-E}\exp\left(-\frac{Ad}{\cos\theta}e^{-E}\right)\right]. \tag{5.20}$$

The diffraction efficiency η is inversely proportional to the square of the number of holograms M, the same dependency as the multiple holograms recording in photorefractive crystals and photopolymers. The dynamic measure $M\#$ is computed using the relation $M\# = \sqrt{\eta}M$, where η is the maximum of equalized M hologram diffraction efficiencies obtainable for a given optical density. And $M\#$ in Eq. (5.20) only depends on the normalized optical density of the material: the burnable part $\frac{Ad}{\cos\theta}$ and the nonburnable part $\frac{Bd}{\cos\theta}$. Here, we define a normalized amplitude optical density of the material as $OD = \frac{\alpha d}{\cos\theta}$, which is different from the optical density $(-\log T)$ by a factor of $0.5 \ln 10 \approx 1.15$, where α is the amplitude absorption constant and T is the intensity transmission.

Fig. 5.1 gives the diffraction efficiency in Eq. (5.17) as a function of the total exposure energy E, which shows a maximum peak at a certain exposure energy. When the exposure energy is small, the diffraction efficiency increases as the grating strength is recorded and enhanced during exposure. When the diffraction energy is over the maximum peak, the material is running out of the bleachable dynamic range. Continuing exposure erases the previously recorded gratings and decreases the diffraction efficiency. For the maximum efficiency in the Fig. 5.1, the exposure energy verifies the approximation $E/M \ll 1$ for $M = 10$ or larger as we previously assumed. Fig. 5.2 shows the calculated $M\#$ versus normalized optical density $OD = \frac{\alpha_0 d}{\cos\theta}$ of the material. The three curves are plotted for three values of the nonburnable absorption

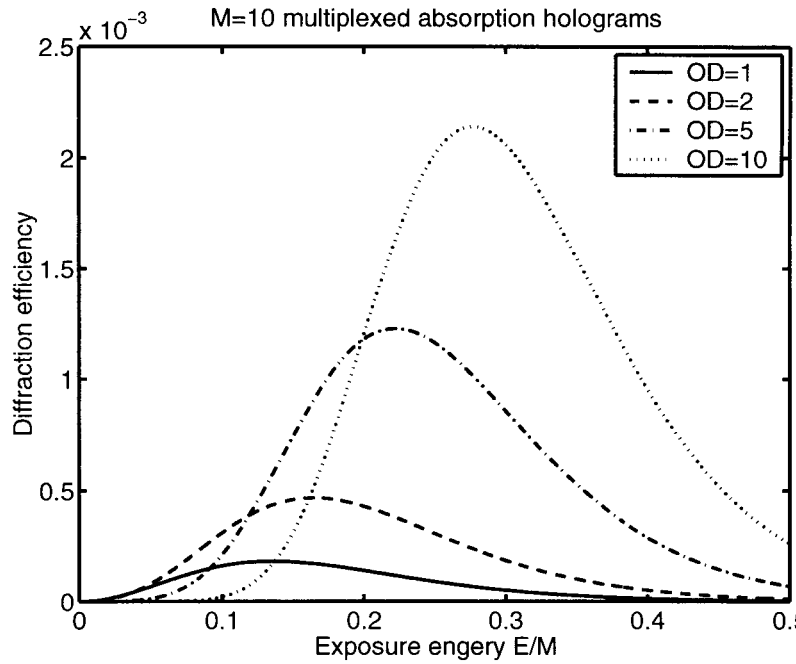

Figure 5.1: Diffraction efficiency η versus the average exposure energy E/M for $M = 10$ multiplexed absorption holograms. The normalized optical density $OD = \frac{Ad}{\cos\theta}$ and the nonburnable absorption constant $B = 0$.

B. When $B = 50\%\alpha_0$, $M\#$ reaches its maximum value of 0.05 at normalized optical density $OD = 1.52$. $M\#$ increases when B decreases, due to a more transparent medium after all holograms recorded. In the ideal case with B=0, the theoretical model predicts that $M\#$ increases logarithmically with the normalized optical density OD. However, when the optical density is getting larger, the approximation of uniform grating strengths of each hologram through the thickness starts to fail. And the diffraction efficiency in Eq. (5.20) is not accurate any more for large optical density as shown in later numerical simulation. Considering the effects by the nonburnable absorption B in Eq. (5.20), it only adds a constant term $\exp\left(-\frac{Bd}{\cos\theta}\right)$ to $M\#$. The recording kinetics depends only on the bleachable range Ad of the optical density, as long as the uniform grating approximation is satisfied. However, this would not be true when the optical density is large, and the nonuniform grating recording process inside the material has to be considered. This is studied and proved by the following numerical simulation.

Index holograms:transmission geometry

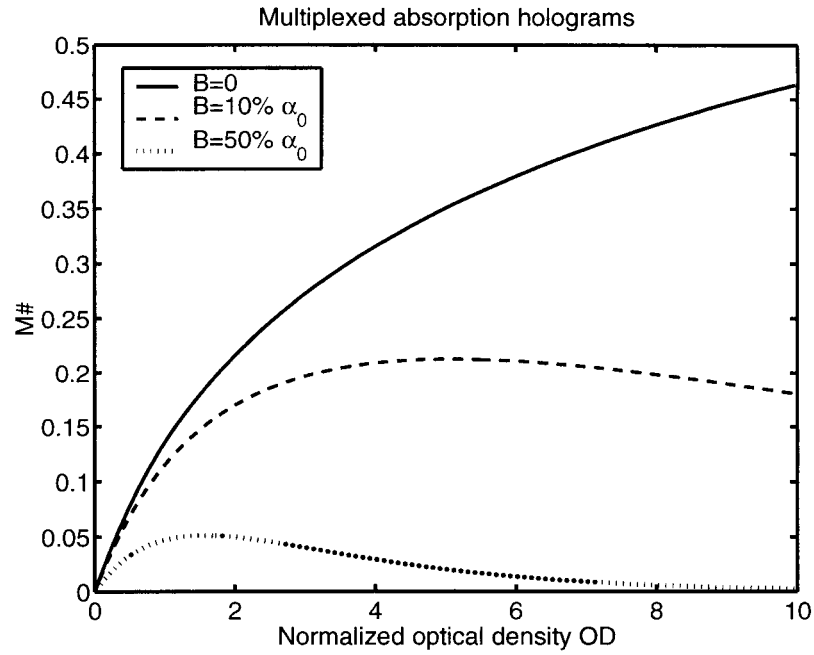

Figure 5.2: $M\#$ of absorption holograms ($\lambda_{write} = \lambda_{read}$) as a function of the normalized optical density $OD = \frac{\alpha_0 d}{\cos\theta}$, where $\alpha_0 = A + B$.

Based on the Kramers-Kronig relations, when an absorption grating is generated inside the material, there is also an index grating existing. The FPS method makes use of the superposition of multiple index gratings generated by recording identical absorption grating at multiple frequencies. The advantages are a strong index grating recorded at the expenses of the frequency range and the possibility of maximal bleaching of the absorption without affecting the index grating at the readout frequency.

For simplicity, we study the properties of multiplexing pure index gratings at the same location and frequency, where each pure index grating is generated by two holographic exposures at two optical frequencies with a π phase shift between the two holographic exposures (Π-index hologram). We start by assuming Lorentzian lineshapes for the average absorption constant $\overline{\alpha_o}$ and grating strength α_1 in Eq. (5.13

– 5.14) during the spectral hole burning at frequency ω_b

$$\overline{\alpha_o}(\omega,\omega_b) = \overline{\alpha_0}(\omega_b)\frac{\gamma^2}{(\omega_b-\omega)^2+\gamma^2} \tag{5.21}$$

$$\alpha_1(\omega,\omega_b) = \alpha_1(\omega_b)\frac{\gamma^2}{(\omega_b-\omega)^2+\gamma^2}, \tag{5.22}$$

where γ is the homogeneous linewidth, ω_b is the recording (hole burning) optical frequency. An index grating β_1 was induced by the absorption grating according to the Kramers-Kronig relation as

$$\beta_1(\omega) = \alpha_1(\omega,\omega_b)\frac{\omega-\omega_b}{\gamma}, \tag{5.23}$$

where ω is the readout frequency. A Π-index hologram is recorded with a first exposure at frequency ω_{b1} and a second exposure (same exposure energy and same grating) at frequency ω_{b2}. Due to the very small difference between ω_{b1} and ω_{b2}, the difference between the two spatial intensity patterns inside the material is negligible. The induced diffraction field E_d from an incident beam E_r at the readout frequency ω from the two hologram exposures is given as

$$\begin{aligned} E_d(\omega) &= E_r \exp\left(-\frac{\overline{\alpha_o}(\omega)d}{\cos\theta}\right)\left[\left(\frac{\alpha_1(\omega,\omega_{b1})d}{2\cos\theta}+j\frac{\beta_1(\omega,\omega_{b1})d}{2\cos\theta}\right)e^{j\phi_1}\right. \\ &\left.+\left(\frac{\alpha_1(\omega,\omega_{b2})d}{2\cos\theta}+j\frac{\beta_1(\omega,\omega_{b2})d}{2\cos\theta}\right)e^{j\phi_2}\right], \end{aligned} \tag{5.24}$$

where ϕ_1 and ϕ_2 are the phases of the gratings in exposure 1 and 2 respectively. If we choose $\phi_2-\phi_1=\pi$, Eq. (5.24) gives a diffraction efficiency as

$$\begin{aligned} \eta(\omega) &= \exp\left(-\frac{2\overline{\alpha_o}d}{\cos\theta}\right)\frac{d^2}{4\cos^2\theta}\left[(\alpha_1(\omega,\omega_{b_2})-\alpha_1(\omega,\omega_{b_1}))^2\right. \\ &\left.+(\beta_1(\omega,\omega_{b_2})-\beta_1(\omega,\omega_{b_1}))^2\right]. \end{aligned} \tag{5.25}$$

Assuming that the two exposures have the same grating strengths and we readout the hologram at the central frequency $\omega=\frac{\omega_{b_1}+\omega_{b_2}}{2}$, the absorption grating cancels

and only a pure index grating prevails due to the lineshapes in Eq. (5.22 - 5.23):

$$\eta(\omega) = \exp\left(-\frac{2\overline{\alpha_o}d}{\cos\theta}\right)\frac{d^2}{\cos^2\theta}\alpha_1^2(\omega_b)\left[\frac{\Delta\omega\gamma/2}{(\Delta\omega/2)^2+\gamma^2}\right]^2, \tag{5.26}$$

where $\Delta\omega = |\omega_{b_1} - \omega_{b_2}|$. The diffraction efficiency has a maximum for $\Delta\omega = 2\gamma$. When readout for a long time at frequency $\omega = \frac{\omega_{b_1}+\omega_{b_2}}{2}$, the index grating will be much less sensitive to the bleaching than the absorption constant at this frequency [14, 100]. If we assume the ideal case that the index grating is remained while we bleach the remaining absorption constant at readout frequency to the nonburnable absorption B, it yields the following upper bound for the diffraction efficiency of a Π-index hologram:

$$\eta = \exp\left(-\frac{2\,B\,d}{\cos\theta}\right)\left(\frac{\alpha_1(\omega_b)d}{2\cos\theta}\right)^2. \tag{5.27}$$

This expression is similar to a pure absorption hologram in Eq. (5.15), except the exponential absorption term. In the same way as $M\#$ results for the absorption grating in Eq. (5.20), the diffraction efficiency for pure index grating generated with Π-index holograms is given as

$$\eta = \left(\frac{M\#}{M}\right)^2 \tag{5.28}$$

$$\begin{aligned} M\# &= \exp\left(-\frac{Bd}{\cos\theta}\right)\left(\frac{Ad}{2\cos\theta}\right)\max_{overE}\left(Ee^{-E}\right) \\ &= \exp\left(-1-\frac{Bd}{\cos\theta}\right)\left(\frac{Ad}{2\cos\theta}\right). \end{aligned} \tag{5.29}$$

The calculated $M\#$ results are shown in Fig. 5.3 for different normalized optical densities $OD = \frac{(A+B)d}{\cos\theta}$. If the material is assumed to be transparent after exposure, *i.e.*, $B = 0$, the $M\#$ is proportional to the normalized optical density. Otherwise, it shows the same dependency on the optical density as the pure absorption gratings in Fig. 5.2. When $B = 50\%\alpha_0$, $M\#$ reaches a maximum 0.068 at $OD = 2.02$. Comparing $M\#$ between multiplexing Π-index holograms and pure absorption holograms, $M\#$ of index holograms is higher than that of the pure absorption holograms,

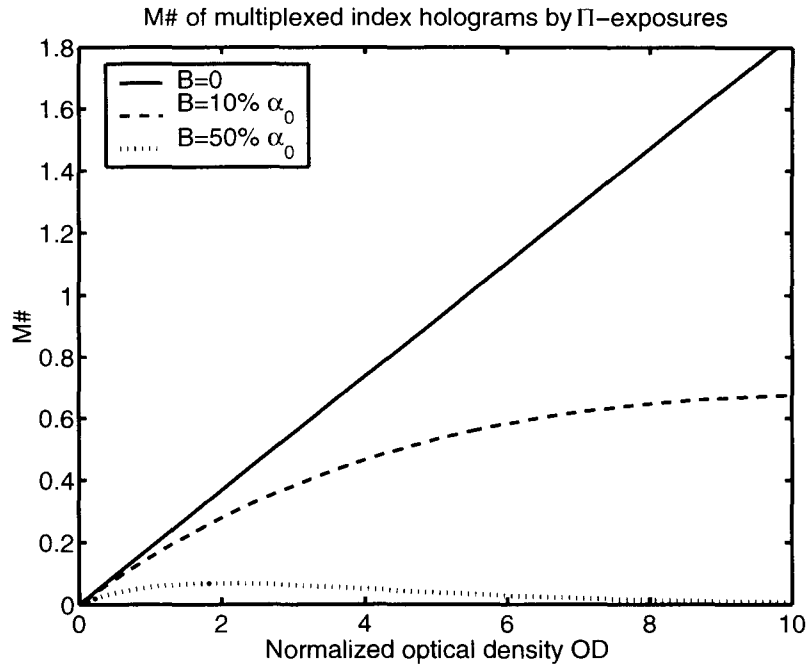

Figure 5.3: $M\#$ of Π-index holograms ($\lambda_{read} = (\lambda_{b1} + \lambda_{b2})/2$) as a function of the normalized optical density $OD = \frac{\alpha_0 d}{\cos\theta}$, where $\alpha_0 = A + B$.

especially when the optical density is large, as shown in Fig. 5.4. From Eq. (5.20) and (5.29), $M\#$ ratio between the Π index holograms and the pure absorption holograms increases as the bleachable optical density $\frac{Ad}{\cos\theta}$ increases, and is independent of the nonburnable absorption B. However, due to the theoretical approximation under small optical density, the advantage of multiplexing using Π holograms at large optical density have to be re-examined carefully by detailed numerical studies in next section.

5.3 Dynamic modeling

For a material with large optical density, the intensity pattern and its induced absorption/index grating is nonuniform due to the energy depletion inside the material. Considering a simple transmission geometry recording, the distribution of *incident* light intensity inside the material is limited to a layer at the front surface depending on the local absorption constant profile. Starting with a fresh material with a large

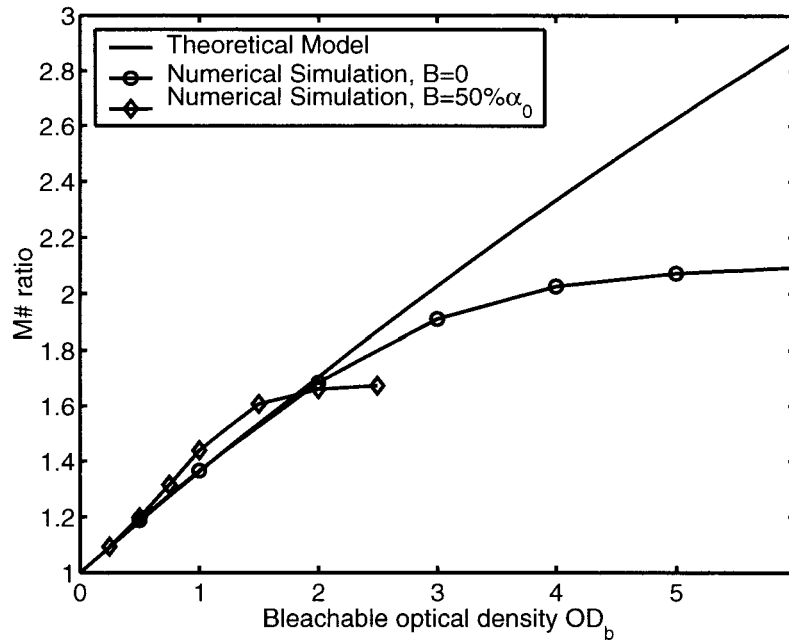

Figure 5.4: $M\#$ ratio between index holograms by Π-exposure ($\lambda_{read} = (\lambda_{b1} + \lambda_{b2})/2$) and pure absorption holograms as a function of the normalized bleachable optical density $OD_b = \frac{Ad}{\cos\theta}$. For the theoretical approximation model, $M\#$ ratio is independent of the nonburnable absorption B. For dynamic numerical simulation results, $M\#$ does depend on B.

uniform absorption constant, a strong grating is first recorded at the front surface. Then the absorption constant at the front surface is bleached and the intensity pattern gradually penetrates deeper into the material. By finite difference time domain method, we can numerically simulate the dynamics of the absorption constant changes and the light intensity pattern distribution during the bleaching process. Different holograms have different grating strength distribution through the volume medium due to the dynamic bleaching process.

For a nonuniform grating in transmission geometry, the diffraction efficiency can be derived in the same way as Eq. (5.7) from Kogelnik's couple wave theory [67]. Assuming a nonuniform absorption constant $\alpha_0(z)$, absorption and index gratings

$\alpha_1(z), \beta_1(z)$ along the depth z, the diffraction efficiency is derived in section 5.4 as

$$\eta(t) = \exp\left(\int_0^d \frac{-2\alpha_0(\tau,t)}{\cos\theta}d\tau\right)\left[\sinh^2\left(\int_0^d \frac{\alpha_1(\tau,t)}{2\cos\theta}d\tau\right) + \sin^2\left(\int_0^d \frac{\beta_1(\tau,t)}{2\cos\theta}d\tau\right)\right]. \quad (5.30)$$

By numerical optimization, we calculate the optimal recording schedule to get the diffraction efficiencies for all holograms equalized and maximized. Due to the limitation of computing power and time, we studied numerically 10 holograms multiplexing inside the material. The calculated M# as a function of the normalized amplitude optical density $OD = \frac{(A+B)d}{\cos\theta}$ is shown in Fig. 5.5, where the residual absorption B=0 or 50% α_0.

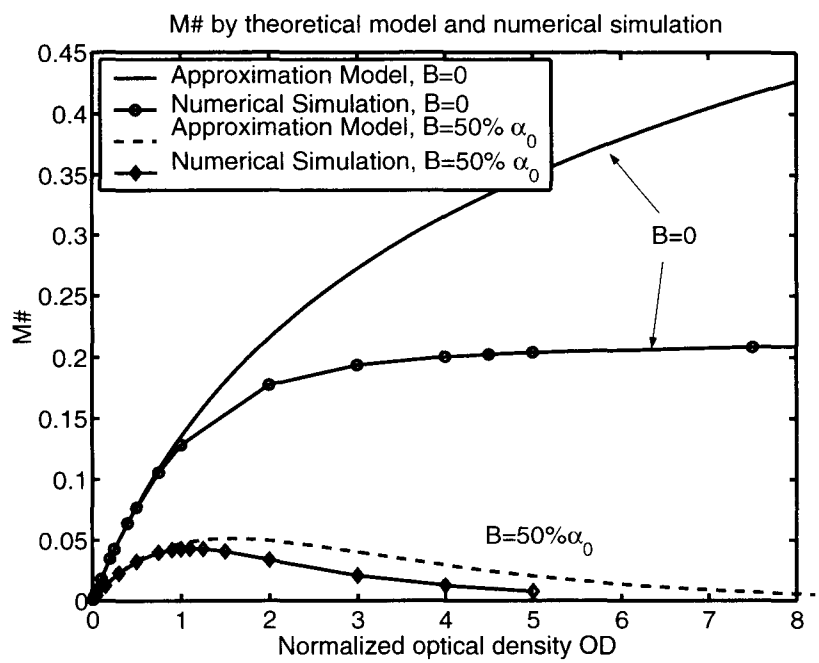

Figure 5.5: Comparison of $M\#$ for absorption holograms between theoretical approximation model and the numerical simulation ($\lambda_{write} = \lambda_{read}$) as functions of the normalized amplitude optical density $OD = \frac{\alpha_0 d}{\cos\theta}$, $\alpha_0 = A + B$.

Comparing with the results by previous theoretical approximation model, which are also shown in the Fig. 5.5, the simulated M# is consistent with the theoretical model when the normalized optical density $OD \leq 1$. When the normalized optical

density is getting larger, the simulated $M\#$ no longer follows the approximation model. For $B = 0$, it reaches a saturation value $M\# = 0.2$ at the optical density around 5. The saturation is due to the spatial limitation of grating strength within a thin layer inside the material of a large absorption constant. This is also proven by the recording schedule and the grating strength distribution within the medium in Fig. 5.6 and Fig. 5.7,

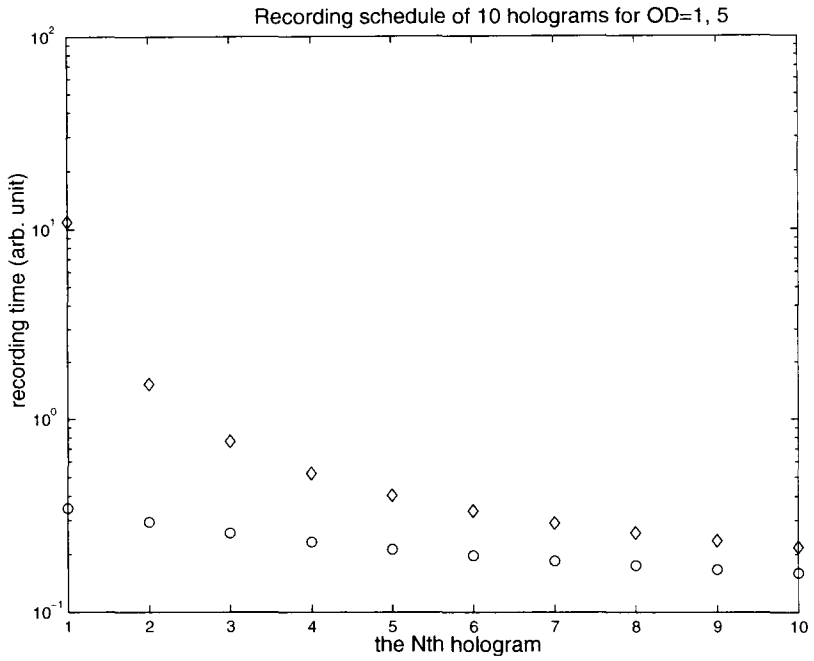

Figure 5.6: The recording schedule of 10 equalized holograms for OD=1 or 5.

where 10 holograms are multiplexed with equal diffraction efficiencies inside the material of optical density $OD = 1$ or 5.

When the optical density is small, the recording time for each hologram is similar and the grating strength is uniform inside the material, which also matches the assumption of the theoretical approximation model. As the optical density getting larger, the extra part of the dynamic range is peeled off during recording of first hologram with extra long exposure time, as shown in Fig. 5.6 for $OD = 5$. All the gratings are finally located near a limited space near the end surface of the material in Fig. 5.7, and the rest of the material was bleached uniformly without effective grating strength recorded.

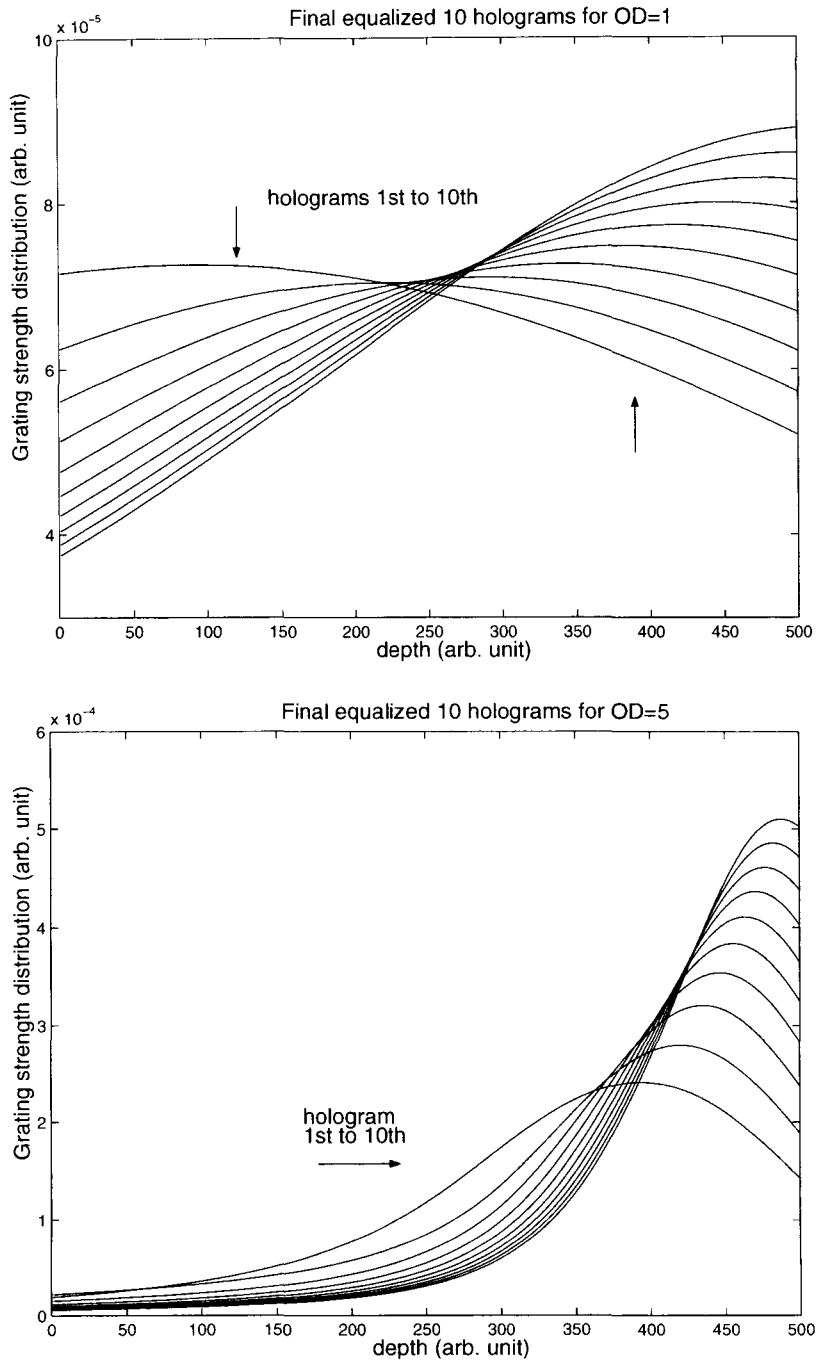

Figure 5.7: The grating strength distribution of 10 holograms with equal diffraction efficiency inside the material with OD =1 or 5, $B = 0$.

In most practical materials used for spectral hole burning, there is always a non-burnable part of the absorption B due to the broad phonon wing and a large Debye-Waller factor [84]. For $B = 50\%\,\alpha_0$ in Fig. 5.5, the numerically simulated $M\#$ is consistent with the theoretical approximation model as $OD \leq 1$, and then getting smaller when OD getting larger. Simulation in Fig. 5.5 shows that $M\#$ reaches a maximum 0.043 at optical density $OD = 1.1$, which is slightly smaller than the theoretical maximum prediction $M\# = 0.05$ at $OD = 1.52$.

The independence of $M\#$ on the number of holograms M is also confirmed in the simulation of the dynamic recording. Fig. 5.8 shows $M\#$ for recording $M = 2, 5, 10$ or

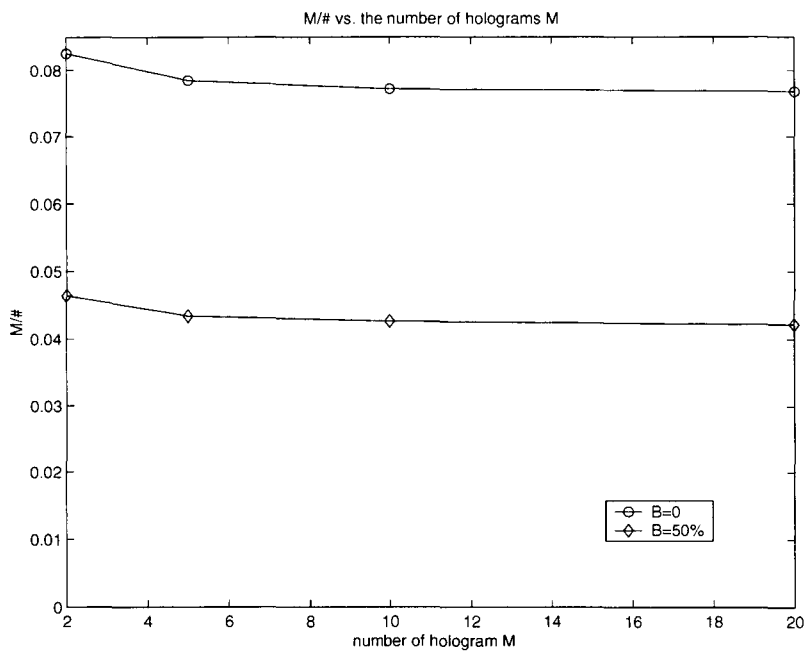

Figure 5.8: $M\#$ for absorption holograms as a function of the number of holograms in materials of normalized optical densities $OD = 0.5$, $B = 0$ and $OD = 1.0$, $B = 0.5\,\alpha_0$, $(\lambda_{write} = \lambda_{read})$.

20 holograms in the absorption material with normalized optical density $OD = 0.5$, $B = 0$ or $OD = 1$, $B = 0.5\,\alpha_0$. When the number of hologram M is getting larger than 10, $M\#$ becomes a constant, and consistent with the prediction from the theoretical model.

For the Π-index grating of nonuniform grating distribution, $M\#$s are numerically simulated and compared with the simulated absorption gratings in Fig. 5.9. With the

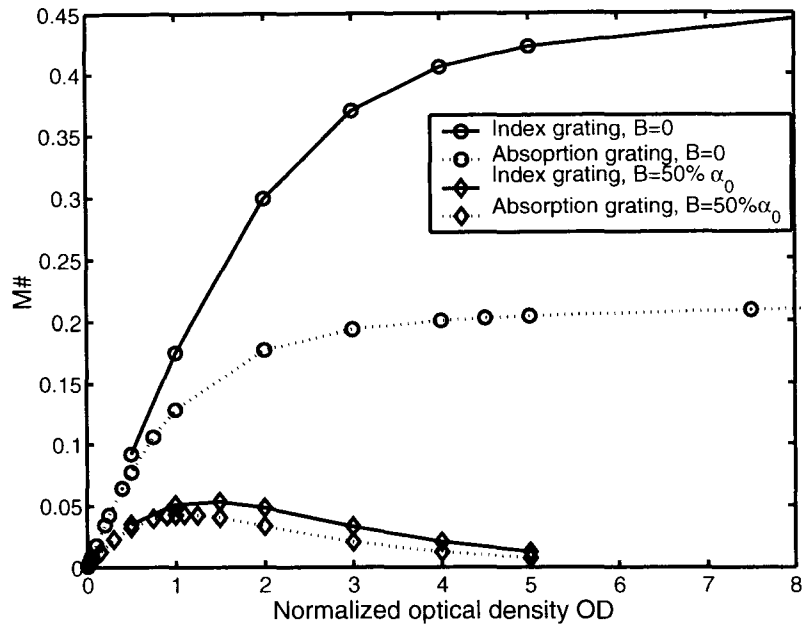

Figure 5.9: Comparison of $M\#$ for Π-index holograms and pure absorption holograms by dynamic numerical simulation. The normalized optical density $OD = \frac{\alpha_0 d}{\cos\theta}$, and $\alpha_0 = A + B$.

same dependency on the normalized optical density OD as the absorption gratings, $M\#$ of index grating saturates at 0.5 for $OD > 10$ if $B = 0$. For $B = 50\%\,\alpha_0$, $M\#$ of Π-index gratings has a maximum of 0.053 at $OD = 1.5$. Under both conditions, the $M\#$s of index gratings is larger than those of pure absorption gratings. The simulated results of $M\#$ ratio between Π-index and absorption gratings are shown in Fig. 5.4. Compared with the results of theoretical approximation model, the theoretical model gives correct prediction when the optical density is small. When the optical density is larger, the simulation results indicate that $M\#$ of Π-index hologram is larger than the pure absorption by only factor of two, which also depends on the residual absorption constant B.

5.4 Couple wave theory for nonuniform grating

From the coupled wave theory by Kogelnik [67], the diffraction efficiency of a uniform non-slant transmission grating is given as η,

$$\eta(t) = \exp\left(\frac{-2\alpha_0 d}{\cos\theta}\right)\left[\sinh^2\left(\frac{\alpha_1 d}{2\cos\theta}\right) + \sin^2\left(\frac{\beta_1 d}{2\cos\theta}\right)\right], \tag{5.31}$$

where the average absorption constant α_0, the phase and absorption grating β_1, α_1 are uniform constants throughout the thickness d of the medium. Now we are considering a nonuniform distribution along the depth direction $\hat{\boldsymbol{z}}$ for transmission geometry: $\alpha_0(z)$, $\beta_1(z)$, and $\alpha_1(z)$.

Following the derivation in coupled wave theory [67], the coupling constant $\kappa(z) = (\beta_1(z) - j\alpha_1(z))/2$, where $\beta_1(z) = 2\pi n_1(z)/\lambda$, and assuming the propagating modes in the grating are the superposition of two waves,

$$E = R(z)e^{-j\boldsymbol{\varrho}\cdot\boldsymbol{x}} + S(z)e^{-j\boldsymbol{\delta}\cdot\boldsymbol{x}}, \tag{5.32}$$

where the propagation vector of diffraction $\boldsymbol{\delta}$ is determined by the reference beam $\boldsymbol{\varrho}$ and the grating vector $\boldsymbol{K}$ by

$$\boldsymbol{\delta} = \boldsymbol{\varrho} - \mathbf{K}. \tag{5.33}$$

Substitute it into the wave equation inside the grating medium and neglecting the second order differentials: R'' and S'', we will get the same coupled equations as Kogelnik's coupled wave theory [67], except the depth dependency of the couple constant,

$$c_R R' + \alpha_0(z)R = -j\kappa(z)S \tag{5.34}$$

$$c_S S' + (\alpha_0 + j\vartheta)S = -j\kappa(z)R, \tag{5.35}$$

where the dephasing factor ϑ defined in Kogelnik's paper is zero for Bragg phase-

matching condition, and the coefficients c_R, c_S determine the incident angle of reference and signal beam.

To solve these coupled wave equations, we have to assume a more general solution rather than the assumption in Kogelnik's paper as

$$R(z) = r_1 e^{\gamma_1(z)} + r_2 e^{\gamma_2(z)} \tag{5.36}$$

$$S(z) = s_1 e^{\gamma_1(z)} + s_2 e^{\gamma_2(z)}, \tag{5.37}$$

where the r_i and s_i are constants depending on the boundary conditions. Substitute the solution (5.37) into the coupled equations (5.35) and find the solutions for $\gamma_i(z)$:

$$\begin{aligned}\gamma_{1,2}(z) = \int_0^z d\tau \{ & -\frac{1}{2}\left(\frac{\alpha_0(\tau)}{c_R} + \frac{\alpha_0(\tau)}{c_S} + j\frac{\vartheta}{c_S}\right) \\ & \pm\frac{1}{2}\left[\left(\frac{\alpha_0(\tau)}{c_R} - \frac{\alpha_0(\tau)}{c_S} - j\frac{\vartheta}{c_S}\right)^2 - 4\frac{\kappa(\tau)^2}{c_R c_S}\right]^{\frac{1}{2}}\}.\end{aligned} \tag{5.38}$$

This equation (5.38) and equation (5.37) with the consideration of boundary conditions give the general solution for the coupled wave equations of nonuniform grating absorption and grating along the depth direction $\hat{z}$. For the special cases of uniform gratings throughout the depth, equation (5.38) gives the same results shown in [67]. It can be simplified for the special case of non-slant ($c_R = c_S = cos\theta_0$) transmission geometry and Bragg incidence ($\vartheta = 0$), which we are interested in, as

$$\gamma_{1,2}(z) = \int_0^z d\tau \left(-\frac{\alpha_0(\tau)}{cos\theta_0} \pm \frac{j\beta_1(\tau) + \alpha_1(\tau)}{2cos\theta_0}\right), \tag{5.39}$$

$$\begin{aligned}\eta(t) = \exp\left(\int_0^d \frac{-2\alpha_0(\tau,t)}{\cos\theta_0} d\tau\right) & \left[\sinh^2\left(\int_0^d \frac{\alpha_1(\tau,t)}{2\cos\theta_0} d\tau\right)\right. \\ & \left. + \sin^2\left(\int_0^d \frac{\beta_1(\tau,t)}{2\cos\theta_0} d\tau\right)\right].\end{aligned} \tag{5.40}$$

5.5 Experimental measurement

In all previous experimental works on spectral hole burning [14, 100, 84], only the frequency domain is explored for multiplexing holograms. Here, we demonstrate the conventional angle multiplexing of holograms in the spectral hole burning material and compare the experimental results with our theoretical investigation. Our experiment setup is shown in Fig 5.10. The material used in our experiments is a 400 μm

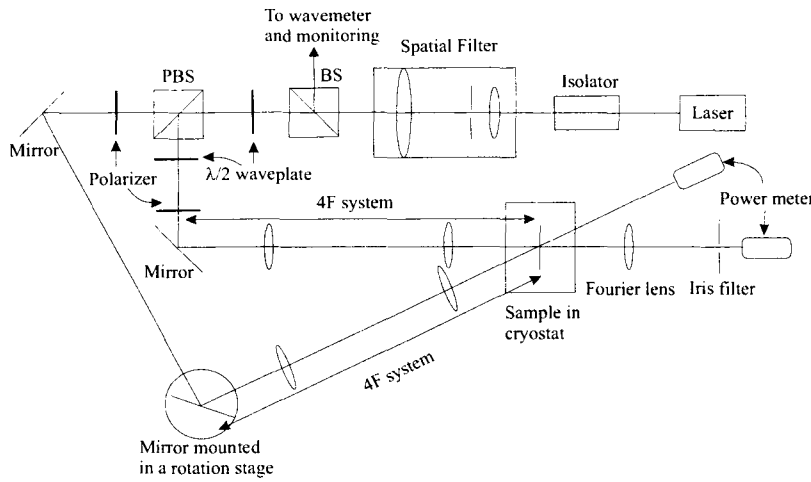

Figure 5.10: Experimental setup for spectral hole burning.

thick sample of H_2TBN with a concentration of 5×10^{-5} mol/l polyvinyl butyral (PVB) cooled down to 2.0 Kelvin by liquid helium in a cryostat. The absorption constant bleaching kinetics is measured in Fig. 5.11 by a bleaching intensity of 10 $\mu W/cm^2$. The normalized amplitude nonburnable optical density $\frac{Bd}{\cos\theta} \simeq 0.67$ and the material dynamic range of the bleachable optical density $\frac{Ad}{\cos\theta} \simeq 0.35$. The numerical simulation of $M\#$ predicts $M\# \simeq 0.025$, as shown in the inset of Fig 5.11.

Single plane wave holograms are recorded at different wavelengths with both the reference and the signal intensity of 10 $\mu W/cm^2$. Fig. 5.12 shows the reading curves of the single plane wave hologram with the unattenuated original reference beam. The hologram diffraction efficiency decreases fast during readout process because of the bleaching by reference beam. In addition, the oscillation of the bulky cryostat makes it difficult to get consistent grating growth curves. However, a diffraction efficiency of 1×10^{-4} can be consistently obtained. The optimal recording time lies

between 5 – 8 seconds. Fig. 5.13 shows the measured selectivity curve without using the iris filter (Fig. 5.10). The selectivity is about 0.6 degree and agrees with the theoretical result well. The data is very noisy due to the scattering from the sample. An additional iris filter in Fig. 5.10 is used at the back focal plane of the Fourier lens behind the sample to reduce the scattering and background noise. For thin material, if the reference beam angle is changed slightly, the reconstructed signal beam angle is changed accordingly and can get partially blocked by the iris filter. The filter gives us a combined effect of both angle and peristrophic selectivity. The selectivity curve with the iris filter is shown in Fig. 5.14 . A selectivity of about 0.2 degree is obtained, which is consistent with the iris diameter of about 1 mm and the Fourier lens focal length of about 24 cm.

Three, five, seven and ten plane wave holograms are then multiplexed and the comb functions are shown in Fig. 5.15. We have used equal time (1s – 2s) exposure schedule, instead of the optimal exposure from simulation for maximal diffraction efficiency. Fig. 5.16 shows the measured $M\#$ of each case. As we multiplex 3,5,7 and 10 holograms, $M\#$ has a trend to increase, and is about 0.01, which is smaller than the simulated $M\# = 0.025$. There are two possible reasons for the factor of 2 – 3 difference. First, the exposure time is not optimized for the number of holograms in the experiments. Second, the oscillation of the cryostat and erasure of the holograms during the measurement leads to a smaller measured $M\#$.

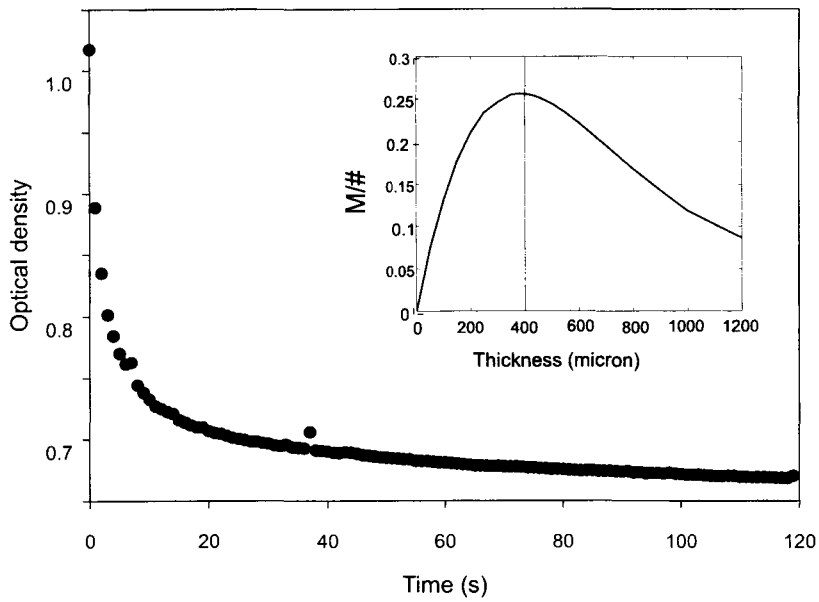

Figure 5.11: Experimental absorption kinetics and the prediction of $M\#$ by numerical simulation.

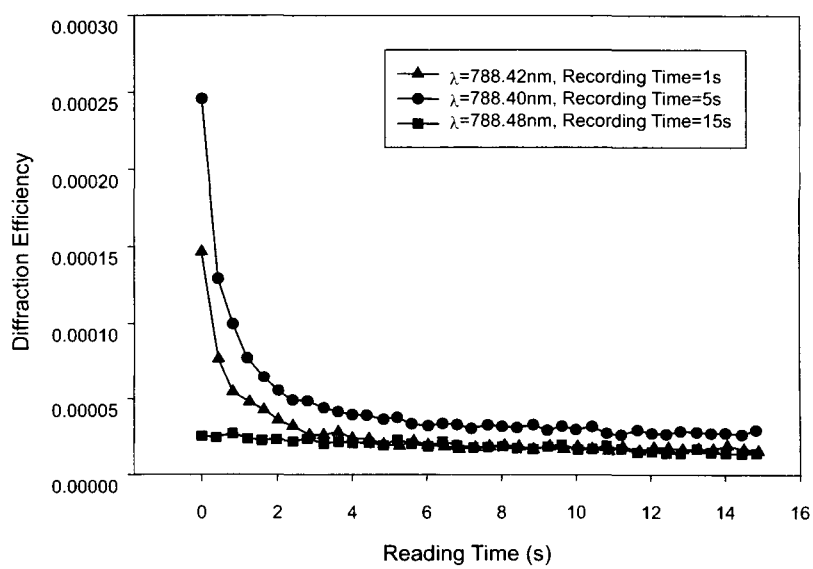

Figure 5.12: Hologram reading curve by a plane wave .

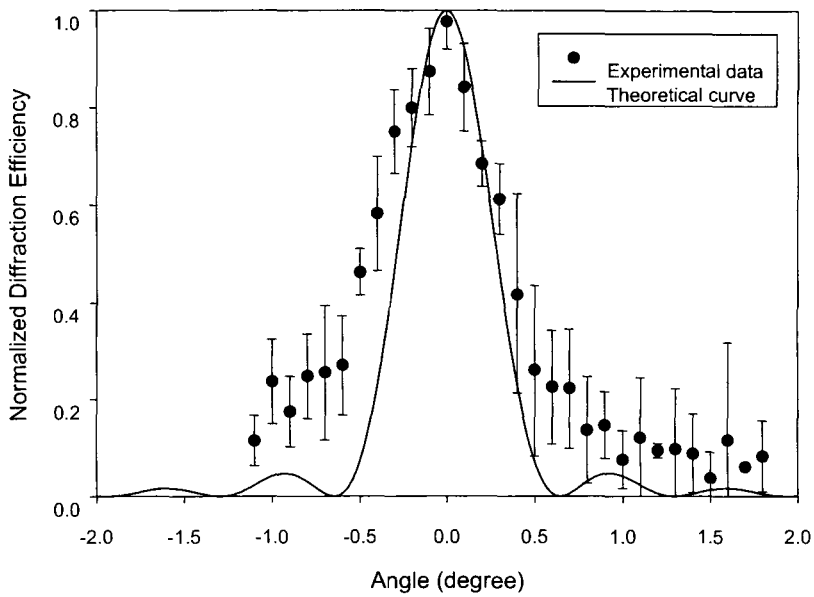

Figure 5.13: Angle selectivity without the iris filter.

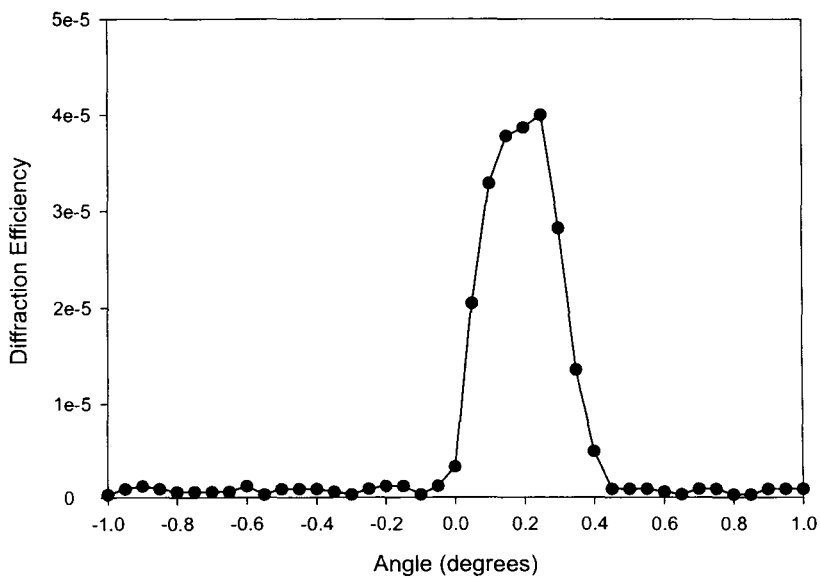

Figure 5.14: Angle selectivity with the iris filter.

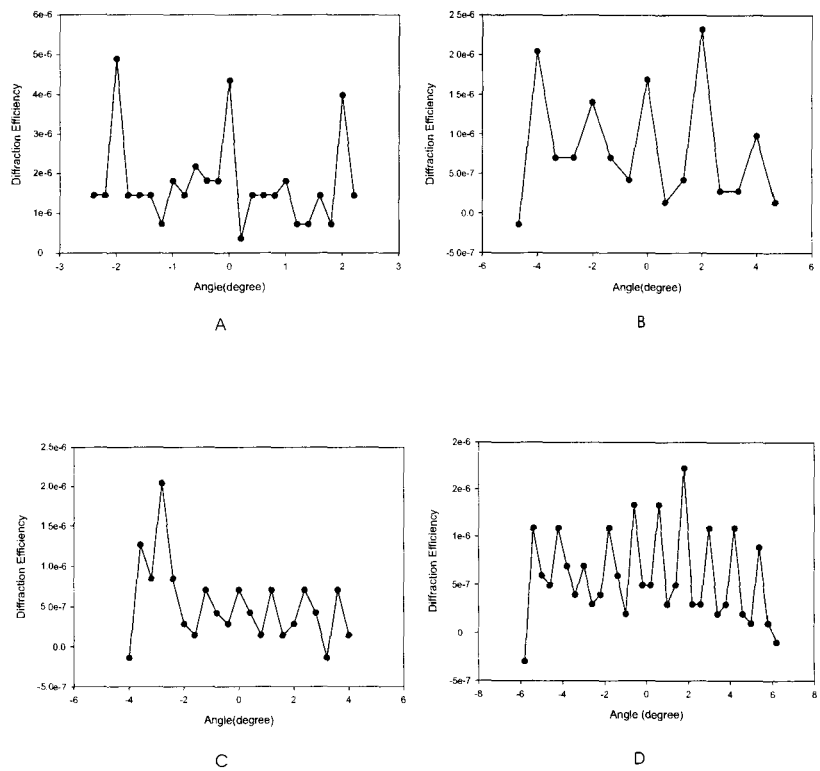

Figure 5.15: Multiplexing $3(A), 5(B), 7(C)$, and $10(D)$ plane wave holograms in spectral hole burning material.

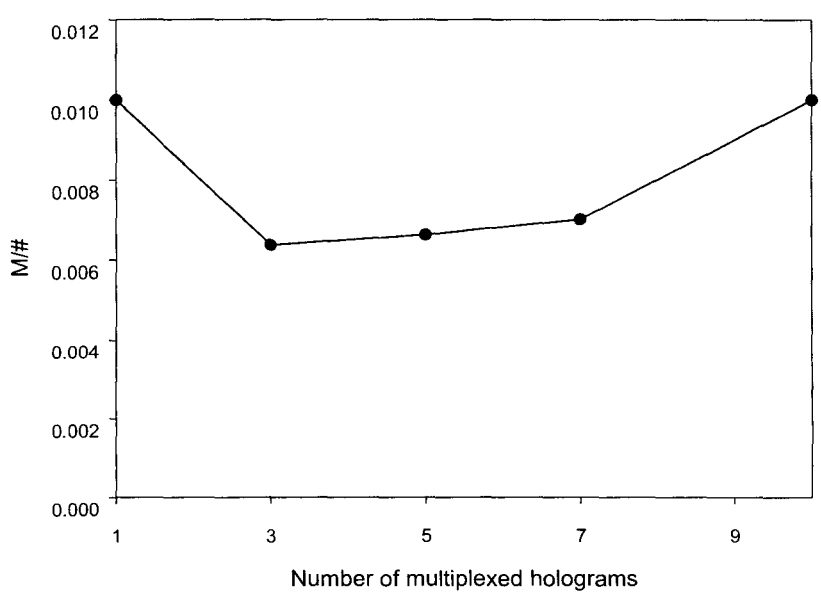

Figure 5.16: Experimentally measured $M\#$.

Bibliography

[1] *The national technology roadmap for semiconductors*, Tech. report, Semiconductor Industry Association, 1997.

[2] A. Adibi, *Persistent holographic storage in photorefractive crystals*, Ph.D. thesis, California Institute of Technology, 2000.

[3] G. B. Airy, Trans. Camb. Phil. Soc. **5** (1835), 283.

[4] L. Allen and J. H. Eberly, *Optical Resonance and Two-level Atoms*, Wiley, New York, 1975.

[5] X. An and D. Psaltis, *Thermal fixing of 10,000 holograms in $LiNbO_3$:Fe*, OSA Annual Meeting, Paper MAAA5 (Rochester, NY), 1996.

[6] X. An, D. Psaltis, and G. W. Burr, *Thermal fixing of 10,000 holograms in $LiNbO_3$:Fe*, Appl. Opt. **38** (1999), no. 2, 386–393.

[7] G. Barbastathis, *Intelligent holographic databases*, Ph.D. thesis, California Institute of Technology, 1998.

[8] G. Barbastathis, M. Balberg, and D. J. Brady, *Confocal microscopy with a volume holographic filter*, Opt. Lett. **24** (1999), no. 12, 811–813.

[9] G. Barbastathis and D. J. Brady, *Multidimensional tomographic imaging using volume holography*, Proc. IEEE **87** (1999), no. 12, 2098–2120.

[10] G. Barbastathis, M. Levene, and D. Psaltis, *Shift multiplexing with spherical reference waves*, Appl. Opt. **35** (1996), 2403–2417.

[11] G. Barbastathis and D. Psaltis, *Shift-multiplexed holographic memory using the two-lambda method*, Opt. Lett. **21** (1996), no. 6, 429–431.

[12] J. M. Barker and J. A. Liburdy, *Directionally sensitive double-pulses holographic particle velocimetry*, Laser Anemometry **229** (1995), 45–49.

[13] D. H. Barnhart, R. J. Adrian, and G. C. Papen, *Phase-conjugate holographic system for high-resolution particle image velocimetry*, Appl. Opt. **33** (1994), 7159–7170.

[14] S. Bernet, S B. Altner, F. R. Graf, E. Maniloff, A. Renn, and U. P Wild, *Frequency and phase swept holograms in spectral hole-burning materials*, Appl. Opt. **34** (1995), no. 22, 4674–4684.

[15] E. Betzig and R. J. Chichester, *Single molecules observed by near-field scanning optical microscopy*, Science **262** (1993), 1422–1425.

[16] M. Born and E. Wolf, *Principles of Optics*, 6 ed., Cambridge University Press, 1980.

[17] D. Brady and D. Psaltis, *Control of volume holograms*, J. Opt. Soc. Am. A **9** (1992), no. 7, 1167–1182.

[18] D. J. Brady and D. Psaltis, *Holographic interconnections in photorefractive wave-guides*, Appl. Opt. **30** (1991), no. 17, 2324–2333.

[19] G. Burr, *Volume holographic storage using the* 90° *geometry*, Ph.D. thesis, California Institute of technology, 1996.

[20] G. W. Burr, H. Coufal, J. A. Hoffnagle, C. M. Jefferson, M. Jurich, B. Marcus, and R. M. Macfarlane, *Optical data storage enters a new dimension*, Physics World **13** (2000), no. 7, 37–42.

[21] G. W. Burr and D. Psaltis, *Effect of the oxidation state of linbo:Fe on the diffraction efficiency of multiple holograms*, Opt. Lett. **21** (1996), no. 12, 893–895.

[22] K. Buse, A. Adibi, and D. Psaltis, *Non-volatile holographic storage in doubly doped lithium niobate crystals*, Nature **393** (1998), no. 6686, 665–668.

[23] A. Bruce Carlson, *Communication Systems*, 3 ed., McGraw-Hill Book Company, 1986.

[24] E. B. Champagne, *Nonparaxial imaging, magnification, and aberration properties in holography*, J. Opt. Soc. Am. **57** (1967), 51–55.

[25] ———, *Resolution in holography*, Appl. Opt. **8** (1969), 1879.

[26] W. W. Chow, K. D. Choquette, M. H. Crawford, K. L. Lear, and G. R. Hadley, *Design, fabrication, and performance of infrared and visible vertical-cavity surface-emitting lasers*, IEEE Journal of Quantum Electronics **33** (1997), no. 10, 1810–1824.

[27] E. Chuang, *Methods and architecture for rewritable holographic memories*, Ph.D. thesis, California Institute of Technology, 1998.

[28] E. Chuang and D. Psaltis, *Storage of 1000 holograms with use of a dual-wavelength methoid*, Appl. Opt. **36** (1997), no. 32, 8445–8454.

[29] A. Corney, *Atomic and laser spectroscopy*, Clarendon Press, Oxford, 1977.

[30] L. K. Cotter, T. J. Drabik, R. J. Dillon, and M. A. Handschy, *Ferroelectric-liquid-crystal/silicon-integrated-circuit spatial light modulator*, Opt. Lett. **15** (1990), no. 5, 291–293.

[31] K. Curtis, A. Pu, and D. Psaltis, *Method for holographic storage using peristropic multiplexing*, Opt. Lett. **19** (1994), no. 13, 993–994.

[32] H. de Vries and D. A. Wiersma, *Photophysical and photochemical molecular hole burning theory*, J. Chem. Phys. **72** (1980), no. 3, 1851–1863.

[33] H. Debregeas-Sillard, A. Vuong, F. Delorme, J. David, V. Allard, A. Bodere, O. LeGouezigou, F. Gaborit, J. Rotte, M. Goix, V. Voiriot, and J. Jacquet, *DBR module with 20-mw constant coupled output power, over 16 nm (40 × 50-ghz spaced channels)*, IEEE Photonics Technology Letters **13** (2001), no. 1, 4–6.

[34] R. C. Desai, M. D. Levenson, and J. A. Barker, *Forced rayleigh-scattering - thermal and acoustic effects in phase-conjugate wave-front generation*, Phys. Rev. A **27** (1983), no. 4, 1968–1976.

[35] R. DeVre, J. F. Heanue, K. Gurkan, and L. Hesselink, *Transfer functions based on bragg detuning effects for image-bearing holograms recorded in photorefractive crystals*, J. Opt. Soc. Am. A **13** (1996), no. 7, 1331–1344.

[36] A. Diaspro, S. Annunziata, M. Raimondo, P. Ramoino, and M. Robello, *A single-pinhole confocal laser scanning microscope for 3-d imaging of biostructures*, IEEE Engineering in Medicine and Biology Magazine **18** (1999), no. 4, 106–110.

[37] J.-J. P. Drolet, G. Barbastathis, J. S. Patel, and D. Psaltis, *Liquid crystal devices for volume holographic memories*, OSA Annual Meeting (Portland, OR), September 1995.

[38] J.-J. P. Drolet, G. Barbastathis, and D. Psaltis, *Optoelectronic interconnects and packaging*, SPIE Critical Reviews, Vol. CR62, 1996, pp. 106–131.

[39] J.-J. P. Drolet, E. Chuang, G. Barbastathis, and D. Psaltis, *Compact, integrated dynamic holographic memory with refreshed holograms*, Opt. Lett. **22** (1997), no. 8, 552–554.

[40] J.-J. P. Drolet, E. Chuang, G. Barbastathis, and D. Psaltis, *Compact, integrated dynamic holographic memory with refreshed holograms*, Opt. Lett. **22** (1997), no. 8, 552–554.

[41] J. P. Drolet, J. Patel, K. G. Haritos, W. Xu, A. Scherer, and D. Psaltis, *Hybrid–aligned nematic liquid-crystal modulators fabricated on VLSI circuits*, Opt. Lett. **20** (1995), no. 21, 2222–2224.

[42] B. Dubik, J. Masajada, J. Nowak, and M. Zajac, *Aberrations of holographic lenses in image quality evaluation*, Opt. Eng. **31** (1992), no. 3, 478–490.

[43] D. A. Eastham, *Atomic physics of lasers*, Taylor & Francis, London and Philadelphia, 1986.

[44] A. Elschner and H. Bassler, *Kinetics of growth and decay of spectral holes in a tetracene-doped mthf glass*, Chem. Phys. **123** (1988), no. 2, 305–315.

[45] Z. O. Feng and K. Sayano, *Compact read-only memory with lensless phase-conjugate holograms*, Opt. Lett. **21** (1996), no. 16, 1295–1297.

[46] D. Gabor, *A new microscope principle*, Nature **161** (1948), 777–778.

[47] ———, *Microscopy by reconstructed wavefronts*, Proceeding of the Royal Society A **197** (1949), 454–487.

[48] ———, *Microscopy by reconstructed wavefronts II*, Proceeding of the Royal Society B **64** (1951), 449.

[49] ———, *Associative holographic memories*, IBM J. Res. Dev. **13** (1969), 156–159.

[50] J. W. Goodman, *Introduction to Fourier Optics*, second ed., McGraw-Hill, New York, 1996.

[51] M. Gower and D. Proch, *Optical phase conjugation*, Springer-Verlag, New York, 1994.

[52] M. C. Gower, *Phase conjugation*, J. Mod. Optic. **35** (1988), no. 3, 449–472.

[53] M. C. Gower and P. Hribek, *Mechanisms for internally self-pumped phase-conjugate emission from $BaTiO_3$ crystals*, J. Opt. Soc. Am. B **5** (1988), no. 8, 1750–1757.

[54] C. Gu, J. Hong, H. Y. Li, D. Psaltis, and P. Yeh, *Dynamics of grating formation in photovoltaic media*, Journal of Applied Physics **69** (1991), no. 3, 1167–1172.

[55] J. F. Heanue, M. C. Bashaw, and L. Hesselink, *Recall of linear combinations of stored data pages based on phase–code multiplexing in volume holography*, Opt. Lett. **19** (1994), no. 14, 1079–1081.

[56] B. Herman and J. J. Lemasters, *Optical Microscopy*, Academic Press, 1993.

[57] T. Hirata, M. Maeda, M. Suehiro, and H. Hosomatsu, *Fabrication and characteristics of gaas-algaas tunable laser-diodes with dbr and phase-control sections integrated by compositional disordering of a quantum-well*, IEEE Journal of Quantum Electronics **27** (1991), no. 6, 1609–1615.

[58] P. R. Hobson and J. Watson, *Accurate three-dimensional metrology of underwater objects using replayed real images from in-line and off-axis holograms*, Meas. Sci. Technol. **10** (1999), 1153–1161.

[59] J. H. Hong, I. McMichael, T. Y. Chang, W. Christian, and E. G. Paek, *Volume holographic memory-systems: Techniques and architectures*, Optical Engineering **34** (1995), no. 8, 2193–2203.

[60] G. Isenberg, *Modern Optics, Electronics, and High Precision techniques in Cell Biology*, Springer, 1998.

[61] R. Jankowiak, L. Shu, M.J Kinney, and G.J Small, *Dispersive kinetic processes, optical linewidths and dephasing in amorphous solids*, J. Lum. **36** (1987), no. 4-5, 293–305.

[62] B. Javidi and E. Tajahuerce, *Three-dimensional object recognition by use of digital holography*, Opt. Lett. **25** (2000), no. 9, 610–612.

[63] J. L. Jewell, K. F. Huang, K. Tai, Y. H. Lee, R. J. Fischer, S. L. Mccall, and A. Y. Cho, *Vertical cavity single quantum well laser*, Applied Physics Letters **55** (1989), no. 5, 424–426.

[64] K. M. Johnson, D. J. McKnight, and I. Underwood, *Smart spatial light modulators using liquid crystal on silicon*, IEEE Journal of Quantum Electronics **29** (1993), no. 2, 699–714.

[65] N. V. Joshi and H. Medina, *Multiple beam interference confocal microscopy: Tool for morphological investigation of a living spermatozoon*, Microscopy and Microanalysis **6** (2000), no. 5, 471–477.

[66] Y. Kitaoka, T. Yokoyama, K. Mizuuchi, and K. Yamamoto, *Miniaturized blue laser using second harmonic generation*, Japanese Journal of Applied Physics part 1-regular papers short notes & review papers **39** (2000), no. 6A, 3416–3418.

[67] H. Kogelnik, *Coupled wave theory for thick hologram gratings*, Bell Syst. Tech. J. **48** (1969), no. 9, 2909–2947.

[68] N. V. Kukhtarev, *Kinetics of hologram recording and erasure in electrooptic crystals*, Soviet Technical Physics Letters **2** (1976), no. 12, 438–440.

[69] N. V. Kukhtarev, V. B. Markov, S. G. Odulov, M. S. Soskin, and V. L. Vinetskii, *Holographic storage in electrooptic crystals. I. Steady state*, Ferroelectrics **22** (1979), 949–960.

[70] H. Külich, *Reconstructing volume holograms without image field losses*, Appl. Opt. **30** (1991), no. 20, 2850–2857.

[71] H. Lee, X.-G. Gu, and D. Psaltis, *Volume holographic interconnections with maximal capacity and minimal cross talk*, Journal of Applied Physics **65** (1989), no. 6, 2191–2194.

[72] E. N. Leith, A. Kozma, J. Upatnieks, J. Marks, and N. Massey, *Holographic data storage in three-dimensional media*, Appl. Opt. **5** (1966), no. 8, 1303–1311.

[73] E. N. Leith and G. J. Swanson, *Holographic aberration compensation with partially coherent-light*, Opt. Lett. **7** (1982), no. 12, 596–598.

[74] E. N. Leith and J. Upatnieks, *Wavefront reconstruction with diffused illumination and three–dimensional objects*, Journal of the Optical Society of America **54** (1964), 1295–1301.

[75] M. Levene, *Optics in neural computation*, Ph.D. thesis, California Institute of Technology, 1998.

[76] M. Levene, G. J. Steckma, and D. Psaltis, *Method for controlling the shift invariance of optical correlators*, Appl. Opt. **38** (1999), no. 2, 394–398.

[77] M. D. Levenson, *The applications of phase conjugate wavefront generation to fine line lithography*, Appl. Phys. B **28** (1982), no. 2-3, 206–206.

[78] ———, *Photolithography experiments using forced rayleigh-scattering*, J. Appl. Phys. **54** (1983), no. 8, 4305–4313.

[79] H.-Y. S. Li and D. Psaltis, *Three dimensional holographic disks*, Appl. Opt. **33** (1994), no. 17, 3764–3774.

[80] H.-Y. S. Li, Y. Qiao, and D. Psaltis, *Optical network for real-time face recognition*, Appl. Opt. **32** (1993), no. 26, 5026–5035.

[81] E. S. Maniloff, S. B. Altner, S. Bernet, F. R. Graf, A. Renn, and U. P. Wild, *Recording of 6000 holograms by use of spectral hole burning*, Appl. Opt. **34** (1995), no. 20, 4140–4048.

[82] B. Matsumoto, *Methods in Cell Biology*, Academic Press, Inc., 1993.

[83] R. W. Meier, *Magnification and third-order aberrations in holography*, J. Opt. Soc. Am. **55** (1965), 987–992.

[84] A. J. Meixner, A. Renn, and U.P. Wild, *Spectral hole-burning and holography. I. Transmission and holographic detection of spectral holes*, J. Chem. Phys. **91** (1989), 6728–6736.

[85] J. Michaells, C. Hettich, J. Mlynek, and V. Sandoghdar, *Optical microscopy using a single-molecule light source*, Nature **405** (2000), 325–327.

[86] F. Micheron and G. Bismuth, *Field and time thresholds for the electrical fixation of holograms recorded in* $(Sr_{0.75}Ba_{0.25})Nb_2O_6$ *crystal*, Appl. Phys. Lett. **23** (1972), no. 2, 71–72.

[87] K. Mizuuchi, K. Yamamoto, and M. Kato, *Harmonic blue light generation in x-cut* $MgO{:}LiNbO_3$ *waveguide*, Electronics Letters **33** (1997), no. 9, 806–807.

[88] M. G. Moharam and L. Young, *Hologram writing by the photorefractive effect*, Journal of Applied Physics **48** (1977), no. 8, 3230–3236.

[89] ———, *Recording and optical erasure of holograms stored by the photorefractive effect in lithium niobate*, Appl. Opt. **17** (1978), no. 17, 2773–2778.

[90] F. H. Mok, *Angle-multiplexed storage of 5000 holograms in lithium niobate*, Opt. Lett. **18** (1993), no. 11, 915–917.

[91] F. H. Mok, G. W. Burr, and D. Psaltis, *System metric for holographic memory systems*, Opt. Lett. **21** (1996), no. 12, 896–898.

[92] F. H. Mok, D. Psaltis, and G. W. Burr, *Spatially– and Angle– multiplexed holographic random access memory*, SPIE Proceedings **1773c** (1992), 1.

[93] F.H. Mok, G.W. Burr, and D. Psaltis, *System metric for holographic memory systems*, Opt. Lett. **21** (1996), no. 12, 896–898.

[94] Inc. Molecular Probes, *Handbook of Fluorescent Probes and Research Chemicals*, 7 ed., http:www.probes.com, 2001.

[95] C. Moser, *Optical information processing in crystals and polymers. Three dimensional wavefront sensors*, Ph.D. thesis, California Institute of Technology, 2001.

[96] C. Moser, I. Maravic, B. Schupp, A. Adibi, and D. Psaltis, *Diffraction efficiency of localized holograms in doubly doped $LiNbO_3$ crystals*, Opt. Lett. **25** (2000), no. 17, 1243–1245.

[97] C. Moser, B. Schupp, and D. Psaltis, *Localized holographic recording in doubly doped lithium niobate*, Opt. Lett. **25** (2000), no. 3, 162–164.

[98] J. Nowak and M. Zajac, *Numerical investigations of holographic imaging quality*, Opt. Appl. **15** (1985), no. 3, 239–248.

[99] W. Phillips and D. L. Staebler, *Control of the Fe^{2+} concentration in iron-doped lithium niobate*, Journal of Electronic Materials **3** (1974), no. 2, 601–617.

[100] B. Plagemann, F. R. Graf, S. B. Altner, A. Renn, and U.P. Wild, *Exploring the limits of optical storage using persistent spectral hole-burning: holographic recording of 12,000 images*, Appl. Phys. B **66** (1998), 67–74.

[101] D. Psaltis, *Parallel optical memories*, Byte **17** (1992), no. 9, 179.

[102] D. Psaltis, D. Brady, and K. Wagner, *Adaptive optical networks using photorefractive crystals*, Appl. Opt. **27** (1988), no. 9, 1752–1759.

[103] D. Psaltis, D. Brady, X. G. Xu, and S. Lin, *Holography in artificial neural networks*, Nature **343** (1990), no. 6256, 325–330.

[104] D. Psaltis and G. W. Burr, *Holographic data storage*, Computer **31** (1998), no. 2, 52.

[105] ———, *Holographic data-storage*, Computer **31** (1998), no. 2, 52–60.

[106] D. Psaltis, X. G. Gu, and D. Brady, *Fractal sampling grids for holographic interconnections*, SPIE–963, 1988.

[107] D. Psaltis, M. Levene, A. Pu, G. Barbastathis, and K. Curtis, *Holographic storage using shift multiplexing*, Opt. Lett. **20** (1995), no. 7, 782–784.

[108] D. Psaltis and F. Mok, *Holographic memories*, Scientific American **273** (1995), no. 5, 70–76.

[109] D. Psaltis and Y. Qiao, *Adaptive multilayer optical networks*, Progress in Optics **31** (1993), 227–261.

[110] A. Pu, R. Denkewalter, and D. Psaltis, *Real-time vehicle navigation using a holographic memory*, Optical Engineering **36** (1997), no. 10, 2737–2746.

[111] A. Pu and D. Psaltis, *High-density recording in photopolymer-based holographic 3-dimensional disks*, Appl. Opt. **35** (1996), no. 14, 2389–2398.

[112] G. A. Rakuljic, V. Leyva, and A. Yariv, *Optical data storage by using orthogonal wavelength–multiplexed volume holograms*, Opt. Lett. **17** (1992), no. 20, 1471–1473.

[113] A. Renn and U. P. Wild, *Spectral hole burning and hologram storage*, Appl. Opt. **26** (1987), 4040–4041.

[114] J. Rosen, M. Segev, and A. Yariv, *Wavelength–multiplexed computer–generated volume holography*, Opt. Lett. **18** (1993), no. 9, 744–746.

[115] D. K. Serkland, K. D. Choquette, G. R. Hadley, K. M. Geib, and A. A. Allerman, *Two-element phased array of antiguided vertical-cavity lasers*, Appl. Phys. Lett. **75** (1999), no. 24, 3754–3756.

[116] K. Sholes and P. V. Farrell, *Optical alignment-induced errors in holographic particle image velocimetry*, Appl. Opt. **39** (2000), no. 31, 5685–5693.

[117] O. Sild and K. Haller, *Zero-Phonon Lines and Spectral Hole Burning in Spectroscopy and Photochemistry*, Springer-Verlag, New York, 1988.

[118] L. Solymar and D. J. Cooke, *Volume holography and volume gratings*, Academic Press, Inc., 1981.

[119] A. Stadelmaier and J. H. Massig, *Compensation of lens aberrations in digital holography*, Opt. Lett. **25** (2000), no. 22, 1630–1632.

[120] M. R. Taghizadeh, P. Blair, B. Layet, I. M. Barton, A. J. Waddie, and N. Ross, *Design and fabrication of diffractive optical elements*, Microelectronic Engineering (1997), no. 3-4, 219–242.

[121] H. Talon, M. Orrit, and J. Bernard, *Model for burning kinetics and shape of fluence-saturated spectral holes*, Chem. Phys. **140** (1990), no. 1, 177–185.

[122] K. L. Tan, W. A. Crossland, and R. J. Mears, *Dynamic holography for optical interconnections. I. Noise floor of low-cross-talk holographic switches*, J. Opt. Soc. Am. A **18** (2001), no. 1, 195–204.

[123] K. L. Tan, S. T. Warr, I. G. Manolis, T. D. Wilkinson, M. M. Redmond, W. A. Crossland, R. T. Mears, and B. Robertson, *Dynamic holography for optical interconnections. II. Routing holograms with predictable location and intensity of each diffraction order*, J. Opt. Soc. Am. A **18** (2001), no. 1, 205–215.

[124] J. Upatnieks, A. Vander Lugt, and E. N. Leith, *Correction of lens aberrations by means of holograms*, Appl. Opt. **5** (1966), no. 4, 589–593.

[125] P. J. van Heerden, *A new optical method of storing and retrieving information*, Appl. Opt. **2** (1963), no. 4, 387–392.

[126] ———, *Theory of optical information storage in solids*, Appl. Opt. **2** (1963), no. 4, 393–400.

[127] R. S. Weis and T. K. Gaylord, *Lithium niobate: summary of physical properties and crystal structure*, Appl. Phys. A **37** (1985), 191–203.

[128] A. Yariv, *Optical Electronics in Modern Communications*, 5 ed., Oxford University Press, 1997.

[129] A. T. Yariv and P. Yeh, *Optical waves in crystals: propagation and control of laser radiation*, Wiley, New York, 1984.

[130] S. Yin, H. Zhou, F. Zhao, M. Wen, Z. Zhang, and F. T. S. Yu, *Wavelength–multiplexed holographic storage in a sensitive photorefractive crystal using a visible–light tunable diode laser*, Optics Communications **101** (1993), 317–321.

[131] F. T. S. Yu, S. Wu, A. W. Mayers, and S. Rajan, *Wavelength multiplexed reflection matched spatial filters using* $LiNbO_3$, Optics Communications **81** (1991), no. 6, 343–347.

[132] F. Zernike and B. R. A. Nijboer, Colloq. Int. C. N. R. S. (1949), no. 1, 227–235.

[133] J. Zhang, B. Tao, and J. Katz, *Turbulent flow measurement in a square duct with hybrid holographic PIV*, Exp. Fluids **23** (1997), 373–381.

[134] T. Zhang and I. Yamaguchi, *Three-dimensional microscopy with phase-shifting digital holography*, Opt. Lett. **23** (1998), no. 15, 1221–1223.

[135] X. H. Zhang, J. J. Xu, Q. Sun, S.M. Liu, G. Q. Zhang, H. J. Qiao, F. F. Li, and G. Y. Zhang, *Dual-wavelength nonvolatile holographic storage*, Optics Communications **180** (2000), no. 4-6, 211–215.

[136] F. Zhao, H. Zhou, S. Yin, and F. T. S. Yu, *Wavelength–multiplexed holographic storage by using the minimum wavelength channel separation in a photorefractive crystal fiber*, Optics Communications **103** (1993), 59–62.

[137] H. Zhou, F. Zhao, and F. Yu, *Angle-dependent diffraction efficiency in a thick photorefractive hologram*, Appl. Opt. **34** (1995), no. 8, 1303–1309.